Multi-Sensor System Design for In-Situ Ocean Surface Monitoring Using Wave-Energy-Harvesting

Vom Promotionsauschuss der
Technischen Universität Hamburg
zur Erlangung des akademischen Grades
Doktor-Ingenieur (Dr.-Ing.)

genehmigte Dissertation

von
Julius Harms

aus
Monaco

2023

1. Gutachter: Prof. Dr.-Ing. Thorsten A. Kern
2. Gutachter: Prof. Dr.-Ing. Bernd-Christian Renner
Prüfungsvorsitzender: Prof. Dr.-Ing. Robert Seifried

Tag der mündlichen Prüfung: 20.07.2023

DOI: https://doi.org/10.15480/882.8544

ORCID: Julius Harms
https://orcid.org/0000-0001-6172-5345

Abstract

Multi-Sensor System Design for In-Situ Ocean Surface Monitoring Using Wave-Energy-Harvesting

As the demand for high-spatial-resolution in-situ ocean monitoring to study the impacts of climate change increases, there is a growing need for adaptable and cost-effective technologies that enable large-scale deployments. Conventional oceanographic instruments, while effective for traditional measurements, are expensive and lack modularity for innovative setups. Additionally, the mainly battery-powered operation limits the capability for long-term monitoring. In this thesis, a systematic design approach for a multi-sensor monitoring system is proposed to improve the availability and accessibility of in-situ sea surface observations. To address these challenges, this thesis proposes a system design based on a flexible measurement module, an embedded conductivity and temperature sensor, and a wave energy harvester. The modular architecture of the measurement system includes essential sensors for GPS position, acceleration, and environmental parameters, and allows hardware-agnostic sensor extension and custom configuration of measurement settings. Design principles for an embedded conductivity and temperature sensor for salinity measurement are derived to present a cost-effective and compact solution tailored to the requirements of sea surface monitoring. In addition, a model-based design approach for a compact wave energy harvester is presented to propose a self-sufficient system for long-term deployments. This autonomous multi-sensor drifter system can pave the way for the next generation of in-situ sea surface monitoring, enabling innovative, high spatial resolution measurement deployments in large quantities.

Contents

Symbols

Symbol	Description	Unit
A	Surface area	m^2
α	Temperature coefficient	-
B	Magnetic field	$\mathrm{T} \mid \frac{\mathrm{Vs}}{\mathrm{m}^2}$
$\beta_{\mathrm{t,s}}$	Ratio of translator to stator pole width	-
C	Electric capacitance	F
D_1	First order damping coefficient	$\frac{\mathrm{kg}}{\mathrm{s}}$
D_2	Second order damping coefficient	$\frac{\mathrm{kg}}{\mathrm{m}}$
D_3	Third order damping coefficient	$\frac{\mathrm{kgs}}{\mathrm{m}^2}$
d_{coil}	Diameter of coil wire	mm
δ_{p}	Translator pole shift	-
E	Electric field	$\frac{\mathrm{V}}{\mathrm{m}}$
ε_0	Vacuum permittivity	$\frac{\mathrm{F}}{\mathrm{m}}$
ε_{r}	Material permittivity	-
$\mathbb{E}[X]$	Expected value	-
F	Force	N
f	Frequency	Hz
f_{r}	Resonance frequency	Hz
f_{s}	Sampling frequency	Hz
G	Gain of operational Amplifier	dB
g	Gravity constant	$\frac{\mathrm{m}}{\mathrm{s}^2}$
γ_{flap}	Wave flume flap angle	$^\circ$
H	Geometric parameter of height	m
H_0	Distances between water surface in equilibrium and lower boundary of float	m
H_{air}	Airgap of generator	m
H_{s}	Significant wave height	m
H_{T}	Translator pole height	m
I	Electric current	A
J	Electric current density	$\frac{\mathrm{A}}{\mathrm{m}^2}$

Symbol	Description	Unit
j	Imaginary unit, $j = \sqrt{-1} \in \mathbb{C}$	-
k	Inductive coupling factor	-
κ_{cell}	Conductivity sensor cell constant	$\frac{1}{\text{m}}$
K_{s}	Spring constant	$\frac{\text{N}}{\text{m}}$
L	Electric inductance	H
ℓ	Geometric parameter of length	m
λ_{exp}	Tuning parameter for damping forces in experiment	$\frac{\text{kg}}{\text{s}}$
m	Mass	kg
μ_0	Vacuum permeability	$\frac{\text{H}}{\text{m}}$
μ_{r}	Material permeability	-
N	Number of coil turns	-
n	Integer counter for a number of ...	-
$n_{\text{c,pair}}$	Number of coils pairs	-
n_{s}	Number of coils in stator	-
ω	Angular frequency	$\frac{\text{rad}}{\text{s}}$
ω_{P}	Peak frequency of wave spectrum	$\frac{\text{rad}}{\text{s}}$
P	Electric power	W
Φ	Magnetic flux	Wb | Vs
Ψ	Coil independent power potential of generator	m V^2
Ψ_{N}	Coil independent power potential of generator normalized to its maximum	-
r_{T}	Translator radius	m
r	Geometric parameter of radius	m
R	Electric resistance	Ω
$\mathscr{R}$	Magnetic Resistance	$\frac{1}{\text{H}}$
$r_{\text{M,i}}$	Inner radius of generator magnet	m
$r_{\text{M,o}}$	Outer radius of generator magnet	m
$r_{\text{S,i}}$	Inner radius of stator pole	m
$r_{\text{S,o}}$	Outer radius of stator pole	m
s	Complex frequency domain parameter of Laplace transformation	$\frac{\text{rad}}{\text{s}}$
σ	Water conductivity	$\frac{\text{S}}{\text{m}}$
T	Temperature	°C | K
t	Time	s
τ_{p}	Pole pitch of translator	m
τ_{s}	Slot pitch of stator	m
Θ	Magnetomotive force	A turns
V	Electric voltage	V
v	Velocity	$\frac{\text{m}}{\text{s}}$

Symbol	Description	Unit
v_{rel}	Relative velocity of translator, $v_{\mathrm{rel}} = \dot{x}_{\mathrm{rel}}$	-
W_{CM}	Width of generator coil and magnet	m
W_{C}	Width of generator coil	m
W_{M}	Width of generator magnet	m
W_{S}	Width of stator pole	m
W_{T}	Translator pole width	m
x	Movement coordinate of translator	m
ξ	Deflection of buoy or plate to still water level	m
$\Delta\xi$	Relative deflection between buoy and plate	m
x_{rel}	Relative translator position, $x_{\mathrm{rel}} = \frac{x}{\tau_{\mathrm{p}}}$	-
Z	Electric impedance	Ω

Indices and Distinctions

Symbol	Description
$\widehat{\blacksquare}$	Peak value
$\overline{\blacksquare}$	Mean value
$\vec{\blacksquare}$	Vector property
$\dot{\blacksquare}$	First time derivative
$\ddot{\blacksquare}$	Second time derivative
$\blacksquare_{\mathrm{b}}$	Parameter of WEC buoy
$\blacksquare_{\mathrm{coil}}$	Parameter of coil
$\blacksquare_{\mathrm{damp}}$	Damping parameter
$\blacksquare_{\mathrm{el}}$	Electric property
$\blacksquare_{\mathrm{max}}$	Maximum value
$\blacksquare_{\mathrm{meas}}$	Measurement result
$\blacksquare_{\mathrm{mech}}$	Mechanical property
$\blacksquare_{\mathrm{min}}$	Minimum value
$\blacksquare_{\mathrm{p}}$	Parameter of WEC plate
$\blacksquare_{\mathrm{sim}}$	Simulation result

Abbrevations

AC	alternating current
ADC	analog-digital-converter
API	application programming interface
ASF4	Advanced Software Framework 4
AUV	autonomous underwater vehicle
AWG	arbitrary waveform generator
BJT	bipolar junction transistor
CAN	Controller Area Network
CARTHE	Consortium for Advanced Research on Transport of Hydrocarbon in the Environment
CMOS	complementary metal-oxide-semiconductor
CODE	Coastal Ocean Dynamics Experiment
CT	conductivity and temperature
CTD	conductivity temperature depth
DAC	digital-analog-converter
DAE	differential algebraic equation
DC	direct current
DDS	direct digital synthesis
DOF	degrees of freedom
ECAL	electronic abstraction layer
ECV	essential climate variables
EMF	electromotive force
EOOS	European Ocean Observing System
ESA	European Space Agency
FEM	finite element method
FFT	fast fourier transformation
FSM	finite-state machine
FSPMLM	flux switching permanent magnet linear machine
GBWP	gain bandwidth product
GDP	Global Drifter Program
GOOS	Global Ocean Observing System
GOSIC	Global Observing Systems Information Center
GUI	graphical user interface
I^2C	inter-integrated circuit
IC	integrated circuit
ICBM	Institute of Chemistry and Biology of the Sea
ICON-ESM	ICON Earth system model
iMEK	Institute for Mechatronics in Mechanics

IMU	inertial measurement unit
IoT	Internet of Things
ISR	interrupt service routine
ITS-90	International Temperature Scale of 1990
JONSWAP	Joint North Sea Wave Project
LDO	low-dropout regulator
LEO	low-earth orbit
MCAL	microcontroller abstraction layer
MCU	microcontroller unit
MEO	medium-earth orbit
MPPT	maximum power point tracking
NOAA	National Oceanic and Atmospheric Administration
NSD	noise spectral density
NTC	negative temperature coefficient
op-amp	operational amplifier
OSI	Open Systems Interconnection
PCB	printed circuit board
PHT	pressure, humidity and temperature
PSS-78	Practical Salinity Scale of 1978
PTC	positive temperature coefficient
PTO	power takeoff
PU	polyurethan
PWM	pulse width modulation
RTD	resistance temperature detectors
RTOS	real-time operating system
SAIMIDRIS	Sailing Intelligent Micro Drifter Swarms
SPI	serial peripheral interface
SPMLM	synchronous permanent magnet linear machine
SRLM	switched reluctance linear machine
SRPA	self-reacting point absorber
SSS	sea surface salinity
SST	sea surface temperature
SVP	Surface Velocity Program
TICS	transformer type inductive conductivity sensor
TTL	transistor–transistor logic
TUHH	Hamburg University of Technology
UART	universal asynchronous receiver transmitter
USV	unmanned surface vehicle
VRPMLM	variable reluctance permanent magnet linear machine
WEC	wave energy converter

1 Introduction

The impacts of climate change are becoming increasingly evident, with significant and far-reaching ramifications for both, current and future generations. In response, the international community joined forces to address this global challenge through initiatives such as the Paris Agreement [1] aimed at limiting global warming to 1.5 degrees Celsius above pre-industrial levels. To achieve this goal a thorough understanding of the state of the ocean, one of the largest and most important components of Earth's climate system needs to be established.

Ocean monitoring and in-situ data collection are vital for predicting weather patterns and validating climate models. Traditional ocean observation using research vessels, autonomous underwater vehicles (AUVs), gliders, and Argo floats are commonly used to observe the distribution of climate variables, in particular in the vertical direction from the surface to great depth. However, the investigation of horizontal scales at the sea surface becomes increasingly important for climate science [2–4]. Monitoring the boundary layer between ocean and atmosphere is crucial, as it plays a critical role in the exchange of heat, moisture, and greenhouse gases. The exchange processes cause effects on small horizontal scales, partly observable by remote sensing methods. However, satellite-based observations provide only a few environmental parameters, they must be validated against in-situ data, and their accuracy and spatial resolution are limited. As a result, in-situ monitoring of the ocean surface on small horizontal scales is of growing significance for ocean science.

Ocean drifters without propulsion are suitable instruments for providing valuable data on sea surface effects, and they have become a vital tool for climate scientists. Drifters have a rich history as traditional oceanographic instruments, with diverse applications ranging from measuring ocean currents to monitoring plastic pollution [5] and tracking oil spill dispersions [6]. However, the way drifters are used is rapidly changing, advancing their potential use for climate science. Due to lower instrument costs, deployments can be implemented in large numbers to increase the measurement resolution of the sea surface. Lower costs will democratize the field of ocean observation [7, 8]. Innovative research projects aim to use intelligent drifter swarms to explore oceanographic frontal dynamics with high measurement resolution, and to study accumulation processes

(e.g., the SAIMIDRIS project [9]).
Despite the growing need for low-cost drifter instruments with enhanced monitoring capabilities, current systems in the market lack innovation and are primarily traditional designs, often too expensive and inflexible for widespread usage. Furthermore, smaller systems developed by research groups for specific research applications are often unsuitable for other purposes due to a lack of a systemic approach or modularity. This, in turn, makes it difficult to expand or improve these systems without incurring significant additional development and expenses.

The focus of this thesis is to improve the accessibility of cost-effective, user-friendly multi-sensor monitoring to support innovative sea-surface monitoring approaches. This will be achieved through a systematic analysis of methods leveraging modular design and self-sufficiency. A configurable architecture will be devised, facilitating hardware agnostic integration of various sensor technologies while enabling wave energy harvesting to oppose increasing energy demands due to more complex instrumentation. The fundamentals of sensors for critical measurement variables are investigated, with the overall goal of identifying new approaches that allow for meeting the systemic requirements for a compact and cost-effective design. This cross-disciplinary approach is expected to enable higher quantity deployments while improving the ability to perform more complex measurement tasks in the upper ocean.

The thesis is divided into several chapters, beginning with contextualizing existing solutions and deriving the research question in chapter 2. Chapter 3 presents a comprehensive system design of a monitoring platform, with its main components discussed in chapters 4, 5, and 6. Chapter 4 covers a hardware and software architecture that enables flexible monitoring through a modular system design. Chapter 5 focuses on cost-effective salinity measurement methods, particularly the electromagnetic fundamentals of inductive conductivity sensors and the design of a low-cost and fully-embedded sensor. Salinity sensors are crucial for ocean monitoring, primarily through conductivity and temperature measurements. Chapter 6 addresses the power demand of more complex instrumentation by proposing a wave energy harvesting system based on a linear generator for power take-off. A multi-domain optimization approach is presented that utilizes model-based design methods to estimate the potential energy throughput of the harvesting system. Finally, the results of all components will be reviewed and the potential of the developed system will be evaluated in the conclusion chapter 7.

2 System Analysis and Problem Definition

This chapter introduces the research question of this thesis. Beginning with an introduction to the importance of different environmental parameter and their impact on the climate and the Earth's ecosystem. Subsequently, instruments for ocean monitoring are introduced and relevant areas of sensor technology and energy supply to monitoring systems are examined. The drawbacks of existing monitoring platforms are presented and the chapter concludes with the formulation of the research questions.

2.1 Environmental Monitoring: Understanding Earth's Ecosystems and Climate

Human life significantly influences the planet, its climate, and its ecosystem. The enormous emission of greenhouse gases such as carbon dioxide and methane is the primary driver of global climate change, affecting life on earth [10]. The effects of climate change and environmental pollution from plastics, chemicals, and oil are destroying Earth's ecosystems at an alarming rate [11]. Accurately monitoring and comprehending changes of the environment is crucial to evaluate potential impacts on the planet. Systematic monitoring of a range of environmental parameters, along with data collection and model calculations, provides the scientific community with the means necessary to estimate the extent of changes and devise strategies to mitigate their impact. As a result, scientific insights play a critical role in shaping the decisions made by society's policymakers.

Monitoring the oceans plays a critical role as they regulate Earth's climate system and hold a vast diversity of species. Ocean currents transport heat around the globe, affecting both temperature and precipitation patterns. Therefore, a large area of oceanography focuses primarily on ocean currents and circulations. Oceanographic climate science focuses on the interface between the ocean and the atmosphere by observing heat fluxes, carbon transports, and waves. The Global Observing Systems Information

Center (GOSIC) defines essential climate variables (ECV) to study the empirical evidence needed to understand and predict climate evolution [12]. Water temperature and salinity, the density-defining parameters of ocean water, are important ECVs in oceanography. Next to wind and tides density is an essential driving mechanism for the flow and movement in the ocean and contributes to the exchange of energy with the atmosphere. The density profile determines the three-dimensional water movement, resulting in the transport of salt, heat energy, and greenhouse gases across the global ocean. Accordingly, a determination of density is important in order to derive, for example, the extent of the change in heat transport from the tropics to the Arctic. Quantifying the fluctuations of this climate process is crucial to be able to separate the natural variability from climate-related changes. Numerical climate models such as ICON Earth system model (ICON-ESM) [13] are valuable tools for these tasks and must be validated with measurement data.

Changes in ocean currents and temperatures can also impact marine ecosystems and the distribution of marine species, highlighting the need to monitor additional parameters in order to accurately assess and maintain the health of the ocean's biodiversity and ecosystems. Furthermore, ocean currents determine areas that are particularly affected by plastic and oil pollution [14, 15]. By tracking the distribution of plastic debris and monitoring the impacts of oil spills, areas that are particularly vulnerable to these pollutants can be identified to prioritize efforts to reduce their impacts. Coastal regions, rivers, and estuaries in particular play a major role in the release of pollutants into the ocean.

Overall, ocean monitoring is crucial in maintaining the health and resilience of the planet's ecosystems, making access to measurement data a critical component of this process. Unfortunately, ocean measurements are often associated with significant costs and effort, which can hinder large-scale monitoring with high spatial resolution through the deployment of measuring instruments in large quantities. This can also prevent developing countries and research groups with low research budgets from monitoring their regional impacts [7, 8, 16]. Thus, finding cost-effective ways to collect accurate and comprehensive ocean data is essential to promote equitable and sustainable monitoring efforts globally.

2.2 Monitoring the Upper Ocean: Essential Parameters and Challenges

The ocean surface, usually defined as the top 100 m of the ocean, plays a crucial role in modern climate research because important exchange processes occur at the boundary layer between the ocean and the atmosphere. Many of these processes are turbulent

and occur on very small scales, down to a few meters [17, 18]. An example is vertical convection induced by atmospheric cooling or evaporation: The rising density at the ocean surface leads to instabilities in the vertical direction and a locally constrained overturning of the water column. As a result, three-dimensional turbulence is induced and previously homogeneous surface conditions become scattered. Quantifying these small-scale vertical flows clearly poses a challenge in observational climate research. Another example are surface flows often appearing as meanders and eddies rather than laminar currents. In particular, in coastal waters or freshwater estuaries, strong frontal dynamics evolve due to turbulent surface flow [4, 14, 19]. These fronts are highly variable in space and time which makes long-term and large-scale in situ observation and detection still problematic with traditional oceanographic instruments [2]. In the horizontal dimension, climate scientists lack measurement data with high spatial resolution. This is mainly addressed by satellite observations, but remote sensing requires ground-truth validation by in-situ measurements. In addition, the accuracy and spatial resolution of remote sensing is limited.

Apart from climate science, many other research fields including meteorology, biology, and chemistry require a variety of additional parameters to monitor water pollution, biodiversity, ecosystem health, wave patterns, and many more. Accurately determining chemical and biological indicators, such as chlorophyll, dissolved oxygen, pH values, or microplastic concentrations, is a complex process that cannot be entirely accomplished using compact and low-cost sensor technology.

To address these challenges, a monitoring platform is required that enables cost-efficient multi-sensor monitoring of the ocean surface, allowing for deployments in large numbers, including coastal areas. The sensor technology applied must be suitable for use in the upper ocean and appropriate to be implemented into small and low-cost measurement platforms. Given the significant importance of temperature and salinity parameters, the following will provide further details about the variables measured and the sensor technology utilized in their monitoring.

2.2.1 The Importance of Sea Surface Salinity Monitoring

For ocean circulation models, sea surface salinity (SSS) is an essential variable acquired by e.g. the European Space Agency (ESA) via remote sensing missions such as SMOS, Aquarius, and SMAP. Global SSS observations have improved the understanding of climate variability, ocean evaporation, salt transport, and salinity fronts, and have contributed to many other important insights in oceanography and biogeochemistry [20]. Although remote sensing has greatly improved ocean observations, in-situ monitoring with conductivity sensors remains essential.

In oceanography, the salinity of the water is determined by ionic conductivity and temperature according to the Practical Salinity Scale of 1978 (PSS-78) [21] (cf. appendix A.2). The PSS-78 defines a unitless measure, given by the practical salinity unit PSU, which can be understood as $\frac{g}{kg}$ or parts per thousand (ppt). The salinity of the global ocean ranges from 5 to 40 PSU, the largest parts of the ocean having a salinity of about 35 PSU (cf. figure 1). The associated conductivity ranges from 0.1 to 6.5 $\frac{S}{m}$ with a volumetric weighted mean of 3.31 $\frac{S}{m}$ [22].

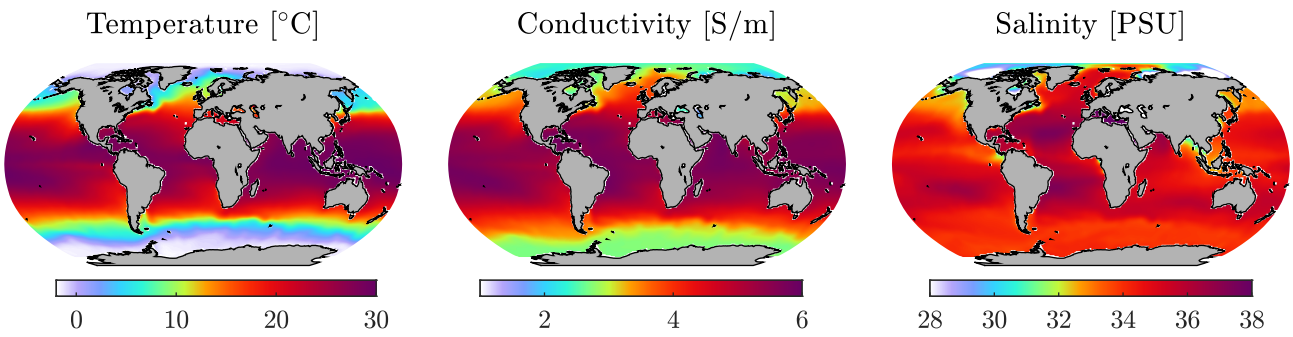

Figure 1: *Global map of sea surface temperature, sea surface conductivity, and sea surface salinity. Yearly average between 2005 and 2017 [23].*

The accuracy and spatial resolution of remote sensing are limited. The Aquarius mission has a target accuracy of 0.2 PSU, provides a spatial resolution of 40 to 150 km, and measures only surface parameters [24]. Observing effects at smaller scales, at higher accuracy, or in different depths requires the use of in-situ oceanographic sensors. Mesoscale eddy currents, for example, typically have a horizontal extent of less than 100 km [17].

2.2.2 The Importance of Sea Surface Temperature Monitoring

Water temperature is another ECV calling for in-situ measurements for a variety of reasons, often with accuracy requirements of 10 mK or even less than 1 mK. For once, accurate salinity and density determination rely on accurate temperature and conductivity measurements. Temperature gradients and profiles provide information on heat fluxes and stratification, allowing the monitoring of global warming. To increase the spatial resolution of temperature measurements, the cost of the instrument is an important factor weighing against the required accuracy of the research question. The sea surface temperature (SST) is often determined by remote sensing from satellites, which requires ground-based reference data for validation, as in the NorthSat-X project [25]. While deep ocean measurements require an accuracy of greater than 1 mK [26], surface temperature measurements with an accuracy of 100 mK to 10 mK are usually sufficient.

Globally, ocean temperature ranges from −5 °C to 35 °C, providing the required sensor range for an ocean surface temperature sensor (cf. figure 1).
The Joint Panel on Oceanographic Tables and Standards recommends the use of the International Temperature Scale of 1990 (ITS-90) for all reported oceanographic data [27]. This is of great importance because ITS-90 has significant implications for the calculation of seawater properties such as salinity.

2.3 Oceanographic Sensors: State-of-the-Art Devices and their Drawbacks

Oceanographic sensors are essential devices for measuring and monitoring key ocean parameters. Following the general definition of the sensor terminology used here, the technologies used for measuring conductivity and temperature are considered in more detail.

2.3.1 Terminology of Sensor Devices

In the context of this work, the term sensor describes a device that senses a physical measurand; it converts and processes the corresponding data to provide a measurement result. The stages of the measurement chain are shown in figure 2. The primary sensor

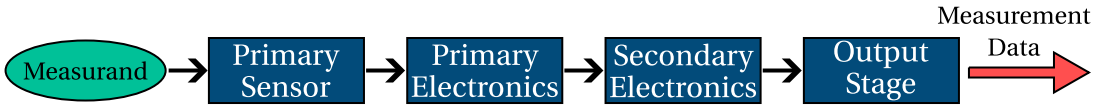

Figure 2: *Terminology for defining the measurement chain of a sensor device.*

refers to the physical component that senses the measurand. E.g. for a temperature sensor, the thermistor defines the primary sensor, that senses the temperature. The primary sensor is connected to the primary electronics that convert the measured signal into an electrical signal. The primary electronics also act as a transducer that can use measurement bridges, amplifiers, and other analog circuitry to convert the measurement into an electric signal. The electrical signal is then further processed by the secondary electronics, which convert the analog signal into a machine-readable property. Typically, this involves digital-to-analog conversion and the use of a microcontroller unit (MCU). Finally, the output stage of the sensor device defines the means by which the measurement data is connected and transmitted. This may include, among other things, the implementation of a serial communication interface.

For the comparison and evaluation of different sensor technologies and their measurement uncertainty, the parameters of accuracy, precision, and resolution are considered. A clear definition of the terms and examples can be found in appendix A.1.

2.3.2 CTD Probes: The State-of-the-Art Oceanographic Sensor

The most important measurement device in oceanography is the conductivity temperature depth (CTD)-Probe, used for temperature, conductivity, and density determination. Sea-Bird Scientific[28] and Sea & Sun Technology[29] are common suppliers of these types of probes and other oceanographic sensors. The requirements for a CTD system are defined by UNESCO in the *Manual of Quality Control Procedures for Validation of Oceanographic Data* [30] and specify the ratings shown in table 4.

	Range	Accuracy	Resolution	Stability / month
Conductivity	0.1 - 6.5 $\frac{S}{m}$	0.5 $\frac{mS}{m}$	0.1 $\frac{mS}{m}$	0.3 $\frac{mS}{m}$
Temperature	−2 - 32 °C	3 mK	0.5 mK	1 mK

Table 4: *UNESCO requirements for conductivity and temperature sensors on CTD systems [30]*

Sensors for deep-sea measurements today achieve accuracy values of less than 0.3 $\frac{mS}{m}$ and allow salinity readings with an accuracy of below 0.003 PSU [26]. Measurements at the surface show much larger variations in salinity and are therefore adequate with accuracy around 0.1 to 0.05 PSU (10 to 5 $\frac{mS}{m}$ at 35 PSU and 15 °C). Additionally, to protect CTD sensors from pressure, they can be implemented with expensive titanium housings. CTDs are therefore over-equipped and inconvenient for low-cost measurements of surface salinity and temperature. Alternatively, universal solutions, e.g. from the process industry or water monitoring, can be used. However, these sensors are often part of a measurement system consisting of the sensor and additionally required measurement or logging devices, which makes integration into a small monitoring platform difficult. In the following, sensors for conductivity and temperature measurement are examined, the most common measurement methods are presented and technologies available on the market are compared.

2.3.3 Water Conductivity Measurement Approaches

Most conductivity sensors available on the market are intended for the process industry, oceanography, hydroponics, or aquaculture. Typically, the sensors are either

electrode-based cells or inductive sensors. In contrast to the devices used for temperature measurement, there are more high-precision conductivity sensors available than low-cost consumer products. Before commercial products are evaluated in more detail, the working principles of electrode-based and inductive sensors are introduced.

Electrode-based Conductivity Cell The measurement principle of the conductivity cell can be compared to a simple resistance measurement between two electrodes. For this purpose, an alternating current (AC) flow is generated between electrodes immersed in water, and the voltage potential at the electrodes is measured. This results in a resistance value, which is converted to conductivity using the specific conductance and the electrode spacing. The use of AC over direct current (DC) prevents polarization at the electrodes, since DC potentials could cause ion accumulation on the electrode surface [31]. The construction of conductivity cells differs in the arrangement and material of the electrodes. In a simple two-electrode cell (cf. figure 3b), the voltage and current are measured between the same pair of electrodes. A four-electrode measurement uses two electrodes to create a current flow and two electrodes placed within the flow to measure the voltage drop. For arrangements with more than four electrodes (cf. six-electrode in figure 3c), a homogeneous electric field is created with a series of electrodes and the current flow within the field is measured. This reduces the influence of fringe effects and field distortion. Common materials are platinum, and for designs less expensive graphite. [32]

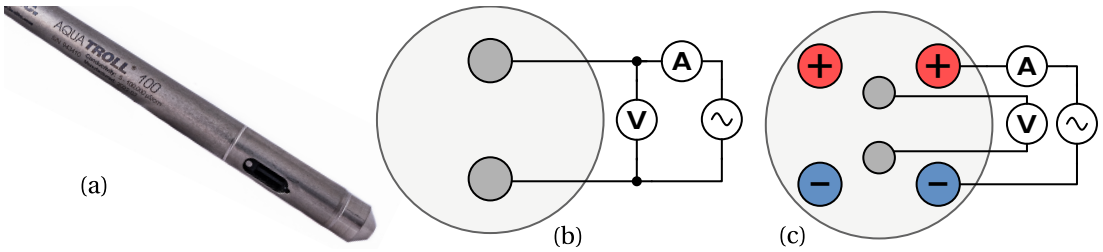

Figure 3: *a: Electrode-based conductivity sensor Aqua TROLL 100 by In-Situ [33]; b: Concept sketch of two-electrode cell; c: Concept sketch of the six-electrode cell.*

Any AC resistance measurement can be used as a measurement circuit (primary electronics). Similar to oceanographic temperature sensors, high-precision oceanographic conductivity sensors are based on the Wien bridge oscillator circuit [34].

Transformer Type Inductive Conductivity Sensor The established inductive measurement principle for measuring the conductivity of liquids is a transformer type inductive conductivity sensor (TICS) based on two coaxially aligned toroidal coils: one serves as the excitation coil and the other as the sensing coil. The AC-current flowing through the primary coil generates an alternating magnetic flux in its core, inducing an

ionic current in the water loop surrounding the sensor (cf. figure 4). This AC-current, in turn, generates an alternating magnetic field in the core of the sensing coil and hence induces a voltage.

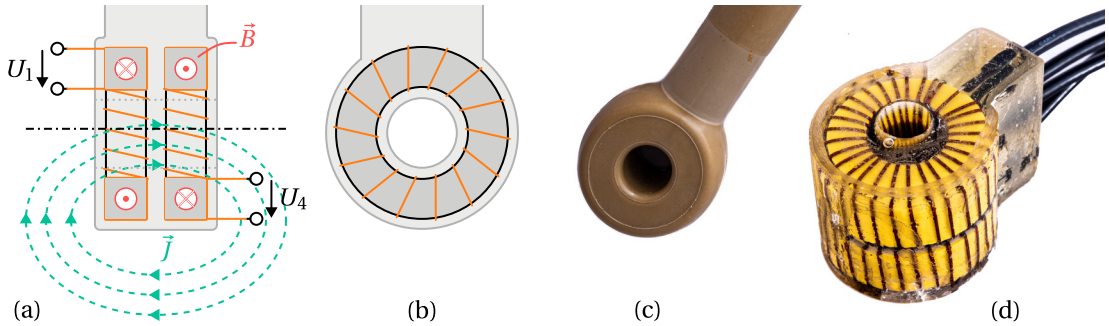

Figure 4: *a: Schematic diagram of a transformer-type sensor surrounded by a conductive fluid. Green vectors display the current density, red the magnetic field strength; b: Schematic sketch of a side view of a TICS; c: Inductive conductivity sensor Indumax CLS50D by Endress & Hauser; d: Own prototype of a TICS with a transparent housing.*

The first transformer type concept was introduced by Relis [35, 36] in 1947, further developed and patented by Esterson [37, 38] and Hinkelmann [39–41] in the late 1950s. While Relis presented this concept as a general electrodeless method for measuring the conductivity of electrolytes, Esterson and Hinkelmann were already adapting the TICS principle for the development of an inductive conductivity sensor for the ocean [37, 39]. Striggow and Dankert [42] also explicitly describe the sensor theory for oceanographic applications. Numerous other patents by sensor manufacturers in the process industry [43–49] show the interest in inductive sensors to this day.
A recent contribution to the development of low-cost inductive conductivity sensors is published by Hui et al. [50] who present a low-cost, compact electronic conductivity sensor based on the TICS concept. The sensor presented has a maximum error of 60 $\frac{\text{mS}}{\text{m}}$ with material costs of $30.

Comparison of Conductivity Sensor Types It is more difficult to achieve the same measurement accuracy with inductive sensors as with electrode-based sensors. The small distance between the electrodes results in a defined current flow that is robust to distortion. Inductive sensors are more susceptible to interference from external fields. The sensor manufacturer RBR finds, that disturbances of the field within 15 cm of the sensor can significantly affect the measurement [51]. To reduce the influence of external disturbances, various housing approaches and shields between coils have been developed [52]. Other approaches reduced the influence of the external fields by defining a measuring tube for the water around the sensor [53], which is difficult to apply to oceanographic sensors. Industrial research continues to increase the inductive sensor

sensitivity [54, 55] to achieve similar accuracy as electrode-based sensors. For many other oceanographic applications, therefore the electrode cell sensor is the widely used standard. While it is true that for measurements with very high accuracy requirements (deep-sea measurements) a conductivity cell provides more reliable precision, inductive sensors come close to meeting these requirements and may be a sufficient alternative for many applications.

In terms of long-term stability, inductive sensors have a large advantage, since polarization and precipitation on the electrode surfaces cannot occur. Conductivity cells with electrodes directly exposed are sensitive to biofouling and corrosion. Biofouling refers to the accumulation of marine organisms, such as algae, barnacles, and other small marine animals, on the surface of the sensors, which can interfere with their ability to function properly. While UV LEDs can be used to prevent biofouling on the measurement cell, electrode corrosion is a persistent problem with an unprotected sensor over long periods of use. Near-surface long-term observations are particularly susceptible to biofouling and sensor degradation, due to high biodiversity in the upper water layer. Minimal maintenance required for non-contact measurement principles offers a better solution. For this reason, the process industry prefers low-maintenance inductive sensors for fixed installations. In marine research, the use of inductive sensors is less common. Just a few long-term observations rely on inductive sensors, e.g., a small number of Argo floats [51]. In addition, flushing of inductive sensors is improved due to their larger opening compared to the smaller electrode-based sensors. For measurements of high dynamic changes in salinity, such as in polar regions, estuaries, or for surface salinity measurements, the increased flushing factor results in faster response times [56].

One reason for the strict use of conductivity cells could be that oceanographic science relies on a traditionally established sensor technology allowing comparability of measurement results. Although electrode-based sensors are commonly used in oceanographic applications, the inductive CTD from RBR demonstrates that this sensor type is also appropriate. RBR claims to achieve better resistance to surface fouling, resulting in a more robust measurement for floats and extending reliable lifetime [57]. The sensor meets UNESCO specifications for CTD systems [30] and achieves a typical drift of less than 1 $\frac{\mathrm{mS}}{\mathrm{m}}$ per year, with a simple two-point calibration [56].

Overview of Commercial Conductivity Sensors A closer look at the sensor technology available on the market (cf. table 5) confirms the dominant use of electrode-based conductivity sensors in oceanography. While common oceanographic sensor manufacturers mainly offer electrode-based conductivity sensors, inductive devices are more common in the process industry. The most prominent conductivity sensors in oceanographic research are from Sea-Bird (SBE4 [58]) and Sea & Sun [59] (cf. figure 5).

Both sensors have similar specifications and are intended for high-precision CTD measurements to great depths. Only two inductive sensors are marketed for oceanographic purposes, the embedded sensor from Aandreaa and the CTD logger from RBR. RBR's inductive sensor is not available as a stand-alone solution (cf. figure 5). For lower accuracy requirements for surface measurements, the AquaTroll 100 from In-Situ or the InduMax from Endress & Hauser offer more cost-effective solutions, still priced above 1000 € per sensor. In addition, industrial sensor integration is difficult due to the need for external transducers that are not designed for compact implementations.

	UNESCO CTD [30]	Sea & Sun [29]	Sea-Bird SBE4 [58]	Aanderaa 3919B [60]	RBRbrevio[3] [61]	Endress + Hauser CLS50D [62]	In-Situ Inc. AquaTroll 100 [63]	D2 inc. Ocean CT [64]
Type	-	Cell 7-pole	Cell 3-pole	Inductive	Inductive	Inductive	Cell 4-pole	Inductive
Industry	-	Ocean.	Ocean.	Ocean. Aquacul.	Ocean.	Process Industry	Aquacul. Industry	Ocean.
Range	0.1 to 6.5 $\frac{S}{m}$	0 to 7 $\frac{S}{m}$	0 to 7 $\frac{S}{m}$	0 to 7.5 $\frac{S}{m}$	0 to 8.5 $\frac{S}{m}$	200 $\frac{\mu S}{m}$ to 200 $\frac{S}{m}$	0 to 10 $\frac{S}{m}$	0 to 6 $\frac{S}{m}$
Accuracy	0.5 $\frac{mS}{m}$	0.2 $\frac{mS}{m}$	0.3 $\frac{mS}{m}$	1.8 $\frac{mS}{m}$	0.3 $\frac{mS}{m}$	15 $\frac{mS}{m}$ (0.5%)	15 $\frac{mS}{m}$ (0.5%)	2 $\frac{mS}{m}$
Depth	-	12 000 m	10 500 m	6000 m	6000 m	130 m	210 m	50 m
Price	-	€€	€€€	€€	*€€€	€	€	€€

Table 5: *Overview of different commercially available conductivity sensors. The price indication is based on manufacturer quotes for the lowest price sensor configuration.*
€: < 2000 €; €€: 2000 € to 4000 €; €€€: >> 4000 €
**RBR's inductive sensor is not available as a stand-alone solution.*

However, the demand for low-cost and small-size conductivity sensors is evident in many publications addressing the cost-effective measurement of water salinity [65–68], most of them for near the surface measurements or in estuarine areas. At the same time, the application of this low-cost sensor technology is often intended for long-term monitoring, such as the multi-sensor drifter considered here or other environmental monitoring tasks [68]. The CTD probes traditionally used for salinity measurements in oceanography do not provide a good cost-benefit ratio for long-term, near-surface measurements with lower accuracy requirements.

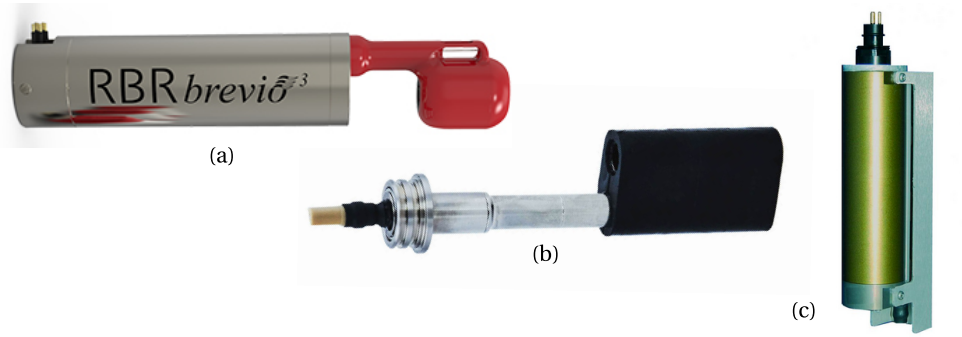

Figure 5: *Overview of different oceanographic conductivity censors. a: Inductive conductivity logger RBRbrevio³ by RBR [61]; b: Conductivity cell by Sea & Sun Technology [59]; c: Conductivity cell SBE4 by SeaBird [58]. Further conductivity sensors are depicted in figures 3, 4 and 34.*

2.3.4 Temperature Sensors for Oceanographic Applications

Temperature is one of the most common measurement parameters across industries and applications; therefore, countless sensor technologies and measurement approaches exist. Accuracy up 0.1 K, can be performed in countless different cost- and energy-efficient ways. Ocean temperature measurement with low accuracy requirements, e.g. for simple water temperature monitoring or meteorological purposes, can be easily implemented. However, jumping from a measurement accuracy of 100 mK to 10 mK presents a much more challenging task that requires thorough considerations to achieve a reliable instrument.
Temperature measurement can be performed with contacting and non-contacting sensors. State-of-the-art non-contacting optical temperature sensors, often based on Fabry-Pérot interferometer technology, can provide exceptional performance with high resolution of less than 1 mK and response times of less than 1 ms [69, 70]. These sensors are comparatively complex in design and require precise alignment and calibration of the interferometer components, requiring specialized expertise and equipment. Alternatively, infrared temperature sensors offer a less expensive and more straightforward option, but their accuracy is often very limited (±1 K). Contacting sensors providing high accuracy and repeatability continue to be the best compromise between accuracy and cost.

The best compromise between accuracy and cost is therefore still offered by contacting sensors, which can provide high accuracy and repeatability.
Traditional high-precision ocean temperature sensors, such as the Sea-Bird SBE 3S (cf. figure 6), are based on technology 50 years old: resistance measurement using the Wien Bridge oscillator circuit, introduced by Pederson [71] in 1969. Pederson later implemented the Wien bridge oscillator in high-precision conductivity cells [34].
Table 6 compares commercially available temperature sensors used in ocean monitoring.

Temperature sensors from industrial vendors are not listed due to a large number of options available. All sensors shown have similar specifications. For measuring SST, the SoundNine temperature sensor shows a good balance between accuracy and cost.

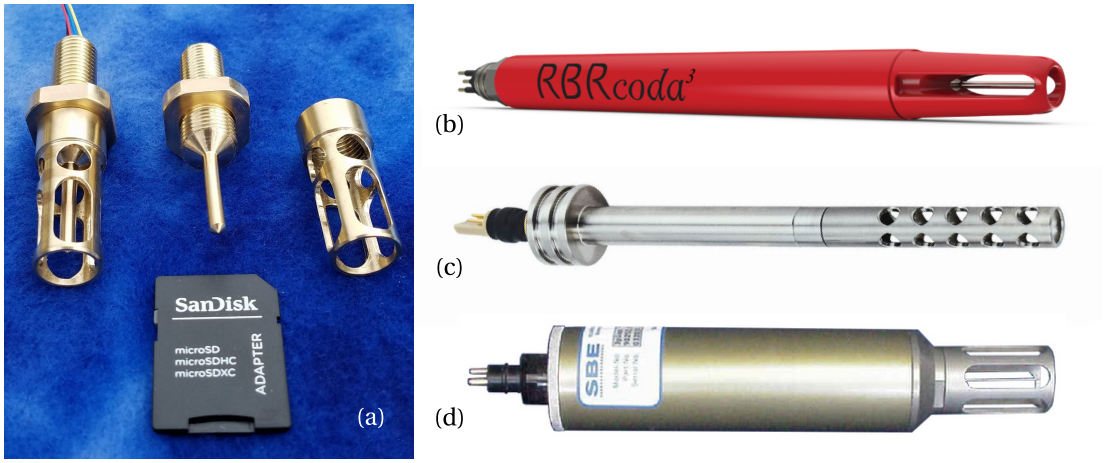

Figure 6: *Overview of different oceanographic temperature sensors. a: SoundNine temperature sensor with and without probe guard [72]; b: RBRcoda^3 temperature logger by RBR [73]; c: Sea & Sun temperature sensor [74]; d: SeaBird temperature probe SBE3 [75].*

	UNESCO CTD requirements [30]	SoundNine [72]	SeaBird SBE3S [75]	Sea & Sun [74]	RBRcoda^3 [73]
Initial Accuracy	3 mK	5 mK	1 mK	2 mK	2 mK
Resolution	0.5 mK	0.1 mK	0.04 mK	0.5 mK	0.05 mK
Stability	12 mK/year	3 mK/year	2 mK/year	not specified	2 mK/year
Range	−2 to 32 °C	−5 to 45 °C	−5 to 35 °C	−2 to 36 °C	−5 to 35 °C
Time Constant	-	800 ms	600 ms	150 ms	< 100 ms
Primary Sensor	-	Thermistor NTC	Thermistor NTC	RTD PT-100	Thermistor NTC
Transducer	-	not specified	Wien bridge	not specified	not specified
Price	-	€	€€€	€€	€€

Table 6: *Overview of different commercially available temperature sensors for ocean monitoring. The price indication is based on manufacturer quotes for the lowest price sensor configuration. €: < 500 €; €€: 500 € to 3000 €; €€€: > 3000 €*

2.4 Measurement Instruments for Ocean Monitoring

In recent decades, the demands of the scientific community for oceanographic data have increased significantly. The oceans and seas must be continuously monitored to predict their evolution. This has led to the development of advanced monitoring instruments, allowing real-time communication with high-precision sensors and outperforming traditional, expensive data collection on research vessels. One of the most important developments has been the transition from traditional static single-node short-term observations to dynamic multi-node long-term observations increasing the density of temporal and spatial sampling [76]. The advances in ocean observing technology are being driven in part by several programs operating internationally. The Global Ocean Observing System (GOOS) [77] is a global network of organizations working to develop and implement a coordinated ocean observing system. GOOS includes contributions from many countries and organizations around the world and provides a wide range of data on the physical, chemical, and biological properties of the oceans and on ocean-atmosphere interactions. The European Ocean Observing System (EOOS) [78] is a similar European-based program focused on improving understanding of the oceans around Europe and their role in Earth's climate and weather system. The programs rely on the collection of data by satellite remote sensing, in-situ sensors and buoys, ship-based observations, and specialized research vessels.
Ocean observation is mainly distinguished by vertical profile observation technologies and horizontal sea surface observation technologies [76]:

2.4.1 Instruments for Vertical Profiling Observations

Profiling observation collects data as a function of depth. This type of observation is often used to study the vertical distribution of parameters in the ocean, such as water temperature and salinity. Measurements in the water column at different depths are used to understand a variety of oceanographic phenomena, such as ocean circulation, the mixing of different water masses, the circulation of nutrients, and the distribution of marine organisms. Traditional profiling uses ship-based observations with CTD instruments, which are CTD sensors incorporated into an array of Niskin bottles (cf. figure 8a).
High operation costs of research vessels and the sparse resolution provided by them led to the development of AUVs [79]. An AUV is an unmanned vehicle, equipped with sensor technologies, allowing it to autonomously perform various oceanographic missions. One type of AUVs are Argo floats [80], playing an important role in profile measurements. Argo float is a free-floating buoy able to dive in the upper 2000 meters of the ocean, designed to drift with ocean currents, descend and resurface, and to transmit the collected data via satellite from the surface. Argo floats are deployed in large numbers

(close to 4000 in 2022 [81] cf. figure 7) around the world and cover most of the world's oceans. Aside from a bladder for vertical movement, the floats have no propulsion. Another type of AUVs, allowing propulsion to a certain degree are underwater gliders

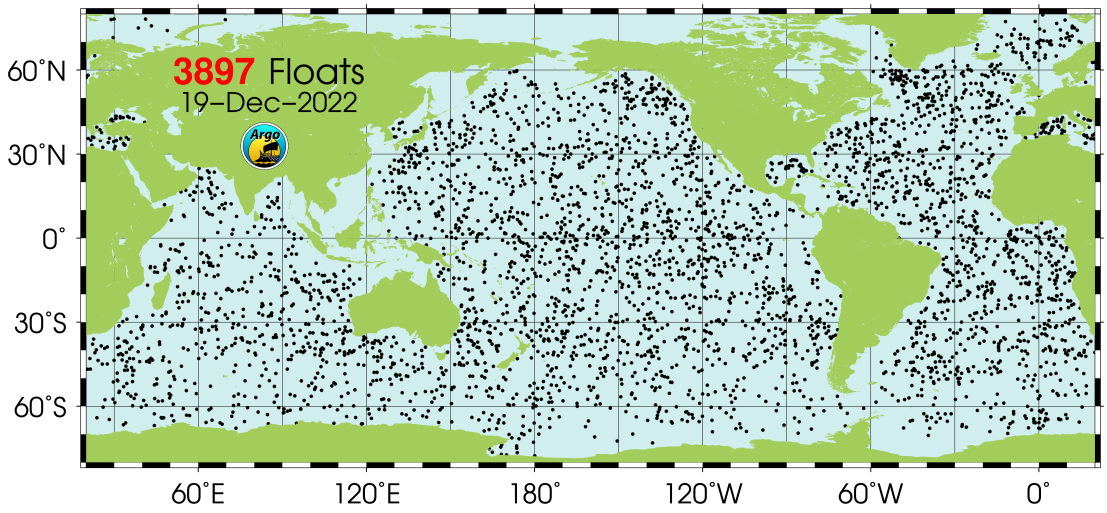

Figure 7: *Global map showing Argo float locations on the 19.12.2022 [81]*

[82, 83], which can ascend and descend similar to floats but are also equipped with wings that allow them to move forward vertically. Gliders are often used for long-term observations of the ocean, as they can remain at sea for weeks or months at a time. Profiling instruments are unsuitable for observing effects on the sea surface, as they only offer a very low horizontal resolution.

2.4.2 Instruments for Horizontal Sea Surface Observations

Ocean surface observation is mainly used to study surface circulation and transport processes. Since the first satellite missions, remote sensing has become essential for global ocean observation [76]. Today, much of the ocean surface geophysical parameters, such as temperature, salinity, and wave height, can be determined directly by remote sensing [76]. While oceanographic satellites provide global-scale data, small/sub-mesoscale observations require in-situ sensors. The spatial resolution and parameter accuracy of remote sensing are limited and require in-situ sensors such as moored buoys, drifters, and ships. Research projects like NorthSat-X [25] aim to support existing satellite data with in-situ measurements of a remote-controlled catamaran, sea marks, and drifters. To increase the temporal and spatial resolution of the North Sea satellite data, comprehensive validation especially in coastal areas is crucial.
In addition to observations from research vessels, other ship-based measurements can be obtained by ferry boxes [84]. A ferry box is a type of in-situ ocean observing instrument mounted on a ferry or other commercial vessel and is typically equipped

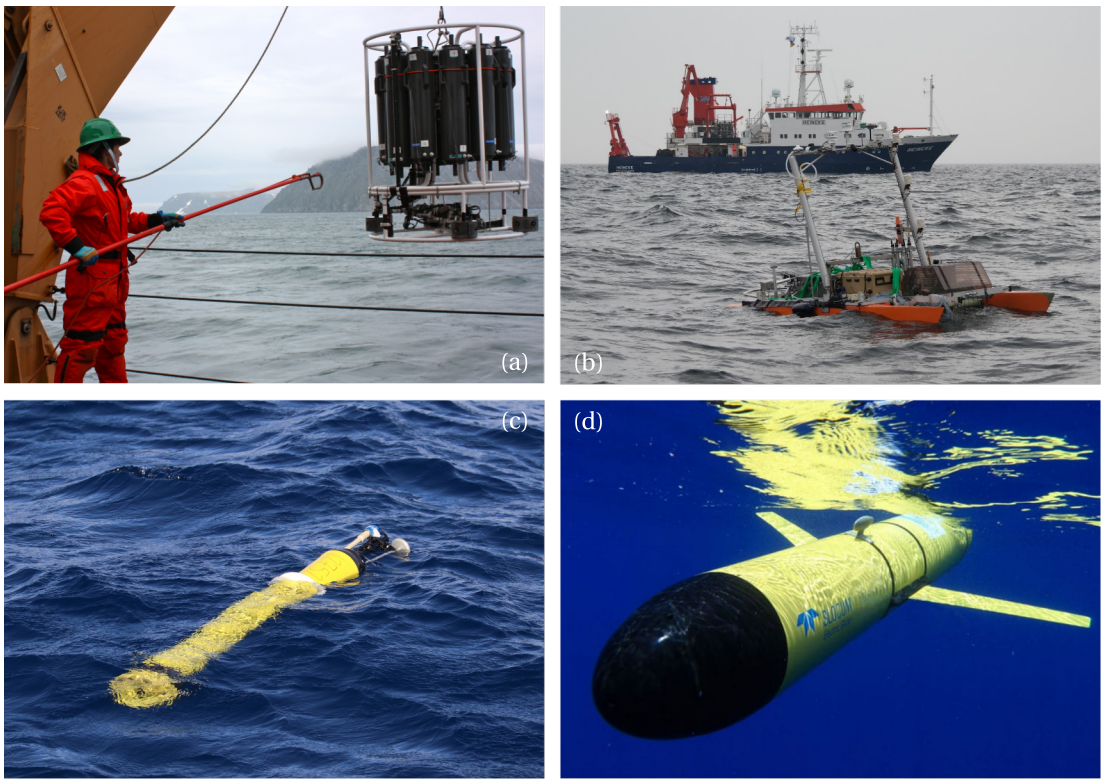

Figure 8: *a: Ship-based retrieval of CTD-profiling instrument. b: Research Vessel Heincke and an autonomous surface catamaran. c: Surfacing Argo Float. d: Slocum Glider at the water surface [82]. Photo credits: a: Retrieving the CTD/Rosette from NASA/Kathryn Hansen, licensed under CC BY 2.0; b: Universität Oldenburg - Institut für Chemie und Biologie des Meeres c: 2_12752_float2_HughVenables_BAS from SOCCOM Project, licensed under CC BY 2.0 d: by Ben Allsup, Teledyne Webb Research*

with a variety of sensors. Ferry boxes are used to collect data continuously during a ship's voyage to create a long-term record of the oceans and their properties. Stationary measurements can be made by moored buoys [85] or virtually moored unmanned surface vehicle (USV), using active position control to maintain a fixed location. USVs are self-propelled platforms that can navigate and measure surface parameters [86] (cf.figure 8b). Shaped like a catamaran [87, 88], for example, and are often powered by solar cells. Although the methods listed are effective in providing precise measurements, they are primarily point measurements and require a significant investment of resources and equipment. As a result, scaling these measurements to achieve high spatial, horizontal resolution from multiple measurement points is challenging. Additionally, instruments with active propulsion may interfere with the flow pattern at the surface, thus altering measurements and preventing the resolution of frontal dynamics and mesoscale eddies. A drifter, on the other hand, is a simple surface observation instrument addressing these concerns as it drifts with the ocean current, not requiring any propulsion. This thesis focuses on ocean surface monitoring using drifters, the

following section will discuss this instrument in more detail.

2.4.3 Review of Drifter Instruments for Surface Monitoring

The measurement principle of drifters is a historic method in oceanography, dating back to the mid-19th century, where messages were placed in bottles to track ocean currents. Remarkably, the longest-traveled message in a bottle was discovered in 2018, off the coast of Australia, having been cast adrift 132 years earlier from a Hamburg ship [89]. Modern drifters, also known as drifting buoys or floats, can be equipped with sensors that collect data on a range of oceanographic variables [90]. This comparably small and low-cost instrument offers versatile use and is easy to deploy. Large-scale drifter deployments help to improve the spatial resolution of marine data acquisition. Furthermore, the drifting platforms also proved very helpful in the visualization and assessment of frontal dynamics [3, 91, 92]. Apart from oceanographic uses, ocean drifters are used for practical applications, such as tracking the movements of oil spills or monitoring the movement of marine debris. A comprehensive review of the advances in the application of surface drifters is presented by Lumpkin et al. [90].

Drifter can vary in size and shape to suit the varying conditions from global ocean observations to coastal areas and near shore observations [93] (cf. figure 9). All drifters consist of a buoy floating on the water surface, optimized for minimal wind impact, some of them having a drogue ranging in length from 50 centimeters [5] (cf. figure 9d) to more than 30 meters [94] (cf. figure 9a). Drifters typically use satellite transmission modules (cf. section 4.1.2) allowing to transmit their position and, if equipped, other sensor parameters from the global ocean. The power supply of most systems is based on either rechargeable lithium-ion battery packs or single-use D-Cell batteries. Some drifter systems also facilitate solar power modules to extend their lifespan. The following presents the most common drifter models, highlighting their capabilities and differences. For a more comprehensive overview of systems used in research, refer to table 7.

The largest drifter monitoring program is the Global Drifter Program (GDP) [95], funded by the National Oceanic and Atmospheric Administration (NOAA). More than 1250 surface drifters are in operation in 2022, the fleet is constantly maintained. The GDP mostly uses drifter designs of the Surface Velocity Program (SVP) [94]. The Surface Velocity Program (SVP) drifter is equipped with a spherical surface buoy of 35cm diameter equipped with satellite transmission for position data (cf. figure 9a and b). Optional additional sensors for water temperature, atmospheric pressure, wind, salinity, and wave measurements can be added. Equipped with a 30-meter holy sock as drogue, the SVP drifter is mainly suited for deep water monitoring [94]. Depending on the

battery capacity and the instrumentation, the SVP drifter deployment lifetime is about 2 years.

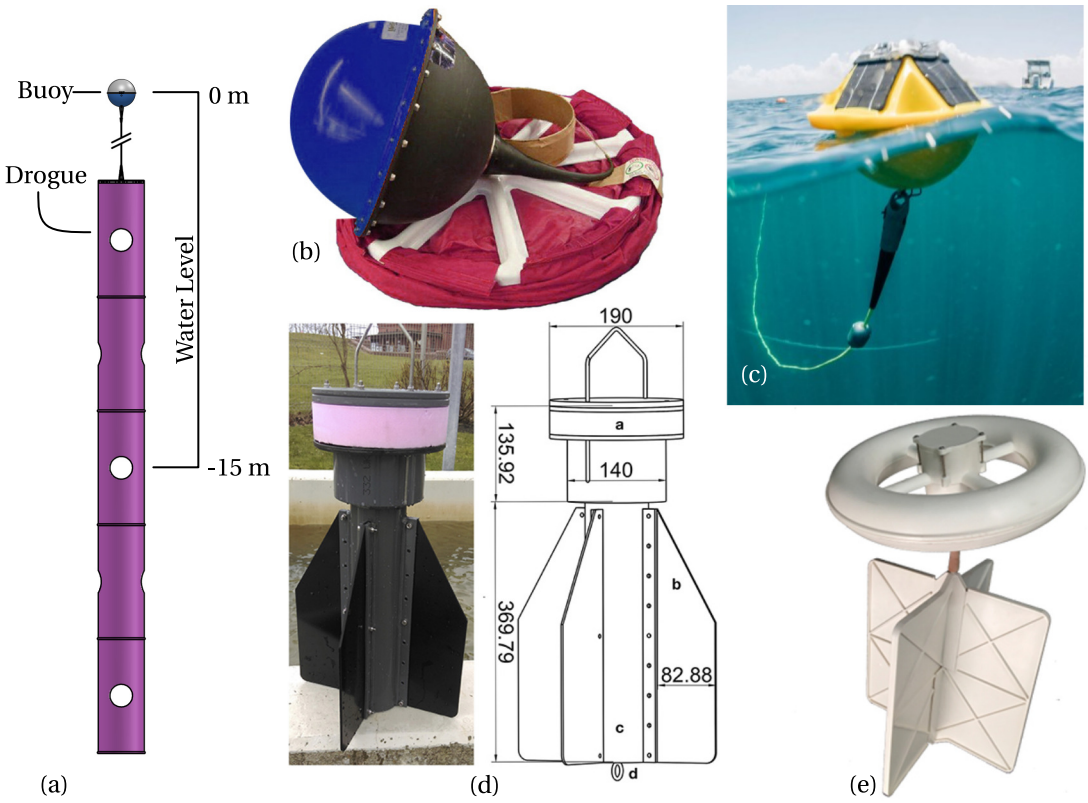

Figure 9: *a: Sketch of the SVP-Drifter with* 30 m *holy sock [96]; b: Packed iSVP-Drifter by metOcean [97]; c: Spotter Buoy by SofarOcean [98]; d: EDDY drifter by ICBM [5]; e: 3D model of the CARTHE-Drifter [6, 99].*

The Coastal Ocean Dynamics Experiment (CODE) drifter (Davis drifter), created by Russ E. Davis [100, 101] is another drifter design, developed for measurements in coastal areas. The CODE drifter aims to follow near-surface (1 meter) currents while minimizing wave and wind influence. The drogue consists of a simple construction of four 50-centimeter-long underwater sails, allowing for a low-cost self-build.

Prompted by the deep water horizon accident in the Gulf of Mexico, another drifter design aimed for massive scale deployments was developed by the University of Miami [6] to track the oil dispersion (cf. figure 9e). The Consortium for Advanced Research on Transport of Hydrocarbon in the Environment (CARTHE) used 300 CARTHE drifter for a single experiment and uncovered some logistical challenges and assembly requirements for drifter designs intended for high-volume use. They proposed a compact drifter design allowing for compact storage aboard the ship, as well as fast assembly and deployment times. The used material of the CARTHE drifter is biodegradable to reduce maritime pollution. The biggest disadvantage of the compact drifter is that it is only

equipped with a GPS tracker and does not allow the transmission of other sensor data.

Company	Name	Sensors	Comm.	Ø Buoy × *H* Drogue	Weight	Autonomy	Energy Harvesting
Pacific Gyre [99]	CARTHE [6]	GPS	Globalstar	40 cm × 60 cm	4 kg	3 months @ $t_i = 5$ min	-
	Microstar [102]	GPS, T	Iridium	40 cm × 122 cm	4.5 kg	1-12 months	-
	SVP [96]	GPS, T, B, W	Iridium	35 cm × 15 m	20 kg	1 - 2 years @ $t_i = 1$ h	-
SofarOcean [98]	Spotter [103]	GPS, IMU, T, W	Iridium	42 cm × 36 cm	5.4 kg	Unlimited @ $t_i = 1-2$ h	5 × 2 W PV
Zunibal [104]	Anteia	GPS, IMU	GSM or Iridium	Ø 60 cm	26 kg	n/a	n/a PV
	ZGT	GPS	Iridium	25 cm × 18 cm	1.3 kg	n/a	1.7 W PV
Fastwave [105]	Voyager V3	GPS, T	Iridium	25 cm × 66 cm	6 kg	300 days @ $t_i = 3$ h	-
	Voyager Solar	GPS, T	Iridium	31 cm × 68 cm	6.7 kg	Unlimited @ $t_i = 3$ h	2.8 W PV
MetOcean [106]	CODE	GPS, T	Iridium or Argos	10 cm × 1.4 m	8 kg	3-12 months	-
	iSVP	GPS, T, B	Iridium	Ø 40 cm	18 kg	18 months	-
	iSPHERE	GPS, T	Iridium	Ø 34 cm	13.15 kg	6-12 months	-
QuinetiQ [107]	Riverine [108]	GPS, T, D	Iridium	Ø 15 cm	1.8 kg	24 hours	-
MELOA [109]	WAVY OCEAN	GPS, T, IMU	Argos	Ø 20 cm	3.5 kg	3 - 4 months @ $t_i = 20$ min	0.6 W PV
	WAVY Littoral	GPS, IMU	GSM	Ø 12 cm	0.75 kg	n/a	-
	WAVY Basics	GPS, T	GSM	Ø 10 cm	0.4 kg	n/a	-
ICBM [110]	EDDY [5]	GPS	Globalstar	Ø 19 cm × 50 cm	<5 kg	9 months	-

Table 7: *Drifter comparison, adapted from Carandell [111] with additional data. T = Near Surface Sea Temperature, B = Near Surface Atmospheric Pressure, W = Wind Speed and Velocity, GPS = Position, IMU = Inertial Measurement Unit, D = Single Beam Depth Sensor, Ø = Diameter, H = Height, t_i = Interval between data transmissions, PV = Photovoltaics.*

Due to the long drift sail of the SVP Drifter, especially the local German coastal waters of the North and Baltic Sea are not covered by the GDP. For this reason, more compact drifter designs (shallow water floats) are needed in the North Sea and other coastal waters, which also allow the transmission of sensor data. For this reason, the EDDY Drifter has been used to measure surface currents by the Institute of Chemistry and Biology of the Sea (ICBM) of the University of Oldenburg since 2017 [5]. Due to the compact design, the 50-centimeter draft and the robust housing, the drifter is protected against shocks and strandings (cf. figure 9d). However, the EDDY drifter can also be used on the open ocean. Its position tracking allowed studying the propagation pathways of e.g. marine litter [112]. This work involves a collaborative effort with the University of Oldenburg's ICBM to enhance the observation capabilities of the EDDY drifter. One goal is to implement a multi-sensor system able to transmit in-situ sensor data via satellite. The ICBM's Sailing Intelligent Micro Drifter Swarms (SAIMIDRIS) [9] aims to develop a multi-sensor drifter network capable to investigate oceanographic fronts and filaments with high measurement resolution, in order to study accumulation processes. To achieve this goal, passive floating systems are necessary as propulsion would affect the measurement. Small drifters are ideal as they offer turbulence-free observation. The SAIMIDRIS project plans to develop a swarm of intelligent drifters that can analyze measurement data using artificial intelligence. This requires a multi-sensor system with a powerful computing unit facilitating communication within the drifter swarm.

Overall, there is a clear trend towards enhancing the instrumentation and intelligence of drifter systems [113]. However, commercially available options are limited in terms of sensor selection and come at a high cost. For example, the SVP Drifter, which is currently the most widely available option, costs at least $2000 in its standard configuration, including GPS positioning only [114]. Moreover, adding further sensors can increase the price range to anywhere from $2500 to over $10000. These high costs pose a challenge for research projects with small budgets or those looking to deploy multiple units. Additionally, the SVP Drifter has limited modularity, as only certain sensors can be added, and it is difficult to customize measurement cycles and sensor settings.

Although there are several approaches to developing cost-efficient alternatives, many of them lack a comprehensive engineering system approach or only offer GPS tracking. A more flexible and affordable system is needed allowing for custom sensors and measurement settings to be user-friendly, and adaptable to a broad range of applications. A flexible multi-sensor drifter system, which can be deployed cost-effectively in large numbers, could provide high-resolution spatial measurement data of the sea surface and thus make an important contribution to ocean monitoring.
One of the main challenges in the development of drifters is extending their deployment times, which is commonly achieved through energy harvesting methods [90].

2.5 Energy Harvesting Methods on Oceanographic Platforms

Energy harvesting is a common approach to supply remote measurement platforms in the ocean to reduce the necessity of large energy storage. The Wave Glider [115] is a prominent example of energy harvesting in the ocean, that should not go unmentioned. The glider directly uses the up and down motion in the wave for forward propulsion without the need to convert it to electrical energy. Since a drifter does not require additional propulsion, but rather electrical power to operate its measuring instruments, attention is focused mainly on energy conversion systems suitable for the supply of a drifter. The Wave Gliders electronics, for example, are powered by additional 86 W (peak) solar panels, mounted on the large 2.1 m × 0.6 m surface float. Smaller systems, such as the Spotter Buoy [98, 116], a drifter made by Sofar Ocean, also uses 5 × 2 W (peak) solar panels [103] for the supply of a compact drifter (cf. figure 9c). Despite the fact that this harvesting method is a cost-effective solution for many deployment scenarios, continuous operation in dark seasons near polar regions (cf. figure 10) is not feasible. As the polar regions are frequent areas for the use of drifters, an exclusive solar power supply is not desirable.

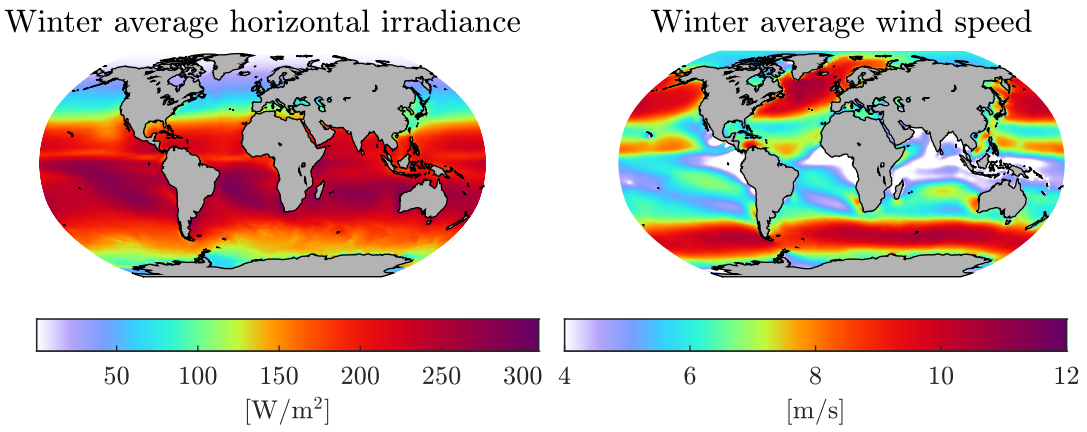

Figure 10: *Global heat maps of the Northern Hemisphere winter average (Dec. to March) for the horizontal irradiance (left) and the wind speeds (right) on the ocean surface. Irradiance data averages between March 2000 and December 2022; Wind data averages from March 2000 to December 2021. Source: NASA CERES EBAF Ed4.1 [117] and NASA CERES CldTypHist Ed4A [118]*

In addition to the conventional energy sources of wind and waves, there are also implementations that use thermal energy like the thermal glider [119]. Although the thermal glider uses thermal energy for the glider's propulsion, it is possible to convert heat fluxes to electric power by thermometric generators based on the Seebeck effect [120]. Compared to the potential of wind and wave energy, thermometric generators show

very small efficiencies and power outputs. Wind energy on the other hand shows a much larger potential, is mostly independent of the daytime, and is highly available in polar regions during the winter (cf. figure 10). In order to directly utilize wind energy, an area must be exposed to the wind. This is undesirable for the drift behavior since the drifter should be primarily influenced by ocean currents and wind effects should be minimized [93, 121]. Aside from the solar and wind energy sources available on land, the ocean also provides wave energy showing a large potential for both large and small power plants [122, 123]. The ocean waves are primarily induced by the wind and are therefore an excellent alternative energy source with the same availability as wind.

2.6 System Level Problem Identification

As this chapter has demonstrated in detail, there is a need for cost-effective, customizable, multi-sensor drifter systems, to facilitate large-scale sea surface monitoring. Measurements with high spatial resolution using large sensor quantities can provide advantages in observing small-scale effects such as mesoscale eddies or salinity fronts but the current market prices of available systems prevent large-scale deployments.
Furthermore, available drifter systems do not meet the need for individual sensor integration, only provide GPS tracking or carry specific sensors that may be unsuitable for the application. Existing drifter systems with integrated fixed sensor technologies are inflexible and cannot meet the broad monitoring demand. The increasing complexity of monitoring capabilities requires more powerful processing units to enable a broader spectrum of monitoring tasks.
As instrumentation increases, so does energy demand, which is especially critical for long-term deployments. As a result, deployment times of a system dependent primarily on battery storage are limited. A viable option for dealing with higher levels of power consumption is energy harvesting. Simple solar modules often do not provide enough energy in the polar regions, which are a common area of application. Wave energy harvesting can potentially provide an energy source with high availability, but its applicability to drifters needs to be evaluated.
The costs of monitoring platforms are largely influenced by the equipped sensors. Cost-efficient deployments require a good trade-off between costs and measurement uncertainty. While technological innovations in consumer electronics drastically reduce sensor costs, measurements in oceanography often rely on comparatively expensive instruments. Many oceanographic observations rely on high-precision instruments for which the high cost is appropriate; however, other research questions such as sea surface observations, investigate larger parameter variations, justifying the use of sensors with lower accuracy. The market provides a large number of reasonably priced temperature sensors with low accuracy requirements (>50 mK). Also for stand-alone temperature sensors with higher requirements (< 10 mK), solutions appropriate prices (< 400€) exist (cf. SoundNine in table 6). For salinity and conductivity measurements, on the other hand, there is a gap between high-precision instruments and low-cost consumer products. Despite the need and benefit of low-cost conductivity sensors suitable for long-term monitoring, the availability is insufficient. A combined temperature and conductivity sensor with a better trade-off between cost and accuracy is needed. The conductivity measurement should be contactless to be more robust in the upper water layer, an inductive method could be advantageous [51, 124].
A cost-effective multi-sensor monitoring system, enabling individual sensor technology is needed. The system should provide energy harvesting, to allow long-term deployments and provide application-appropriate sensors for deployments in coastal areas.

2.7 Research Question

This work aims to enhance the availability and accessibility of in-situ sea surface monitoring by facilitating a systematic design approach. Several application scenarios are identified that demonstrate the need for adaptable and cost-effective multi-sensor ocean observation. The work primarily focuses on the application of drifter observations but the system design methods can be applied to other scenarios.
To address the formulated problem description, a number of central questions can be raised: How can ocean surface data acquisition be simplified to provide a holistic solution for a wide range of applications? Which elements are driving the high prices of existing systems, and how can a trade-off be achieved between reliability and cost-effectiveness? To what degree can the increased power requirements of additional electronics and sensors be met by energy-efficient systems and the use of wave energy? Three key development questions can be identified:

1. What are the key characteristics of a flexible and user-friendly system architecture that enable modular sensor implementation?
2. What design principles can be established for temperature and conductivity sensors intended for long-term, near-surface deployment, balancing measurement uncertainty against cost?
3. What methodological approach can be used to design a wave energy harvesting system for a self-sufficient monitoring platform, and what is the potential energy yield achievable for a compact surface drifter using this approach?

A major focus of this work is the methodical approach to system design through the use of model-based development. The challenge of interdependencies in the development process is considered, particularly for the design of a wave energy harvesting system. The question of how the mutual dependencies of different model domains can be taken into account in the optimization of the overall system is answered.

3 System Design: Next Generation Ocean Surface Monitoring

This chapter outlines the systematic approach for designing a flexible multi-sensor drifter with suitable sensor technology and energy harvesting capabilities. First, the design approach is presented and the basic system requirements are identified. A subsequent functional decomposition describes the global functions of the monitoring system and enables the definition of system components of the following development approaches. The larger perspective of the system design is emphasized throughout this chapter. In the end, a development perspective is defined for each component, which will be elaborated on in the subsequent chapters.

3.1 Design Approach: Methodology and System Structure

The main focus of this chapter is on the system design approach. The system level describes the whole system of monitoring platform, sensors, and power supply and follows the methodological process of the V-diagram (cf. figure 11b). The research question in the previous chapter illustrates the system-level problem identification, allowing to derive the resulting system-level requirements in the following. The development task is then structured into functions that describe the key roles of the system. In order to fulfill these functions, components are defined, which are considered the object of development. The components may have interdependencies that must be taken into account during the design process. At the system level, each component describes a subsystem that undergoes a detailed design process in the following chapters, which in turn follows the V-cycle (cf. figure 11a). The system level thus describes the fulfillment of the overall requirements and the subsystems describe the specific consideration of a particular component. For component design, a model-based development approach is used to optimize the system component before implementation.

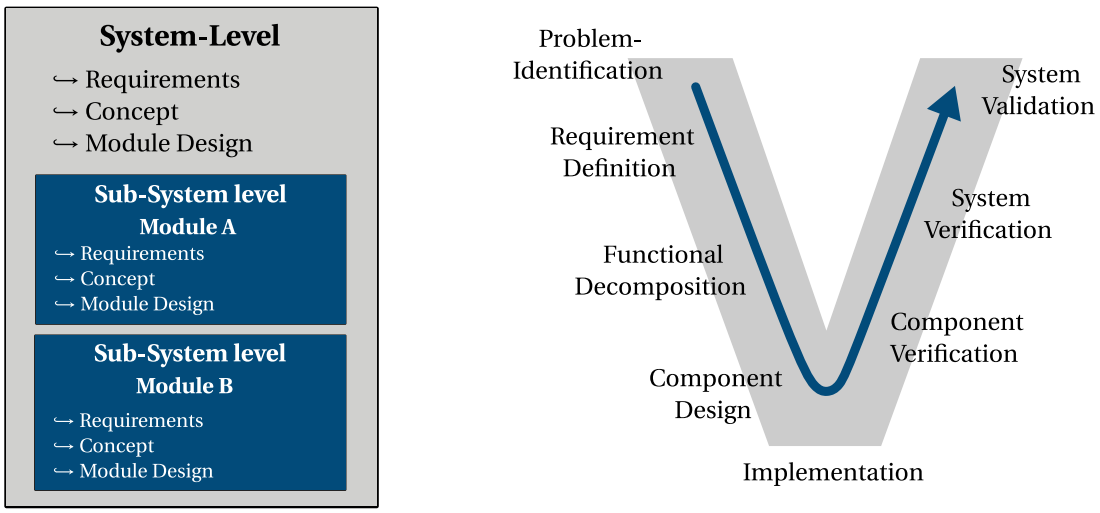

Figure 11: *Left: Schematic representation of the system design approach and the system levels of this work. Right: V-diagram of the system design procedure.*

3.2 System Level Requirements

Based on the previous problem description, system-level requirements for a multi-sensor ocean monitoring system can be derived to achieve improvements over existing solutions. The system level requirements (cf. table 8) are the highest level requirements and also apply to subsystems derived later. Due to their high rank, some requirements are not quantified to ensure broad validity. More detailed specifications are derived for concrete subsystems in the following chapters.

To increase the availability of ocean monitoring, the main objective is to enable in-situ measurements that are flexible for different sensor technologies. The system under development should be versatile to allow various measurement scenarios. For optimized user experience, the system configuration must prioritize ease of use. This entails a user-friendly interface for non-technical users and minimal time commitment to operating the system.
As the expeditions to deploy the drifters involve a lot of effort and cost, the reliability of the systems is of great importance and the measurement data has a high value. Continuous data collection is crucial and must be ensured throughout the planned deployment period. As deployment from ships often has to take place in difficult conditions, a fast set-up time and easy handling are crucial. This also means that the dimensions and weight can be easily handled by one person.

From an energy point of view, a long service life of the system should also be ensured. To keep the size of the storage capacity small, the entire system must be designed to be as energy-efficient as possible. In order to extend the operating time even for configurations with higher energy requirements, the system should also allow for self-sufficient

#	Description	Value	Rating
Operation			
D01	Facilitate in-situ measurements of multiple sensor parameters	> 3 parameter	M
D02	System shall be independent of used sensor technology	-	M
D03	Provide a user-friendly system configuration	-	M
D04	Provide a reliable availability of data during the deployment period	< 10% loss	M
D05	Ensure a long system lifetime	> 1 year	M
D06	Full-functional application area	Global ocean	M
D07	Low storage to deployment assembly time	< 5 minutes	O
Phyiscal Dimensions			
D08	All components shall fit into compact drifter housing	< ∅50 cm ×h15 cm	M
D09	Deployment-ready storage area shall not exceed housing diameter	< ∅50 cm	O
D10	The total system weight should be suitable for handling by one person	< 10 kg	M
Energy Supply			
D11	System components shall be energy efficient	-	M
D12	System shall allow self-sufficient operation	-	O
Manufacturing and Costs			
D13	Total cost of the monitoring system	< 1000€	M
D14	System shall qualify for manufacturing of large quantities	< 1000 pcs.	O

Table 8: *Overview of system-level requirements. Rating: Mandatory (M), Obligatory (O).*

operation by wave energy.
In order to offer an attractive alternative to existing solutions, the cost of the overall system must be kept low. Manufacturability should also be guaranteed for larger quantities of more than 1000 units. The overview of table 8 specifies the requirements at system level:

3.3 System Level Component Definitions

Based on the given requirements, the functions of the monitoring system can be derived. A function tree (cf. figure 12) represents the main functions of the system. The main objective of the multi-sensor platform is the acquisition of measurement data, which is represented by the *Data Acquisition* function. At the same time, this data must be made available to the end user, which is described by the *Provide Data* function. The entire system is controlled by a central function that processes the user configurations and ensures that the system operates correctly. The *Provide Energy* function covers energy generation, conversion, and provision for the monitoring system. The *Provide Protection*

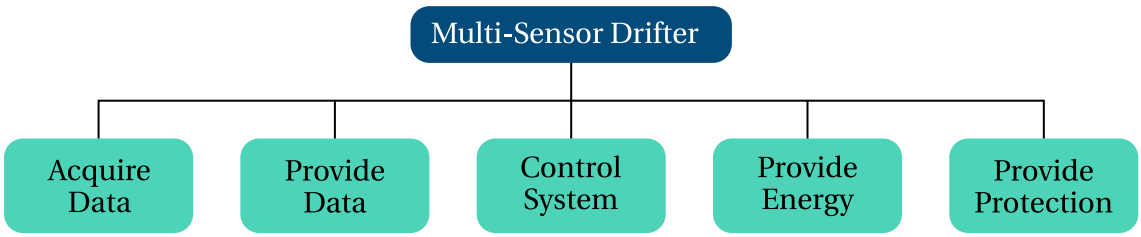

Figure 12: *Function tree of the monitoring platform at system-level.*

function emphasizes the importance of watertight protection for all subsystems. A breakdown of the generally formulated functions into more detailed sub-functions is not considered at the system level but is done for the subsystems in each chapter. The three components of the modular measurement platform (cf. figure 13), the embedded conductivity and temperature (CT)-sensor, and the wave energy harvester are derived from the five system-level functions.

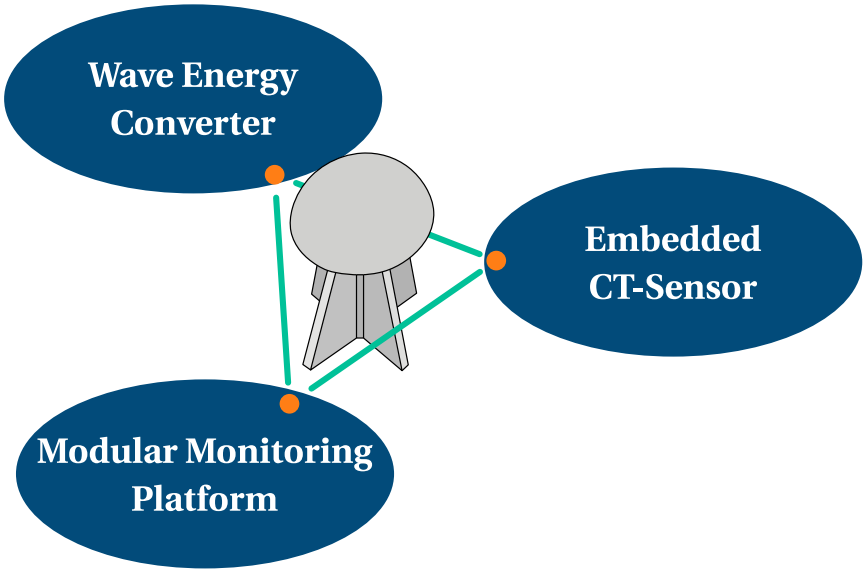

Figure 13: *The three main components of the system-level design are the modular monitoring platform, the embedded CT-sensor and the wave energy converter.*

Modular Monitoring Platform The first component is the modular monitoring platform. It performs the *System Control* functions and provides the measurement data. The main task of the modular platform is to simplify in-situ monitoring for oceanic measurement platforms, enable cost-effective monitoring, and facilitate data access. An architecture for a measurement platform needs to be identified, that offers a high degree of modularity in terms of the sensor technology used and the configurations of the measurement cycles. A platform is needed that allows different sensor technologies

to be used with different cycle settings that can be easily adapted by the user. A modular design approach facilitates easy configuration for different applications.

Embedded CT-sensor The function of *Data Acquisition* generally describes the acquisition of measurement data by sensor systems. Although available systems can be used, it has been shown that cost-effective trade-offs for measuring SSS are limited. In particular, biofouling and corrosion become a problem for electrode-based sensors in long-term applications, so inductive, cost-effective alternatives with good long-term stability are needed. Therefore, a method for non-contact measurement of CT that can be attached to small monitoring platforms in a compact size is needed. The goal is to find design principles that can be established for a fully self-contained inductive CT-sensor to achieve a good balance between required accuracy and cost for near-surface measurements.

Wave Energy Converter The energy demand of the system should be sustainable through wave energy for long-term deployments. To fulfill this objective, a wave energy converter component has been identified. The component contains the energy conversion, storage, and supply for the overall system, and has to meet the system-level requirements, while also being cost-effective. The component should be able to be integrated into existing shallow-water drifter systems without significantly altering their appearance to enable self-sufficient long-term sea surface monitoring.

Each presented component will be examined in detail in the following chapters.

4 Architecture of a Modular Sea Surface Monitoring Module

As traditional ocean surface monitoring instruments show limited capabilities, a need for a flexible module that allows more complex monitoring tasks was identified. To facilitate a modular monitoring approach, this chapter proposes a system architecture that enables user-friendly measurement for a broad variety of application scenarios. First, similar existing concepts are reviewed and the requirements for flexible sea surface monitoring are identified. After considering the functions of the subsystem, a modular system architecture is proposed. Finally, a prototype implementation of the module is tested with a drifter deployment to validate the system concept. The goal of this chapter is to demonstrate the potential of a modular monitoring device to improve the versatility of ocean surface monitoring systems.

4.1 Recent Advances of Sea Surface Monitoring Technologies

In order to provide context for the proposed modular architecture, this section begins by providing an overview of existing technologies and solutions for cost-effective sea surface monitoring. Specifically, the section will describe the available monitoring electronics and explore various communication and data transmission solutions. These include the use of satellite modems and cellular networks, along with their respective advantages and limitations. The main objective is to provide a comprehensive understanding of the current state of low-cost sea surface monitoring technologies and their capabilities, as well as to highlight the opportunities for development undertaken here.

4.1.1 Review of Monitoring Modules

This work defines a monitoring module as an electronic system that facilitates and regulates the recording of measurement data from diverse sensors. The module is responsible for the data processing and enables real-time transmission for in-situ monitoring, or alternatively, writes the data on storage for later evaluation. In this context, *real-time* refers to the availability within minutes, in accordance with the understanding of the oceanographic community.

Many electronic monitoring devices traditionally used for ocean surface monitoring, such as the Spot Trace from SPOT LLC (Globalstar) [125], only allow for position tracking (cf. figure 14a). This is the case for devices used in the CARTHE Drifter [6] or the Meyerjuergens et al. [5] EDDY Drifter. While the Spot Trace can provide accurate and reliable GPS position data, it cannot transmit data from additional sensor technologies. It is specifically designed for asset tracking and is often connected to an external battery carrier to extend its life when tracking the movement of ocean drifters.

To enable the recording of further measurement parameters, a processing unit is required that controls the connected external sensors. The electronics of the SVP Drifter, developed by the Lagrangian Drifter Laboratory [96], allows in-situ monitoring of different oceanographic sensors. However, only a specific list of sensors is available [114], limiting the possible application scenarios with this design.

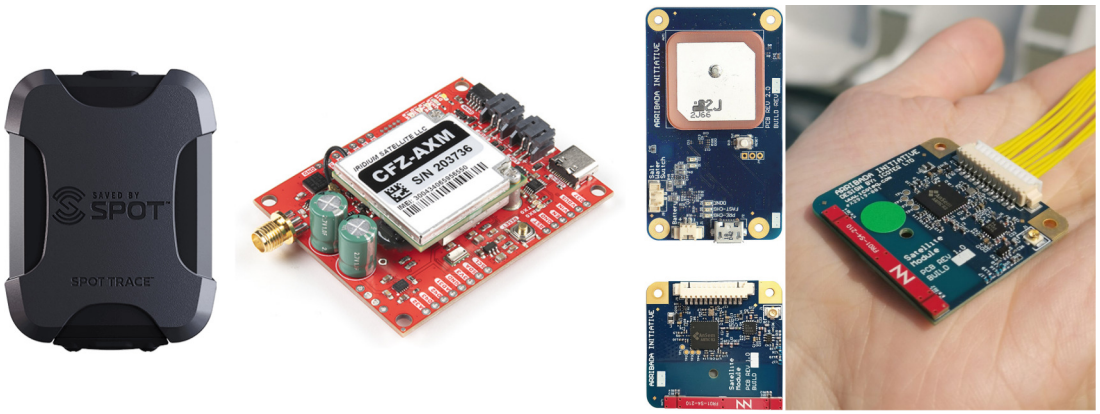

(a) (b) (c)

Figure 14: *a) Spot Trace from SPOT LLC [125] b) SparkFun Artemis Global Tracker [126] c) Arribada Horizon ARTIC R2 Developer's Kit [127]*

To implement further sensor technology, research groups often use a combination of commercially available technologies to build their own custom monitoring solution. One helpful tool with that regards is the SparkFun Artemis Global Tracker [126] (cf. figure 14b), designed and manufactured by SparkFun Electronics, a company specializing

in open-source electronics. The Artemis Global is a powerful and versatile GPS tracking device that can be used for a variety of applications. It uses an Arduino-compatible Artemis module, a 48MHz ARM Cortex-M4F microcontroller, an Iridium 9603N short burst data modem, a u-blox ZOE-M8Q GNSS receiver, and a pressure, humidity and temperature sensor. At a price of 400$, its major limitation is that it is tied to Iridium communication and has no defined interface for external sensors. For each application scenario, research groups are required to develop their own software implementation to set up their required measurement configuration. The device was e.g. facilitated by Rabault et al. [128] to implement the OpenMetBuoy, a system for the oceanographic in-situ measurement of drift and waves in sea ice and the open ocean. The OpenMetBuoy adds a six-degree-of-freedom (6 DOF) accelerometer and a precision temperature sensor and streams data directly through the Iridium satellite modem to a Rock7 platform. A number of other publications attempt to develop similar low-cost solutions that provide an IOT-like approach to ocean monitoring, with the goal to make measurements more affordable [7, 8, 129]. Low-cost drifter designs can allow e.g. developing countries to study regional changes due to climate change in their coastal areas [16].
Another module that offers monitoring capabilities in addition to GPS tracking is the [127] Arribada Horizon ARTIC R2 (cf. figure 14c). The Horizon Developer Kit is a device that enables tracking of the location of objects or animals using GPS and other sensor technology, and transmits that data via 3G cellular or the Argos ARTIC R2 transmitter. It was developed in conjunction with the Zoological Society of London and is being used by the National Geographic Society to track plastic waste in the Ganges Delta [130]. It is also compatible with the ARGOS-4 next-generation satellites and the future Kineis constellation of nanosatellites. However, if specific sensor technologies are to be used, the existing Python code must be adapted, requiring more programming effort.

Various devices for ocean surface monitoring are available, each with their own strengths and limitations. The Spot Trace is primarily used for position tracking, while the SparkFun Artemis Global Tracker is a versatile instrument capable of tracking multiple parameters, as demonstrated in the OpenMetBuoy implementation. The Arribada Horizon Kit also offers a promising solution, but it is limited by its dependence on the ARGOS satellite system and the need for advanced programming skills in Python to add further sensors. To address these limitations, a user-friendly module that supports modular monitoring and easy integration of various sensor technologies is needed. This would enable researchers and organizations to collect and analyze data more efficiently and effectively, leading to a better understanding of oceanic processes and the impact of human activities on the marine environment.

4.1.2 Solutions for Communication and Data Transmission

An important aspect of in-situ ocean monitoring systems is the type of data transmission and communication used. In addition to various satellite transmission providers, there are alternative approaches such as using cellular networks and Internet of Things (IoT)-based methods.
Cellular networks can be a cost-effective option for data transmission, but they are typically limited to near-shore communications due to their limited coverage area. For more remote areas of the ocean, where coverage is limited and unreliable satellite systems are the preferred method for data transmission as most of them provide global coverage. Therefore satellite communication systems have become an essential tool for ocean surface monitoring, providing a reliable and efficient means of collecting and transmitting data from remote areas of the ocean. There are several satellite systems available on the market, each with their own strengths and weaknesses. Globalstar [131], ARGOS (CLS) [132], and Iridium [133] are some of the most established satellite providers, offering both low-earth orbit (LEO) and medium-earth orbit (MEO) satellite constellations for reliable and stable connections for data transmission. The Global Drifter Program and the ARGO-float system is availabe with ARGOS or Iridium for their global data transmission.
Newer companies, such as Swarm Technologies [134], and Kineís (CLS) [135], specialize in nano-satellites for IoT devices. These nano-satellites are smaller, less expensive, and can be launched in larger numbers than traditional satellites, providing new features and options for ocean monitoring. For example, Swarm Technologies provides a low-cost satellite-based communication and positioning solution for IoT devices, while Kineís is developing a new global nanosatellite constellation for IoT and Machine-to-Machine communication. These companies are expected to revolutionize the satellite industry, providing new low-cost options for ocean monitoring and other industries, especially in providing connectivity to remote and hard-to-reach areas.
Furthermore, the role of rising global internet coverage in ocean monitoring is significant. One notable example is Starlink [136], a satellite internet service provider developed by SpaceX. Starlink is a large-scale satellite internet project, planning to put thousands of satellites in low Earth orbit to provide high-speed, low-latency internet connectivity to people around the world. Starlink and similar satellite-based internet providers have the potential to revolutionize ocean monitoring by providing near-global coverage of the Earth's surface, including remote areas of the ocean. This would allow for greater access to oceanic data and a significant expansion of monitoring capabilities. Starlink could support ocean-based IoT sensors and connected devices, which can be strategically placed on buoys, ships, and other monitoring modules to provide real-time data on ocean conditions.
Other IoT-approaches for network communication are currently based on LoRa net-

work implementations. Gerin et al. [16] implemented a sustainable ocean drifter for developing countries based on LoRa communication in the coastal area of the Gulf of Triest. The LoRa network allowed several drifters to operate simultaneously, providing a rich and homogeneous database with a reliable transmission of up to 10 km distance from the gateway. This demonstrates the potential of LoRa networks as a cost-effective solution for ocean monitoring in coastal areas.

Overall, there are many innovative approaches to enable data transmission from remote areas, but at this stage, the use of satellites and nano-satellite systems remains without alternatives. It is foreseeable that in the near future, lower-cost alternatives will greatly change data transmission in the ocean.

4.2 Concept Development: Requirements, Functions, and Components

To address the drawbacks of traditional monitoring systems, the key characteristics of an architecture that allows modular monitoring are derived in the following. The requirements are first defined and the system functions and components are derived to present the solution concept of a modular monitoring device.

4.2.1 Requirements for Modular Monitoring

The application scenarios for a monitoring module are diverse. Three arbitrary examples are provided to illustrate some use cases:

Case 1: An ocean drifter must log water temperature and conductivity data every 10 minutes and reliably transmit a summary every 30 minutes via satellite. The deployment time is at least 1 year.

Case 2: For pollution monitoring along a river course, a drifter shall log PH-Values every 2 minutes. Only the position needs to be transmitted every 15 minutes to allow localization. The river is located in an inhabited area, which allows the use of a cellular network. The deployment time is a couple of days.

Case 3: A weather monitoring station shall be deployed on a fixed-position buoy close to the coast. Different environmental parameters shall be streamed on request via LoRa network.

While all application scenarios are different, similarities can be found and formulated into requirements (cf. table 9). The monitoring module must meet several key requirements to effectively collect and transmit environmental data from various sensors in real-time. To ensure accurate localization, GPS-positioning shall be integrated into the module. Additionally, the module shall include acceleration and temperature sensors to measure basic environmental parameters and monitor onboard health. The module shall allow the connection of external sensor hardware to be flexible in the type and number of sensors that can be used at the same time. Users should have the ability to custom configure measurement and transmission cycles to meet their specific needs. The module should also prioritize ease of configuration, allowing for quick and simple set-up and management without the need for advanced technical or programming skills.
For data transmission, a range of technologies should be supported, including reliable satellite modules for global ocean coverage and low-cost cellular network modules. Two-way communication should also be implemented to facilitate system configuration during deployment.
To ensure consistent data acquisition, regular timing shall be reliable. To support long deployment periods, the module should be energy-efficient and feature low-power modes for energy conservation. The power supply must work with rechargeable storage such as lithium-ion batteries or super-capacitors if energy harvesting is used, or with disposable D-Cell batteries for single use. Lithium-ion batteries typically provide between 3 to 4.2 V. This voltage level can be matched by 2 or 3 1.5 V D-Cell batteries connected in series, providing a voltage between 2.7 and 5 V, which defines the required operating voltage of the module.

#	Description	Value	Rating
Hardware Compatibility			
M01	Be hardware agnostic and able to operate with any sensor hardware		M
Sensor Integration			
M02	Support the connection of multiple sensors simultaneously		M
M03	Customizable measurement cycles with user-defined intervals, transmission, and logging preferences.		M
Data Transmission			
M04	Provide user-selectable transmission modules, including satellite and cellular options.		O
M05	Enable two-way communication to adapt settings during deployment.		O
M06	Enable sufficient accuracy for transmission and storage of acquired data.	32 bit	M
M07	Enable in-situ measurements, meaning it shall be collected and transmitted from the location where it was acquired.	delay < 15 min.	M
M08	Ensure low failure rate, ensuring reliable and consistent data transmission.	< 5%	M
Power Management			
M09	Run on a battery power supply.	2.7 V to 5 V	M
M10	Provide regulated power supply for connected sensors.	5 V	M
M11	Provide regulated power supply for connected transmission modules.	5 V	M
M12	Provide switch for external power supply.	up to 24 V and 2 A	M
M13	Be power efficient, minimize power consumption and prolong battery life.	< 1 mW in sleep < 500 mW active	M
Maintenance and Troubleshooting			
M14	Provide indication of functionality and failures, allowing for easy troubleshooting and maintenance.		M
M15	Provide means for easy switching on, allowing quick and effortless activation.		M
M16	Implement means to monitor the health status of the module's internal components.		M

Table 9: *Overview of the requirements of the monitoring module. Rating: Mandatory (M), Obligatory (O).*

4.2.2 Functional Decomposition: Deriving Subcomponents

The tasks of the monitoring module are first transformed into a general functional description (cf. figure 15) in order to identify subcomponents and find component solutions. One of the most important functions of the module is data acquisition, which

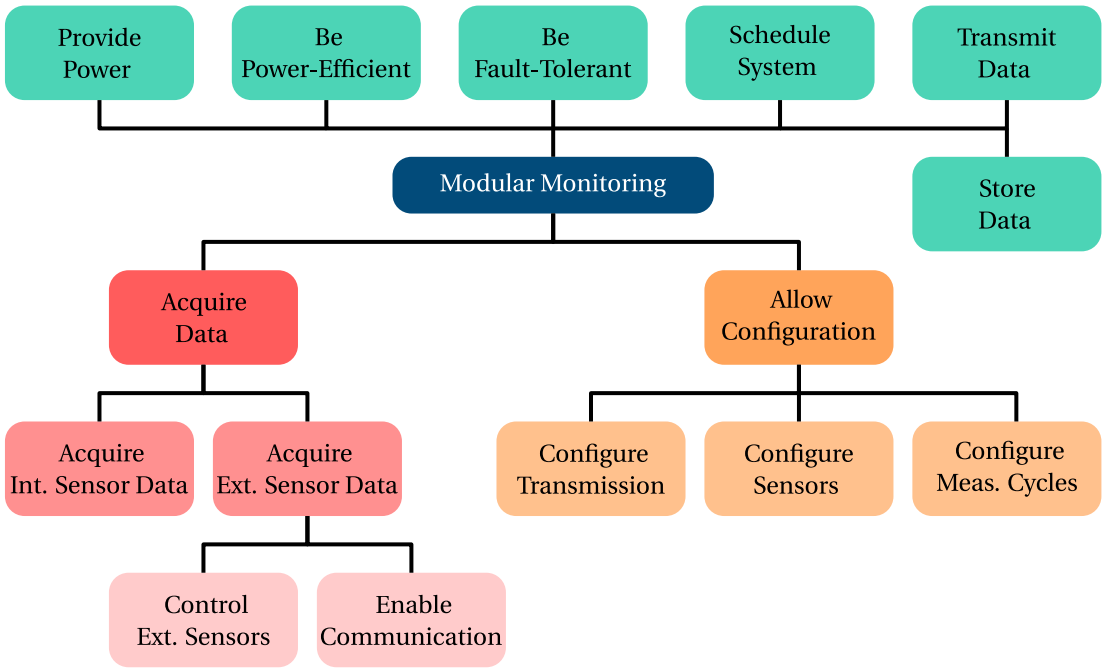

Figure 15: *Function tree of the monitoring module.*

must be able to collect a number of different types of data. The function can be divided into the acquisition of data from internal sensors and from any external sensors. To control and communicate with the connected sensors, the module must have a modular communication interface. This allows the module to control the sensors, configure their settings, and schedule measurements. Measurement configuration must allow easy setup of measurement cycles, sensor settings, and data transfers. These features allow users to customize the system to their specific needs and ensure that the data received is sufficient for the intended application.
Another important function of the module is data storage and transmission. The module must be able to store the data collected by the sensors in a format that can be easily accessed and used for analysis. Moreover, the module must be equipped with the ability to transmit the data to a remote location, such as a shore station or research vessel. To reduce overall power consumption, the module must be energy-efficient. A fault-tolerant design is essential to ensure the module's uninterrupted functionality even if one or more components fail. This is particularly important as it guarantees the reliable and continuous collection of data.

4.2.3 Component Solutions and Modular Concept Definition

To fulfill the identified system functions, the concept of a modular monitoring architecture is derived. (cf. figure 16).
The central hub for the modular architecture is the main board, integrating essential functions for data processing, scheduling, and storage. The main board can be configured through a user-friendly graphical user interface (GUI) and does not require programming. The GUI generates a config file that can be loaded onto an SD card and provided to the main board. The module includes essential sensors for GPS position, acceleration, and a combined pressure, humidity and temperature (PHT)-sensor. The main board can also be used as a standalone data logger with embedded sensors, writing measurements to an SD card.

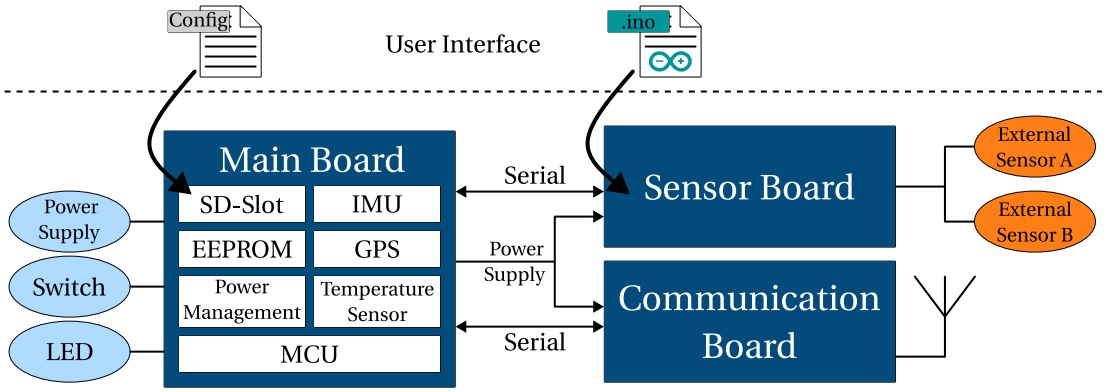

Figure 16: *Concept sketch of the monitoring module with visualization of the user interface, main-board, sensor-board, and communications board.*

To connect additional external sensors, a sensor board is used for interfacing and can be implemented using any microcontroller, such as an Arduino, with a serial connection to the main board. A predefined library facilitates communication between the sensor board and main board. The main board controls the sensor board via a generic protocol and requests measurements of connected sensors. This allows for easy customization of the sensor board without the need to reprogram the main board. The main board also provides power to the sensor and sensor board, allowing for power conservation. A communication board can be connected to the main board for flexible data transmission, and the main board can be set up via the GUI to include the necessary libraries. Additionally, a switch and LED can be connected to the main board for status indication and power state.

The proposed monitoring module is a modular and user-friendly system for monitoring various environmental conditions, with the main board integrating essential functions and the sensor and communication boards customizable to meet specific sensor and data transmission requirements

4.3 Hardware Design and Modular Architecture

The proposed concept includes a main board, acting as the central component of the modular architecture. The hardware of the main board consists of a MCU implemented on a printed circuit board (PCB) and communicates via different serial interfaces with the onboard components, the sensor board, and the communication board (cf. figure 17). The onboard components are a GPS module, inertial measurement unit (IMU), PHT-sensor, and an EEPROM for the temporary storage of large measurement data. An SD card is implemented for the permanent logging of measurement data. To enhance the power efficiency of the system, different voltage power and logic levels have been implemented, as explained in detail below. This section outlines the design decisions made at the component level.

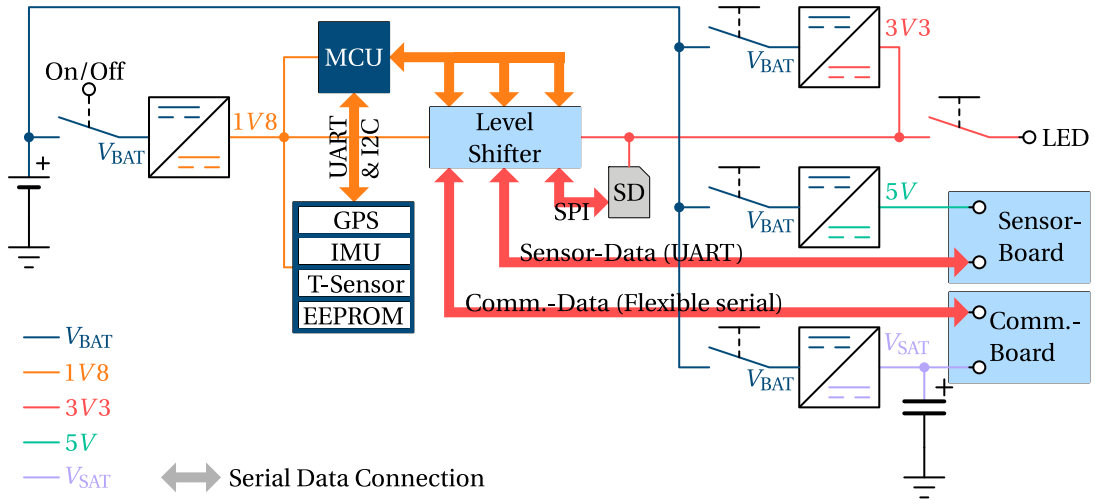

Figure 17: *Sketch of the mainboard's power and communication concept with visualization of all voltage levels.*

Microcontroller The MCU must be selected to strike a balance between power efficiency and performance. Several manufacturers offer a variety of suitable microcontrollers, with ST and Microchip (Atmel) being the most common suppliers. Based on good experiences with Microchip microcontrollers in previous projects, a MCU from the Microchip product family is selected. The SAM Microcontrollers based on Arm Cortex-M Cores provide a good trade-off between performance and power efficiency, particularly the M0+ and M4 processors, which offer low-power modes while providing a 32-bit high-performance architecture with clock management. In this case, an M4 is selected as it has a more powerful processor with a larger instruction set and supports floating-point arithmetic compared to the M0, and has a more advanced memory management unit and a larger amount of on-chip memory [137]. The *ATSAME51J18A* [138]

is chosen, which features a 32-bit Arm Cortex-M4 processor running at up to 120 MHz, 256 KB of SRAM, and provides two Controller Area Network (CAN) ports, which may be useful if bus communication shall be implemented in a later stage. The MCU supports five low-power modes and operates at a voltage between 1.7 and 3.6 volts [139]. With the microcontroller selected, the power levels and other system components can be chosen.

Power Supply and Voltage Levels An internal switch-mode power supply is implemented in the selected MCU that converts the input voltage to a 1.2 V core voltage [138]. To improve efficiency, the power supply of all onboard components is therefore selected close to the core voltage to be 1.8 V, allowing for the use of low-power components. This defines the onboard-logic level to 1.8 V, requiring the implementation of a level shifter (*TXU0204BQAR* [140]) to be compatible with external components using 3.3 V or 5 V logic level (cf. figure 17). Furthermore, the SD card must be powered at 3.3 V to allow the use of standard MicroSD cards.
An additional 5 V supply level for the external sensor board and a power supply capable of providing large currents to the connected satellite module is needed. In summary four voltage levels of 1.8 V, 3.3 V, 5 V and V_{SAT}, which is close to 5 V but facilitates super capacitor storage and inrush protection circuits, need to be provided (cf. figure 17 and table 10). All voltage levels must be supplied by the $V_{\mathrm{BAT}} = 2.7\,\mathrm{V}$ to 5 V external power supply, and the main MCU must be able to switch the power supplies for power conservation.
To convert V_{BAT} to 1.8 V, a Buck converter (*TPS62737* [141]) is selected. Buck converters provide a higher conversion efficiency compared to low-dropout regulators (LDOs) when the voltage difference is high [142]. However, since the voltage difference between V_{BAT} and 3.3 V is considerably lower, and since the 3.3 V level is mainly used for communication and therefore has only low currents, an LDO (*ADP165* [143]) is selected for the conversion. The LDO is more cost-effective, allows for a simpler circuit design, and provides a smooth output voltage. However, since the supply voltage V_{BAT} can fall below 3.3 V, the LDO is not able to maintain a constant output. Both 3.3 V logic level and transistor–transistor logic (TTL) level have minimum *high*-states of 2.4 V and 2.7 V, respectively, which can still be reached. The SD card is also affected by the 3.3 V line but is able to operate down to 2.7 V supply voltage.
To provide the 5 V output to the sensor board, an efficient synchronous boost converter (*TPS61032* [144]) is selected. To maintain high efficiency over a wide range of load currents, the converter enters power save mode at low load currents.
The power supply for the communication module is designed based on the requirements of an Iridium satellite module [145]. A supercapacitor charger (*LTC3225* [146]) is used to charge two 1 F capacitors to the voltage level of V_{SAT}. The level of V_{SAT} can be selected between 4.8 V and 5.3 V depending on the connected communication module.

The supercapacitors allow for high peak currents required for satellite transmissions. An inrush current limiter (*ADM4210* [147]) protects the circuit from short-circuit failures.

Device	In	Out	Input-Range	$I_{\text{out,max}}$	Type
TPS62737 [141]	V_{BAT}	1.8 V	2.0 V to 5.5 V	200 mA	Buck Converter
ADP165 [143]	V_{BAT}	3.3 V	2.2 V to 5.5 V	150 mA	LDO
TPS61032 [144]	V_{BAT}	5 V	1.8 V to 5.5 V	1 A	Sync. Boost Converter
LTC3225 [146]	V_{BAT}	V_{SAT} (4.8 V/5.3 V)	2.8 V to 5.5 V	150 mA	Supercapacitor Charger

Table 10: *Overview of the selected voltage converter types. $I_{\text{out,max}}$ stands for the maximum load current of the converter.*

GPS-Module The GPS module should allow power-efficient operation at 1.8 V and have a compact footprint that is cross-version-compatible to ensure a consistent PCB layout for future board versions. An external antenna is preferred to allow for a separate orientation of the antenna from the board. Known manufacturers that meet these requirements include the *ERINOME-II* [148] module from Würth Elektronik and the *NEO-M8M* [149] module from U-blox. Both modules support global coverage with satellite systems GPS, GLONASS, Galileo, and BeiDou. Both systems have various power-saving modes and allow for a fast hot start (1 s). Although the *ERINOME-II* states better position accuracy, the *NEO-M8M* has the advantage of lower power consumption (see table 11). While these systems share many similarities, the *NEO-M8M* was selected due to its greater availability and the fact that it belongs to the longer-standing NEO product family, which provides a consistent footprint across versions.

Company	Device	Pos. Accuracy (GPS & GLO)	Supply	Power	Interface
U-blox	*NEO-M8M* [149]	2.0 m	1.65 V to 3.6 V	63 mW	UART, SPI, USB
Würth Elektronik	*Erinome-II* [148]	1.5 m	1.71 V to 1.89 V	99 mW	UART, SPI, I^2C

Table 11: *Overview of considered GPS-modules. Both systems allow a Concurrent reception of up to 3 GNSS (GPS, Galileo, GLONASS, BeiDou).*

Inertia Measurement Unit - IMU To accurately measure wave heights with the monitoring module, a sensor capable of high-frequency sampling is necessary. Rabault et al. implemented a 9-degrees-of-freedom IMU in the OpenMetBuoy [128] to measure waves in sea ice. The 9-DOF sensor is able to acquire wave data by measuring high-frequency

acceleration, angular rates, and magnetic field on the X, Y, and Z axis. For sea ice measurements a sampling rate of 800 Hz was used and the raw data was time-averaged into a low-noise sensor value of 100 Hz using 3-sigma filtering. The signal was then fed in real-time to a Kalman filter to perform a data fusion with the 9-axis MEMS input and produce an accurate estimate for the absolute orientation of the sensor in a North, East, Down frame of reference. For wind-induced sea waves (typical peak frequency 0.2 Hz), 20 Hz sampling frequencies are sufficient [128].
Various low-cost MEMS IMU sensors can meet these requirements, including the ST *ISM330DHCX* [150] together with the *LIS3MDL* [151] used by Rabault et al., the ST *LSM6DSM* [152], or the TDK *ICM-20948*, to name a few. For the selection of the sensor, availability, power consumption, resolution and noise density were considered. The IMUs shown in table 12 all achieve a lower acceleration scale of ±2 g with 16-bit resolution and sufficient sampling rate for wave measurements. Despite the *LSM6DSM* being a superior choice in terms of balancing power consumption and noise spectral density (NSD), the global chip crisis severely limited the availability of IMU sensors during the time of this thesis. Therefore, the *ICM-20948* [153] was chosen from the available options. It boasts an I^2C interface and an integrated digital motion processor that can handle calculations like integrating acceleration data. Additionally, it has a wide measurement range and sufficiently low power consumption, which are crucial factors to consider when selecting a sensor for wave height measurement.

Company	Device	Current (1.8 V)	NSD acc.	NSD gyro.
ST	*LSM6DSM*	0.45 mA	$75\,\mu g/\sqrt{Hz}$	$3.8\,mdps/\sqrt{Hz}$
ST	*ISM330DHCX*	0.7 mA	$60\,\mu g/\sqrt{Hz}$	$5\,mdps/\sqrt{Hz}$
TDK	*ICM-20948*	1.3 mA	$230\,\mu g/\sqrt{Hz}$	$15\,mdps/\sqrt{Hz}$

Table 12: *Comparison of different IMUs. All provide 16-bit resolution at* ±2 g *and* 250 dps. *NSD = Noise Spectral Density. [150, 152, 153]*

Pressure, Humidity Density - PHT-Sensor To monitor the board's health status, a combination pressure, humidity, and temperature sensor (*MS8607-02BA01* [154]) has been integrated. This sensor provides an accuracy of ±2 mbar for pressure, ±3% for relative humidity, and 1 °C for temperature, making it ideal for detecting leaks in the housing and for general health monitoring purposes. Although it can also perform basic environmental monitoring tasks, its accuracy requirements are limited. The sensor operates at a low power consumption (cf. table 13) and communicates with the MCU via I^2C interface.

Company	Device	Supply	I_{PT}	I_H	P accuracy	T accuracy	H accuracy
TE connectivity	*MS8607-02BA01*	1.5 V to 3.6 V	20 µA	6 µA	±2 mbar	±1 °C	±3 %RH

Table 13: *Specifications overview for the MS8607-02BA01 [154] PHT-sensor. I_{PT}: Supply Current for pressure or temperature conversion; I_H: Supply Current for humidity conversion.*

Data Storage Devices The board's data storage consists of the microcontroller's internal memory, the EEPROM storage, and the SD card. The volatile microcontroller memory serves as temporary storage during program execution. The MCU also has eight non-volatile 32-bit backup registers to store the next due dates of the measurement cycles, even during sleep modes. When larger amounts of data need to be stored, a 2KB EEPROM storage (*24FC02T-I/MS* [155]) is utilized, allowing the MCU to enter sleep mode between transmissions. For continuous data logging and to load the module's user settings, the SD card is used, which communicates via an serial peripheral interface (SPI) interface.

PCB Implementation The PCB prototype is designed with a compact 2-layer routing and single-sided assembly, as shown in figure 18. This approach provides an opportunity for space reduction by utilizing a 4+ layer layout with dual-sided assembly. The full schematic is presented in appendix A.5.

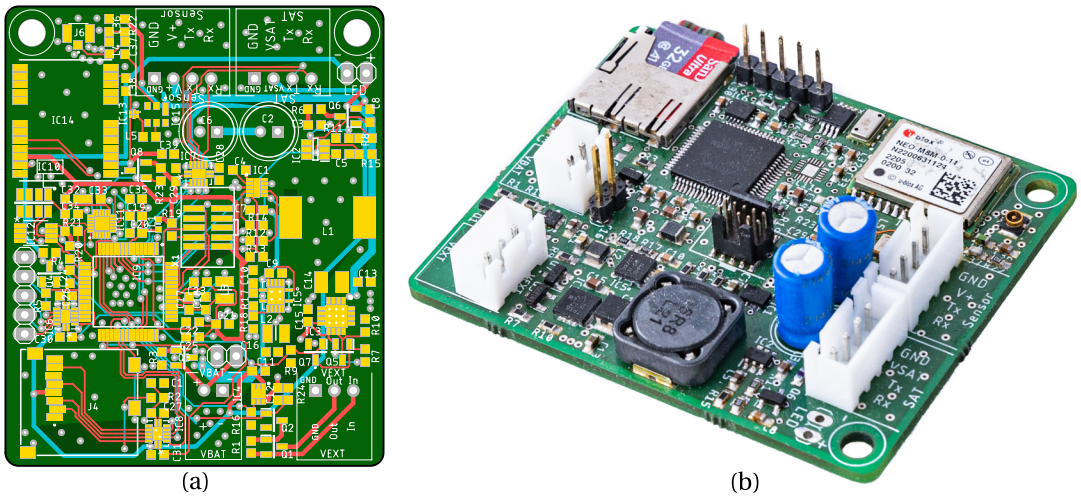

(a) (b)

Figure 18: *Implemented main-board layer-design (a) and assembled PCB (b).*

4.4 Software Framework Definitions and Structure

After the selection of the hardware, the software architecture is presented in the following. The main objective of the software framework for the monitoring module's main board is to efficiently schedule and process measurement cycles from the connected sensors. To achieve this, the software utilizes deterministic state machines to provide a reliable and fault-tolerant system. The state machines are divided into two types: a main state machine that manages the system state of the main board and a sensor state machine for each connected sensor that manages the sensor states (cf. figure 19). These state machines are event-driven allowing them to dispatch events influencing each other. The software framework is a collaborative development of the author and a supervised master thesis by Saleh [156].

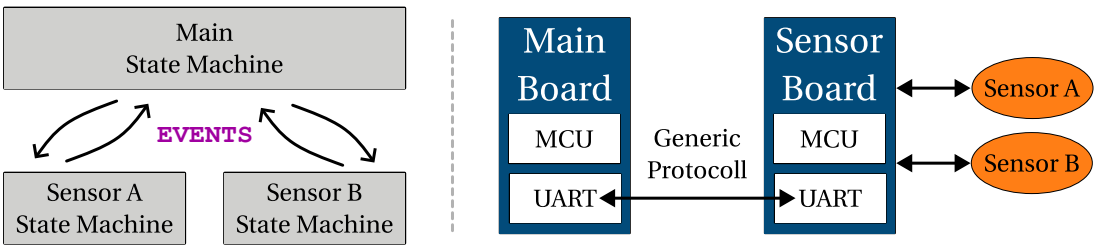

Figure 19: *Left: Basic concept of state-machine interaction; Right: Visualization of communication between Main-Board and sensor-board via the generic protocol.*

In the initial implementation of the software, a self-programmed scheduler is used to manage the state transitions and control the flow of the system. This approach ensures a simple and sequential software design with low-performance requirements. To achieve abstraction from the hardware components and to allow software modularity, the software framework follows a layered architecture (cf. figure 20). The base layer is the physical microcontroller and the connected sensor and communication modules. The ARM microcontroller is programmed in C and compiled with the GNU Compiler Collection (gnu99).
A microcontroller abstraction layer (MCAL) is used to directly access the microcontroller's peripherals and external devices. The MCAL is based on the Advanced Software Framework 4 (ASF4) and is set up using the Atmel START configuration tool. Atmel Start allows to configure the timers and clocks, provides a calendar interface, and configures the GPIOs and serial communication ports. ASF4 provides an abstraction to the hardware by providing an application programming interface (API) for all hardware drivers. The electronic abstraction layer (ECAL) provides an API to interface the device drivers, such as GPS and SD-card, without any dependencies on the physical components. The services layer provides functional services for the main application, including the definitions of the state machines, data structures, and the scheduler. The Services Layer and

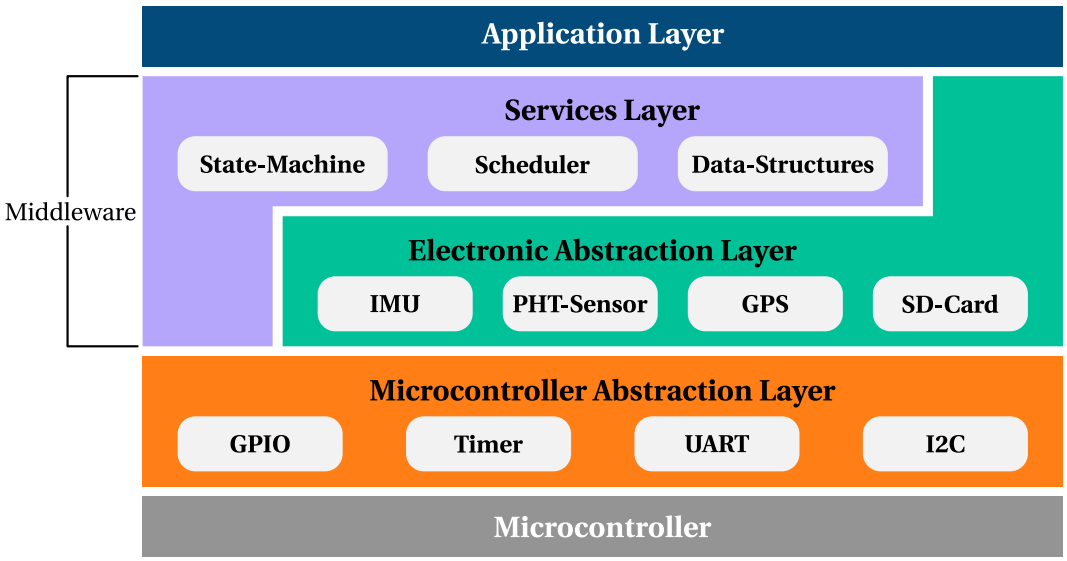

Figure 20: *Diagram of the of the software framework's layered architecture.*

the ECAL constitute the middleware of the software and provide hardware-independent functions to the application layer.

In the following, the software architecture of the monitoring module is described in detail to provide an understanding of its working principle. First, the application layer is described, implementing the software's intended functionality. Then, the underlying components, i.e., the state machine, the scheduler, the generic communication protocol, and the ECAL driver, are explained in more detail.

4.4.1 Application Layer

The application layer provides the monitoring functions to the user. It implements the main function using the APIs of the middleware by initializing the system and executing the scheduler. During initialization, the user configuration is loaded from the SD card and the measurement cycles are configured. The state machines are initialized according to the user configuration. The main flow of the software is shown in figure 21. The state machines add tasks to the scheduler, which are executed in order according to their due dates. Periodic tasks are rescheduled, while aperiodic tasks are removed. The executed tasks can dispatch events that can lead to state changes of the state machines and further scheduled tasks.

A watchdog timer runs in parallel to the software and needs to be triggered in regular intervals to avoid dead-ends. In the case of failure, the watchdog timer resets the MCU and restarts the software including all initialization. Current datetime and next measurement due dates remain stored in the non-volatile backup register of the MCU.

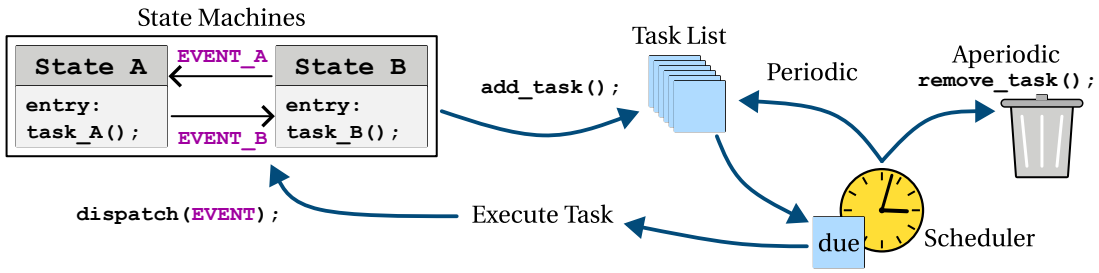

Figure 21: *Visualisation of the interaction between state machines and the scheduler workflow.*

4.4.2 Scheduler Integration

To efficiently use the hardware resources a non-blocking task scheduler that utilizes a single hardware timer is used. This approach helps to overcome challenges such as using multiple timers, which would increase complexity and reduce system performance, as well as blocking interrupt service routine (ISR), which impede the execution of other interrupts. The scheduler allows for concurrent execution of tasks at predefined time periods and uses low-power modes for integrated modules, such as the GPS, IMU, and PHT-sensor, to reduce overall energy consumption and enhance system performance. The initialization of the scheduler is performed in the application layer through the provided API, allowing for the addition and removal of tasks from the task list. State machines add and remove tasks according to their state definitions and the events that occur. The scheduler periodically polls for executable tasks and runs them as they become available. Non-periodic tasks are removed after completion, while periodic tasks are executed in a cycle until they reach the maximum count, at which point they are also deleted. This enables the scheduler to execute multiple tasks efficiently while minimizing the impact of limited hardware resources on system performance and energy consumption.
The description of a scheduled task is provided by the task_ struct, which includes a function pointer to the individual task's description (cf. figure 22). All tasks are stored in a linked list, with the time_expire attribute serving as a counter to indicate the time until execution. An ISR-driven timer executes the update function every millisecond, decrementing the time_expire value of all tasks.

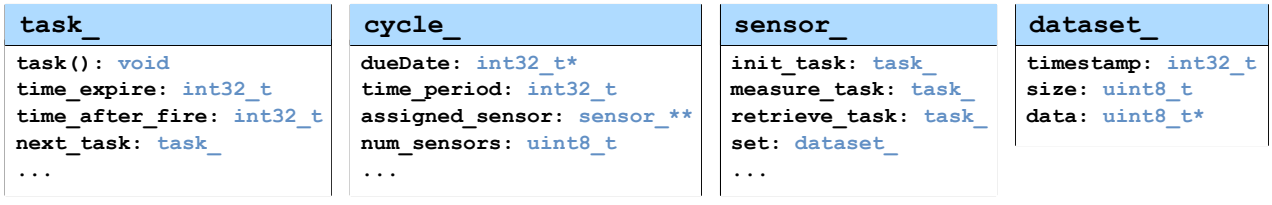

Figure 22: *UML representation showing definitions of software fundamental structs and their contents.*

4.4.3 Measurement Cycle Definitition

A measurement cycle is defined by the cycle_ struct shown in figure 22. The struct contains a pointer to the next due date stored in one of the backup registers of the MCU. The next due date is a Unix timestamp that is compared to the current Unix time provided by the MCAL's calendar interface. The system time is updated by the GPS time on each localization. In addition, the cycle_ struct contains the user configuration of whether the measurement cycle data should be transmitted via satellite or stored on the SD card. The attribute time_period of a cycle_ defines the number of seconds between executions, and the assigned_sensor attribute contains a pointer to all sensor instances assigned to this measuring cycle (cf. figure 22). Multiple measurement cycles can be created in the user interface so that individual measurement settings can be configured. The sensor_ struct is a generic description of an arbitrary sensor instance and contains individual task descriptions for initialization, measurement, retrieval and idle state (cf. figure 22). For onboard sensors, these tasks are defined using the ECAL API. Each sensor_ contains a dataset_ that stores the current measurement data of the sensor (cf. figure 22).

4.4.4 Event Driven State Machine Definitions

An Event-driven finite-state machine (FSM) is an efficient way of handling concurrent and asynchronous events in embedded systems. The framework of Dash et al. [157] combines the event-driven paradigm with a state machine model, which allows for the seamless handling of multiple sensor events. The state machine design effectively handles concurrent and asynchronous events, reducing CPU cycle consumption and code memory footprint. The framework also includes an event dispatching mechanism, execution context and queue structure to map events to the proper handler.
To implement the main software logic while keeping track of the individual state of each sensor, two nested state machine types are defined. The main FSM indicates the main board's overall state in the measurement cycle. Additionally, for each sensor instance, a sensor FSM is created that schedules the sensor measurement process. First the main FSM (cf. figure 23) is considered.
The first state in the main logic is the `Start` state, which schedules the initialization task in the entry condition. The initialization task reads the user configuration and creates a sensor FSM for each connected sensor unit. Once the initialization function is completed the INIT_COMPLETE event is dispatched, which indicates a state change in the main FSM.
The state that follows depends on whether the monitoring board is being switched on for the first time or simply restarted from sleep or reset. The function dueDates_valid() checks whether due dates are stored in the MCU's backup registers. If this is a first

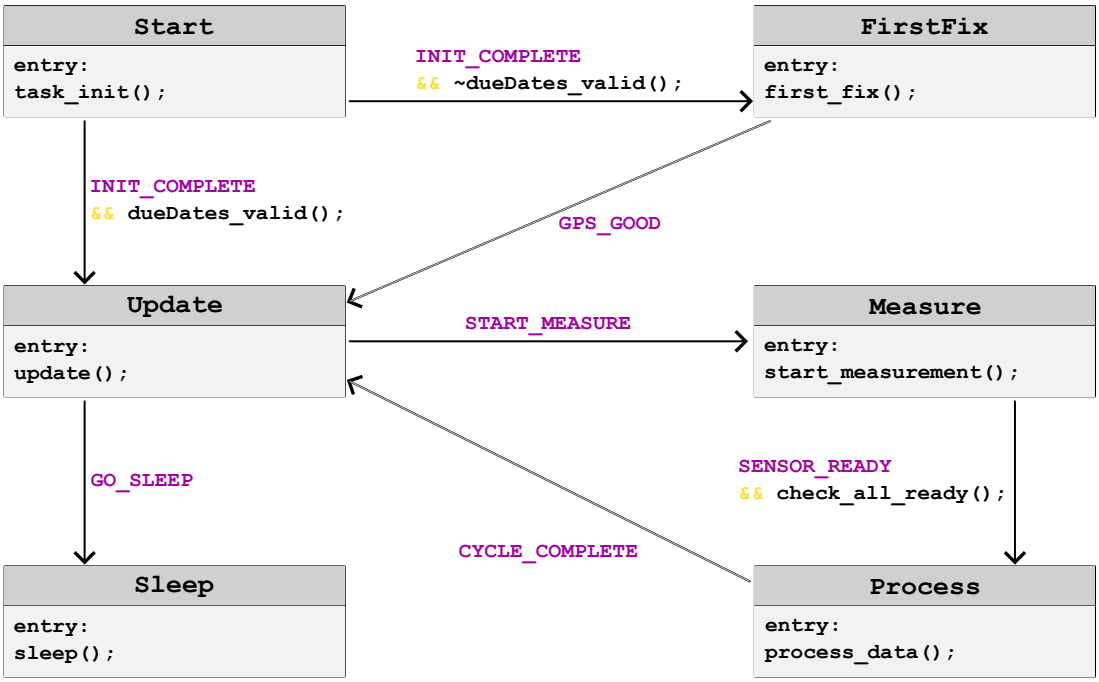

Figure 23: *Diagram of the main FSM logic. Purple text indicates event descriptions.*

startup, the backup register is empty and the system enters the `First Fix` state. In the `First Fix`, the system searches for a GPS location for the first time (cold start) and displays the error-free functionality of the monitoring module via status LED. If there are already valid due dates and a previous GPS position in the backup register, the system may enter the update state, which allows faster GPS localization through a hot start. In the `Update` state, the system waits for the next due date of a measurement cycle.

To start a measurement, the main FSM triggers all sensors of a cycle, if the cycle's due date is reached. The main FSM then changes from the `Update` state to the `Measure` state. Additionally, the event SENSOR_TRIGGER is dispatched to all sensor FSMs, resulting in the transition from the `Start` state to the `Initialization` in each sensor FSMs (cf. figure 24).
In the sensor initialization state, the init_task is scheduled, resulting in the individual initialization of each sensor instance. Once the sensor initialization is complete, the INIT_COMPLETE event is sent to the individual sensor FSM, resulting in a state change to the `Measure` state. Here the measure_task is scheduled, to start the measurement of the sensors instance. From the sensor state `Measure`, the FSM can transition either to `Data Ready`, when the measurement data is immediately available or to `Retrieve`, where the module waits until the measurement is complete. When a sensor reaches `Data Ready`, the SENSOR_READY event is dispatched to the main state machine, which checks the status of all sensors. Only if all sensors are ready, the main state machine

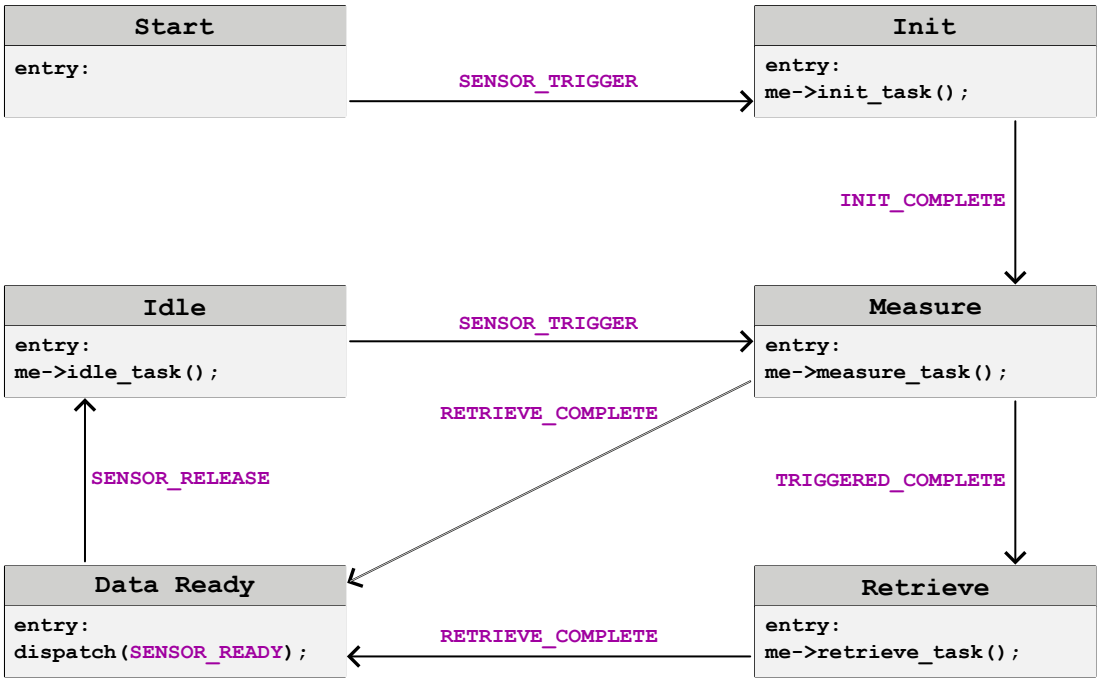

Figure 24: *Diagram of the sensor FSM logic. Purple text indicates event descriptions.*

enters the `Process` state.

In the `Process` state of the main FSM, the process_data() function reads the data set of each sensor and either transmits the collected data via satellite or stores it on the SD card, depending on the measurement cycle setting. Once the data is processed, the main FSM releases each sensor by dispatching the SENSOR_RELEASE event. This frees the memory of each sensor data set and transitions the sensor instance to the `Idle` state. In the `Idle` state, the sensor instance waits for the next SNESOR_TRIGGER event to restart a measurement cycle.

4.4.5 Sensor Error Handling

To ensure fault-tolerant architecture, the sensor's FSM includes a dedicated seventh state, described as the `Sensor Error` state, which can be accessed from any of the sensor's states. When a sensor instance is not performing as expected, such as when it sends an error code or does not respond at all, the sensor FSM transitions into the error state. Once in the error state, the sensor attempts to recover by reinitializing the sensor instance. If the error persists even after reinitialization, the sensor remains in the error state, and no data is collected. By implementing this error-handling mechanism, the monitoring module can continue to collect other sensor data reliably and minimize the impact failures by a single sensor instance.

To ensure the reliability of the system, a watchdog timer has been implemented above the main process. The watchdog timer needs to be triggered regularly, which is done by the scheduler after each successful task completion. In case the watchdog timer is not triggered within a pre-defined period of 16 seconds, the main application undergoes a complete reset, causing the entire system to start over. However, the due dates and the last GPS positions, stored in the backup registers of the MCU, are preserved. This mechanism helps to prevent the system from running into an unrecoverable state and provides a fail-safe mechanism to maintain reliable operation.

4.4.6 Design of a Flexible Communication Protocol

The communication protocol between the main board and the sensor board is designed to offer a standardized interface. This enables the module to connect with a variety of sensor technologies, without requiring any firmware updates on the main board. The sensor board is typically implemented using an Arduino, running the external sensor unit application (cf. interface library in section 4.4.9) to simplify communication with the main board. This facilitates the process of adding new sensors to the module.
The communication protocol is based on the Open Systems Interconnection (OSI) model [158]. The OSI model is a reference model for how communication systems should operate. It is a conceptual framework that describes the functions of a networking system without regard to its underlying internal structure and technology. In the following, the definition of the developed generic protocol is explained according to the seven layers of the OSI model:

Physical Layer The Physical Layer specifies the physical characteristics of the interface, such as voltage levels, signaling methods, and cable types. The main board and the sensor board use a serial interface to establish a physical connection and exchange data. The physical layer is therefore defined by the pin assignments for the communication, a single pair of wires, and the 3.3 V logic level. To improve the physical reliability of the communication, a more robust signal level standard as e.g. RS-232 or RS-485 could be used. However, this would require a different hardware design capable of driving and receiving these standards. Since the main board and the sensor board can be kept very close, the 3.3 V logic level is sufficient.

Data Link Layer The Data Link Layer of the OSI model establishes and terminates the node-to-node communication between the main board and the sensor board based on the universal asynchronous receiver transmitter (UART) protocol. This layer provides error-free transmission of data between devices on the same network.
The communication between the main board and the sensor board is conducted using

consecutive request and response operations. The main board initiates the process by sending a request message to the sensor board using a write operation, followed by a read operation to receive the sensor board's response message (cf. figure 25). The data transmitted during UART communication varies depending on the request and response commands. The message packets are predefined at the Presentation Layer to facilitate communication between the main board and the sensor board.

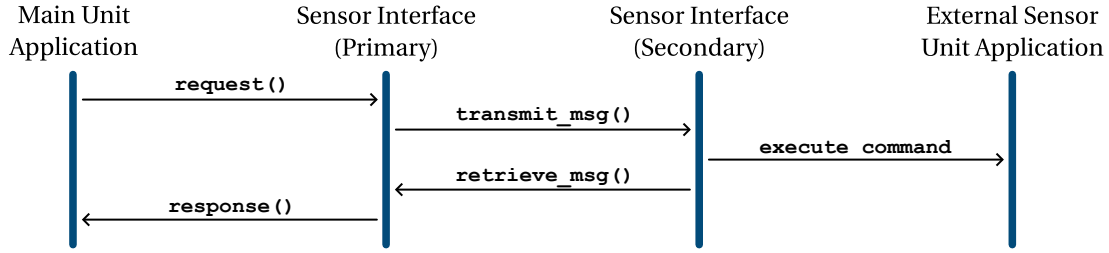

Figure 25: *Visualization of the communication procedure between sensor and main-board on the data link layer.*

The maximum number of bytes that can be transmitted during UART operations is set to 255 bytes. However, this restriction can be adjusted based on the data transfer requirements. The sensor board waits for communication commands initiated by the main board and immediately responds with a confirmation message upon receipt of a command. Since the sensor board can only respond with available sensor data, it will respond with an error code if the measurement is still ongoing. The main board attempts to retrieve the measurement data for a fixed period of time, and if unsuccessful, the process is terminated.

Network Layer The Network Layer of is not included in this project since the communication between main board and sensor board happens over the same line. This layer is responsible for routing the data between different networks and determining the physical path for data transmission. However, the framework could be extended to define a Network Layer using a multiplexer that handles individual point-to-point connections [156].

Transport Layer The Transport Layer is responsible for ensuring reliable and error-free data transfer between the main board and the sensor board. It guarantees that the data is delivered to the correct application on the receiving device and manages any issues such as data loss or errors that may occur during transmission. To accomplish this, the communication request and response messages are defined in packet frames. A consistent frame structure is utilized for both request and response messages (cf. figure 26).

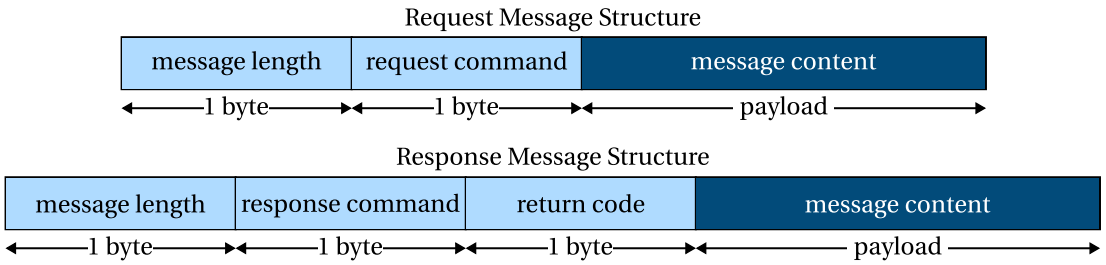

Figure 26: *Visualization of the transport layer structure for request and response messages.*

The response message has a similar frame format to the request message, but it includes a return status code. The payload message frame is specified by individual packet commands represented in hexadecimal format with the most significant bit transmitted first (Big-Endian). This ensures that the communication between the main board and the sensor board is efficient and reliable.

Session Layer The Session Layer is responsible for managing the connections between the main board and the sensor board. It establishes, maintains and terminates sessions between the applications. In this project, the session is only maintained until the data transmission is completed, after which it is promptly terminated. As a result, the session layer is not utilized as the communication is executed as a single transfer of request and response messages.

Presentation Layer The Presentation Layer is responsible for converting data into a format that the Application Layer can understand. It may also encrypt or compress data for security or efficiency. In this project, the request and response commands are predefined hex values (cf. appendix A.3) to simplify communication. Whenever the main board sends a request including a command ID to the sensor board, the sensor board responds with the corresponding response ID. The defined minimum and maximum command values are reserved for debugging purposes. The response message includes the transmitted message and a return status code. The list of predefined return codes is defined by table 37 in appendix A.3.

Application Layer The Application Layer of the OSI model is responsible for providing the interface between the communication protocol and the application that uses the data received from the sensor board. It enables the main board to retrieve the measurement data, convert it into human-readable information, process it and store it on the SD card. In this project, the Application Layer of the communication protocol can be described by the Application Layer of the software architecture that sits on top

of it. This layer uses the APIs of the state machines, scheduler, and communication protocol to implement the monitoring task.

4.4.7 Electronic Abstraction Layer Implementation

The electronic abstraction layer provides an API to access the board's peripherals, including drivers for onboard sensors such as the PHT-sensor and GPS module, as well as libraries for different external transmission modules. The API is hardware-independent, allowing for easy adaptation to hardware changes. Most implementations are straightforward functions based on publicly available documentation and examples. Basic functions e.g. to read the GPS position and switch on low-power modes are provided. Therefore, only the implementation of the Iridium module and the SD card are given as examples for two ECAL drivers.
The SD card communicates with the system using an SPI interface and employs the FatFS driver [159]. This open-source, lightweight driver is designed to optimize small-footprint systems and provides support for various file and directory operations, as well as a FAT/exFAT file system compatible with DOS and Windows. The initialization and storage functions of the SD card's API are invoked by the main FSM in the `Process Data` state to store the data set obtained from measurement cycles on the SD card. To save a measurement cycle, all stored sensor data is first loaded from the cycle pointer into a temporary buffer, and then the FatFS library is used to write the raw data bits in a binary file on the SD card. The data structure of the binary file follows a consistent format, making it easy to decrypt (see figure 27). Only the sensor data type is required for evaluation.

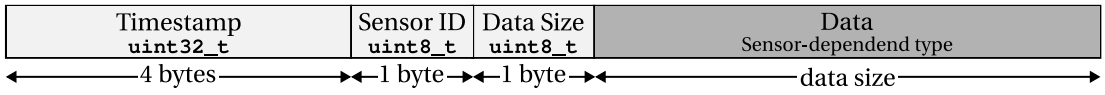

Figure 27: *Visualisation of the data structure of binary data stored on the SD -Card.*

The driver of the satellite module follows a similar approach by providing initialization and data handling functions. For a satellite transmission, the API receives a data buffer of know length and forwards it to an iridium module library written by Reyes [160] in the context of a supervised master thesis.

4.4.8 Graphical User Interface Design

A GUI was developed for configuration of the measurement cycles, sensor settings, and transmission setups. The GUI, developed as a supervised student work [161], utilizes the python library DearPyGUI and adheres to UX-Design guidelines for optimal user

interaction. The GUI allows for the configuration of the deployment scenario on a desktop computer (windows) and export of the settings in a *.json* file format. These settings can be imported onto the main board via an SD card, where upon startup, the main application scans for the config file and loads the user-specified configuration if present.

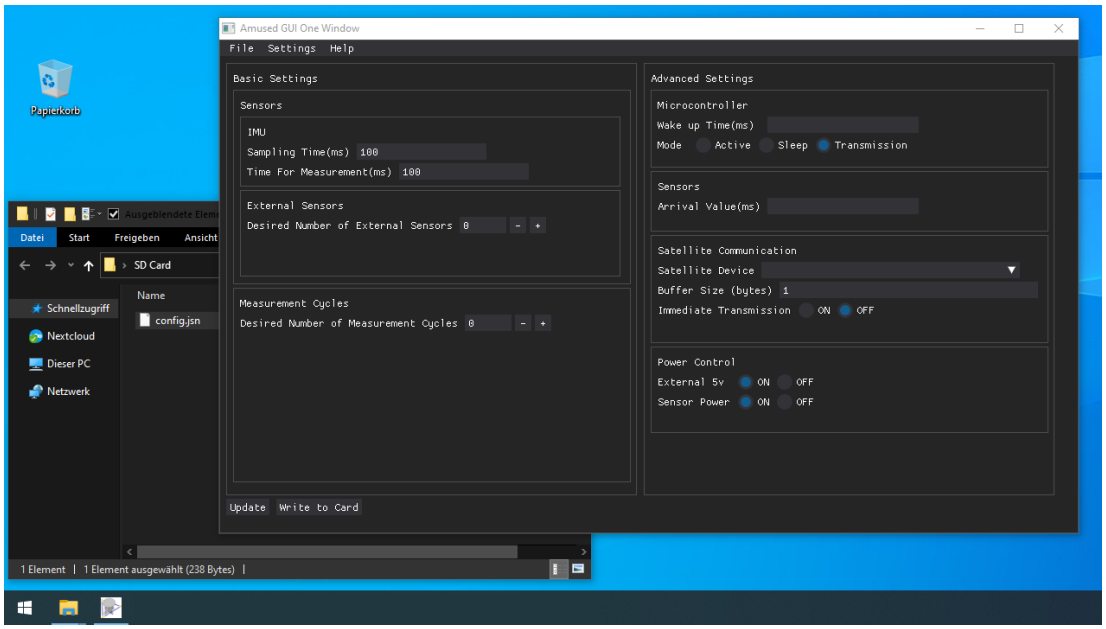

Figure 28: *Graphical user interface of the monitoring module and the config.json file output.*

4.4.9 Sensor Board: Communication Interface Library

The Sensor Board is a crucial component of the modular monitoring device, as it acts as the interface to various sensors and communicates the measurement data to the main board via the generic communication interface. In terms of hardware, the sensor board consists of a microcontroller that supports a serial connection (UART) interface to the main board. The microcontroller can be of any type that is compatible with the communication interface provided by the main board. For prototype tests, an Arduino Nano was used. A 5 V power supply is provided by the main board, allowing to switch the sensor board on and off when necessary.
In terms of software, the sensor board runs the provided external sensor unit application, implementing the communication interface library, to establish communication with the main board. This library comprises message commands listed in table 36 of appendix A.3, as well as two ISR-driven functions for sending and receiving data. The sensor board library implements a straightforward state machine, which utilizes a switch-case branch that mirrors the sensor states of the main board software. In

each state, the user is required to define sensor-specific tasks for e.g. initialization and measurement. For instance, in the measurement state, the user must implement the sensor-specific procedure to initiate a measurement by the sensor. The resulting data must then be provided to the interface library, which manages the data transmission to the main board.
When the main board sends a message to the sensor board, a receive event is triggered on the sensor board, which reads and decodes the message command according to table 36. The sensor board library then decides on necessary state changes and prepares the response message containing e.g. the measurement data.

4.5 Evaluation of Module Capabilities: Implementation and Test

To test the designed monitoring system a prototype was implemented and deployed. The prototype was tested in cooperation with the ICBM of the University of Oldenburg. The monitoring board was integrated into an EDDY drifter design by the ICBM [5], and consisted of the main board, a sensor board based on an Arduino Nano, and a communication board based on the Iridium 9603 module [145], which were all mounted on a carrier board and fit into the Drifter (cf. figures 29 and 31).

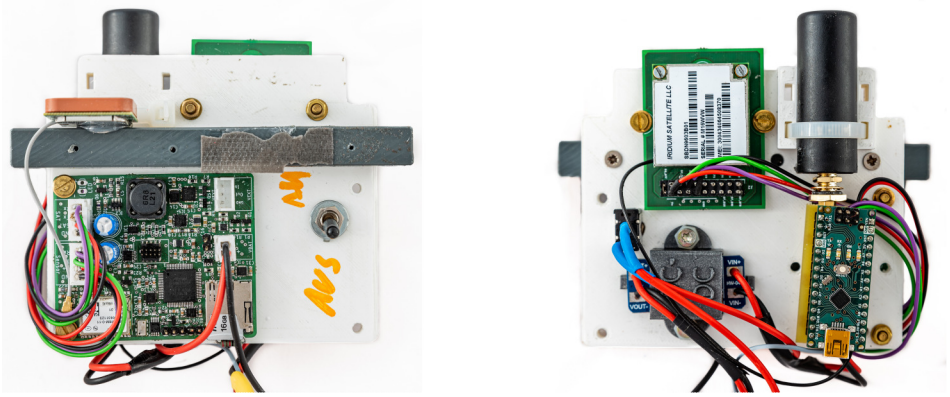

Figure 29: *Assembled monitoring system on a carrier board, consisting of: Main board, Ardunino Nano, Iridium module and 12V boost converter (for sensor supply)*

The goal of the test was to measure water temperature and conductivity using the Aqua TROLL 100 sensor by in-situ [63]. The sensor's supply voltage was provided by an external boost converter, which converted the 5 V output voltage of the main board to the 12 V sensor supply voltage. The power supply for the main board was provided by a rack of D-Cell batteries with pairs of 3 series batteries providing a nominal voltage of 4.5 V. Every 2 minutes, a measurement was taken and stored on the SD card, and every 6 minutes, the last three measurement results were transmitted via the satellite board.

In between the measurements, the board went into sleep mode for power conservation. Before deployment, the power consumption of the measurement cycle was evaluated. To do this, a constant voltage of 3.7 V was supplied to the main board and the current draw was recorded (cf. figure 30).

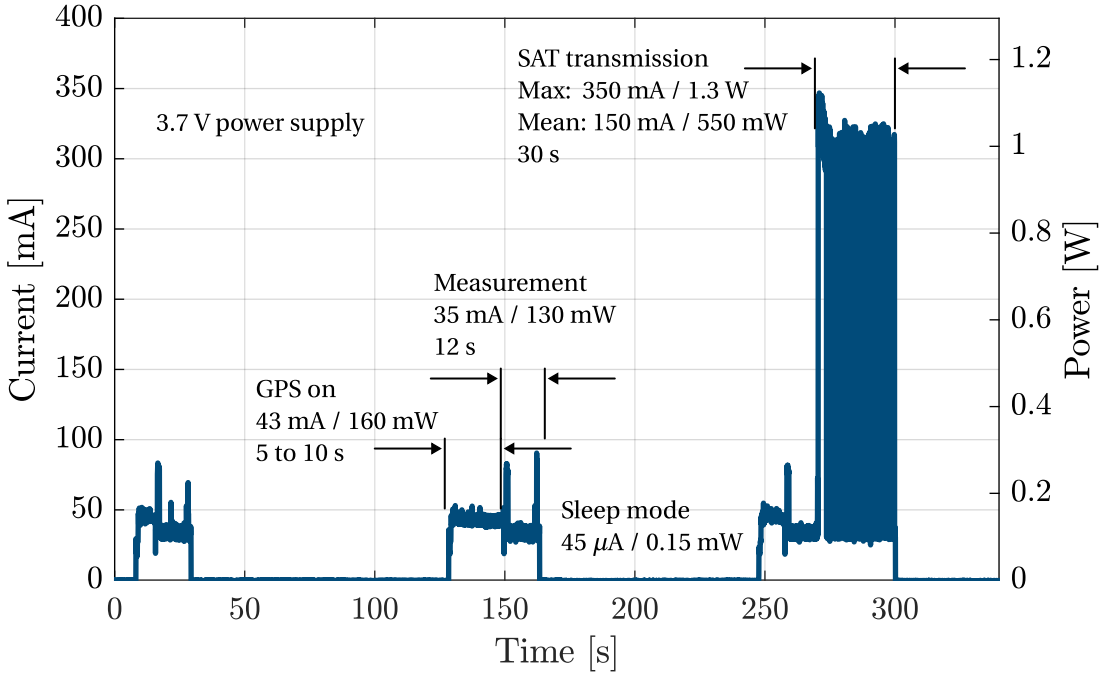

Figure 30: *Plot of the power and current consumption of the main board over the period of three measuring cycles. Supply voltage:* 3.7 V.

The recorded power consumption illustrates the different states of the monitoring module. During sleep mode, between measurement tasks, the module consumes less than 50 µA of current, meeting the low-power requirement. The idle module consumes less than 20 mA of current, which increases to 45 mA during active GPS localization. Around 35 mA are consumed during external sensor measurements. The average power consumption remains relatively low and peaks during satellite transmission, which occurs every third cycle. The satellite module has the highest power demand with a peak current of 350 mA and an average current draw of 150 mA over the 30 second transmission time. The average power consumption strongly depends on the duration of sleep modes and active periods. The here presented measurement cycle, has very frequent satellite transmissions and therefore shows a large average consumption of 20 mA or 75 mW.

On the evening of October 21st, 2022, a set of four Drifters were deployed in the German Bight (North Sea) (cf. figure 31). Due to an upcoming storm, three drifters were collected on October 23rd and the remaining one on October 25th.
The recorded position data of the drifters clearly indicate the tidal back-and-forth

(a) (b) (c)

Figure 31: *a: Deployed Eddy Drifter in the North Sea; b: Lined up Eddy Drifter in front of the CTD profiling instrument; c: Implementation of the monitoring system in the Eddy Drifter. Photos a,b and c: Universität Oldenburg - Institut für Chemie und Biologie des Meeres*

motion, in addition to the general drift movement from southeast to northwest (cf. figure 32). The onset of the storm is observable through the increasing distance in the tidal periods from the remaining three drifters. Furthermore, a slight cooling of the water temperature can be observed in the temperature data (cf. figure 32).
During the evaluation of the salinity measurements, it becomes evident that there is a relatively high level of noise present in the measurement data. In addition, there are significant spikes in the measured values both upwards and downwards. It is suspected that these spikes are caused by air bubbles being washed onto the electrodes of the sensor by the rough sea conditions (cf. figure 33).
The satellite transmission state was evaluated afterward, and it was found that out of 428 transmission trials, only 307 were received and 121 could not be received. It is suspected that the main reasons for the high transmission failures are the low-lying antenna of the satellite module. Due to the motion of the waves, the alignment of the antenna is not always optimal, which can result in these interruptions.

In general, the test deployment can be considered a success. The data logging functionality operated without any failures, and the power modes and GPS tracking of the monitoring modules were effective, providing evidence of the modular monitoring device's feasibility. However, the data transmission success rate was lower than anticipated, likely due to the sending antenna's low position.

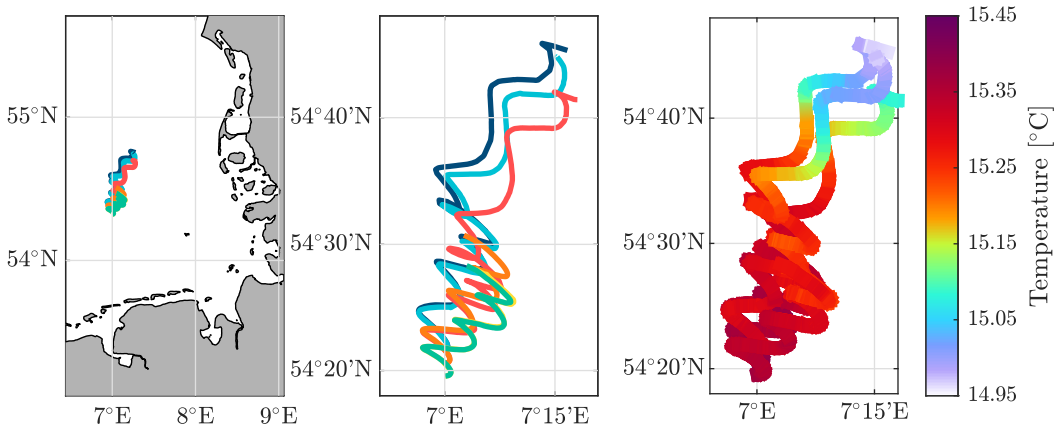

Figure 32: *Visualisation of the drifter pathsways for the operational period between 22. and 23. October 2022. Right: measured water temperature along the drifter's path.*

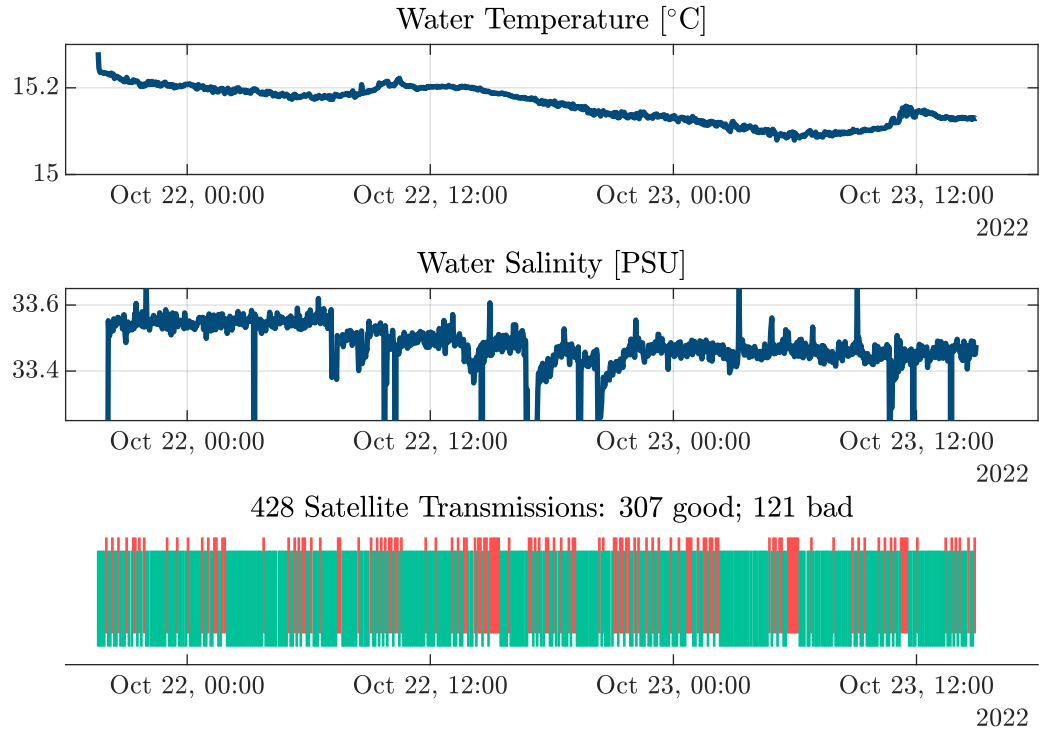

Figure 33: *Data collected from the monitoring system showing water temperature, salinity and an assessment of the success rate of the satellite transmission.*

4.6 Conclusion: Versatile Modular Ocean Surface Monitoring

The existing systems for ocean surface monitoring lack flexibility and are not adaptable to a broad range of applications. Typically, these systems offer only a fixed set of expensive oceanographic sensors, and cannot be extended with custom sensor technology. As a result, the high costs prohibit in-situ ocean surface observations with a high spatial resolution of measurement points.

To overcome these limitations, a more flexible and user-friendly system architecture was proposed. This system offers modular hardware and is adaptable to a broad range of measurement setups. The hardware-agnostic design of the main board enables the integration of custom sensor technology, requiring only the implementation of external sensor technology via e.g. an Arduino. The modular design allows for the exchange of communication boards, offering a selection of communication technology ranging from low-cost GSM to reliable satellite transmission with global coverage. A user-friendly GUI enables the configuration and setup of the measurement parameters. Additionally, the software framework follows a flexible architecture for future extensions.

This module offers a versatile solution for ocean surface monitoring and provides a framework for future advancements in the field. The hardware-agnostic architecture allows for the integration of custom sensors and makes ocean monitoring accessible to a wide range of research fields. With component costs of around 100€ (excl. communication and sensor board), the module can be implemented with further low-cost sensor technology, providing a more cost-effective solution for ocean surface monitoring. The proposed improvements have the potential to increase the spatial and temporal resolution for ocean surface monitoring by simplifying the deployment of larger quantities.

The proposed concept was tested in a drifter prototype, which proved its functionality. However, the cost analysis revealed that the largest expense in the monitoring system is the sensor technology, with the Aqua Troll costing over 1000€. To ensure cost-effective monitoring, it is evident that low-cost sensor technology is required. Therefore, the next chapter will focus on deriving design principles to reduce the costs of ocean temperature and salinity measurements.

5 Cost-Effective Embedded CT Sensor for Sea Surface Monitoring

The high cost of oceanographic sensors is a significant barrier to large-scale in-situ monitoring of the ocean surface. While many research questions in oceanography often require high-precision sensors, the lower accuracy requirements of sea surface observation allow the use of adapted sensor technology. Despite the demand, the availability of low-cost conductivity and temperature (CT) sensors suitable for long-term sea surface observation is limited.
This chapter aims to establish design principles for an embedded CT sensor that meets the specific requirements of sea surface monitoring. To achieve this goal, different measurement approaches are considered and the physical principles and environmental effects are systematically analyzed to balance measurement uncertainty against cost. Finally, this chapter evaluates the potential of a combined conductivity and temperature sensor concept as a solution for a low-cost sea surface salinity (SSS) sensor. The goal is to provide design principles for low-cost embedded CT sensors that enable sea surface monitoring with high spatial resolution. The results of this chapter contribute to the development of improved, low-cost sensor technology for future ocean surface monitoring.

5.1 Embedded CT-Sensor Concept Development

By reviewing comparable existing solutions, this section describes the core concept of the embedded CT-sensor. The analysis of the current state of the art leads to the determination of a development outlook and the requirements for the system under development.

5.1.1 Exploring Prospects for Inductive Conductivity Measurement

Despite the availability of multiple CT-sensors for measuring water conductivity (cf. section 2.3.3), none meet the requirement for cost-effective measurement at the ocean surface. At the sea surface there is a higher risk of bio-fouling and more contaminants, so inductive sensors are advantageous. At the same time, there are greater changes in salinity, so a higher measurement uncertainty is acceptable for many applications. A fully integrated compact sensor is required that can easily be used on small surface floats. A sensor similar to this description is the inductive sensor from Aanderaa (cf. section 2.3.3 and figure 34a). However, this sensor is designed for deep water measurements and therefore meets different requirements for precision and pressure resistance. In different versions, the sensor is available as a fully self-contained sensor with RS-232 or RS-422 interfaces. In the highest accuracy version, the sensor achieves an accuracy of 0.4 $\frac{\text{mS}}{\text{m}}$ and can be used to a depth of up to 6000 m. This brings the compact sensor close to the resolutions of high-precision CTD systems, but it is also in a similar price range and therefore not a cost-effective solution for sea surface monitoring.
Another similar design, more suitable for surface measurements is the *Ocean CT Sensor* from D-2 Incorporated [162] (cf. figure 34b). There is little information available about this product since it is less well known. However, D-2 promotes its sensor as a *low-cost alternative for upper ocean conductivity and temperature measurements* [162] targeting the exact concept identified. The sensor offers a conductivity resolution of 2 $\frac{\text{mS}}{\text{m}}$ with a stability of 0.5 $\frac{\text{mS}}{\text{m}}$ per month. Temperature resolution is 20 mK and the compact housing allows for use at depths of up to 50 m. Available communication interfaces are RS-232 and RS-485.

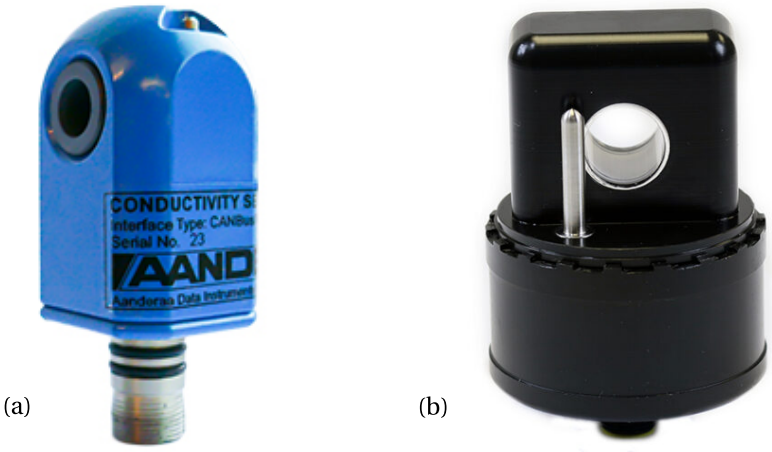

Figure 34: *Fully embedded CT-Sensors by a: Aanderaa [163] and b: D-2 Incorporated [162]*

Both sensors are similarly expensive and, at more than 2000 €, far from a cost-effective

solution. A comprehensive overview of the sensors is provided in table 5.
The aim is therefore to derive design principles for a compact, low-cost sensor that is completely self-contained and specifically tailored to the measurement requirements for measuring salinity at the sea surface. A sensor with lower accuracy compared to existing systems would be acceptable if it could reduce costs.

5.1.2 Defining the Requirements for an Embedded CT-Sensor

The requirements for the CT-sensor ratings result from the application of SSS measurements. For most areas in the global ocean, a measurement range of 0.5 to 7 $\frac{\mathrm{S}}{\mathrm{m}}$ and -5 to 35 °C is sufficient. By setting the lower limit for conductivity higher than other sensors (cf. UNESCO CTD-requirements in table 4), the challenge of detecting weaker signals is reduced. To provide an advantage over satellite-based observations, a measurement uncertainty of less than 0.1 PSU and 20 mK shall be achieved (cf. measurement uncertainty in appendix A.1). According to PSS-78, this corresponds to to a conductivity accuracy of at least 10 $\frac{\mathrm{mS}}{\mathrm{m}}$ at 35 PSU and 15 °C. To produce usable measurement results for the oceanographic community, salinity readings must be calibrated to PSS-78 and temperature readings to ITS-90.
To enable reliable long-term monitoring, a stability of 5 $\frac{\mathrm{mS}}{\mathrm{m}}$ and 20 mK shall be maintained over one year. From the comparison of different conductivity measurement principles, it has been found that a non-contact inductive approach offers advantages for near-surface measurements. This approach shall be pursued in the following.
The device to be developed shall be compatible with the modular monitoring system from section 4. This requires an energy efficient operation from a 5 V power supply and a serial interface for communication. The overall size of the device shall allow installation on a drifter and therefore not exceed the longest edge length of 10 cm. To be fully self-contained, the primary sensors, as well as the primary and secondary electronics shall be embedded in the same housing. To protect the system from seawater the housing shall provide means against biofouling.
A detailed list of requirements is given in table 14, further requirements could be defined to specify the electronics and software implementation, however, the initial focus of the following development is the primary sensor design and the implementation of embedded system is secondary.

#	Description	Value	Rating
Sensor ratings			
S01	Conductivity range of operation	0.5 to 7 $\frac{S}{m}$	M
S02	Temperature range of operation	−5 to 35 °C	M
S03	Measurement uncertainty of conductivity	< 10 $\frac{mS}{m}$	M
S04	Measurement uncertainty of temperature	< 20 mK	M
S05	Resolution of conductivity reading	< 5 $\frac{mS}{m}$	M
S06	Resolution of temperature reading	< 10 mK	M
S07	Allow salinity calibration to PSS-78	-	M
S08	Allow temperature calibration to ITS-90	-	M
S09	Stability of conductivity reading	< 5 $\frac{mS}{m}$/year	M
S10	Stability of temperature reading	< 20 mK/year	M
Power Supply			
S11	Low-Voltage Power Supply	5 V	M
S12	Energy-efficient operation	< 100 mW	M
S13	Low-power sleep mode	<< 1 mW	O
Housing			
S14	Provide protection from water	> 30 m	M
S15	Provide protection from biofouling		O
S16	Compact Housing with embedded transducer	< 10 × 10 × 10 cm	M
Costs and operation			
S17	Low component and manufacturing costs	< 100€	M
S18	Digital output of measurement reading	UART or I^2C	M

Table 14: *Requirement list of the embedded CT-sensor; Rating: Mandatory (M), Obligatory (O)*

5.1.3 Concept Derivation and Component Definition

To effectively develop a concept for the CT-sensor, a function tree of the system is obtained (cf. figure 35). The main function of the sensor is to determine salinity, which comprises two sub-functions: temperature measurement and conductivity measurement.

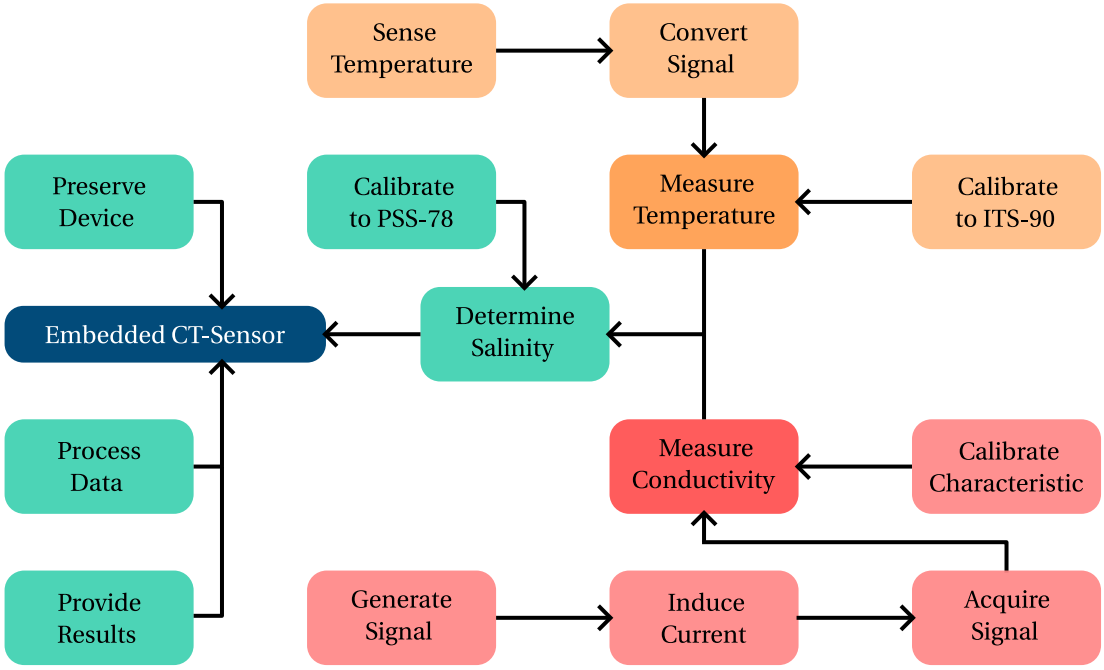

Figure 35: *Function tree of the embedded CT-sensor including functions for temperature and conductivity measurement.*

To sense temperature, the water needs to have a physical effect on the primary sensor, allowing the conversion into an electric signal. Furthermore, the temperature measurement shall be calibrated according to ITS-90 to provide a comparable temperature reading.
As the CT-sensor is to incorporate a non-contact conductivity measurement method, the development focuses on inductive sensor types. The functions of the inductive conductivity sensor are to induce and sense a current in the water. The signal induced first needs to be generated and the measurement signal must be acquired and converted into a digital reading. The conductivity reading must be calibrated according to the specific characteristics of the sensor.
With the given temperature and conductivity readings, the embedded CT-sensor has to process the data into a salinity result according to PSS-78. The final salinity measurement must then be provided via serial communication. To protect the device from e.g. water damage and other hazards, the CT-sensor needs to incorporate means of protection.

The CT-sensor comprises five main components: the primary conductivity sensor, the primary electronics for conductivity measurement, the primary temperature sensor, the primary electronics for temperature measurement, and a shared secondary electronics acting as the processing unit (cf. terminology of section 2.3.1).
The primary sensor of the conductivity sensor includes the coil arrangement that induces a current into the water, while the primary electronics amplify and filter the signal. The shared secondary electronics converts the analog signal to a digital measurement reading and facilitates signal generation. Similarly, the primary sensor of the temperature sensor senses the temperature, with the primary electronics serving as transducer circuits. The shared secondary electronics convert the analog signal from the temperature sensor into a digital signal, enabling further processing. Data processing, calibration, and communication of both sensors occur via the same processing unit. In the following sections, the performance of the primary temperature and conductivity sensors is evaluated individually.
Initially, alternatives to the conventional inductive conductivity sensor type are investigated, trying to find a better balance between accuracy and effort. Subsequently, a transformer-type inductive conductivity sensor with integrated secondary electronics (processing unit) is developed and a prototype is tested. For the temperature sensor, established oceanographic practices and cutting-edge technologies are reviewed. The most appropriate measurement methods for the embedded CT-sensor are then evaluated to present a design approach of a compact and cost-effective sea surface CT-Sensor.

5.2 Evaluation of Alternative Inductive Conductivity Measurement Approaches

In section 2.3.3, the TICS was presented as the standard approach for inductive conductivity sensors. However, several other inexpensive and simple methods to determine salinity contactless have been proposed by the scientific community. To explore alternative and innovative approaches for developing a cost-effective conductivity sensor, this section evaluates the potential of alternative solutions. In particular, the eddy current type conductivity sensor is examined, representing a promising and straightforward approach. First, an overview of low-cost conductivity sensors is given, with the eddy current type conductivity sensor highlighted. The basic operation of eddy current sensors for water conductivity measurement is then discussed, including the design of an equivalent model representation. Possible implementations for eddy current sensors are evaluated, including a prototype implementation used to identify measurement uncertainties. Finally, the potential of the eddy current sensor as a low-cost alternative to the established TICS is discussed.

5.2.1 Overview of Alternative Inductive Conductivity Measurement Approaches

Various approaches, including optical (e.g. [164, 165]), electrostatic, and electromagnetic sensors, have been tested for water conductivity measurement. A robust salinity sensor based on capacitance measurement was proposed by Kantkack et al. [166]. The low-cost approach is very energy efficient and shows a sensitivity of 1 PSU for a measurement duration of several seconds. Averaging over longer periods of time reduces the standard deviation of the average, giving a sensitivity of less than 0.1 PSU for a stable measurement period of two minutes.
A combination of inductive and capacitive sensing functions has been proposed to measure the conductivity of low-concentration electrolytic solutions by Ismail et al. [167]. The sensor proposed showed a distinct response to various concentrations and a capability to measure solutions as low as 1 ppm.
Other low-cost sensor developments have centered mainly around inductive concepts. For instance, Parra et al. [168] have experimented with arbitrary combinations of solenoids and toroidal coil pairs to create a sensor that relies on empirical observations of the sensed amplitude.
The primary effect used in this context is the presence of alternating magnetic fields in the water, resulting in the induction of eddy currents. The eddy currents lead to an electromagnetic interaction with the sensing coil, by affecting the inductance and coupling of the setup, measurable in changes in amplitude and phase. In contrast, the conventional TICS is based on a toroidal coil pair that primarily induces an electric current into the water, while concentrating the magnetic fields in the high-permeability coil cores, making the deliberate use of changing magnetic fields in the water the primary difference between inductive sensors based on eddy currents compared to TICS. Ismail et al.[169] also proposed a measurement method based on this effect, that detects the change of inductance for a solenoid, due to changing conductivity in the water core. Sonehara et al.[170] utilized the changing inductance, employing a phase shift detection in combination with high-frequency excitation. To reduce manufacturing costs and size, recent research [171–173] has focused on using coplanar coils implemented in printed circuit boards. These studies rely on the eddy current effect provoking changes in the inductance of the integrated PCB coils. A phase-detection circuit is utilized here to measure the surrounding liquid's conductivity.
In this work, eddy current sensors will be analyzed as an alternative for water conductivity measurement. Despite the term *eddy current sensor* often referring to displacement sensors or other types of sensors that interact with conductive solid materials, the principle of operation is similar.

The literature indicates that the eddy current effect is primarily utilized in low-cost water conductivity measurements, where the theory is often disregarded and studies

rely on empirical data. To address this, the theoretical foundations of eddy current sensors for both single-coil and two-coil configurations will be derived. A basic sensor design will be established and evaluated for its potential, with the aim of determining if eddy current sensors can serve as a cost-effective alternative to inductive conductivity sensors, due to their simpler construction.

5.2.2 Equivalent Model Representation of Eddy Current Conductivity Sensors

To describe the behavior of the Eddy Current sensor, a coil submerged in a conductive liquid is modeled (cf. figure 36). An equivalent transfer function that describes the behavior of the inductance taking into account the damping due to the eddy currents I_w in the water is derived based on the consideration of the field quantities and Maxwell's equations. Line and surface integrals are simplified by one-dimensional products, which are used as tuning parameters later.

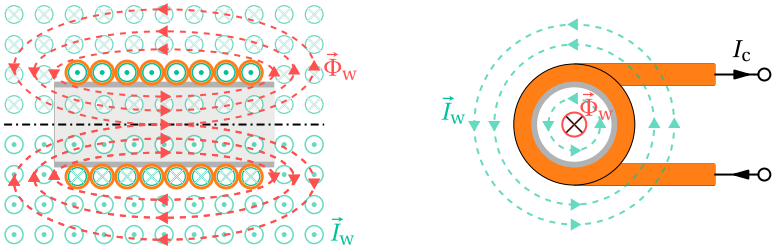

Figure 36: *Schematic diagram of an eddy current sensor. Green arrows display the current density J, red the magnetic flux* Φ*. The sensors are surrounded by a conductive fluid.*

The total magnetic flux Φ_w through the water is given by the magnetic flux of the coil inductance Φ_c and the magnetic flux due to the eddy currents Φ_E:

$$\Phi_w = \Phi_c + \Phi_E \tag{1}$$

$$\Phi_c = L_c \cdot I_c. \tag{2}$$

The magnetic flux Φ_E is induced due to the electromagnetic interaction described by Maxwell's equations 3 and 4:

$$\oint \vec{E}_w d\ell = -\frac{\delta \vec{\Phi}_w}{\delta t} \tag{3}$$

$$\oint \vec{B}_w d\ell = \mu_w I_w + \mu_w \epsilon_w \int_A \frac{\delta \vec{E}_w}{\delta t} dA \tag{4}$$

where μ_w and ϵ_w describe the properties of the surrounding liquid:

$$\mu_w = \mu_0 \cdot \mu_{r,w} \tag{5}$$

$$\epsilon_w = \epsilon_0 \cdot \epsilon_{r,w} \tag{6}$$

Measurement of water conductivity σ_w can be achieved by facilitating the damping effect on the coil flux. As pointed out by Ding et al. [172], the influence of the permeability μ_r of the liquid has a negligible effect for NaCl concentrations occurring mainly in the ocean, but must be considered for other salt solutions such as $CuSO_4$ [174].
Integrating Faraday's law of induction of eq. (5) along the unknown line ℓ_E gives:

$$\vec{E}_w \cdot \ell_E = -\frac{\delta \vec{\Phi}_w}{\delta t} \tag{7}$$

which can be applied to Ampère's circuital (eq. (6)):

$$\begin{aligned} I_w = \frac{V_w}{R_w} &= \vec{E}_w \cdot \ell_E \frac{\sigma_w}{\kappa_{cell}} \\ &= -\frac{\sigma_w}{\kappa_{cell}} \frac{\delta \vec{\Phi}_w}{\delta t} \end{aligned} \tag{8}$$

$$\begin{aligned} \mu_w \epsilon_w \int_A \frac{\delta \vec{E}_w}{\delta t} dA &= \mu_w \epsilon_w A_E \frac{\delta \vec{E}_w}{\delta t} \\ &= -\mu_w \epsilon_w \frac{A_E}{\ell_E} \frac{\delta^2 \vec{\Phi}_w}{\delta t^2} \end{aligned} \tag{9}$$

$$\vec{B}_w \ell_B = -\mu_w \left(\frac{\sigma_w}{\kappa_{cell}} \frac{\delta \vec{\Phi}_w}{\delta t} + \epsilon_w \frac{A_E}{\ell_E} \frac{\delta^2 \vec{\Phi}_w}{\delta t^2} \right) \tag{10}$$

where σ_w describes the water conductivity, κ_{cell} the unknown cell constant of the water resistance and A_E an unknowns surface area. By multiplying eq. (10) with $\frac{A_B}{\ell_B}$, where A_B stands for the magnetic flux area, all unknown geometric entities can be simplified to A_1 and A_2:

$$\vec{\Phi}_w = -\mu_w \left(\sigma_w A_1 \frac{\delta \vec{\Phi}_w}{\delta t} + \epsilon_w A_2 \frac{\delta^2 \vec{\Phi}_w}{\delta t^2} \right) \tag{11}$$

Applying that to eq. (1) allows deriving a differential equation to describe the total magnetic flux in the water:

$$\Phi_w = L_c \cdot I_c - \mu_w \left(\sigma_w A_1 \frac{\delta \vec{\Phi}_w}{\delta t} + \epsilon_w A_2 \frac{\delta^2 \vec{\Phi}_w}{\delta t^2} \right) \tag{12}$$

After Laplace transformation, $\mathscr{L}\{f(t)\} = F(s)$, the transfer function of an inductance submerged in conductive fluid is given by:

$$Z_\mathrm{t} = \frac{L_\mathrm{c} \cdot s}{1 + \mu_\mathrm{w}\sigma_\mathrm{w}A_1 s + \mu_\mathrm{w}\epsilon_\mathrm{w}A_2 s^2} \tag{13}$$

The derived transfer function can be represented by an equivalent RLC circuit as shown in figure 37a.

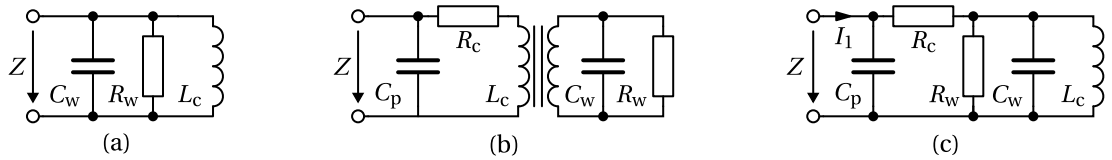

Figure 37: *a: Equivalent RLC circuit of the eddy current transfer function; b: Equivalent drawing of a single coil, inducing eddy currents in the water; c: Simplified equivalent drawing of a single coil considering eddy effects.*

Comparing the RLC transfer function

$$Z = \frac{L_\mathrm{c} \cdot s}{1 + \frac{L_\mathrm{c}}{R_\mathrm{w}} s + L_\mathrm{c}C_\mathrm{w}s^2} \tag{14}$$

to eq. (13), allows to model the water resistance with R_w and the displacement current with C_w accordingly:

$$R_\mathrm{w} = \frac{L_\mathrm{c}}{\mu_\mathrm{w}\sigma_\mathrm{w}A_1} \qquad \left[\Omega\right] \tag{15}$$

$$C_\mathrm{w} = \frac{\mu_\mathrm{w}\epsilon_\mathrm{w}A_2}{L_\mathrm{c}} \qquad \left[\frac{\mathrm{s}}{\Omega}\right] \tag{16}$$

The model of the coil can be completed by also considering the copper resistance R_c and the parasitic effects C_p (cf. figure 37c). Alternatively, the conductive liquid can also be viewed as a short-circuited coil turn in an equivalent transformation model with water resistance R_w and parasitic effects C_w (cf. figure 37b).
An eddy current sensor concept based on two copper coils serving as excitation and sensing coil is considered in the following. The sensor model can be represented by a transformer model based on the derived submerged coil representation (cf. figure 38). The sensor characteristic with current excitation I_1 and voltage output V_2 is given by

$$\frac{V_2}{I_1} = \frac{L \cdot s}{C_\mathrm{p} \cdot C_\mathrm{w} \cdot L \cdot R_\mathrm{cu} \cdot s^3 + \left(C_\mathrm{p} \cdot \frac{L}{R_\mathrm{w}} \cdot R_\mathrm{cu} + C_\mathrm{p} \cdot L + C_\mathrm{w} \cdot L\right) \cdot s^2 + \left(\frac{L}{R_\mathrm{w}} + C_\mathrm{p} \cdot R_\mathrm{cu}\right) \cdot s + 1} \tag{17}$$

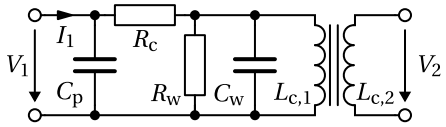

Figure 38: *Equivalent drawing of a two-coil transformer, considering the influence of eddy currents.*

Assuming that the parasitic effects of the coil are much larger than the displacement current in the water ($C_p >> C_w$) allows to simplify eq. (17) to

$$\frac{V_2}{I_1} = \frac{L \cdot s}{\left(C_p \cdot \frac{L}{R_w} \cdot R_{cu} + C_p \cdot L\right) \cdot s^2 + \left(\frac{L}{R_w} + C_p \cdot R_{cu}\right) \cdot s + 1} \tag{18}$$

Given the proportionality $R_w = \frac{\kappa_{cell}}{\sigma_w}$, the sensor output decreases with increasing water conductivity, resulting in inversely proportional sensor output. The changes in permeability for seawater are negligible, only temperature influence needs to be considered. In the following, all temperature depended parameters are modeled by their mean value at the reference temperature $T_{20°} = 20\,°C$ and a temperature coefficient α:

$$L = L_{20°} \cdot \left(1 - \alpha_L \cdot \left(T_{20°} - T\right)\right) \tag{19}$$

$$R_c = R_{c,20°} \cdot \left(1 + \alpha_R \cdot \left(T_{20°} - T\right)\right) \tag{20}$$

$$C_p = C_{p,20°} \cdot \left(1 + \alpha_C \cdot \left(T_{20°} - T\right)\right) \tag{21}$$

5.2.3 Evaluation of Eddy Current Sensor Prototype

For model validation, the derived transfer function (eq. (18)) for the two coil eddy current sensor is compared with experimental results [175]. To reduce the magnetic resistance and increase the magnetic flux in the water, a ferrite rod is used to hold both coils. This reduces the leakage flux and increases the coupling between the two coils. According to eq. (12), the damping of the magnetic flux due to eddy currents increases with the excitation frequency, suggesting the use of a high measurement frequency. The upper limit for the frequency is given by the resonance point of the coil, which is shifted by an additional capacitor to keep the measurement frequency below 1 MHz. A prototype based on this design is implemented and provided with a waterproof housing by casting it in polyurethan (PU)-resin (cf. figure 39).
The prototype is tested on a temperature- and conductivity-controlled test bench. Starting at 5 $\frac{S}{m}$, the conductivity is slowly decreased to 1.5 $\frac{S}{m}$ and then increased back to 5 $\frac{S}{m}$ in a hysteresis-like progression (cf. figure 40).
A temperature-compensated inductive conductivity sensor (Endress & Hauser Indumax

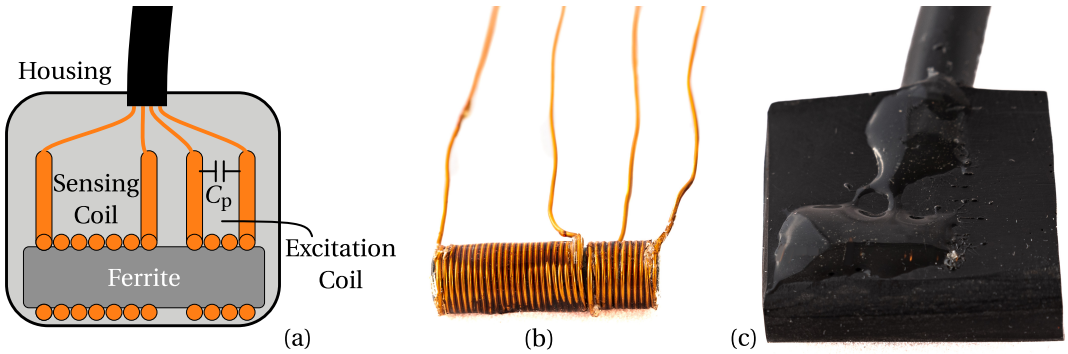

Figure 39: *Implementation of the eddy current sensor. a: concept drawing; b: coils on ferrite rod; c: encapsulated coils in PU-resin.*

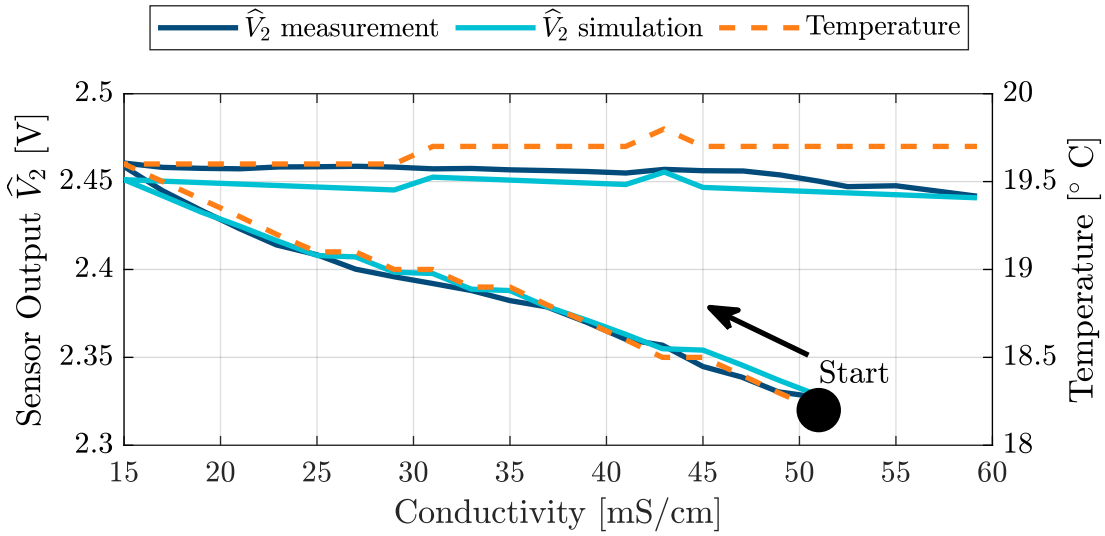

Figure 40: *Comparison of simulated and measured peak amplitude of output voltage $\widehat{V}_2$ for varying conductivity and temperature along the conducted measurement cycle.*

CLS50D [62]) is used as a reference for temperature and conductivity measurement. The water is continuously mixed to ensure high homogeneity. The conductivity is reduced by adding purified water to the sample. Due to the slightly higher temperature of the mixed water, the temperature of the sample increased from 18.2 °C at the beginning to 19.6 °C at the lowest conductivity level. The increase in conductivity was facilitated by mixing a highly concentrated NaCl solution with the water sample. During this phase, the temperature remained nearly constant between 19.6 °C and 19.7 °C. Twenty measurements were taken in each cycle, for a total of 41 measurement points. One measurement consisted of a frequency sweep between 750 kHz and 1 MHz, with a constant excitation current of 10 mA. Using a nonlinear regression parameter fitting, the parameters of $L_{20°}$, $R_{c,20°}$, $C_{p,20°}$, α_L, α_R, α_C, and A_1 of the model from eq. (18) are determined.
Figure 41 shows the frequency response of the secondary coil voltage output for measurement and simulation.

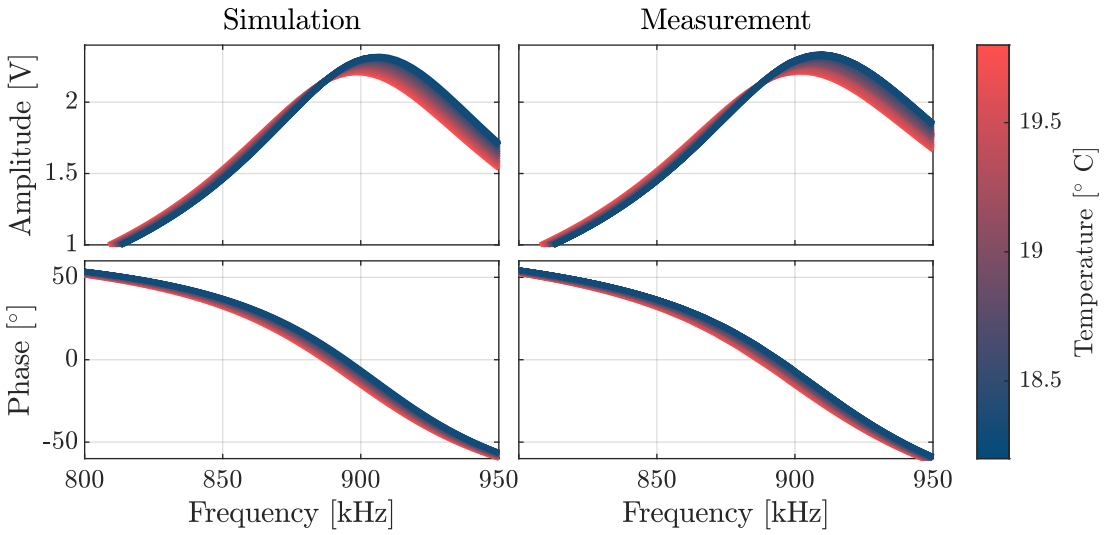

Figure 41: *Frequency response comparison of the secondary coil voltage output for measurement and simulation, with plot color indicating the water temperature.*

The results of the experiment primarily show a strong and dominant temperature dependence of the sensor output voltage (cf. figure 41). This is related to the changing copper resistance, core permeability and the amplification by the resonance point. In the second phase of the experiment, the water temperature is more stable while the conductivity increased. The correlation of the voltage with the conductivity can be seen, as the voltage decreases while the conductivity of the water increases.

The test confirms the model behavior and shows a decreasing output of the coupling with increasing water conductivity. The derived equivalent model can therefore be used to represent the eddy current effect for this type of sensor. The resulting influence of conductivity is, however, much less than the temperature sensitivity.
Analyzing the temperature influence on the equivalent model further shows, that for lower frequencies the temperature has a proportional behavior to the sensor output, which changes to an inverse-proportional behavior close to the resonance point. This allows to find frequencies with low temperature influence and shows that a frequency spectrum analysis provides much more information than a unique consideration of the peak output voltage. Observing the sensor output at 890 kHz, gives a nearly linear sensor output behavior, that shows only little temperature influence for this temperature range (cf. figure 42).
A simulation of the full required conductivity and temperature range for this eddy current sensor prototype shows the extent of the temperature influence compared to the conductivity sensitivity (cf. figure 43).

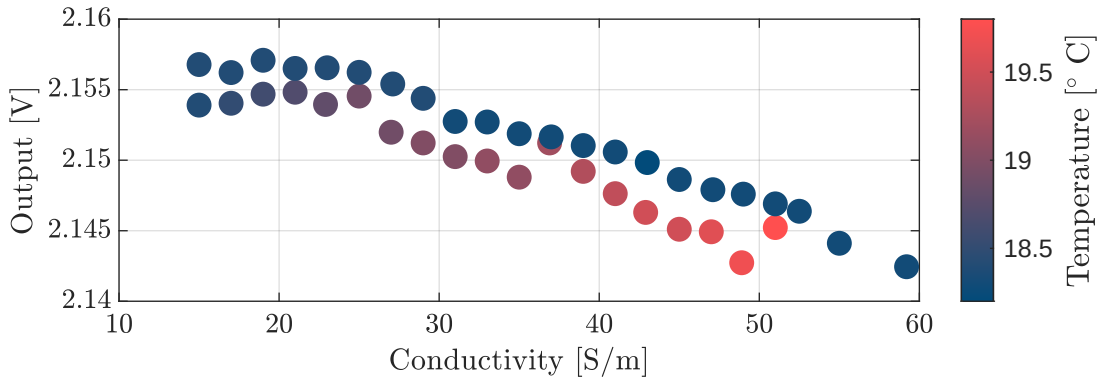

Figure 42: *Plot of sensor output voltage vs. water conductivity at* 890 kHz*, exhibiting a nearly linear behavior, regardless of temperature.*

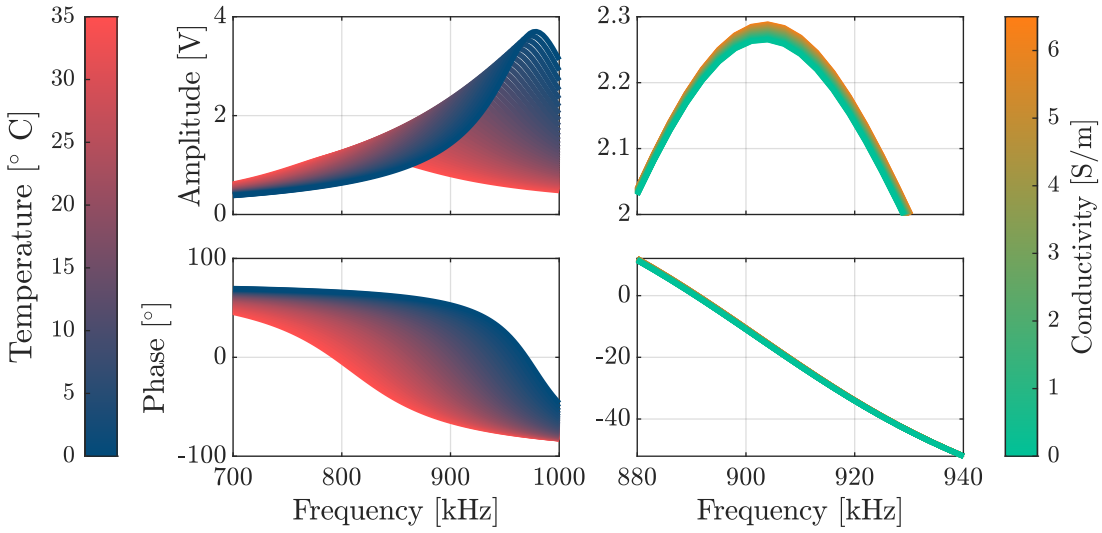

Figure 43: *Simulation of the full conductivity and temperature range for the eddy current sensor prototype, demonstrating the impact of temperature versus conductivity sensitivity across the frequency spectrum.*

5.2.4 The Potential of Eddy Current Sensors

The experiment and model analysis demonstrates the potential of eddy current sensors for inductive conductivity measurement. It was found that the temperature influence on the sensor output is highly frequency-dependent. Spectral analysis of the sensor output combined with advanced evaluation methods like machine learning algorithms could help to separate temperature effects from conductivity influence. However, the current sensor setup exhibits insufficient dependence on conductivity and is highly sensitive to temperature changes. To address this, further research on alternative coil arrangements such as co-planar coils on a PCB (as seen in [171–173]) could result in increased sensitivity. Despite the general confidence that eddy current sensors have

the potential to present a cost-effective alternative, no concept has been found here that offers a clear advantage over the TICS. Therefore, the following section considers the proven concept of TICS to realize an embedded sensor for low-cost conductivity measurements.

5.3 Designing an Embedded Transformer Type Inductive Conductivity Sensor

This section derives the functions of three crucial components of the embedded CT-sensor: the primary conductivity sensor, the primary electronics of the conductivity sensor, and the integrated secondary electronics, acting as processing unit. The temperature sensor component will be addressed in the next section, to complete the fully-integrated CT-sensor.
The conductivity measurement approach is based on the traditional TICS. The primary sensor design starts with an equivalent model description of a TICS.
Once the coil parameters are determined and the measurement principle is defined, the measurement circuit is designed, and a single PCB implementation integrating the processing unit is created. The processing unit can later serve as the primary processing unit of the embedded CT-sensor, including the evaluation of the temperature sensor. The section concludes with experiments to verify the accuracy of the developed conductivity sensor.

5.3.1 Deriving the TICS Model Description

The primary sensor concept can be represented by the equivalent circuit shown in figure 44, which is based on the sensor theory presented by Striggow and Dankert [42] in 1985.

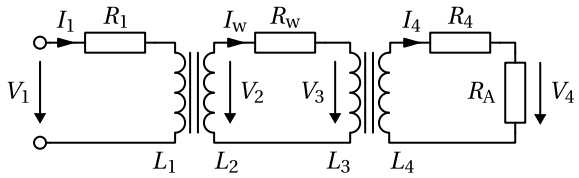

Figure 44: *Equivalent circuit model of the transformer-type conductivity sensor based on the Striggow and Dankert model [42].*

The model description is based on a two-stage transformer, with the inductances L_2, and L_3 representing the water loop. The mutual inductance L_{12}, therefore describes the

coupling of the first coil into the water. Assuming stray fluxes and a non ideal coupling gives [50]

$$L_{12} = k_{12}\sqrt{L_1 L_2}, \tag{22}$$

where k_{12} is the coupling factor. The excitation current I_1 through the first coil, induces the voltage V_2 in the water. Due to the water conductivity, the induced voltage causes an ionic current I_w, taken into account by the resistance R_w:

$$R_\mathrm{w} = \frac{\kappa_\mathrm{cell}}{\sigma_\mathrm{w}}, \tag{23}$$

where the cell constant κ_cell stands for the unknown geometric properties of the current through the water. Applying Kirchhoff's law to the transformer model of figure 44, allows to derive the relationship between the output current I_4 and the input voltage V_1, which is described in more detail by Hui et al. [50]:

$$I_4 = -\frac{L_{12}L_{34}w^2}{\left(\left(R_1 + jwL_1\right)\cdot\left(R_w + jwL_2 + jwL_3 + \frac{w^2L_{34}^2}{R_4+R_\mathrm{A}+jwL_4}\right) + w^2L_{12}^2\right)\cdot\left(R_4 + R_\mathrm{A} + jwL_4\right)}V_1 \tag{24}$$

$$V_4 = I_4 \cdot R_\mathrm{A} \tag{25}$$

The terminating resistor R_A is used to select between an open circuit measurement of V_4 ($R_\mathrm{A} \to \infty$) or a short circuit measurement of I_4 ($R_\mathrm{A} \to 0$). To simplify eq. (24), an ideal coupling with $k = k_{12} = k_{34} = 1$ can be assumed and the copper resistances R_1, R_4 can be neglected [42]. The direct correlation of the conductivity σ_w to the output signal can then be determined by:

$$I_4 = \frac{V_1}{N_1 N_4 R_w} = \frac{V_1}{N_1 N_4 k_\mathrm{cell}}\sigma_\mathrm{w}, \tag{26}$$

where N_1 and N_4 stand for the coil turn numbers respectively.

5.3.2 TICS Primary Sensor: Parameter Influence Analyzation

For the design of the sensor, many parameters like coil winding, core permeability, and measurement principle need to be selected. In the following, the TICS model description is used to investigate the model behavior according to eq. (24).

Measurement Principle To select between the excitation and measurement principles, figure 45 compares the normalized sensor output next to the linearity error for the four scenarios of:

1. Voltage excitation → Current measurement ($V_{in} \rightarrow I_{out}$)
2. Voltage excitation → Voltage measurement ($V_{in} \rightarrow V_{out}$)
3. Current excitation → Current measurement ($I_{in} \rightarrow I_{out}$)
4. Current excitation → Voltage measurement ($I_{in} \rightarrow V_{out}$)

While the voltage is measured in an open circuit configuration ($R_A \rightarrow \infty$), the current can be measured by e.g. a virtual ground circuit ($R_A \rightarrow 0$). To illustrate the influence of the different excitations and measurement setups, a very small value for $\kappa_{cell} = 1\,\frac{1}{m}$ is used. This leads to a water resistance of 0.1 Ω at 7.5 $\frac{S}{m}$ and improves the coupling between coil 1 and 4.

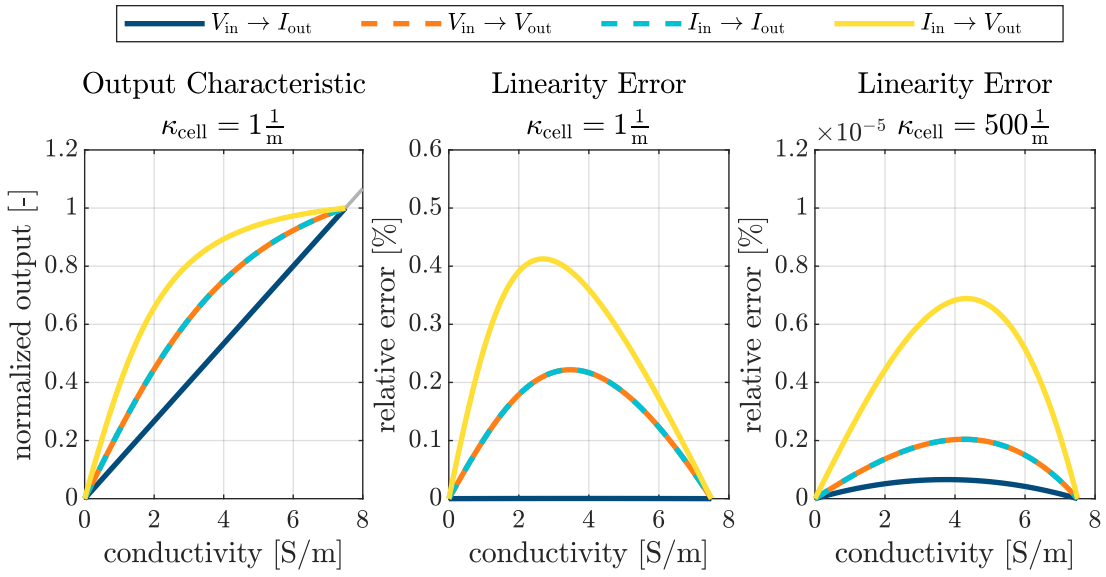

Figure 45: *Comparison of the normalized sensor output and the linearity error for voltage or current measurement and excitation.*

Configuration 1 (voltage excitation and current measurement) shows the best linearity. In fact, after neglecting copper resistance values and setting the coupling factor $k = 1$, this configuration is perfectly linear as described by eq. (26). The linearity error of the other measurement configurations reduces greatly when increasing the cell constant $\kappa_{cell} = 500\,\frac{1}{m}$ but still can not achieve better performances than the non-ideal circuits with copper resistance and $k < 1$ (cf. figure 45c). The following implementation is therefore designed with voltage excitation and current measurement.

Influencing Sensor Parameters To investigate the main influences on the sensor characteristic for the selected measurement principle, figure 46 shows the effect on the

sensor output current (I_4), for changing copper resistance (R_1, R_4), coupling factor (k) and cell constant (κ_{cell}).

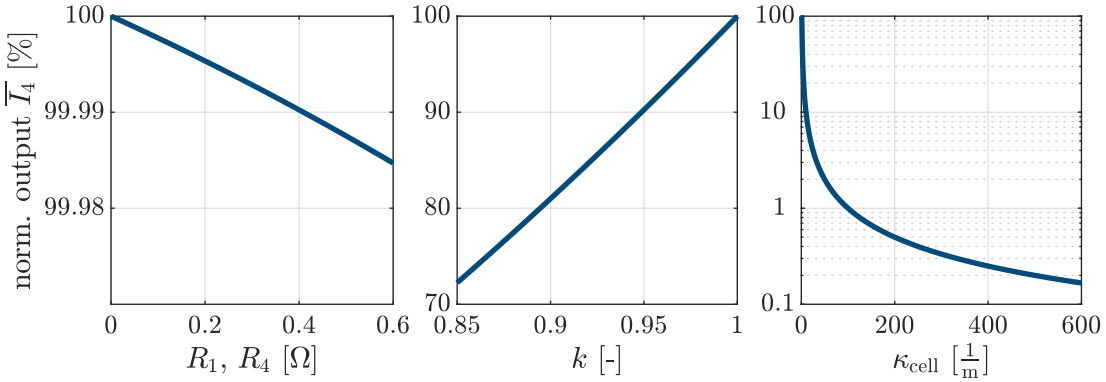

Figure 46: *Impact of copper resistances (R_1, R_4), coupling factor (k), and cell constant (κ_{cell}) on the sensor output current (I_4), normalized to its maximum value.*

The output is normalized to its maximum output value for each parameter consideration. The influence of the copper resistance is linear and comparably small. The resistance is mainly influenced by the number of turns, wire diameter, and core size. Due to the very low number of turns, the influence does not have to be taken into account in the further design. The coupling factor (k) describes the efficiency of the coupling and also shows a linear effect on the sensor output. It can be influenced by the design of the coil inductance, permeability, and geometric properties and should be selected close to 1 to avoid linearity errors.
The largest influence is given by the cell constant (κ_{cell}), which directly influences the water resistance ($R_{\text{w}} = \frac{\kappa_{\text{cell}}}{\sigma_{\text{w}}}$). The output current ($I_4$) shows a logarithmic decrease as the cell constant increases. The cell constant is determined by the geometrical arrangement of the coils and was determined to be in between 400 and 500 $\frac{1}{\text{m}}$ for implementations from earlier publications [176, 177]. It has to be noted, that the parameter shown in figure 46 also affect each other. For example, the influence of the copper resistance is higher, if the coupling factor (k) or the cell constant (κ_{cell}) is reduced.

Inductance Parameterization The main influencing parameters of the coil inductance are the core permeability, coil turns, and geometric properties. For $k = 1$, the permeability has no influence on the sensor output current I_4, only with $k < 1$ the permeability affects the output. Figure 47a shows the influence of the permeability on the coupling efficiency I_4 / I_1 for a coupling factor of $k = 0.99$. While I_4 remains almost constant for all permeability values, the input current is proportional to $I_1 \sim \frac{1}{\mu_{\text{r}}}$. Much more important than the direct influence of the permeability on the inductance is the influence of the permeability on the coupling factor (k). Since low permeability values increase flux leakage, the coupling factor decreases with it.

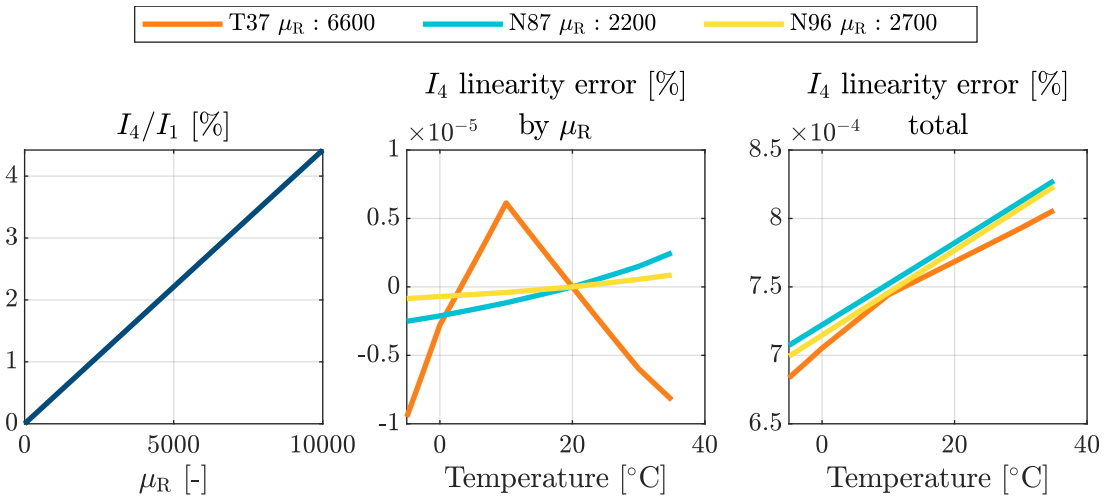

Figure 47: *Effect of various permeability values (N37, N87, N96 by TDK [178]) on the coupling efficiency (I_4/I_1) and linearity error of I_4. The right plot depicts the overall linearity error, including factors such as copper resistances, while the middle plot focuses solely on the permeability influence.*

To investigate the influence of permeability changes due to temperature deviations, the maximum linearity error from a reference reading at 20 °C is compared in figure 47b, neglecting any copper resistance. Figure 47c evaluates the linearity error considering both, copper resistance and permeability changes over temperature. Three different ferrite cores of the company TDK [178] with initial permeability values of 6600, 2700, and 2200 and different temperature characteristics are compared. The changing permeability leads to a smaller linearity error, than the persistent error due to copper resistance. The maximum linearity error over the full temperature range of −5 to 35 °C for $k = 0.99$ and $\kappa_{\text{cell}} = 450\,\frac{1}{\text{m}}$ is 8×10^{-4}%. Although due to the error accumulation of the entire circuit, the actual temperature error in an implementation will be larger, this demonstrates the great temperature stability of the TICS.
Considering the low influence, the main goal of choosing the permeability is to achieve a high coupling factor of k close to 1 [50]. The toroidal ferrite N87 ($\mu_r = 2200$) is selected due to cost-effectiveness and high availability. The core dimensions of 25.3 mm × 14.8 mm show a good trade-off of required power and core size [179]. In order to reduce the mutual coupling of L_{14} due to unwanted stray fluxes even further, a shield between the coils can be implemented.
The winding number strongly influences the Inductivity ($L = \frac{N^2}{\mathscr{R}}$ with $\mathscr{R}$ being the magnetic resistance) and is selected based on the required power consumption and resulting output current. An increased output current improves the signal-noise ratio but requires more energy and more complex circuitry. Considering the simplified model description of eq. (26) shows that the amplitude of the sensor output is reciprocally influenced by the winding numbers. Figure 48 shows the sensor output current (I_4) and the coupling

efficiency (I_4/I_1) for different winding configurations. Increasing the primary winding (N_1), increases the Inductivity (L_1), which lowers the power consumption of the sensor for a constant voltage excitation.

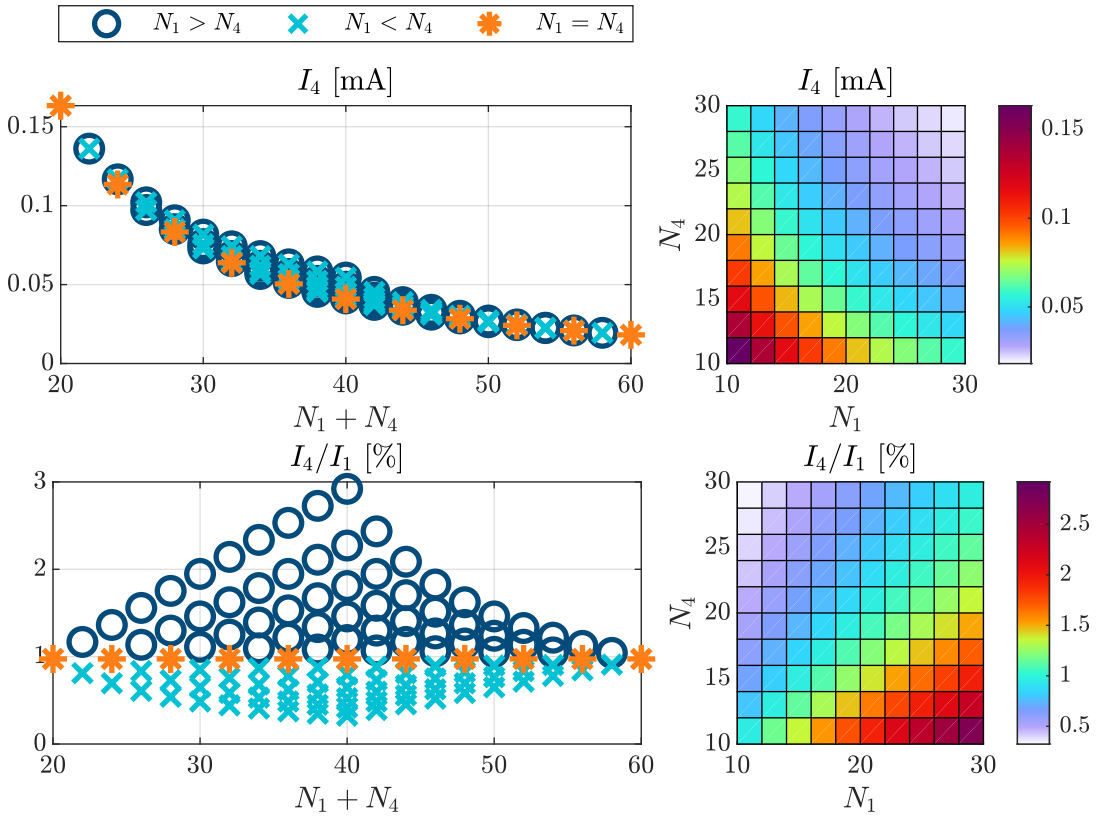

Figure 48: *Impact of winding number on the sensor output current (I_4) and coupling efficiency (I_4/I_1). The winding number (N_1 or N_4) ranges from 10 to 30. The left plots depict the total winding number ($N_1 + N_4$), while the right plots display each winding configuration in a 2D surface plot.*

The sensor output (I_4) decreases with increasing winding number and output inductance (L_4) (cf. figure 49a). With equal winding distribution ($N_1 = N_4$), the efficiency stays constant regardless of the number of windings. The efficiency can be improved by selecting a larger primary winding number ($N_1 > N_4$). The highest output current is obtained with the lowest winding number and equal distribution ($N_1 = N_4$). The lowest possible number of coil turns is determined by the influence of the winding number on the coupling factor. It has to be considered, that figure 48 assumes a constant coupling factor ($k = 1$) for all configurations, but the coupling factor actually decreases as the number of turns decreases, due to the increase in flux leakage. Reducing the number of windings requires finding a balance to avoid reduction of the coupling factor. As shown by preliminary experiments [176, 177] and other sources [50] coils with winding numbers of $N_1 = N_4 = 10$ still show good coupling factors close to $k = 1$.

Sensor Parameter Selection The measurement frequency is chosen to strike a balance between minimizing the sensor's power consumption and achieving adequate sensor gain. As shown in figure 49, the frequency affects the current output (I_4) and the input-output ratio (I_4/I_1) in the range of 0 to 100 kHz. The output current I_4 for a given inductance is nearly frequency-independent for cell constants of 400 to 500 $\frac{1}{\mathrm{m}}$ as the ohmic water resistance (R_w) dominates the total impedance. The influence of the frequency therefore remains small as long as the resistance of the water ($R_\mathrm{w} = \frac{\kappa_\mathrm{cell}}{\sigma_\mathrm{w}}$) is significantly greater than the inductance (L_4).

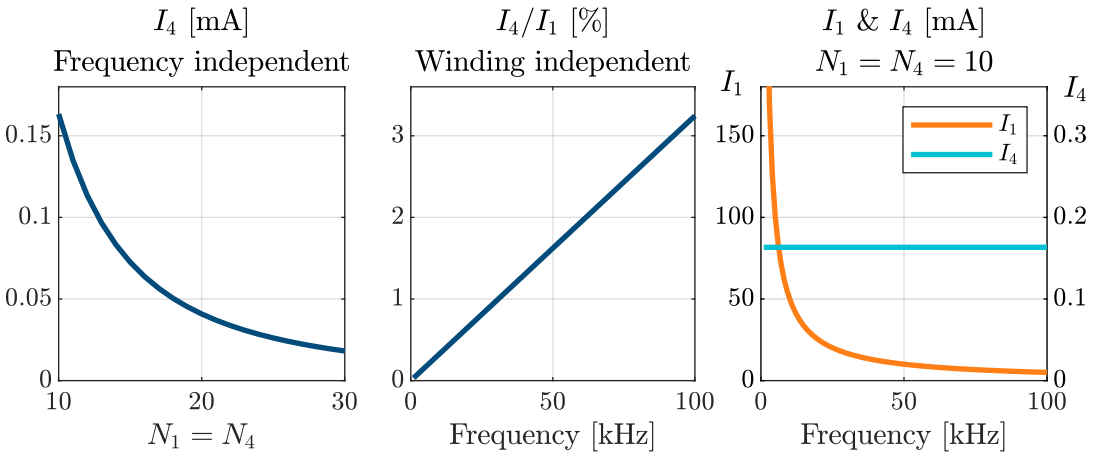

Figure 49: *Influence of winding number ($N_1 = N_4$) and signal frequency on the output current (I_4) and coupling efficiency (I_4/I_1). The output current shows minimal frequency dependency, while the coupling efficiency is constant regardless of the winding number. The right plot presents a comparison of input (I_1) and output (I_4) current for a winding number of $N_1 = N_4 = 10$ at signal frequencies up to* 100 kHz. *In all plots: $\kappa_\mathrm{cell} = 450\,\frac{1}{\mathrm{m}}$ and $k = 0.99$.*

The coupling efficiency (I_4/I_1) shows a frequency dependency because the load for the excitation voltage (V_1) is inductive, causing I_1 to decrease at higher frequencies. Higher frequencies can therefore improve the power efficiency, but this is limited by the increased power consumption of the excitation circuit and the need for a higher sampling rate. Additionally, the maximum gain of the trans-impedance amplifier may be limited by the Gain-Bandwidth product, as discussed in section 5.3.6. The frequency should be selected to minimize the power consumption of the primary inductance while keeping the peripheral demands low. For the implementation, the primary coil is designed to have a maximum drive current of 20 mA, requiring a minimum frequency of 25 kHz. Thus, the excitation frequency is set to 30 kHz. The excitation voltage (V_1), which is proportional to the output current (I_4), can be adjusted to adapt the power consumption and signal-noise ratio in the prototype implementation. The selected sensor parameters are summarized in table 15.

Parameter name	Value	Parameter name	Value
Core material	N87	Radius of copper wire	0.3 mm
Core permeability	2200 ±25%	Core inner diameter	13.5 mm
Winding primary coil	10	Core outer diameter	26.6 mm
Winding secondary coil	10	Core height	11 mm

Table 15: *Selected parameter for the coils and coil-cores (cf. figure 53).*

5.3.3 TICS Primary Electronics: An Embedded Sensor Design

In the following, the design of the electric measurement circuit is presented for the parameterized primary sensor.

Signal Generation The sine wave for the AC-excitation signal can be generated using an analog oscillator circuit or various digital methods. An easy way of a digital sine wave generation is to use the same MCU, that is used for signal evaluation, to generate a pulse width modulation (PWM) and smooth the signal by a low-pass filter. Another approach is to use concepts like arbitrary waveform generator (AWG) or direct digital synthesis (DDS) that are often embedded in the MCU's digital-analog-converter (DAC). An AWG allows to directly generate analog sine waves by the MCU, which approximates the signal over time from provided discrete data points.
For the conductivity sensor in consideration, the embedded AWG of the MCU is selected as the generation method. To supply the necessary excitation current, a differentially coupled inverting amplifier is used (cf. figure 50a), as the MCU's DAC is not capable of providing higher currents. The DAC is operating in differential mode to suppress digital

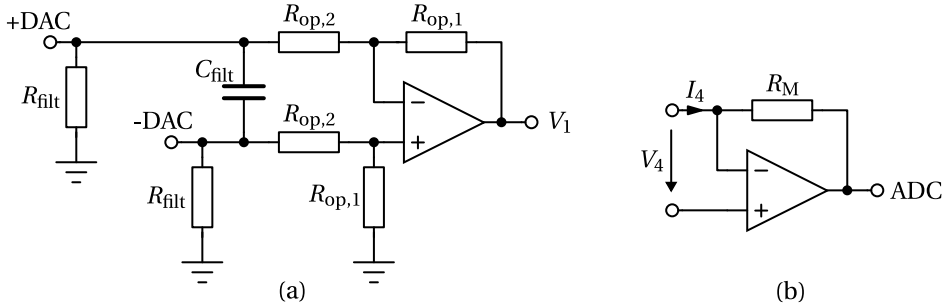

Figure 50: *a) Differential DC coupled output using a dual supply operational amplifier (op-amp). [179]; b) Trans-impedance amplifier for virtual ground configuration.*

noise on the outputs.

Signal Acquisition The short circuit measurement of the sensor output current is implemented by a virtual short circuit. A trans-impedance amplifier as depicted in figure 50b is used to convert the short circuit current I_4 into a voltage signal, readable by the MCU's analog-digital-converter (ADC).
The short-circuit current flows through resistor R_M, defining the amplification gain. The resistor value needs to be selected to convert the maximum output current to be within the range of the ADC's reference voltage V_Ref.

$$R_\mathrm{M} = \frac{V_\mathrm{Ref}}{I_{4,\mathrm{max}}}. \tag{27}$$

The maximum output current can be simulated with the simulation model. Assuming a cell constant of $\kappa_\mathrm{cell} = 500\,\frac{1}{\mathrm{m}}$, gives a maximum short circuit current of 160 µA. With the ADC reference voltage of 2.5 V, a measurement resistance value of around 15 kΩ is required.
Since the exact cell constant κ_cell and the coupling factors k are unknown prior to the implementation, a later adjustment of the measurement resistance R_M might be necessary to scale the actual output current range to the ADC input ratings.

The required ADC properties can be derived from the sensors resolution requirement of $5\,\frac{\mathrm{mS}}{\mathrm{m}}$ [179]:

$$log_2\left(\frac{7.5\,\frac{\mathrm{S}}{\mathrm{m}}}{5\,\frac{\mathrm{mS}}{\mathrm{m}}}\right) \equiv 10.5\text{ bit} \approx 12\text{ bit} \tag{28}$$

$$\frac{7\,\frac{\mathrm{S}}{\mathrm{m}}}{2^{12\text{ bit}}} \equiv 1.7\,\frac{\mathrm{mS}}{\mathrm{m}}. \tag{29}$$

Equation (29) shows, that at least a 12 bit ADC is needed to enable a measurement resolution of $1.7\,\frac{\mathrm{mS}}{\mathrm{m}}$. The maximum aperture jitter can be calculated by [179]:

$$\Delta t_A = \frac{V_\mathrm{LSB}}{\frac{1}{2}V_\mathrm{max}\cdot\omega_\mathrm{max}} = \frac{2.5\ V\cdot\frac{1}{2^{12}}}{\frac{1}{2}\cdot 2.5\ V\cdot 30\,\mathrm{kHz}\cdot 2\pi} = 7.7\,\mathrm{ns}. \tag{30}$$

For a sinusoidal voltage with the maximum amplitude of $V_\mathrm{max} = 2.5\,\mathrm{V}$ and frequency of 30 kHz the maximum jitter for a 12-bit ADC is 2.6 ns.

Data Processing The data acquired from the ADC is transformed into a digital equivalent of the water conductivity. The measurement signal is evaluated in the frequency domain to distinguish noise from the actual measurement signal. The amplitude of the

output signal corresponds linear to the conductivity as shown by the sensor characteristic (cf. figure 45). This transformation is achieved by using a fast fourier transformation (FFT) on the embedded MCU. By implementing the FFT, the discrete-time signal is transformed into the frequency domain, providing a clear representation of the measurement signal amplitude and allowing for accurate calculation of the water resistance.

5.3.4 Implementation of a TICS Prototype

The embedded sensor hardware was designed and implemented as part of a supervised master's thesis by Klar [179]. To reduce the size of the device and the manufacturing cost, the sensor is implemented on a single PCB. The two toroidal coils are placed on the top and bottom of the PCB. To shield mutual coupling between the coils, the PCB contains a large copper ring on the routing plane.
The electronic control unit of the sensor is an Atmel MCU SAME51, which is used for signal generation, acquisition, data processing and as serial output for the final measurement result (cf. figure 51). It runs at an internal clock frequency of 48 MHz

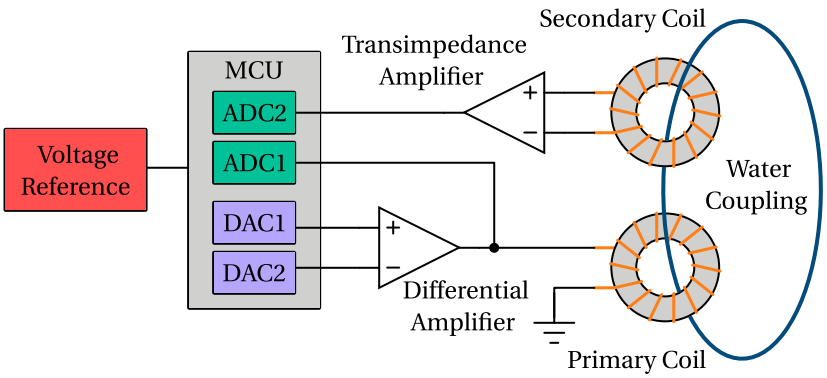

Figure 51: *Simplified block diagram of embedded sensor circuit.*

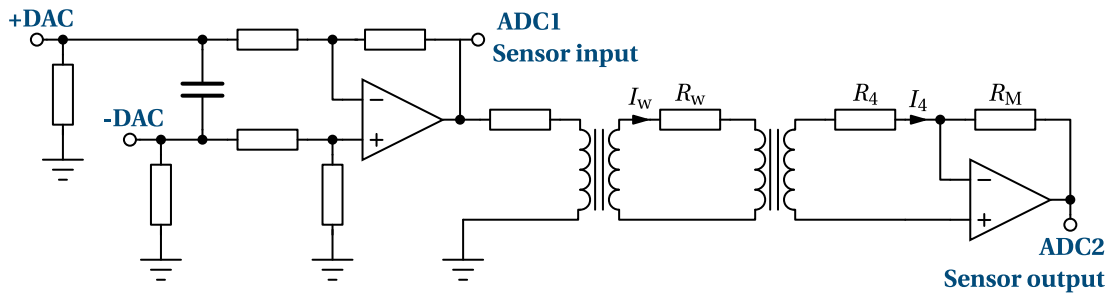

Figure 52: *Concept sketch of the measuring circuit with amplification stages from the master's thesis by Klar [179]*

and the peripherals are configured for synchronous operation. The running time of the

sequences allows real-time measurements with a sampling frequency of up to 50 kHz. The circuit can be powered from an external 5 V source scaled by a DC/DC converter to a 3.3 V supply voltage. Internal ADC (12 bits; 1 MSPS; 0.42 ns jitter) and DAC are used for signal excitation and sampling. Both are configured in differential mode with 2.5 V reference voltage. To reduce the cost of the sensor, a low-cost *MIC920* [180] amplifier from Microchip was chosen for both op-amp.
The assembled PCB is molded in PU-resin (cf. figures 53 and 54). The resulting size of the housing is 90 mm × 68 mm × 30 mm.

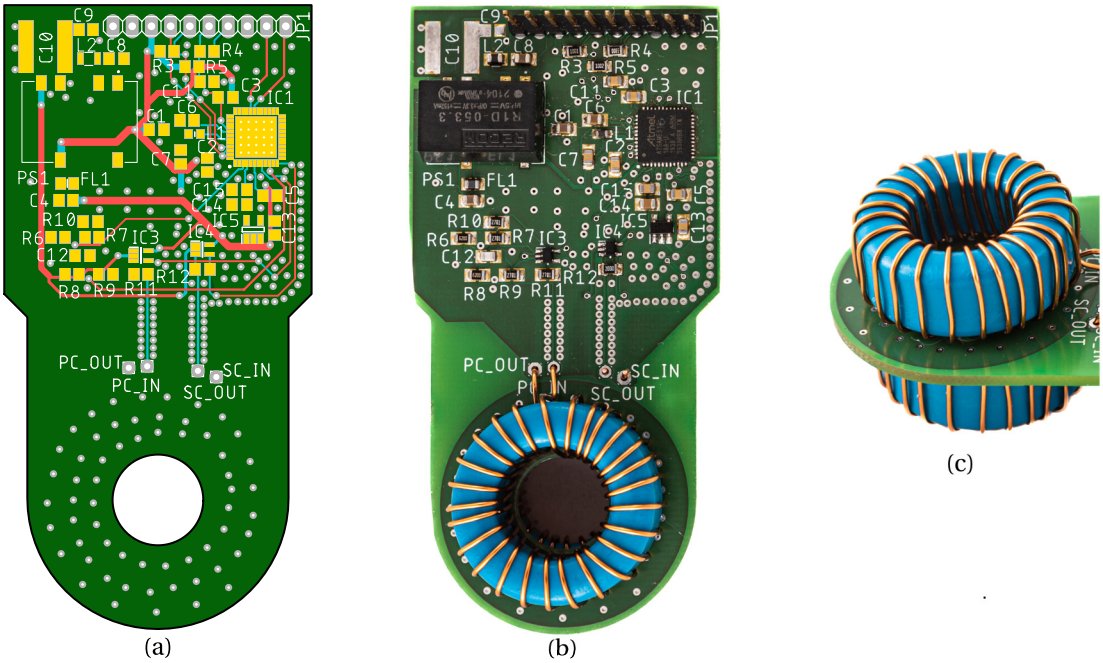

Figure 53: *Photos of the implemented sensor circuit prior to cast molding in resin. a: PCB-Layer design; b: Assembled Sensor: c: side-view of coil assembly with 26 turns.*

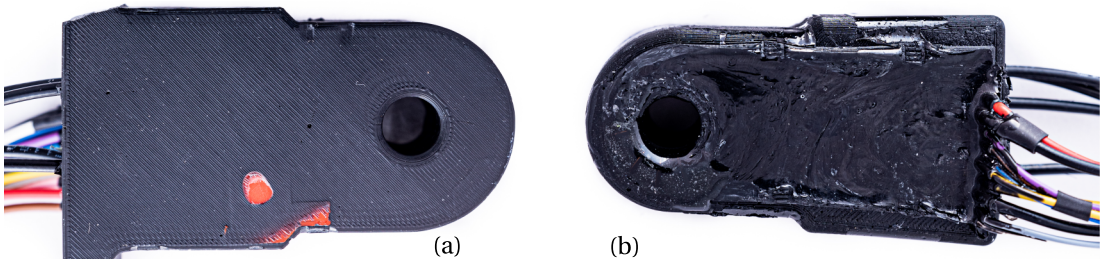

Figure 54: *Sensor prototypes after cast moulding in PU-resin. a: Sensor A; b: Sensor B.*

5.3.5 Prototype Validation and Measurement Uncertainty Analysis

The presented sensor concept is implemented and tested to validate the functionality and quantize the achievable measurement uncertainty. Two sensor prototypes are tested. Sensor A is the result of the master thesis of Klar [179], implementing a higher number of turns (26 turns) and a smaller measurement resistance ($R_M = 600\,\Omega$) due to deviating assumptions and a different design approach. Sensor B implements the parameter proposed by this thesis (cf. table 16).

	Coil Turns	Measurement Resistance R_M
Sensor A	26	600 Ω
Sensor B	10	15 kΩ

Table 16: *Parameter differences of the tested sensor implementations A and B.*

The deviating parameters between sensors A and B were mainly influenced by the unknown cell constant κ_{cell} at the time of the thesis. Since the results of the master thesis showed an unexpected behavior, the sensor output of sensor A is analyzed first. For the following experiments, a $30 \times 30 \times 60$ cm water tank was used. The conductivity of the water was successively increased by adding a NaCl saline solution to the water while the water level was kept constant. An Aqua Troll 100 conductivity cell was used as the reference sensor.

In the first experiment, the sensor excitation and output from the internal ADCs are measured to verify the functionality of the circuit. A strongly distorted signal was observed for two different water conductivities (0.95 and 4.91 $\frac{S}{m}$ at 15.9 °C) (cf. figure 55), indicating a design flaw in the hardware designed by the master thesis. The excitation signals of the circuit are of poor quality and do not represent the desired sine wave. The lower half-wave is clipped, steps occur at the zero crossings and the signal-to-noise ratio is low. At the higher frequency of 30 kHz, the upper half-wave is no longer properly represented. To further analyze the observed behavior, additional coaxial cables are run out from the DAC and ADC pins to allow external excitation and measurement without using the integrated differential amplifier. For optimal excitation, a function generator is connected directly to ADC1, i.e., the primary coil, and the output signal is tapped with an oscilloscope at ADC2, after the trans-impedance amplifier. The signal was excited with three different excitation frequencies of 5, 10, and 30 kHz.

Measurement results with external excitation show an improved signal (cf. figure 56), suggesting a design flaw in the master thesis amplifier circuit. Further measurements with gradually increasing conductivity (0.2 to 6.8 $\frac{S}{m}$), allow further analysis of the sensor behavior. However, even with external excitation, an offset of −0.85 V of the output

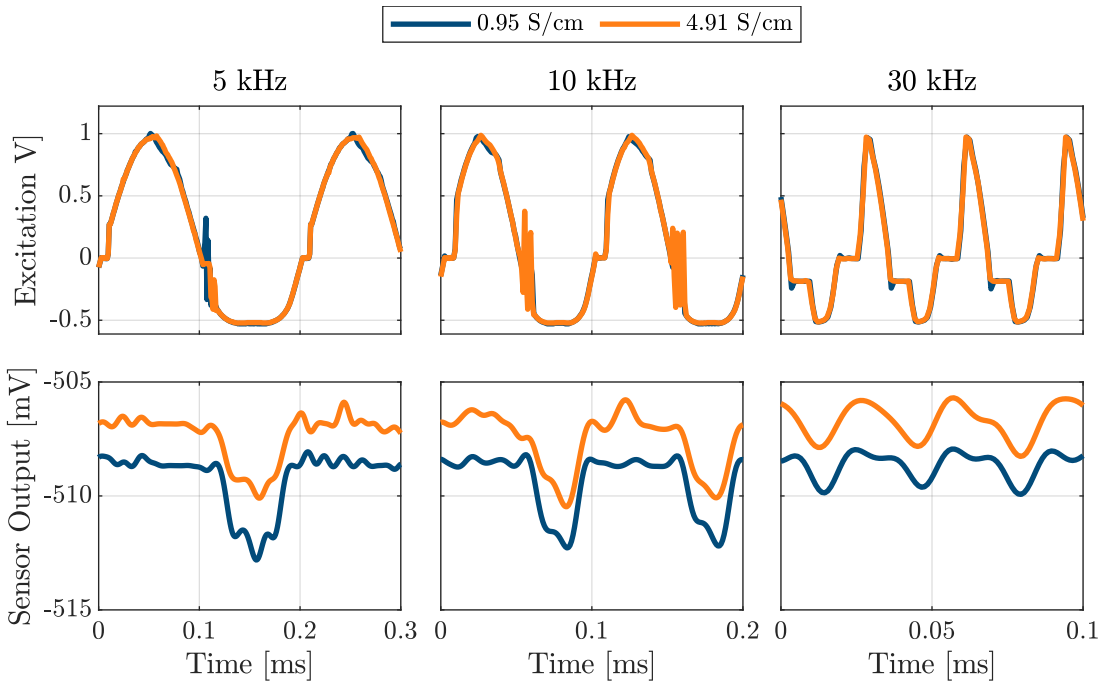

Figure 55: *Acquired data collected via internal ADC shows the disturbed excitation signal by the internal DAC and the amplification stage as well as the sensor output for two different water conductivities and three different frequencies.*

signal occurs. After applying an FFT to both signals, the gain of the sensor is evaluated and compared to the ideal sensor characteristic. The sensor gain is derived from

$$V_{\text{gain}} = \frac{\widehat{V}_{\text{out}}}{\widehat{V}_{\text{in}}}, \tag{31}$$

where $\widehat{V}_{\text{out}}$ and $\widehat{V}_{\text{in}}$ describe the output and input voltage amplitudes. The excitation voltage is selected to $\widehat{V}_{\text{out}} = 1\,\text{V}$. It can be seen that the output of sensor A is independent of the signal frequency and can be roughly described by the ideal characteristic with a cell constant of $\kappa_{\text{cell}} = 450\,\frac{1}{\text{m}}$. The overall sensitivity of the sensor is low due to the small amplitudes and low signal-to-noise ratio.

In order to increase the sensitivity of the sensor compared to the state of the master thesis, sensor B is implemented with the parameters derived previously (cf. table 15). Sensor B uses the same hardware design as the master thesis but is implemented with ten coil turns and a measurement resistance of $R_{\text{M}} = 15\,\text{k}\Omega$. Due to the changed parameters, the sensor gain is expected to be 200 times larger compared to sensor A. Looking at the measurement results of sensor B shown in figure 57, shows that the voltage offset persists due to the use of the same hardware. Furthermore, the larger output signal of Sensor B leads to saturation at the lower end of the signal. Due to the incompleteness of the sine wave, an FFT does not provide the actual output amplitude

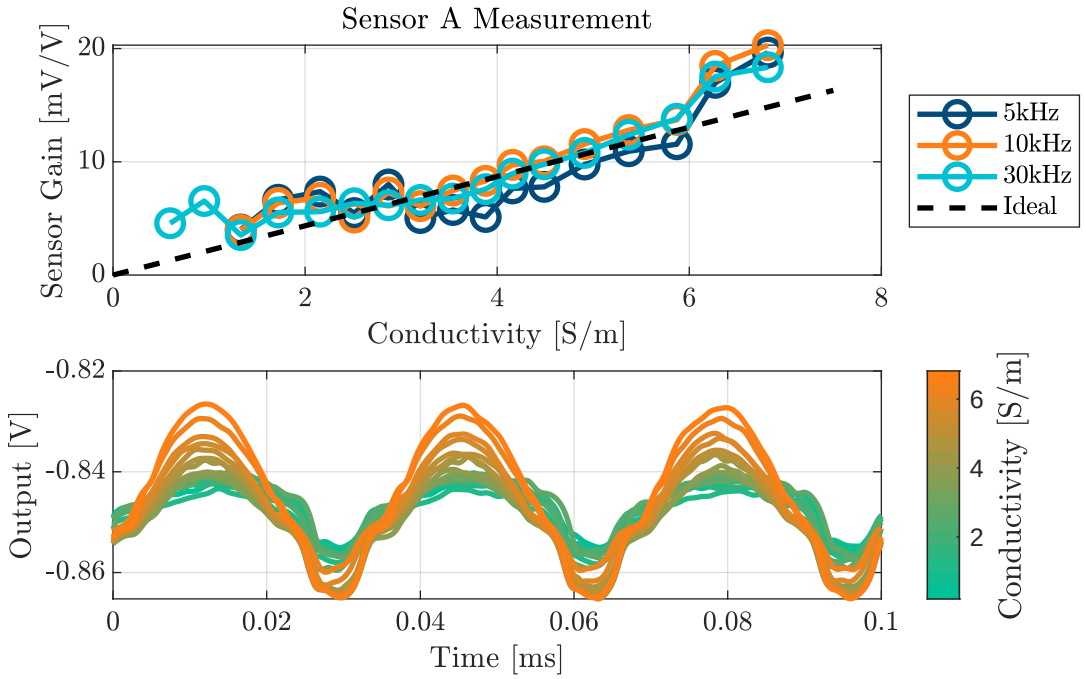

Figure 56: *Data of primary sensor A with external excitation and measurement. Top: Graph of sensor gain versus conductivity of measurement for three frequencies and simulation; Below: Acquired data in the time domain showing the* 30 kHz *output signal for different conductivity values.*

of the signal. Therefore, the average peak height of the signal is evaluated for each measurement. Comparing the average peak height with the ideal sensor characteristic (cf. figure 57) shows a frequency-dependent offset voltage of the output. Furthermore, the measured characteristic is nonlinear for lower conductivity values.
The slope of the sensor characteristic resembles the ideal curve, which confirms the validity of the primary sensor model. The sensitivity of the sensor is improved as expected.

The signal offset and nonlinearity near the saturation voltage can be explained by the use of the *MIC920* amplifier selected for Sensor A. The results of a component-level simulation using the datasheet specifications show that the *MIC920* is not suitable for the design. The source of the −0.85 V offset can be traced to an amplified input offset voltage of 0.43 mV due to the open-loop gain of 10 k. The limited voltage swing of the op-amp results in a signal saturation, causing a constant offset of −0.85 V and limiting the sensor's ability to amplify small voltages, leading to a nonlinear response at low conductivities. The frequency-dependent signal offset can be reproduced by the spice simulation when single-sided saturation occurs. The results of the spice simulation (cf. Fig. figure 57) confirm the derived sensor model and show that the observed output distortion can be attributed to the component behavior described in the datasheet

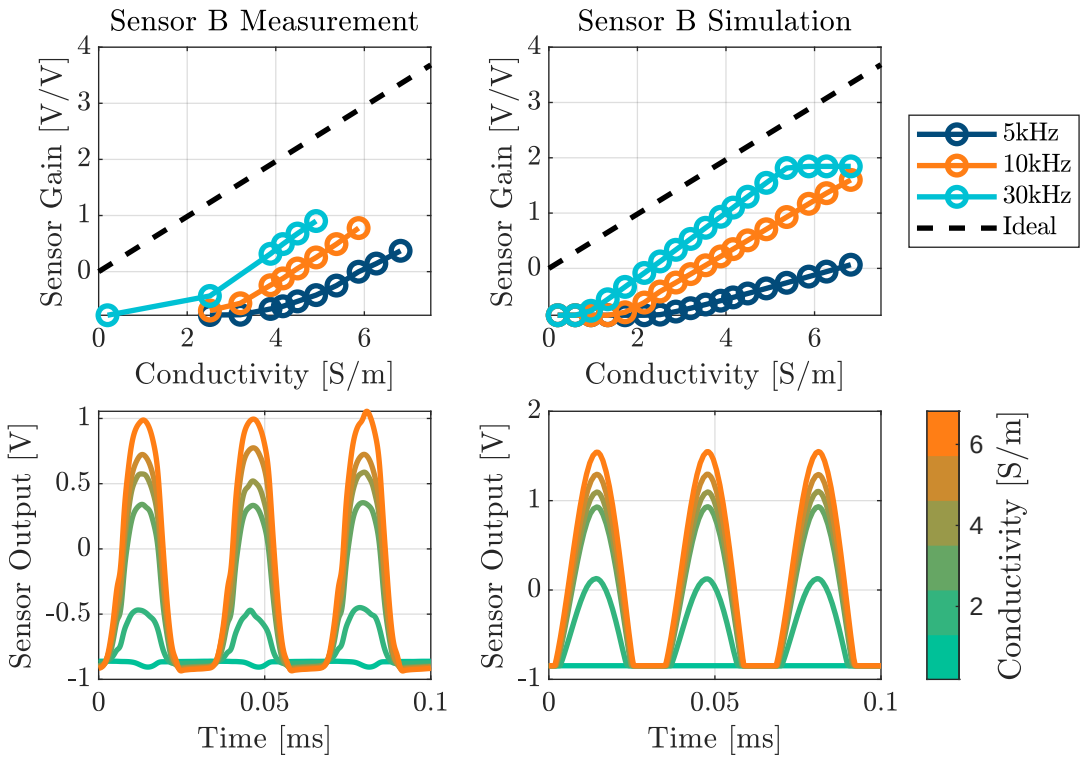

Figure 57: *Measurement and spice simulation data of primary sensor B with external excitation and measurement. Top: Plot of sensor gain versus conductivity of measurement and spice simulation for three frequencies; Below: Acquired data in the time domain showing the measured and simulated* 30 kHz *output signal for different conductivity values.*

[180].

Despite the shifted and saturated signal, the measurement uncertainty of the sensor can be estimated. For that, only data in the linear range of the sensor is considered. For the 30 kHz signal, these are all measurement points between 2 and 5 $\frac{\mathrm{S}}{\mathrm{m}}$, for the 10 kHz signal between 3 and 6 $\frac{\mathrm{S}}{\mathrm{m}}$. The 5 kHz signal is not considered as the amplitude of the output is too small and the measured values are too far from the expected characteristic. To determine the linearity error, a linear fit is made through the linear data and the error for each data point is determined (cf. figure 58).

The 30 kHz signal has a high linearity and shows an average deviation of 10 $\frac{\mathrm{mS}}{\mathrm{m}}$. The 10 kHz signal has a higher variance and has an average linearity error of approximately 30 $\frac{\mathrm{mS}}{\mathrm{m}}$. To determine the precision, the standard deviation of the peak amplitudes in the measurement time frame of 12 ms is considered. The standard deviation is similar for both measurement frequencies, with an average of approximately 30 $\frac{\mathrm{mS}}{\mathrm{m}}$. The lowest measurement uncertainty can be achieved with the 30 kHz signal. If the non-linearity error and standard deviation are combined, an average uncertainty of approximately 50 $\frac{\mathrm{mS}}{\mathrm{m}}$ in the measured range of 2 to 5 $\frac{\mathrm{mS}}{\mathrm{m}}$ is achieved. This value still does not meet the

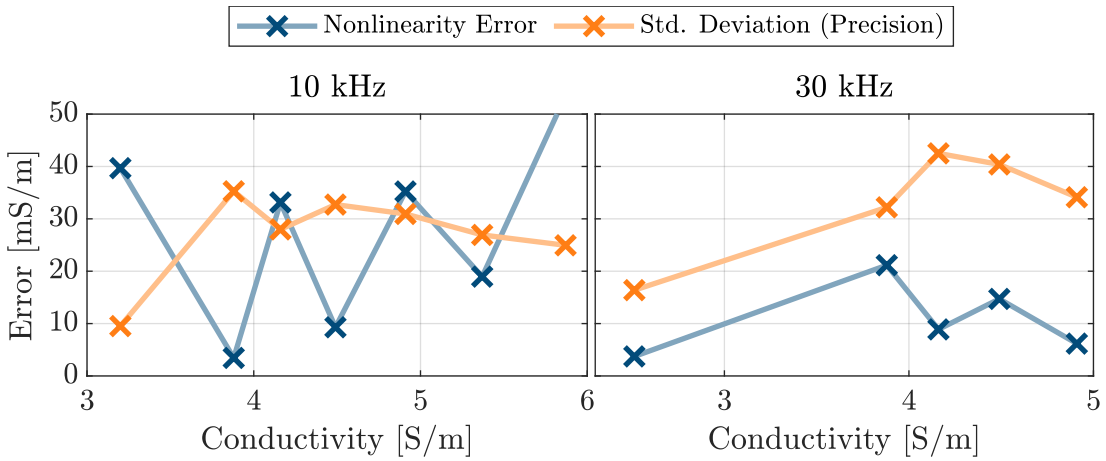

Figure 58: *Visualisation of the linearity error and the standard deviation for the* 10 kHz *and* 30 kHz *measurements on conductivity*

requirement of a measurement deviation of 10 $\frac{\text{mS}}{\text{m}}$ in a measurement range of 0.5 to 7 $\frac{\text{S}}{\text{m}}$, but is comparable to the value achieved by the integrated conductivity sensor by Hui et al. (60 $\frac{\text{mS}}{\text{m}}$). The low linear deviation of the 30 kHz signal is promising, especially considering that the current measurement hardware has significant design flaws and room for improvement. The high precision can be improved through a more stable signal generation and noise filtering. Although the water temperature rose gradually from 15.3 °C to 16.3 °C during the experiment, the fluctuation had no quantifiable impact on the measurement results.

5.3.6 Hardware Revision Proposition: Improvements for Future Designs

The primary sensor was validated and the measurement uncertainty was analyzed. Despite the offset voltage and nonlinearity in the lower measurement range, the sensor shows the expected characteristics and a good baseline sensitivity. The used sensor model is well suited to parameterize the sensor, approximate the characteristics and define the measurement range. To further improve the sensor, it is necessary to reduce the linearity error and increase precision. This can be achieved by revising the hardware developed for Sensor A. Steps that contribute to improvement will be listed below. The main problem identified is the selected op-amp *MIC920*, which is used both for excitation and acquisition.
The concept of generating the signal through the DAC integrated in the microcontroller is a simple and cost-effective solution. However, as shown in figure 55, this method presents specific issues. One of these issues is discrete steps at zero crossing, which occur due to a measured delay of 5 µs in the output stage. To resolve this, a single-ended

output can be used instead of the differential signal from the DAC. The DAC would then oscillate between 0 and 2 V to generate a 2 V amplitude single-ended sine wave. The DC offset doesn't affect the output signal, only the amplifier stage after the DAC should be capable of driving 2 V. With the current *MIC920* amplifier, this is prohibited due to its low maximum voltage swing.
To select an appropriate alternative, a high-precision rail-to-rail amplifier is required. The amplifier should be unity gain stable and allow a sufficient maximum current output (> 20 mA). The *AD8601* (*AD8602* as dual package) fulfills these requirements to a moderate price of < 1 € and is therefore selected.
To enhance the performance of the primary electronics further, a multi-stage amplification can be implemented (cf. figure 59).

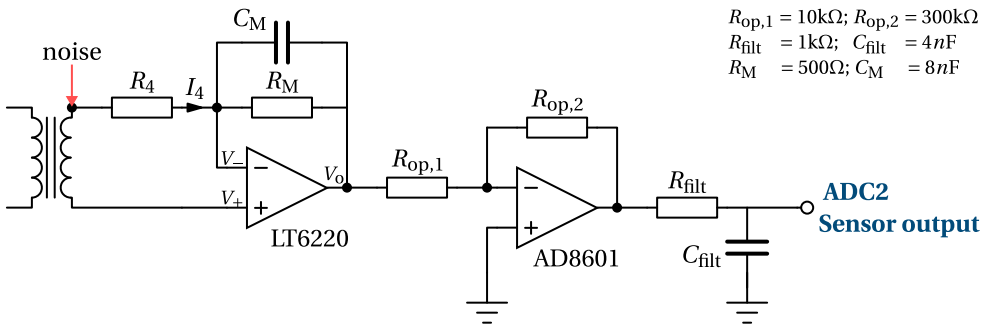

Figure 59: *Revised amplification stage on the secondary side, replacing the single MIC920 with a double amplification stage with LT6220 and AD8601, and R-C filtering.*

The initial stage involves the trans-impedance amplifier, which transforms the current signal into a voltage signal like in the current design. Only the measurement resistance (R_M) is reduced, to reduce the virtual short impedance of the short-circuit measurement. The virtual short impedance is influenced by the gain bandwidth product (GBWP) of the op-amp. An ideal trans-impedance amplifier circuit has a virtual short impedance of zero, since the gain is infinite. For a non-ideal component, the maximum gain is limited by the GBWP and the measurement frequency. Assuming a Gain Bandwidth Product of GBWP = 60 MHz and a measurement frequency of 30 kHz allows a maximum gain of $G_{GBWP} = 2000$. Considering the shown trans-impedance amplifier circuit (cf. figure 59), the voltage at the inverting input can be calculated from the measurement resistor (R_M):

$$V_o = -G_{GBWP} \cdot V_- \tag{32}$$

$$V_- - V_o = I_4 \cdot R_M \tag{33}$$

$$\Rightarrow V_- = \frac{I_4 \cdot R_M}{1 + G_{GBWP}} \tag{34}$$

For a measurement current of I_4, this leads to a virtual short impedance of:

$$|Z_{Amp}| = |\frac{V_-}{I_4}| \tag{35}$$

$$\Rightarrow |Z_{Amp}| = \frac{R_\mathrm{M}}{1 + \mathrm{G}_{GBWP}} \tag{36}$$

This demonstrates that a low GBWP or a high measurement resistor results in a high virtual short impedance. Reducing the measurement resistance, therefore, reduces the linearity error of the sensor (cf. section 5.3.2). Selecting a 500 Ω resistor, with a 60 MHz GBWP, therefore leads to a virtual short resistance of 0.25 Ω.
Since the lower measurement resistance leads to a smaller output of the trans-impedance amplifier, it is amplified by an inverting amplifier. The second amplification stage feeds the signal into the ADC and is designed to provide a maximum output voltage close to the reference voltage of the ADC. To reduce noise in the signal and avoid aliasing, a filter in the form of a passive R-C low-pass filter is incorporated before the ADC. The component parameters are defined by selecting the filter's corner frequency to be 40 kHz. The output signal of the trans-impedance amplifier is further stabilized by using a capacitor in parallel with the measuring resistor, acting as a second R-C filter. Both filters contribute to increasing the signal-to-noise ratio and reducing the precision error.
In order to replace the unsuitable *MIC920* with a suitable trans-impedance amplifier, it is necessary to find a precision rail-to-rail amplifier with a high GBWP. This amplifier should minimize the DC error by having a low input offset and a low input bias current. The amplifier must have a robust output swing to effectively handle the output signal level without saturation. Good solutions are the *LT6220* [181] or the *LTC6268* [182] from Analog Devices (cf. table 17). The *LTC6268* offers an almost 10 times higher GBWP,

op-amp	V_OS	I_B	V_OH	GBWP	Price *
MIC920 [180]	430 µV	260 nA	1.4 V	80 MHz	0.41 €
LT6220 [181]	70 µV	15 nA	5 mV	60 MHz	2.96 €
LTC6268 [182]	0.2 µV	3 fA	70 mV	500 MHz	6.55 €
AD8602 [183]	80 µV	0.2 pA	50 mV	8.2 MHz	0.74 €

Table 17: *Comparison of the specifications of the operational amplifiers under consideration. V_OS: Offset-Voltage; I_B: Input Bias-Current; V_OH Positive Rail Output Swing Voltage.*
Median price for 1000 pcs. obtained from octopart.com on the 22.02.2023.

resulting in a virtual short impedance of 0.03 Ω, compared to 0.25 Ω for the *LT6220* (cf. eq. (36)). However, the linearity error due to the terminating resistance is negligible for this magnitude (cf. figure 45). Therefore, the more cost-effective *LT6220* rail-to-rail operational amplifier can be selected instead.
To test the new hardware design, the sensor model was implemented in a Spice simula-

tion that includes the *AD8602* for the excitation and amplification stage, as well as the *LT6220* as the trans-impedance amplifier. The simulation results show the expected linear response of the sensor and arbitrary white noise added to the coils is filtered (cf. figures 59 and 60). The voltage offset of the output is drastically reduced to ≈ 50 mV and no frequency dependence is observed.

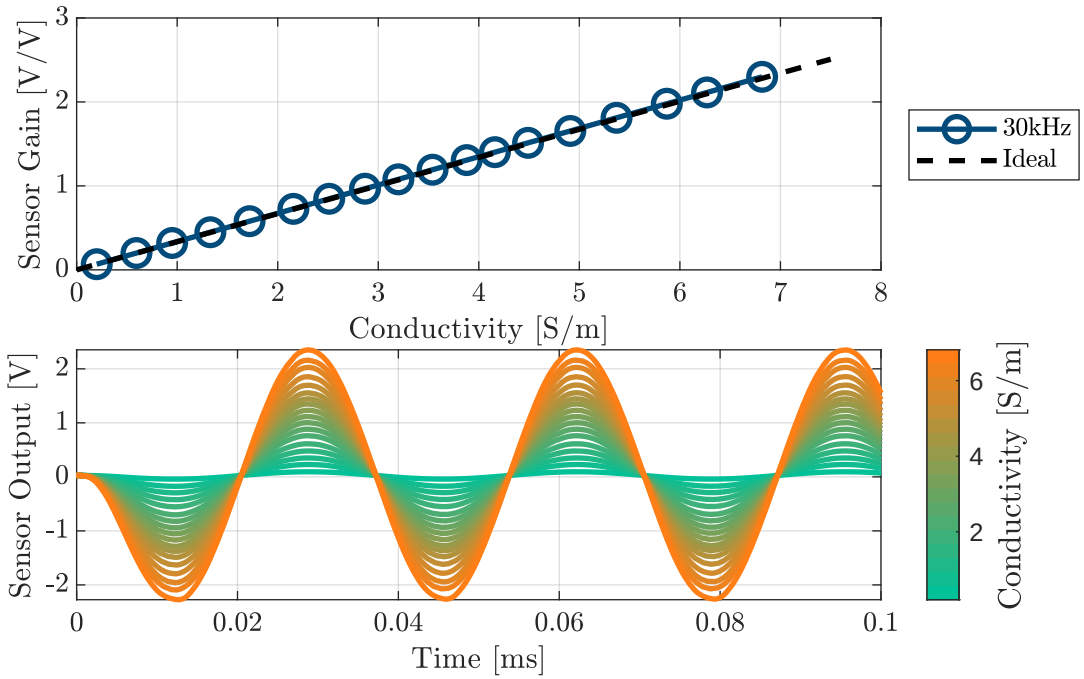

Figure 60: *Spice simulation data of the revised sensor hardware. Top: Sensor gain over conductivity, Below: Output signal in the time domain for different conductivity values*

Compared to the very low price of 0.41€* for each of the two *MIC920*s, the revised hardware now includes an *AD8602* in a double package (0.74€*) and an *LT6220* (2.98€**), increasing the total component cost of the hardware from ≈ 20€ (as derived in [179]) to ≈ 25€.

*Median price for 1000 pcs. obtained from octopart.com on the 22.02.2023.

5.4 Integrated Temperature Measurement for Combined CT-Sensors

So far, the components of the conductivity sensor and secondary electronics for data processing were considered. This section focuses on deriving the components required for measuring temperature - the primary temperature sensor and the primary electronics - in order to complete a fully self-contained CT-sensor. By providing an overview of temperature measurement principles, and comparing state-of-the-art measurement methods, a promising approach is identified. Subsequently, design principles for this concept are proposed, and a prototype implementation is used to validate the findings.

5.4.1 Review of Temperature Measurement Principles for Sea Surface Temperature Measurement

The temperature measurement is separated into two components: the primary sensor, sensing the temperature, and the primary electronics, processing the signal. To give a broad overview of possible measurement implementations, state-of-the-art solutions for both components are presented in the following. First, the primary measurement principle is selected, followed by the consideration of suitable measurement circuits. As illustrated in section 2.3.4, contacting sensors are preferred, as they provide high accuracy, repeatability, and a good compromise between accuracy and cost.

Comparing Primary Sensor Options The most common contact measurement methods are based on thermocouple and thermistor measurements. Due to their low accuracy (1 K [184]), thermocouples are not a viable option compared to an resistance temperature detectors (RTD) such as a PT -100 sensor, which is often used for high-precision measurements with accuracy up to 1 mK. In addition, integrated systems for temperature measurements based on complementary metal-oxide-semiconductor (CMOS), bipolar junction transistor (BJT), and quartz crystal oscillators [185] can be used to develop particularly small and energy-efficient sensors. A recent state-of-the-art survey by Makinwa et al. [186, 187] compares integrated smart sensors and shows that the highest resolutions can still be achieved by resistivity measurements. Therefore, for an ocean temperature sensor focusing on compact design and cost efficiency, RTD sensors should still be preferred based on the current state of research. RTDs are based on either resistance measurements of a material (e.g., platinum such as PT-100) that has a positive temperature coefficient (PTC), and thermistor resistance measurements

that can have a negative temperature coefficient (NTC) due to the semiconductor effect [184].
Considering a PTC sensor, a 100 Ω platinum resistance (PT-100) has the advantage of being standardized by IEC 60751 [188], which allows a limit deviation of 100 mK in the highest accuracy class (AA). This means that a maximum deviation of 100 mK can be achieved even if the platinum resistor is replaced. To achieve higher accuracy, calibration of the sensor characteristic is required, which for the field of oceanography should correspond to the ITS-90. NTC thermistors are also available with tolerances of 100 mK and more, and are less expensive. In addition, due to their smaller size, NTCs have the advantage of allowing even smaller sensor designs and very fast response characteristics [189], which is preferred when measuring ocean temperature [190]. However, one of the biggest differences between a PT-100 resistor and an NTC thermistor is the approximation of the sensor characteristic curve and its calibration to ITS-90. Since ITS-90 is defined by the resistance values of a standard platinum resistance thermometer, between 13.8033 K to 1234.93 K, the PT-100 resistance values can be used directly for temperature interpolation [191, 192]. With the exponential characteristic of the NTC resistance to temperature, the reproducibility of ITS-90 is more challenging due to the nonlinearity of the NTC (cf. figure 61). Calibration of an NTC thermistor to ITS-90 requires an approximation equation such as the Steinhart-Hart [193] or Hoge [194] equation. Several publications [195, 196] compare the calibration equations for NTC thermistors and show that the interpolation residuals can be kept below 1 mK.

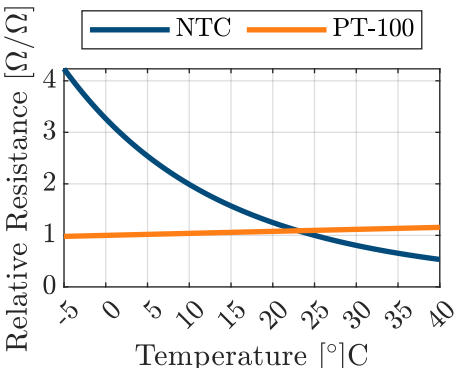

Figure 61: *Comparison of the sensitivity of PT-100 [188] and 10k-NTC [197] thermistors. Shown is the resistance divided by the nominal resistance.*

The high-precision PT-100 sensors are designed in a 4-wire configuration to eliminate lead resistance in the measurement. However, embedded sensors based on NTC thermistors can keep leads much shorter by installing the conditioning circuit closer to the thermistor. In addition, thermistors are available with much larger resistance values, minimizing the wire influence. The higher resistance value also leads to a larger voltage drop for the same power dissipation, which helps to reduce self-heating.

Considering the long-term stability, PT-100 resistors are naturally more stable than NTCs due to the degradation of the semiconductor effect [189]. This can be counteracted by a preaging process involving high-temperature treatments. Sydenham and Collins [198] showed a measured stability of 200 µK/100 h, Li et al. [190] 0.05 mK and 0.12 mK over a duration of three months, and Wudy et al. [189] measured the stability of 30 mK over a period of six months, while they referred to the manufacturer's stability specifications of 97 mK over 9 years. Therefore, the required measurement stability of 5 mK/year can be achieved not only with PT-100 resistors, but also with NTC thermistors. Due to the nonlinear resistance-temperature relationship of NTCs and the higher temperature sensitivity in the measurement range (cf. figure 61), higher precision can be achieved compared to linear PT-100 resistors [190]. With a suitable conditioning circuit, NTC thermistors are therefore a promising option for low-cost, contacting ocean temperature measurements.

Selecting a Primary Electronics With the conditioning circuit, the electrical resistance value is converted into a digitally readable measurement result. This includes amplification, filtering, and analog-to-digital conversion.
A common measurement circuit used for oceanographic temperature and conductivity sensors is the Wien bridge circuit (cf. figure 62). The Wien bridge is a second-order bandpass filter with a temperature-dependent RC time constant (cf. figure 62).

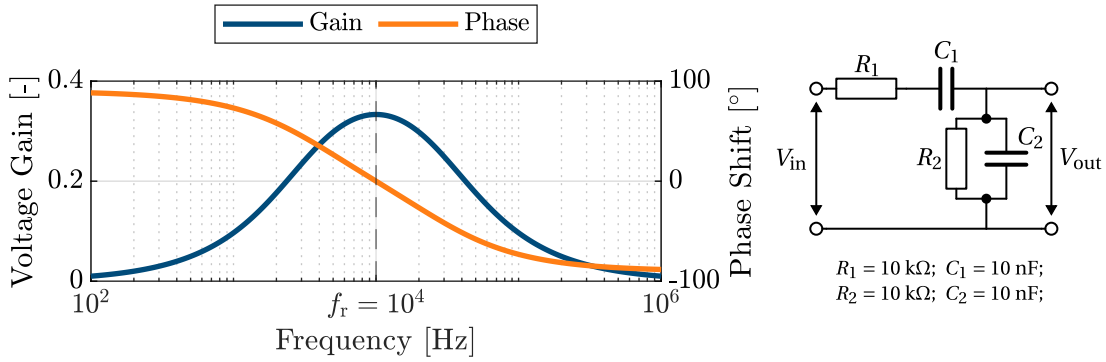

Figure 62: *Circuit of a Wien bridge oscillator and corresponding gain and phase diagram with an indication of the resonance frequency f_r.*

The transfer function and basic circuit principle are explained in detail by Pan and Makinwa [199]. To determine the RC time constant, either the input frequency is fixed and the output phase shift is extracted, or the output phase is controlled and the required excitation frequency is measured [199]. The method using a fixed input frequency is commonly found in small low-power CMOS temperature sensors, which feed the reference frequency of a crystal into the RC filter and determine the phase shift by a phase detector [200]. The output voltage of the phase detector is proportional to the

phase shift and can be converted using a conventional ADC to derive the associated temperature value. Another approach is to use a frequency-locked-loop circuit (similar to phase-locked-loop circuits), to control a variable frequency reference so that the phase shift between the output of the Wien bridge and the reference becomes zero. This determines the resonant frequency f_r of the RC filter, which is inversely proportional to the temperature [199]. A digital counter can be used to convert the output frequency to a digital signal and derive the temperature. A counter-based implementation is presented by Park et al. [201], who preferred the frequency-locked-loop approach over the phase detection method for CMOS temperature sensors. Van Haren et al. implemented a Wien bridge with a frequency counter for high-precision monitoring of ocean temperature and achieved an accuracy of < 1 mK [202–204]. The use of a 48 MHz crystal allows several million counts over the temperature range of −10 °C to 50 °C, resulting in a sensor resolution of several tens of µK [202]. Besides the Wien bridge oscillator, there are other AC-bridge implementations that also successfully implement high-precision temperature sensors with lock-in amplifiers [205]. Wudy et al. [189] point out that semiconductor fabrication has now improved to the point where AC technologies no longer dominate the temperature resolution of DC circuits. They propose a digital approach using a voltage divider processed by an op-amp in an impedance converter configuration with a Butterworth filter and conventional ADC to achieve a temperature resolution of 75 µK. Skinner and Lambert [206] focused on a low-cost implementation for high-precision measurement of water temperature by using low-cost integrated circuit (IC) components to build a voltage-to-frequency converter that achieves a resolution of 3 mK. The circuit implements a Schmitt trigger hysteresis circuit that charges and discharges a capacitor through the temperature resistor. Because of the resistance-dependent current limitation, charging cycles are related to the temperature, measured by counting the frequency of the Schmitt trigger's digital output states. This comparatively simple circuit shows that state-of-the-art IC components enable high-precision temperature measurement even with simple circuit designs.

In summary, despite the large availability of low-cost temperature sensors with 100 mK accuracy, higher precision measurement of 10 mK or lower remains challenging and costly. The Wien bridge oscillator, developed in the 1960s, is still a state-of-the-art concept for high-precision measurements. New developments using the advantage of CMOS technology or integrated DC components have not shown significant improvements in accuracy and resolution. A simplification of the measurement circuit alone may not significantly reduce sensor costs as the manufacturing tolerances still require elaborate calibration procedures.

5.4.2 Function Analysis and Design of the Embedded Temperature Sensor

The selected temperature measurement approach for the embedded CT-sensor is based on the circuit developed by Skinner and Lambert [206]. The circuit operates on the principle of a voltage-to-frequency converter, where the output of the sensor is a digital pulse with a frequency proportional to the temperature (cf. figure 63a).

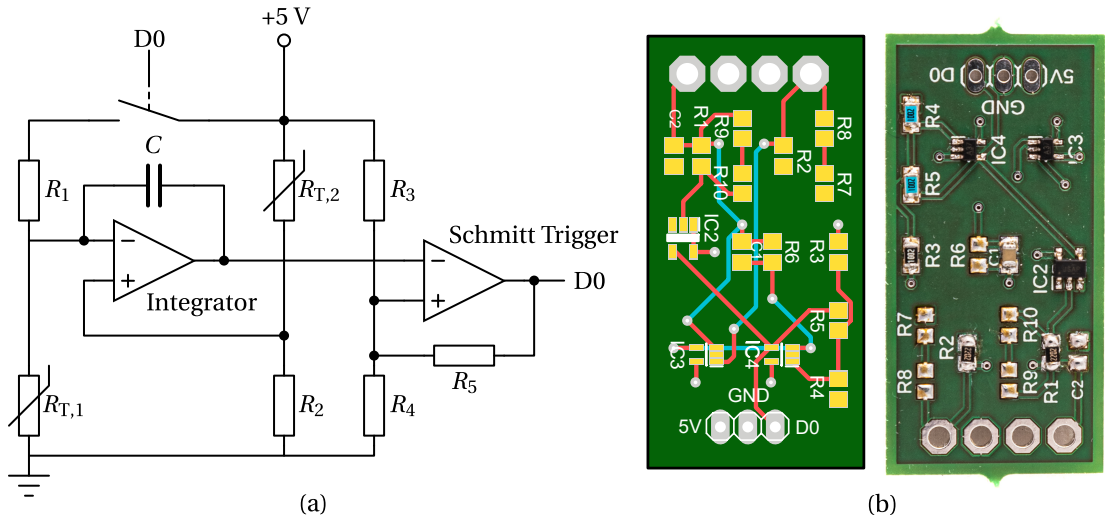

Figure 63: *a: Schematic representation of the measuring circuit of the temperature sensor; b: PCB design and implementation of the sensor circuit.*

The circuit's core component is a capacitor that is charged and discharged through the temperature-dependent thermistors $R_{T,1}$ and $R_{T,2}$. The arrangement of the components is similar to a Wheatstone bridge, and it includes a single integrator op-amp and a Schmitt-trigger which acts as a dual-slope analog to digital converter.
The circuit operates in two phases: charging and discharging. During the charging phase, the switch connected to D0 is open, and the circuit charges the capacitor through the thermistor $R_{T,1}$. The charging time is inversely proportional to the resistance of the thermistor. Once the capacitor voltage exceeds the upper threshold voltage of the Schmitt-trigger, it switches its output signal D0 and closes the switch, starting the discharging phase. The circuit discharges the capacitor through the thermistor $R_{T,1}$ in a time proportional to its resistance. The output signal D0 can be processed by a microcontroller, evaluating the signal frequency to derive the temperature. The circuit resistors R_1 and R_2 balance the bridge, while R_3, R_4, and R_5 set the hysteresis thresholds of the Schmitt-trigger, which helps to ensure a stable output.
The temperature sensor prototype was tested by implementing the circuit in a single PCB (cf. figure 63b) and encapsulating the two NTCs $R_{T,1}$ and $R_{T,2}$ in a brass tube [207]. The components are selected according to table 18.

Component Type	Description	Value	Tolerance
Resistor	R_1, R_2	22 kΩ	±1%
Resistor	R_3, R_4	10 kΩ	±1%
Resistor	R_5	5 kΩ	±1%
Thermistor	$R_{T,1}$, $R_{T,2}$	100 kΩ	±1%
Capacitor	C	2.2 nF	±5%

Table 18: *Selected parameter of the temperature measurement circuit (cf. figure 63). [207]*

The value of the temperature is derived from the Steinhart-hart equation and the circuit's charging and discharging behavior. A microcontroller counts the number of low states n_{low} of the sensor output D0 in a fixed measurement period t_{gate} at a sampling rate of $f_s = 1\,\text{MHz}$. The ratio of charge to discharge time is derived by:

$$\frac{t_{\text{charge}}}{t_{\text{discharge}}} = \frac{f_s \cdot t_{\text{gate}-n_{\text{low}}}}{n_{\text{low}}} \tag{37}$$

It is assumed, that both thermistors have the same resistance R_T, with the relationship:

$$R_T = \sqrt{R_1 R_2 \left(\frac{t_{\text{charge}}}{t_{\text{discharge}}} - 1 \right)} \tag{38}$$

The derived resistance value is then converted into a temperature reading using the Steinhart-hart equation.

5.4.3 Potential Analysis of the Cost-Effective Measurement Approach

To test the sensor's measurement uncertainty, a series of experiments were conducted in the scope of a supervised bachelor thesis [207]. The first experiment tested the stability and precision of the sensor by putting it into a temperature-regulated bath set to a constant temperature of 20 degrees Celsius, along with a reference sensor. The sensor counts n_{low} and the reference temperature T_r were logged and compared over the course of one hour, and it was found that the derived temperature from the counts according to eq. (38), provided a good approximation of the reference temperature (cf. figure 64). The standard deviation over time of the prototype was similar to the reference sensor, with both sensors deviating by 5 mK over the one-hour period. The maximum temperature difference between reference and prototype was determined to 3 mK. For a constant measurement setup, the sensor fulfills the required maximum measurement uncertainty of 20 mK.

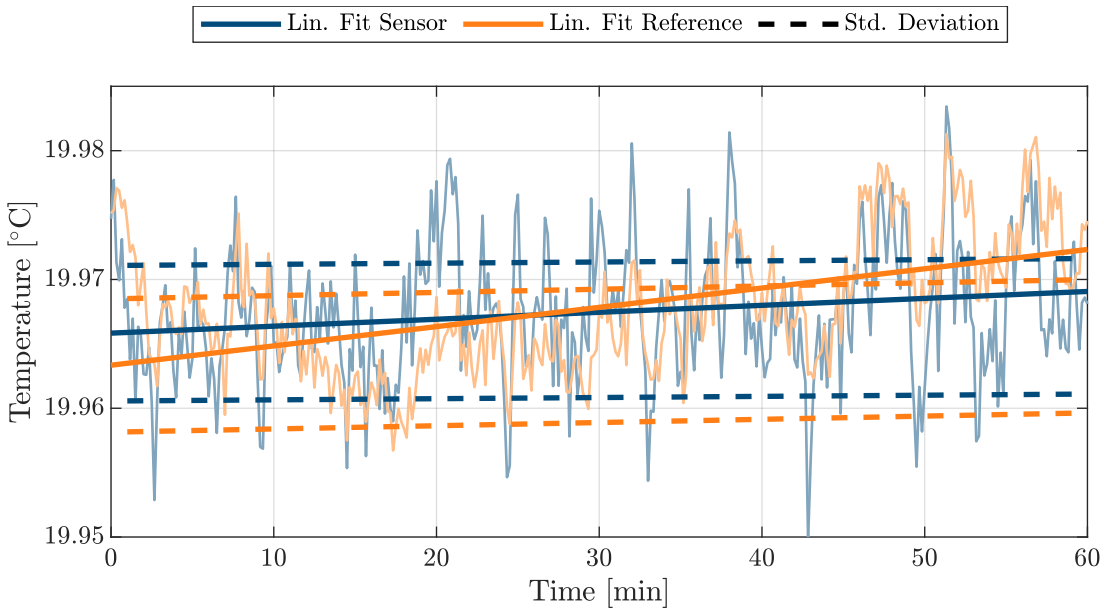

Figure 64: *Temperature data of sensor prototype and reference during a 60-minute stability test. Shown are the raw data (light color), a linear fit, and the standard deviation over the measurement time period.*

In a second experiment, the repeatability and accuracy of the sensor characteristic were tested by repeating a measurement cycle consisting of three heating and two cooling phases over a time span of 7 hours. The results showed that the derived characteristic does not provide an accurate sensor model over the full temperature range (cf. figure 65). Especially for temperatures above 20 °C, the sensor model shows a large deviation from the actual measurement results. The maximum systematic error between measurements and expected value is 2 °C. One identified reason for this was the larger heat capacity of the brass housing of the sensor prototype compared to the reference sensor, leading to a delayed temperature reading. To overcome this issue, a temperature coefficient $\alpha_{\text{correction}}$ was determined from the measurement results, to compensate for the larger heat capacity. The reference temperature was shifted by a value proportional to the heating and cooling rate $\frac{\delta T_\text{r}}{\delta t_\text{r}}$ multiplied with the coefficient [207]:

$$t_{\text{r,corrected}} = t_\text{r} - \frac{\delta T_\text{r}}{\delta t_\text{r}} \cdot \alpha_{\text{correction}}; \tag{39}$$

The value for the temperature coefficient is determined to $\alpha_{\text{correction}} = 1073\,\text{s}^2/\text{K}$ by minimizing the error of a characteristic that converts the recorded sensor counts n_{low} to a prototype sensor reading T_p. For the compensated measurement data, two new characteristics are derived from the average count value of each Temperature. Characteristic (a) considers both, the heating and cooling process, while characteristic (b) only considers the slower cooling process. Figure 65 shows the deviation of each measurement

cycle from the characteristic a and b. Considering the average of all measurement cycles (characteristic a), the maximum systematic error is around 400 mK. Considering only the cooling process (characteristic b), the systematic error becomes lower and provides an accuracy of 50 mK.

The results show, that the temperature sensor can provide sufficient measurement precision but still provides a low measurement accuracy due to large systematic errors. The heat capacity of the sensor needs to be reduced by replacing the brass housing with a thin glass tube or a resin layer, to allow a more profound analysis of the sensor characteristic. In addition, a new approach must be found to improve the accuracy of the sensor characteristic. One approach would be to replace the Steinhart-Hart equation by the more precise Hoge equation [195, 196]. Another approach is to use a lookup table that relies on a calibrated curve. Overall, calibration remains an essential component for the production of high-precision temperature sensors. Even with state-of-the-art approaches, significant manufacturing tolerances, and random errors persist, requiring extensive sensor calibration. Therefore, the calibration process in a controlled temperature bath is still an essential part of the sensor cost.

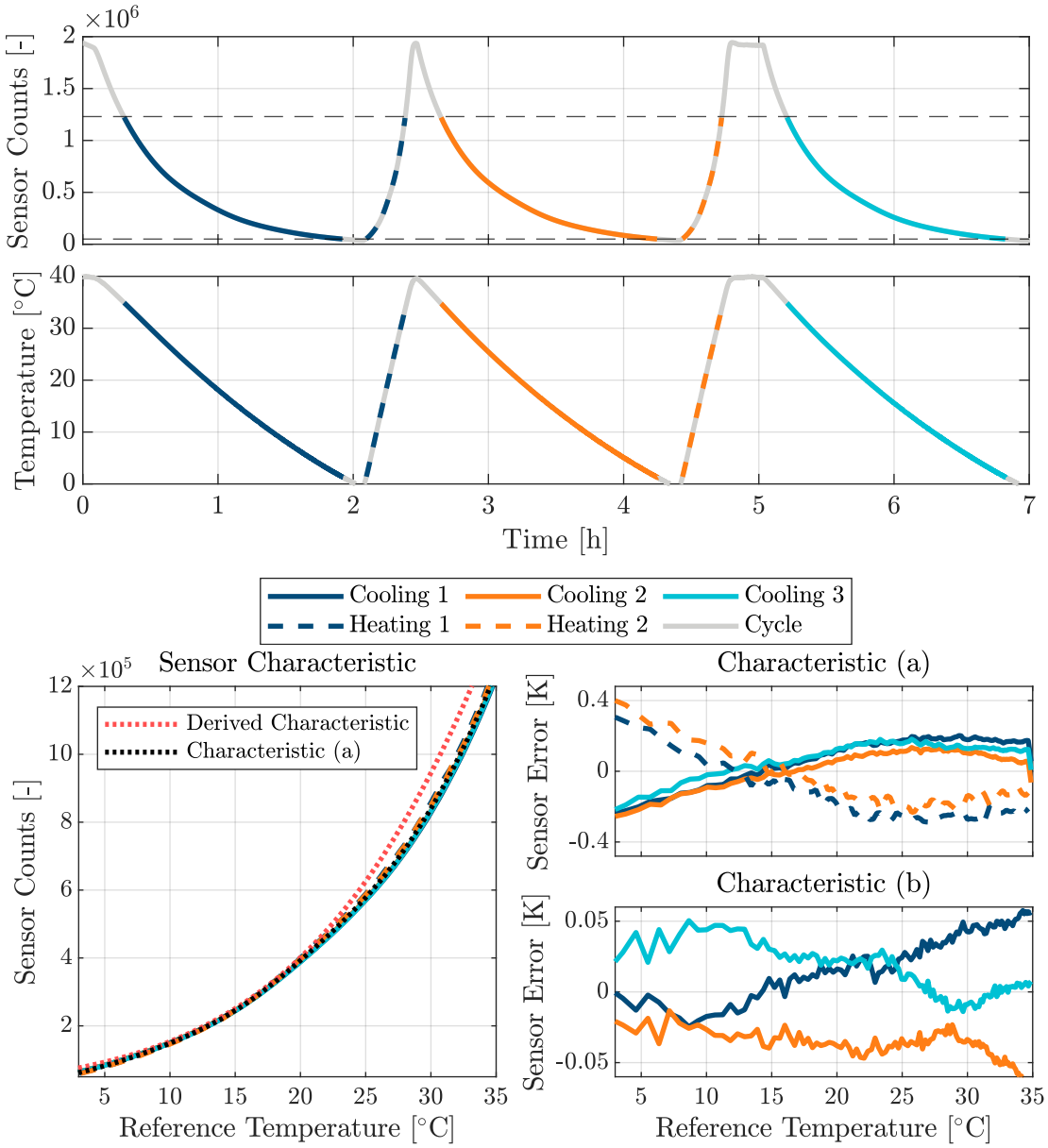

Figure 65: *Top: Sequence of the measurement cycles with the display of the sensor counts and the reference sensor temperature. The cycles are divided into cooling and heating sections;*
Below: Representation of the measured sensor characteristics for each heating and cooling section in comparison with ideal characteristics, as well as the deviation of the cycles from characteristics (a) and (b).

5.5 Evaluation of CT-Sensor Development Results

In this chapter, an architecture for a fully integrated, embedded conductivity and temperature measurement for cost-effective in situ monitoring of the ocean surface was proposed. A thorough consideration of different measurement approaches and an analysis of physical sensor functions led to the definition of design principles that balance cost and accuracy.
Various existing approaches were compared and alternative solutions for temperature and conductivity sensors were evaluated. A concept was derived based on a transformer-type inductive conductivity sensor combined with a temperature-sensing circuit using a dual slope analog-to-digital converter. Both sensors are integrated on a single PCB, with shared secondary electronics for data processing. Equivalent model descriptions were used in the parameterization of the sensor, contributing to a better understanding of the sensor's working principles.
Validation of a sensor prototype was carried out separately for temperature and conductivity measurement functions. The conductivity measurement results show a promising sensor accuracy with low systematic errors (50 $\frac{\mathrm{mS}}{\mathrm{m}}$). Even if the developed sensor does not meet the set requirements, the measured results of prototype sensor B are comparable to state-of-the-art solutions [50]. The sensor's uncertainty and measurement range can be improved further, by implementing the proposed hardware revision. The utilization of enhanced op-amps promises increased precision and the ability to meet the stated requirements.
The temperature sensor circuit provides stable readings with a high precision of up to 5 mK, which is within the specified requirements. However, the overall measurement uncertainty is still too high due to systematic errors. To achieve the targeted overall accuracy of 20 mK, an improved approximation of the sensor properties is required. In addition, an implementation of housing with lower heat capacity is required.

In summary, the proposed concept represents a promising approach for a fully integrated CT-sensor. With a material cost of less than 50 €, the sensor could provide low-cost salinity measurements, advantageous for sea surface monitoring with lower accuracy requirements. The sensor concept could be superior to technologies currently available on the market. The proposed hardware revision can be implemented to meet established sea surface monitoring requirements. The characteristics and adaptability of the sensor make it a valuable tool for various ocean monitoring applications, and further research and development can be conducted to optimize its performance.

A monitoring module facilitating multi-sensor measurements and design principles for low-cost salinity measurement were presented so far. However, the energy demand of the monitoring system has not been considered yet. In the following chapter, methods for wave energy harvesting will be explored to enable self-sufficient operation.

6 Self-Sufficienct Ocean Monitoring: A Model-Based Design Approach

In order to enhance the long-term monitoring capabilities of ocean surface observations, energy harvesting methods are required. Wave energy has emerged as a viable solution to enable self-sufficient surface monitoring. This chapter introduces a methodological approach to designing a compact wave energy harvesting system. The approach begins by reviewing recent advancements in wave energy harvesting methods for drifters. Then, a model-based development is proposed and the design concept is presented. Finally, an optimization of the overall system is carried out, and the results are validated through prototype implementations.

6.1 Wave Energy Harvesting Concepts for Ocean Monitoring

This section is divided into a thorough overview of existing solutions for harvesting wave energy on drifters and a presentation of the energy harvesting concept considered here.

6.1.1 Review and Derivation of Compact Harvesting Approaches for Drifter

Many concepts exist for the harvesting of wave energy which ranges from small power gains below 1 mW [208] up to massive power plants with planned outputs of several Megawatts [209]. Systems with relatively low power output are based on kinetic energy harvesting approaches, which can also be found on land. E.g. Shi et al. [210] implemented a vibration energy harvester in a spherical buoy based on a piezoelectric generator with a power output of 6 mW. A number of similar solutions are based on the motion of the harvester in the waves, such as the triboelectric generator developed by

Rodrigues et al. [211] or the kinetic glider developed by Ding et al. [212]. The majority of the kinetic energy harvesting research on ocean drifters is based on ball-shaped buoys as investigated by Carandell et al. who implemented a gyroscopic energy harvester [208] and followed the concept of a rolling mass with an electromagnetic generator [213] (cf. figure 66a and b) or Li et al. [214] who investigated kinetic harvesting using a pendulum swing. In all cases, the kinetic energy harvesting applied to drifter-sized buoys shows power outputs in the lower milliwatt range. In addition, these spherical drifters are typically used for wave studies and near-shore applications [113]. The drifter considered in this work uses a drogue which stabilizes the buoy's motion in the waves and therefore makes vibration or rolling motion harvesting unsuitable [211].
Energy is harvested in greater quantities by systems that utilize the relative motion between buoys and rigid points, such as moorings. The point absorber concept implemented by Symonds et al. [215], generated a power output of 50 W for a fixed meteorological observation buoy. As mooring lines are against the purpose of a drifter, another option is to facilitate the difference of water particle velocities in different water depths. The orbital motion of water particles due to wind-induced waves decreases with the water depth and therefore allows to utilize the relative motion between objects in the upper and in the deeper water layers (cf. figure 67a).

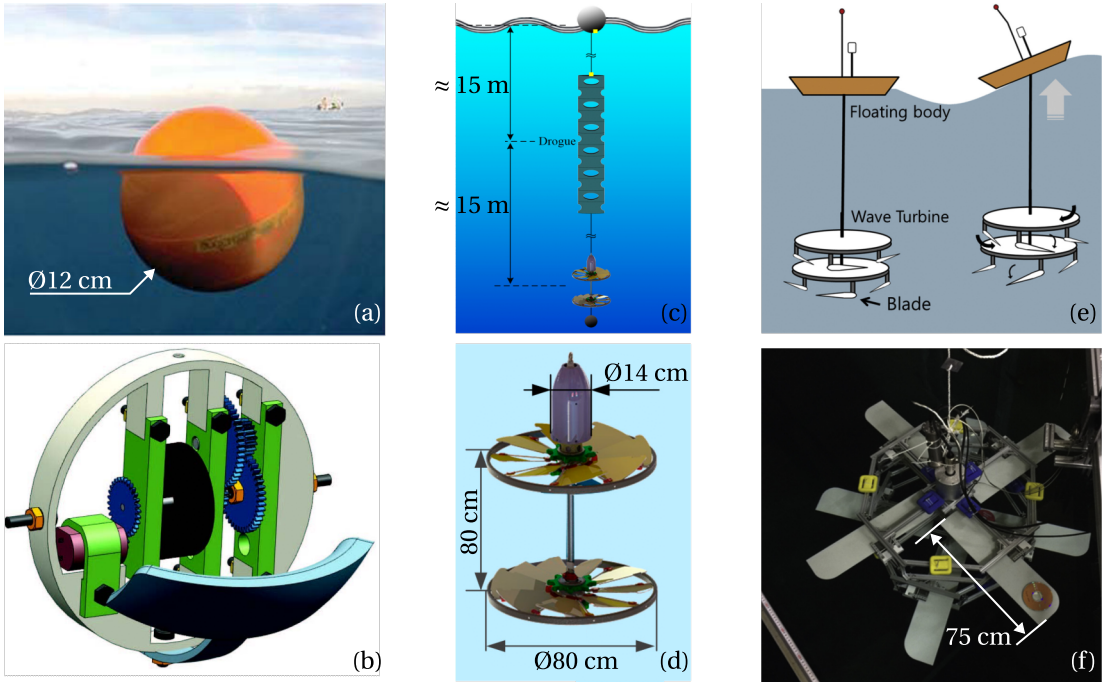

Figure 66: *a&b: Kinetic Energy Harvesting system of the WAVY Drifter by Carandell et al. [208, 213]; c&d: Counter-Rotating Wave Energy Converter for SVP Drifter by Wu et. al [216]; e&f: Flap-type mooring-less wave energy harvesting system by Joe et al.[217]*

Joe et al. [217] applied this concept to an ocean drifter, by attaching a self-rectifying turbine with flap-type blades to the end of the drogue (cf. figure 66e and f). Due to

the up and down movement of the system in the water, the turbine generated a power output of more than 1 W. A similar concept which produced a similar result, was implemented by Wu et al. [216] who connected a counter-rotating wave energy converter to the drogue of an SVP drifter [94] (cf. figure 66c and d). Despite the much higher power output, these solutions have the disadvantage of a rather complex and large mechanical construction, which makes them unsuitable for low-cost drifters.

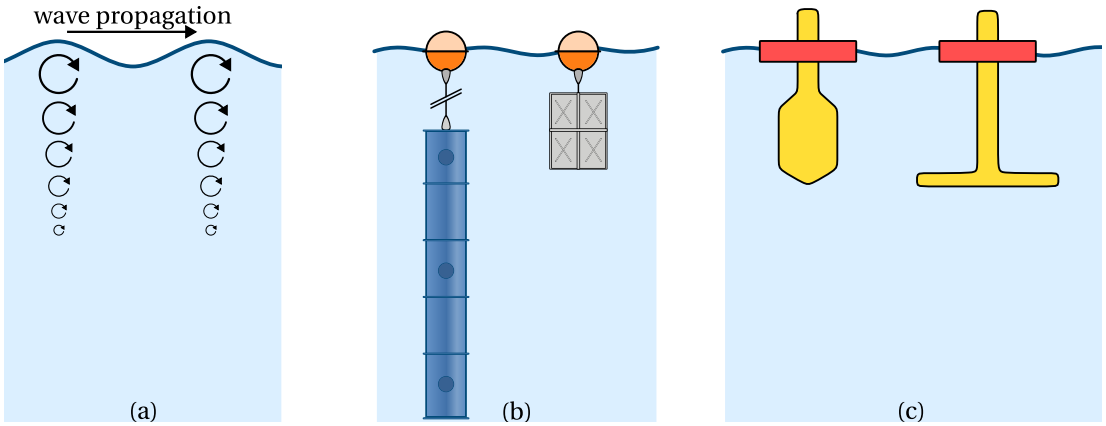

Figure 67: *a: Representation of the decreasing velocity of water particles on their orbital paths in wind-induced waves; b: Not to scale sketch of an SVP drifter (left) with deep reaching drogue, next to a drifter with compact dimensions; c: self-reacting point absorber (SRPA) with the streamlined reacting body (left) and damper plate (right) as investigated by Beatty et al. [218]*

The self-reacting point absorber (SRPA) is a wave energy converter (WEC) concept that exploits the velocity differences in water layers. The SRPA is a two-body WEC based on a float on the water surface and a lower reacting body. This approach is easy to implement and works well with the design of a drifter with a drogue. However, this concept has so far only been designed and tested in larger dimensions for wave energy power plants [218–220] and was seemingly not considered for small-scale use. Several experimental and simulative studies [218, 221–223] analyzed the mechanical dynamics of an SRPA and recommend design guidelines for mechanical system optimization. Beatty et al. [218] studied the influence of the reacting body on the SRPA by the comparison of a WEC with a streamlined reacting body and higher mass to a WEC with damper plate (cf. figure 67c) and concludes that a heave plate produces more power at low frequencies and exhibits a wider-banded power function. This perfectly enables the application of the SRPA concept to a drifter, where the drifters buoy acts as a float and the drogue as a reacting damping plate. In order to allow relative motion between the buoy and the drogue, the drogue must be detached from the buoy. A generator located between the float and reacting body can facilitate power takeoff. This concept can be particularly effective for drifter with long drogue (cf. figure 67b), such as the SVP drifter which reaches to a depth of up to 30 m [94]. However, it is needed to investigate whether a

sufficient power output can also be achieved for a compact drifter system with a draft of only 0.5 m.
Existing small solutions that can be incorporated into drifters without significantly changing the design do not provide enough energy. Other solutions that provide more energy are too complex and cannot be assembled quickly. Large, externally mounted designs do not allow space-saving storage on ships or easy handling by one person, as dictated by system-level requirements. Therefore, this chapter considers a compact wave energy converter for shallow-water drifters that can be integrated into the existing design for coastal applications. The basis is a WEC based on a SRPA that uses an electromagnetic generator for power take-off. The design focuses on a minimalist concept to enable low-cost implementation.

6.1.2 Wave Energy Harvesting Concept Presentation

To integrate the concept of an SRPA into a Drifter, movable connections between the buoy and the drogue as depicted in figure 68 are required. A horizontal plate is added to the drogue, which functions as a reactive plate. Figure 68c visualizes the difference in the up and down movement of the float and plate in the wave and the resulting relative distance $\Delta\xi$ between both bodies with respect to the equilibrium point. The power

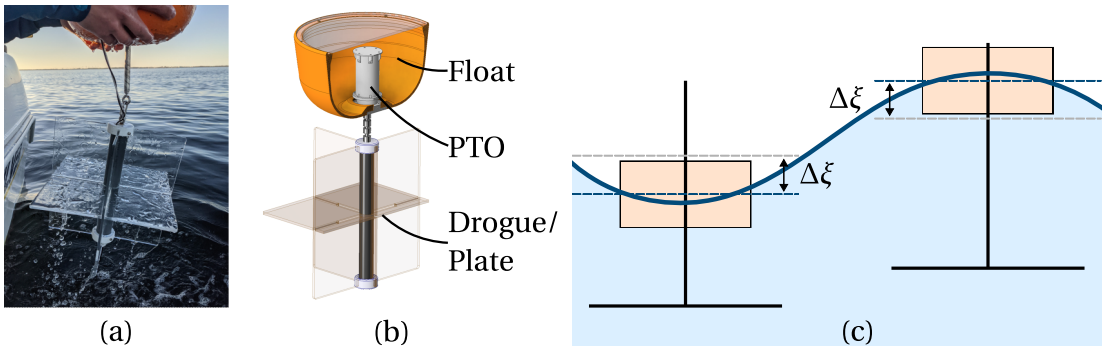

Figure 68: *a: Prototype implementation of a drifter with decoupled buoy and drogue; b: 3D-model of the WEC concept integrated into a drifter with a description of float, power takeoff (PTO) and drogue; c: Sketch of the working principle of the WEC.*

takeoff (cf. PTO figure 68) has the purpose of converting the mechanical energy from the relative motion to electric energy. Electromagnetic generator offer a high energy density and are therefore suitable to meet the power requirements. Unlike rotational generators that require a conversion from linear to rotational movement, direct drive linear generators can reduce the complexity of a system. To reduce mechanical power losses and the manufacturing effort due to gear-boxes or other means of translation, a linear generator is selected.

6.2 Requirements to the Harvesting Module

The requirements for the energy harvesting system component are derived from the operating conditions and the power requirements of the monitoring system. Since wave excitation is highly dependent on prevailing weather conditions, there are changing operating conditions for the WEC. Therefore, an operating sea state is defined by a Pierson-Moskowitz sea spectrum (cf. appendix A.4.1) with a peak frequency of 1 $\frac{\text{rad}}{\text{s}}$ and a significant wave height of 2 m to allow reasonably comparable conditions. Details on harmonic waves and the definition of irregular sea states are described in detail in appendix A.4.1. The considered operating spectrum describes a sea state with a realistic power density for e.g. the North Sea at times when wind is present. To compensate for weather conditions with lower power output on time average, the power output in the operating spectrum must be larger than the required average power. To enable a holistic power consideration, operating spectra with lower power density are also used in the following development.
The power consumption of the measurement electronics is discussed in the previous chapter. Depending on the frequency of the measurement and the transmission setup, the typical average power consumption of the platform ranges from 1 mW to 50 mW. Thus, the energy harvesting method to be developed must provide sufficient power output to meet the average power consumption. Continuous supply from energy harvesting must be possible throughout the year without using energy storage that results in exceeding the weight, size, or cost requirements.
The system-level requirements (cf. table 8) are inherited to the subsystem under consideration. In terms of housing, the focus is on drifters deployed in coastal waters or shallow seas such as the North Sea. This requires a compact drifter outline with a short drogue due to the low water depths. The external appearance of the drifter should hardly be affected by the harvesting method used. Following typical drifter dimensions (cf. section 2.4), the buoy diameter and draft should be less than 50 cm and the total mass less than 5 kg to allow easy handling on ships during deployment. Given the general requirement for a low-cost device, a simple and easy-to-manufacture design is key to this development.

#	Description	Value	Rating
Operating conditions			
W01	Operate in North Sea typical wave frequencies	~ 0.5 to $1.5\,\frac{\text{rad}}{\text{s}}$	M
W02	Operate in North Sea typical wave amplitudes	~ 1 to $2\,\text{m}$	M
W03	Operate in realistic irregular wave spectra	-	M
W04	Operate in North Sea typical depths	$> 2\,\text{m}$	M
Power rating			
W05	Provide sufficient average output power	$> 50\,\text{mW}$	M
W06	Provide DC-voltage supply to monitoring system	3 to5 V	M
W07	Contain storage that ensures gap-free operation	-	M
Inherited from system-level requirements (cf. table 8)			
	...		
D07	Low storage to deployment assembly time	< 5 minutes	O
D08	All components shall fit into compact drifter housing	$< \varnothing 50\,\text{cm} \times \text{h}15\,\text{cm}$	M
D09	Deployment-ready storage area shall not exceed housing diameter	$< \varnothing 50\,\text{cm}$	O
D10	The total system weight should be suitable for handling by one person	$< 10\,\text{kg}$	M
	...		
D13	Total cost of the monitoring system	< 1000€	M
D14	System shall qualify for manufacturing of large quantities	< 1000 pcs.	O
	...		

Table 19: *Requirement list of the wave energy harvesting system; Rating: Mandatory (M), Obligatory (O).*

6.3 Model-Based Design Approach and Methodology

The development approach for the wave energy harvesting system is presented in the following. The key decision steps for the here conducted model-based development are outlined and the structure of this chapter is presented.

6.3.1 Functions and Components of the Wave Energy Harvester

For a systematic development approach, the function tree of the wave energy harvesting system is identified (cf. figure 69).

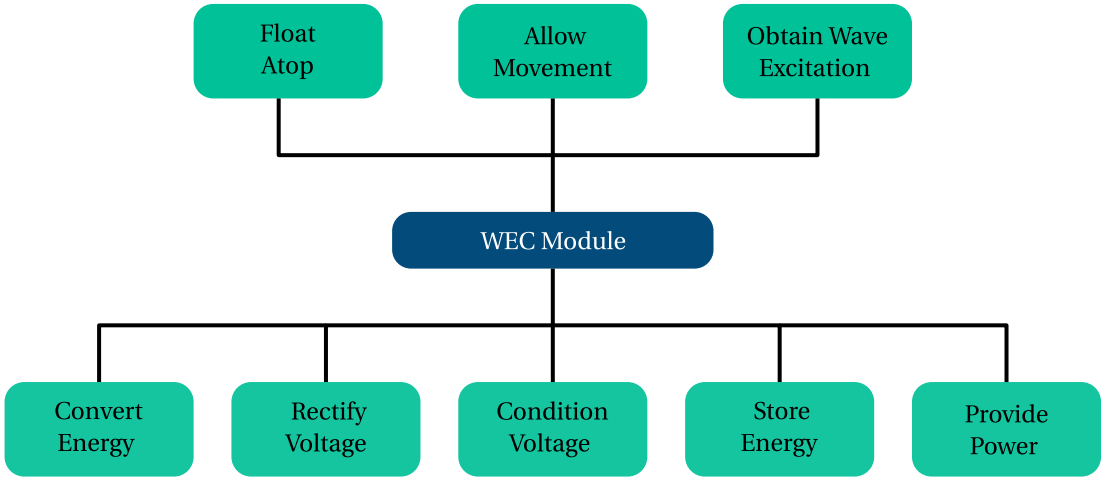

Figure 69: *Function tree of the WEC module.*

The WEC module describes the entire system, starting with the ability to float and ending with the power supply of the monitoring system (*Provide Power*). All functions can be implemented by three main components, presenting the structure of the following development. All mechanical functions are implemented by the SRPA-component, which must be designed to allow relative motion between buoy and drogue and optimized to obtain optimal wave excitation. A second component of the system is the power takeoff, converting mechanical energy into electrical energy through an electromagnetic generator. Finally, the output of the generator must be rectified, conditioned, and stored to provide power to the monitoring system. This is provided by the rectification and charging circuit. In the following, all the components are considered separately but the interdependence between them needs to be considered (cf. figure 70).
The mechanical dynamics function converts the hydrodynamic forces due to the waves into a relative motion between the float and the plate. This component must take into account the electromagnetic damping described by the power take-off. The power take-off has the task of converting the relative motion into an electrical potential that

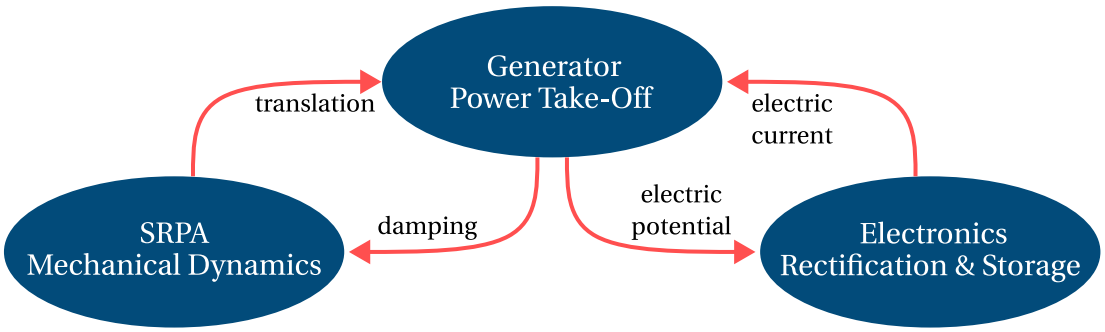

Figure 70: *Components of the WEC and indication of their mutual dependencies.*

is fed to the rectification and charging circuit. The rectification and charging circuit defines the electrical load, which in turn affects the electromagnetic damping and thus the dynamics of the mechanical system. The design of the WEC presented here follows a systematic development approach that takes into account the interaction between all sub-components.

6.3.2 Approach to Model-Based Development of Multi-Physic Systems

The design of the system under development calls for considerations in the physical domains of Mechanics, Electromagnetics, and Electronics. While designing and optimizing components individually is logical, it is critical to consider the interconnections between them. Thus, a methodical development approach that considers system coupling in the optimization process is essential.
In model-based development, this implies that individual component models are created first and subsequently integrated to simulate the behavior of the entire system. In this way, the influences from different areas can be taken into account. For the model coupling, interfaces must be found that describe the interaction of the systems. For the problem considered here, the model interfaces can be represented by figure 71.
In addition to the three components of the mechanical system, the generator, and

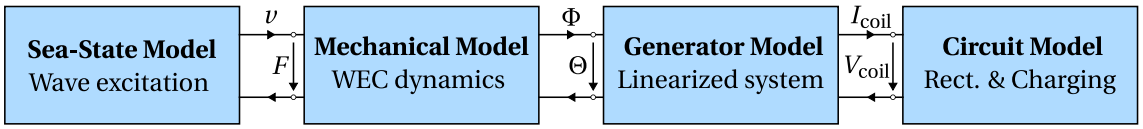

Figure 71: *Block diagram of the coupled simulation model considering the wave excitation, WEC mechanics, generator electromagnetics and the charging electronics.*

the electrical circuit, the sea-state model describes the wave excitation of the system. The interfaces of the model are defined using a physical modeling approach with cross

(potential) and through (flow) variables. The sea state model (cf. appendix A.4.1) describes the excitation by the waves and uses the force and velocity variables to couple with the mechanical model. The WEC response to the wave excitation is described by the mechanical model, which simulates the equations of motion of eq. (43) and the generator forces that depend on the velocity. The coupling between the mechanics and the electromagnetic generator is described in the magnetic domain by the variables of magnetic flux and magnetomotive force. The generator model describes the relationship between the change in magnetic flux and electric power. The interface to the circuit model is therefore given by the variables voltage and current. The connected circuit model simulates the behavior of the electrical load, completing the simulation of the WEC module.

6.3.3 Simulation Tools and Modelling Concept

To simulate a multiphysics system and the interaction of different domains, a thoughtful choice of simulation tools is required. Building a multiphysics finite element method (FEM) simulation model that incorporates fluid simulation, mechanical structure interaction, and electromagnetic field-level simulation for the entire system is feasible, but it would result in a highly complex model with a solution time disproportionate to the information obtained. It is therefore important to decide for each individual model what level of detail is required and where simplifications can be made.
To assess the level of detail in a model, validation is necessary. The most effective way to validate a model is by comparing simulation results with experimental results from implemented prototypes. The model should be validated for a range of parameters to guarantee that it is not only locally accurate, but accurately describes the full operating range of the system.
For the system considered here, the level of detail required for each model of figure 71 can be evaluated. Several references modeling the behavior of an SRPA in harmonic waves [218–220] have shown that a conventional equation-based model is sufficient for the system description. The model exhibits only small nonlinearities and can therefore be described by a set of differential equations. In the context of this work, simulation models with excitation by irregular waves will be used to obtain a realistic estimate of the actual system behavior in the ocean. Therefore, further model validation is required to confirm the validity of an equation-based simulation model for irregular wave excitation. All simulations in irregular waves must consider long time periods to represent the entire wave spectrum. Therefore, the following simulation results for irregular waves consider a duration of at least one hour.
For the development of the generator, a more detailed model description is required, allowing the geometrical influence of the flux-carrying elements on the magnetic field plane to be investigated. Due to the stray fluxes and nonlinear saturation effects that

occur, a conventional one-dimensional equation-based modeling approach may not be sufficient. A more detailed description of the magnetic properties of the generator can be implemented using a permeance network model. A permeance network is a representation of a magnetic network based on an equivalent electrical circuit. Geometric and material properties are represented by permeances, the reciprocal of magnetic resistances, and can be connected either in parallel or in series to represent the outline of a magnetic system. The drawback of this approach is that when geometries change, it is difficult to represent leakage fluxes because the influence of many geometric parameters is unknown. However, such a model is of limited use for generator geometry design. The influence of the geometries on the flux leakage is unknown and the model must be revalidated for each parameter variation. An even higher level of detail is provided by an electromagnetic FEM simulation model, that allows spatial resolution of the fields. Here, the FEM simulation is created using the AC/DC module of the COMSOL Multiphysics software. A parameterized model is developed that allows changing geometric and electrical system parameters. This enables a parametric analysis to optimize the system geometry.
The electrical load for the generator is given by the rectification and charging circuit and can be described by a simple equation-based model, as is common for electrical circuits. Electrical networks can usually be represented as linear models and are therefore well suited for equation-based modeling. Challenges arise only in the representation of realistic diodes since these models usually have a high model stiffness.
There are several approaches for coupling the individual models to the overall model represented in figure 71. It is possible to connect the FEM model of the generator directly with the equation systems of the remaining model descriptions. In the FEM simulation, the motion of the generator would then be excited by the sea state and the SRPA model, and the electrical circuit would simulate the load for the generator. However, this approach still requires a large computational effort, especially since long simulation periods must be considered for irregular sea state. Therefore, the question arises whether a field-resolved simulation of electromagnetics is still necessary for the overall system analysis or whether a reduced-order model can provide a sufficient description of the overall behavior. The reduced-order model can be a simplified equation-based model description that allows for rapid simulation when coupled as a whole system. The derivation of this model and validation is performed in section 6.5.

6.3.4 Structuring Parallel Design and Optimization

To describe the parallel development approach of all three components, figure 72 displays the development structure, organized by the following section titles. The intro-

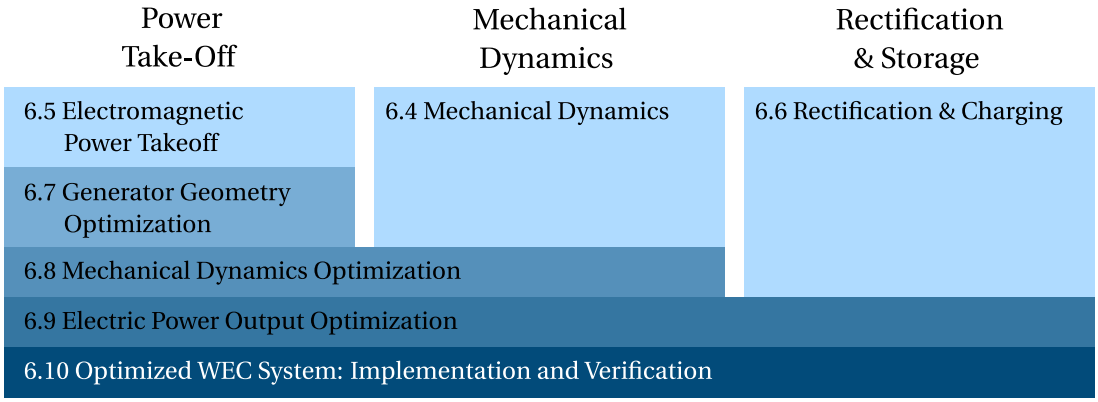

Figure 72: *Titles of the following sections that structure the development steps for a parallel design of the WEC mechanics, power takeoff and charging circuit.*

duced Multi-Physics simulation of figure 71 is gradually built up by first deriving the equations of motion of the SRPA in section 6.4 to define the mechanical system behavior. In this section, the model description is also validated by an experimental implementation before the generator concept is selected for power extraction in section 6.5. In section 6.6, the concept of the rectification and charging circuit is derived. After the individual consideration of each sub-component, the outline of the overall system is more clear, allowing to optimize the electromagnetic geometry of the generator in section 6.7. The geometry optimization is based on a parametric FEM simulation, that compares the open circuit voltage for a constant velocity. From the parametric analysis, a set of generator geometries is selected and the open circuit voltage of the coupled model of mechanics and generator is evaluated. This allows the performance comparison for the excitation with different sea states. After the selection of the best-performing generator, a coupled simulation for the optimization of the mechanical dynamics is performed in section 6.8. This allows taking the electromagnetic damping from the generator into account of the overall system damping. Finally, the electric domain of the charging circuit is coupled with the optimized mechanics and generator to improve the overall power output of the system section 6.9, by matching the load condition to the generator's supply. The model-based development is concluded by a total power estimation of the optimized system in section 6.10.3.

6.4 Mechanical Dynamics of the Wave Energy Harvester

In order to describe the conversion of the wave excitation into the motion dynamics of the system, this chapter describes the derivation of the equations of motion of the SRPA implemented into a drifter. As a result, a model of the mechanical dynamics is presented, that allows to take into account the influences of the water waves as well as the generator's damping. In an earlier publication of the author [224] the development was discussed in detail. To allow an analytic description of the system, the outer appearance

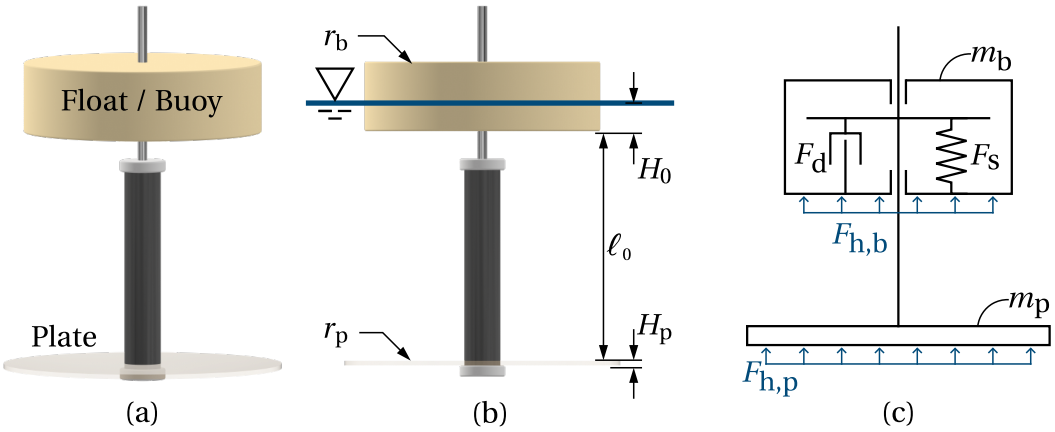

Figure 73: *a and b: Simplified 3D-model of the WEC considered for the model description with: Labels for float and plate (a) and important geometric parameters (b); c: Simplified mechanical model, visualizing the hydrodynamic forces as well as the connection of float and plate by a spring and damper.*

of established, compact drifter designs (cf. section 2.4) is simplified to the construction shown in figure 73a. The adaptation consists of the float - a cylindrical buoy - connected to a submerged circular plate representing the drifter's drogue, acting as the reacting body. This design reduces the model complexity by neglecting the influence of the vertical plates on the vertical motion. This assumption is sufficient since the model only considers the heave motion of the buoy and plate and neglects any pitch of the WEC in the waves. It is assumed that the drogue provides sufficient stability so that the effects of pitch motion are negligible for a first estimation. The model description will be used for an estimate of possible power outputs and to understand the influence of important system parameters on performance. The findings can be considered in the development of the final drifter design.

6.4.1 Deriving the Equations of Motion

Figure 73b shows the parameter description of the considered system on still water surface. The float and the plate are connected by the connecting rod running through the buoy, which is suspended on a spring. Buoy, connection rod and plate have the circular radii of r_b, r_c and r_p respectively. The distances between water surface and the lower boundary of the float is given by H_0, between float and plate by ℓ_0 and the thickness of the plate is H_p. Figure 73c shows a simplified mechanical model description of the connection between the two bodies by a spring and a fixed damper. The float and plate, have the masses m_b and m_p respectively and the influence of the water waves on the two component WEC are described by the hydrodynamic forces $F_\mathrm{h,b}$ and $F_\mathrm{h,p}$ acting on their surfaces. The total damping of the system is a combination of the mechanical friction and the power takeoff, which extracts energy from the relative motion. The equations of motion can be described by the sum of the acting forces with [224]:

$$\begin{aligned} m_\mathrm{b}\ddot{\xi}_\mathrm{b} &= -m_\mathrm{b}g + F_\mathrm{s} + F_\mathrm{d} - \lambda_\mathrm{exp,b}\cdot\dot{\xi}_\mathrm{b} + F_\mathrm{h,b} \\ m_\mathrm{p}\ddot{\xi}_\mathrm{p} &= -m_\mathrm{p}g - F_\mathrm{s} - F_\mathrm{d} - \lambda_\mathrm{exp,p}\cdot\dot{\xi}_\mathrm{p} + F_\mathrm{h,p} \end{aligned} \tag{40}$$

whereby ξ is the heave displacement of the buoy (index b) and plate (index p) with respect to the equilibrium position in still water; g is the gravitational acceleration; λ_exp is the respective tuning parameter to adjust the simulation to experimental results. The spring and damping forces are described by F_s and F_d. To be able to model the system dynamics for harmonic and irregular waves, the hydrodynamic forces need to be calculated for each wave excitation as described in appendix A.4.2. By assuming a linear stiffness constant K_s the spring force F_s is derived from the relative position $\Delta\xi$ (cf. figure 68):

$$\Delta\xi = \xi_\mathrm{p} - \xi_\mathrm{b} \tag{41}$$

$$F_\mathrm{s} = F_0 + K_\mathrm{s}\Delta\xi \tag{42}$$

with F_0 being the force of the spring at equilibrium in still water. Substituting eq. (42) in eq. (40), and accounting that $\vec{F}_\mathrm{h}$ is a force vector depending on $\vec{\xi}$ and its derivatives, the resulting equations of motion can be stated as:

$$\begin{aligned} &\vec{F}_\mathrm{h}(\vec{\xi},\dot{\vec{\xi}},\ddot{\vec{\xi}}) = \\ &\begin{bmatrix} m_\mathrm{b} & 0 \\ 0 & m_\mathrm{p} \end{bmatrix}\begin{pmatrix} \ddot{\xi}_\mathrm{b}+g \\ \ddot{\xi}_\mathrm{p}+g \end{pmatrix} + \begin{bmatrix} \lambda_\mathrm{exp,b} & 0 \\ 0 & \lambda_\mathrm{exp,p} \end{bmatrix}\begin{pmatrix} \dot{\xi}_\mathrm{b} \\ \dot{\xi}_\mathrm{p} \end{pmatrix} + \begin{bmatrix} K_\mathrm{s} & -K_\mathrm{s} \\ -K_\mathrm{s} & K_\mathrm{s} \end{bmatrix}\begin{pmatrix} \xi_\mathrm{b} \\ \xi_\mathrm{p} \end{pmatrix} - \begin{pmatrix} F_0 \\ -F_0 \end{pmatrix} - \begin{pmatrix} F_\mathrm{d} \\ -F_\mathrm{d} \end{pmatrix}. \end{aligned} \tag{43}$$

The damping Force F_d consists of the electrical damping $F_\mathrm{d,el}$ and the mechanical

damping $F_{\mathrm{d,mech}}$:

$$F_{\mathrm{d}} = F_{\mathrm{d,el}} + F_{\mathrm{d,mech}} \tag{44}$$

Where the velocity dependent damping force due to friction is described by [224]:

$$F_{\mathrm{d,mech}} = D_1(\dot{\xi}_{\mathrm{p}} - \dot{\xi}_{\mathrm{b}}) + D_2|\dot{\xi}_{\mathrm{p}} - \dot{\xi}_{\mathrm{b}}|(\dot{\xi}_{\mathrm{p}} - \dot{\xi}_{\mathrm{b}}) + D_3(\dot{\xi}_{\mathrm{p}} - \dot{\xi}_{\mathrm{b}})^3 \tag{45}$$

Thereby, the coefficients D_1, D_2, and D_3 are determined by means of free decay tests. The electrical damping force $F_{\mathrm{d,el}}$ resulting from energy harvesting, is a nonlinear force depending on the relative position $\Delta\xi$, and relative velocity $\Delta\dot{\xi}$. With the nonlinear damping, the equations of motion in eq. (43) become nonlinear as well.

6.4.2 Validating the Description of Mechanical Dynamics Model

The derived mechanical system behavior is validated by experiments. In the following the prototype system shown in figure 74a is considered, which allows to measure the motion of the system in different water waves. To be comparable to a drifter, the dimensions from table 20 were selected as a first guess for a working WEC. The experimental setup is build without any power takeoff and therefore neglects the nonlinear electrical damping force $F_{\mathrm{d,el}}$ from eq. (44).

r_{b}	r_{p}	r_{c}	m_{b}	m_{p}	H_{p}	ℓ_0	K_{s}
0.1275 m	0.149 m	0.0195 m	1.446 kg	1.962 kg	5 cm	0.291 m	209 $\frac{\mathrm{N}}{\mathrm{m}}$

Table 20: *Values of the experimental prototype setup.*

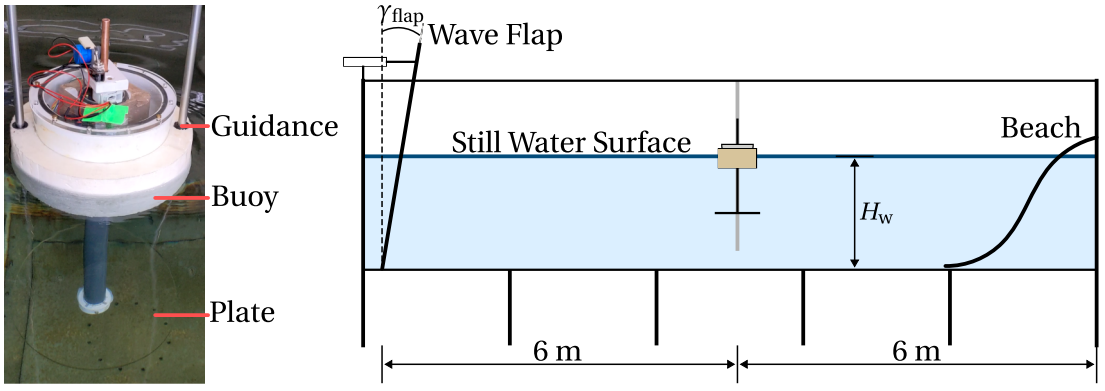

Figure 74: *a: Experimental setup of the WEC prototype, with visualization of the guidance rods; b: Sketch of the used fave flume, with visualization of the wave flap, and experiment positioning.*

For the exciation of the WEC with different water waves, the wave flume of the Institute of Mechanics and Ocean Engineering at Hamburg University of Technology is used. The facility, depicted in figure 74b, can generate harmonic and random waves by the back and forth motion of the wave flap. By the adjustment of the flap angle γ_{flap} and the flap frequency f_{wave}, the wave parameters can be adjusted. Maximum angles and further details can be found in appendix A.4.3. A beach at the end of the wave flume reduces the reflection of the water waves. For all flowing experiments, the water depth was set to $H_{\text{w}} = 1.06\,\text{m}$ and the prototype setup is placed with a distance of 6 m to the flap. Vertical guidance rods are used, to restrict the pitch movement of the WEC prototype, which adds nonlinear friction forces $F_{\text{d,guidance}}$ to the buoys dynamic:

$$F_{\text{d,guidance}} = -D_{1,\text{g}}\dot{\xi}_{\text{b}} - D_{2,\text{g}}|\dot{\xi}_{\text{b}}|\dot{\xi}_{\text{b}} - D_{3,\text{g}}\dot{\xi}_{\text{b}}^{3}. \tag{46}$$

The resulting damping force $F_{\text{d,total}}$, includes the damping between the two bodies F_{d} and the guidance force:

$$F_{\text{d,total}} = \begin{pmatrix} F_{\text{d}} + F_{\text{d,guidance}} \\ -F_{\text{d}} \end{pmatrix}, \tag{47}$$

whereby F_{d} is given by eq. (44) and eq. (45). To allow a comparison between the simulation results and the experiment, the extended damping force is implemented in the equations of motion from eq. (43). All damping coefficients are determined by a free decay test and a parameter fitting as shown in table 21.

D_1	D_2	D_3	$D_{1,\text{g}}$	$D_{2,\text{g}}$	$D_{3,\text{g}}$
$36.2180\,\frac{\text{kg}}{\text{s}}$	$-289.6304\,\frac{\text{kg}}{\text{m}}$	$590.8650\,\frac{\text{kgs}}{\text{m}^2}$	$7.4556\,\frac{\text{kg}}{\text{s}}$	$-17.7224\,\frac{\text{kg}}{\text{m}}$	$11.9825\,\frac{\text{kgs}}{\text{m}^2}$

Table 21: *Damping parameters of the experimental setup.*

In order to derive the experimental correction parameters λ_{exp}, further experiments were conducted. Here again, a parameter fitting is used to adjust the simulated relative motion to the measured data. The tuned simulation model approximates the experimental data very well. Figure 75 shows the results of an experiment in harmonic waves (cf. appendix A.4.1) at a flap angle of $\gamma_{\text{flap}} = 35°$ and an excitation frequency of $f_{\text{wave}} = 0.45\,\text{Hz}$. The position of the water surface is measured by capacitive sensors in the wave flume and the relative position between float and plate is determined by a potentiometer displacement measurement implemented in the prototype. The selected correction parameter for the givin prototype are:

$$\lambda_{\text{exp,b}} = 110.9337\,\frac{\text{kg}}{\text{s}},\ \ \lambda_{\text{exp,p}} = 8.5299\,\frac{\text{kg}}{\text{s}} \tag{48}$$

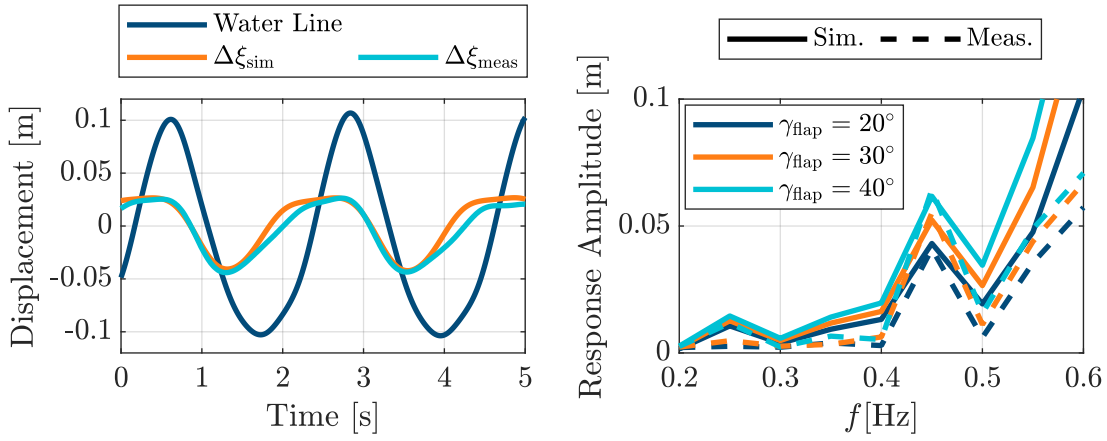

Figure 75: *Comparison of simulation (sim.) and measurement (meas.) data for the relative displacement of the WEC in regular waves (left) and the maximum amplitude of relative motion between buoy and plate for different flap angles γ_{flap} and wave frequencies f_{wave} (right).*

To determine whether the parameterized model is valid for other wave configurations, a series of experiments is compared to simulation data. Figure 75 shows the corresponding measured maximal amplitude of the relative motion for different flap angles and wave frequencies. The comparison visualizes, that for frequencies lower than $f_{\text{wave}} = 0.5\,\text{Hz}$, the model closely approximates the measured relative motion. With higher frequencies, the model becomes inaccurate since the prototype in the experiment reaches its physical limits and gets submerged by waves while the simulation can move without constraints. Typical seawater waves considered here are unlikely to occur at higher frequencies than $f_{\text{wave}} = 0.5\,\text{Hz}$, which proves the derived model from eq. (43) to be appropriate and valid for the simulation of the WEC motion dynamics.

Finally the derived model can be used, to simulate the system response to a realistic random sea surface (cf. appendix A.4.1). The system response is evaluated for the defined operating sea spectrum (a Pierson-Moscowitz spectrum with peak Frequency $\omega_{\text{P}} = 1\,\frac{\text{rad}}{\text{s}}$ and significant wave height of $H_{\text{s}} = 2\,\text{m}$) and the probability of the occurring relative velocities is determined. For the simulation, the same system parameters as those from the experiment are used. Figure 76 shows the normalized histogram for the probability of different relative velocities with an interval size of $0.01\,\frac{\text{m}}{\text{s}}$. It can be seen, that the highest probability for the relative velocity is around $0.1\,\frac{\text{m}}{\text{s}}$ and the range of velocities lies between 0 and $0.3\,\frac{\text{m}}{\text{s}}$. It has to be taken into account, that the considered prototype is not yet optimized and therefore shows a poor system response. In section 6.8, the system dynamics is optimized to increase the probability of velocities above $0.3\,\frac{\text{m}}{\text{s}}$ for the operating spectrum and generally the system response for spectra with lower frequencies. From the system analysis, the operating point for the linear generator can now be derived, which will be considered in the next section. Assuming that the system dynamics can be improved by the subsequent optimization, the linear

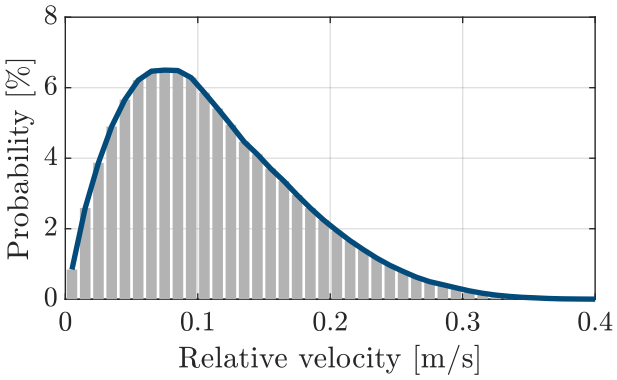

Figure 76: *Normalized histogram of the simulation results for the relative velocity of a WEC with parameters from the experiment in the operating spectrum ($\omega_P = 1\,\frac{rad}{s}$; $H_s = 2\,m$). The histogram intervals for the velocity are* $0.01\,\frac{m}{s}$.

generator should be designed for speeds between 0.1 and $0.3\,\frac{m}{s}$. The available forces depend on the masses of the two bodies and the acceleration between them. From the simulation of the prototype it is foreseeable that forces around 10 N can be achieved even for the non-optimized WEC. A broader analysis of the system response for different peak frequencies ω_P is conducted in section 6.8 to better evaluate the optimization results derived in the same section.

6.5 Electromagnetic Power Takeoff: Generator Concept and Model Description

Having derived and validated the equations of motion, this section focuses on the power takeoff of the WEC. In order to meet the previously described requirements, an electromagnetic direct drive linear generator is considered. In addition to the given operating point, further requirements arise from the overall size of the drifter, which should not be exceeded. The primary armature - the stator - of the generator to be developed, should not exceed a length of 20 cm and a diameter of 10 cm to fit into the drifter's housing. The length of the secondary armature - the translator - is determined in section 6.8, as soon as the response amplitude of the optimized system is determined. As the overall requirements are aimed for an affordable system, same must also be considered for this module. The manufacturing and therefore the construction of the generator should be kept as simple as possible.
In this section, the generator principle is selected from different linear generator types and first design considerations for a small size system are derived. Two generator models will be introduced, which are used in the development process. A parameterized FEM simulation allows the electromagnetic design, and a reduced order model description enables coupling to the mechanical WEC model. First analytic design considerations are developed and validated by the FEM results and an prototype implementation.

6.5.1 Review and Selection of Generator Architecture

Different linear generator types are used for the power-takeoff in wave energy convert systems. For all of them, the functionality at low translation speeds and high thrust forces is a critical design factor [225]. The most common principles[226] can be sorted in two categories with several subcategories:

1. Synchronous permanent magnet linear machine (SPMLM)
    - Double sided
    - Halbach configuration
2. Reluctance linear machines
    - Variable reluctance permanent magnet linear machine (VRPMLM)
    - Vernier Hybrid Machine
    - Synchronous permanent magnet linear machine (SPMLM)
    - Flux switching permanent magnet linear machine (FSPMLM)

Commonly used as a motor, the **synchronous permanent magnet linear machine (SPMLM)** can also be found as generator in WEC-Systems. Especially with its adaptation as double-sided generator [227] or with Halbach array configuration [228], the SPMLM has proved itself for systems with large power outputs. With their generally more complex structure on the other hand, SPMLM are rather unsuitable for low-cost applications [226].

Reluctance linear machines have a more simple nature and can be implemented in low-cost designs, while offering high efficiencies at low speed [226]. Reluctance machines are working based on the reluctance forces of either the transverse or longitudinal effect [229]. While the variable reluctance permanent magnet linear machines (VRPMLMs) [230] requires permanent magnets on the translator, the related venier hybrid machine [225] requires magnets on the stator. In general, for cost and manufacturing reasons, it is preferable to place the permanent magnets on the primary unit. However, the Venier Hybrid machine requires a complex stator design, which cannot be implemented cost-effective in a compact design. Switched reluctance linear machines (SRLMs) do not require any permanent magnets and therefore have a passive translator, which allows low-cost designs [229]. Due to missing permanent magnets the SRLM requires active coil switching control, which makes this approach unsuitable for low power applications. A possible solution, which combines a passive translator, permanent magnets on the primary, a simple design and still allows high switching frequencies at low translator speed, is the flux switching permanent magnet linear machine (FSPMLM). Rauch et al. [231] first introduced the design principles and optimization of flux switching rotary machines [232, 233]. Later, linear applications considered tubular [234–236] and planar [237, 238] linear machines. Tubular FSPMLM are due to its high power density and efficiency [239] better suited for the compact application considered here. The design can be kept simple, to allow an affordable construction, which at the same time is easy to integrate into the Drifter's housing. Therefore, the selected concept for the power takeoff is a tubular FSPMLM, which will be designed in the following.

6.5.2 Generator Structure and Parameterization

Figure 77a shows a sectional view of the FSPMLM design considered here, consisting of the stator and translator armature. The Coils and magnets are arranged inside the stator slots, while the passive translator has a regular arrangement of translator poles. The functionality of an FSPMLM is described in several publications [231, 240, 241] and can be explained using the sketch of figure 77b. The sketch displays the magnetic flux direction for the current translator position. Is the translator moved by half of the pole pitch τ_p the flux direction through the coil changes due to an opposed orientation of the

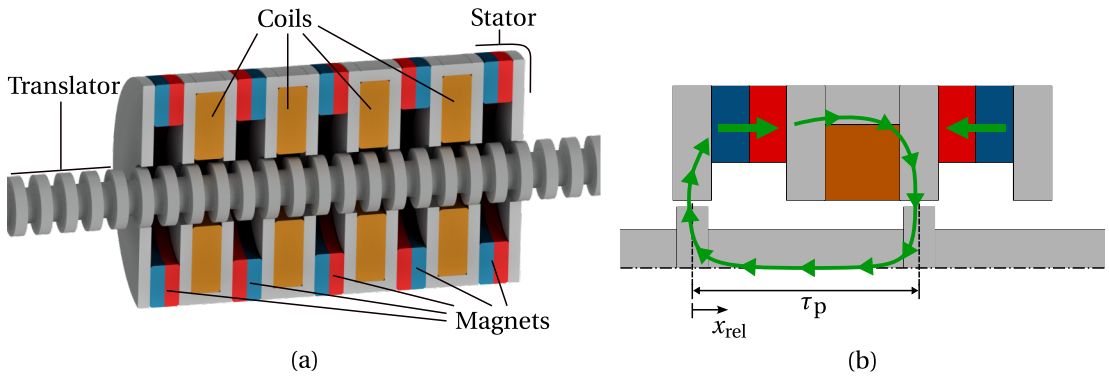

Figure 77: *a: 3D sectional view of an FSPMLM with a description of its components; b: Simplified sketch of one stator segment of the FSPMLM with visualization of the magnetic flux direction (green).*

permanent magnets. Another movement by half of the pole pitch returns the translator to the initial state and a full period is completed. The continuous movement induces an alternating electromotive force (EMF) in the coil. The induced frequency depends on the speed of the translator and the selected pole pitch. The number of coils and the translator pitch for large-scale FSPMLM is typically designed for three-phase operation with a 120° phase shift [234, 242]. For the small-scale harvesting application considered here, a three-phase current is not a requirement. The design can therefore be chosen to maximize the power output while allowing to fit into the drifters dimensions.
The coordinate of the translator movement is described by x_{rel} (cf. figure 77), which describes the translator movement relative to the pole pitch τ_{p}. x_{rel} is always in the range of $[0 \ldots \tau_{\mathrm{p}}]$ and can be derived from the relative movement $\Delta\xi$ of the WEC by:

$$x_{\mathrm{rel}} \equiv \Delta\xi \mod \tau_{\mathrm{p}} \tag{49}$$

while the relative velocity of the translator v_{rel} is equal to the parameter $\Delta\dot{\xi}$. To be able to compare translator geometries with different pole pitch values τ_{p} in the following, the coordinate x_{rel} is often normalized by the pole pitch τ_{p}, which gives the relative movement $x_{\mathrm{rel}}/\tau_{\mathrm{p}}$ in the range of $[0 \ldots 1]$.
In figure 77, the translator is shown in a stable position with zero longitudinal forces. A movement of the translator from this position increases the resistance of the air gap, resulting in an increase of stored energy in the air gap, and thus a force is opposing the movement. Upon reaching half the translator pole-pitch, the translator engages the next stator tooth magnetically, resulting in a longitudinal force toward the direction of movement. These alternating axial forces are referred to as cogging forces and are unavoidable in reluctance machines. The aim of the development is to reduce cogging forces as much as possible in order to provide the mechanical system with the lowest possible damping.

All parts of the generator are designed for easy manufacturing, which allows to keep the generators construction as simple as possible. This also reduces the number of geometric parameters, since complex shapes for improved flux guidance are not considered. Figure 78 shows an overview of the most important geometric parameters, and their discription used in the following. The stator teeth are simple disks with the

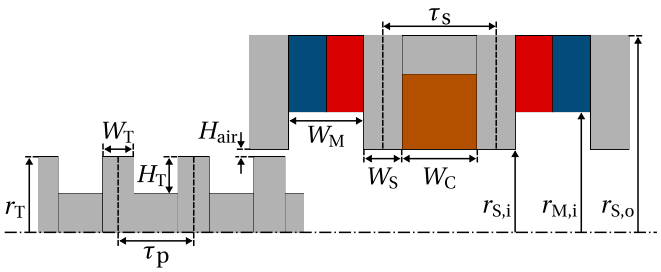

Figure 78: *Geometric parameter of the generator concept displayed for stator and translator dimensions.*

thickness W_S, inner radius $r_{S,i}$ and outer radius $r_{S,o}$. In between the stator disks, the magnets and coils are placed. Since the manufacturing and magnetization of permanent magnets is a cost intensive process, off-the shelf, low-cost magnets shall be used. Taking into account the available installation space, a commonly available magnet with the dimensions given in table 22 is selected. All remaining geometric parameters

Outer radius $r_{S,o}$	Inner radius $r_{M,i}$	Width W_M
20 mm	12.5 mm	5 mm

Table 22: *Dimensions of the selected permanent magnet.*

are derived during the development based on the selected magnet dimensions. The magnet also determines the coil width since the stators slot pitch has to be regular, and therefore $W_M = W_C = W_{CM}$. The translator consists of rectangular poles of the width W_T and height H_T. The translator radius r_T determines together with the height of the air gap H_{air} the inner stator radius $r_{S,i}$.

6.5.3 Deriving the Generator Model: Varied Resolution and Model Order

For the model description of the generator, two approaches are selected with different level of detail. An FEM simulation model is used for geometry optimization on the magnetic field level. A reduced order model using the simplified physics approach

[243] is derived for a traditional equation-based model of the system. While the FEM simulation can be used to create a generator geometry, the parameters of the reduced-order model must be redetermined for each new geometry.

Magnetic Field Level Finite Element Method Simulation An FEM-simulation model is used in the first part of the generator design, to analyze the geometry of the generator with a spatial resolution of the magnetic field. The majority of the presented simulation results are the transient solution of a 2D rotational symmetric model, created with COMSOL Multiphysics (cf. figure 79). The generator model is implemented with

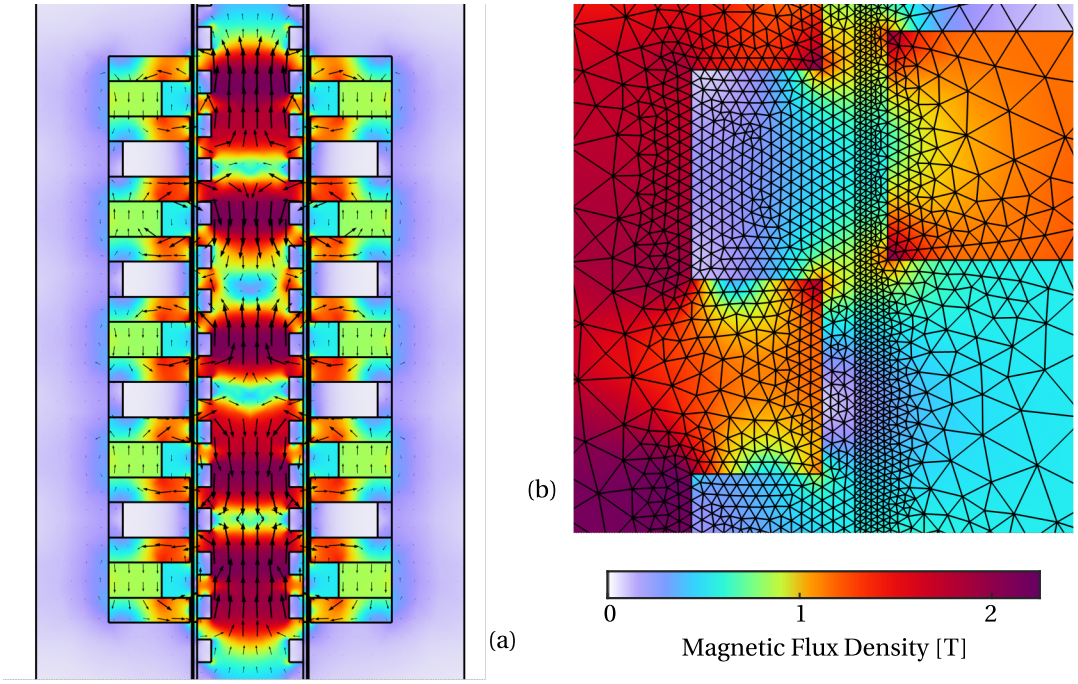

Figure 79: *a: FEM simulation results, visualizing the magnetic flux density of a generator geometry; b: Visualization of the applied meshing resolution.*

variables for the geometric parameter to allow parametric sweep analysis.
The selected materials for the generator are modeled with a nonlinear B-H-curve to take into account saturation effects. Eddy current effects are simulated for all conducting materials. The axial cogging forces are calculated by a volume integral over the Maxwell stress tensor. An accurate estimation requires a well-considered mesh for the air gap and integration volume. The applied meshing can be seen in figure 79b.

The simulation of system behavior in random waves requires the consideration of long time series to allow estimates of the power output in certain sea states. A numerical FEM model is due to its level of detail and computational effort unsuitable for such

simulations. To enable a coupled simulation of the mechanical excitation and the electromagnetic generator in irregular waves, a model with reduced complexity is derived in the following.

Deriving the Simplified Physics Model Description The reduced order model describes the interaction of the electrical with the mechanical domain based on magnetic state variables. The model assumes a linear behavior for each discrete translator position but has an overall nonlinear behavior, due to position-dependent parameters. Different coil inductance values are e.g. determined for each translator position, which provides a linear model behavior for a constant position but considering the inductance for a full translator movement shows a nonlinear inductance parameter. All model parameters are derived from the FEM simulation for a set of discrete translator positions in the range of $x_{\mathrm{rel}} = [0 \ldots \tau_{\mathrm{p}}]$ (cf. figure 77). For a transient simulation of the reduced order model, the discrete parameters are interpolated for smooth simulation output results. In the following, the reduced order model of the generator is derived to describe the electrical and mechanical behavior of the generator.
The following derivation of the linear model description at first considers a single coil and a constant translator position x_{rel}. For a single coil, the total magnetic flux of the generator Φ_{total} consists of the leakage flux Φ_{s} and the coil flux Φ_{coil}, which passes through the coil completely:

$$\Phi_{\mathrm{total}} = \Phi_{\mathrm{coil}} + \Phi_{\mathrm{s}} \tag{50}$$

The flux through the coil Φ_{coil} is mainly influenced by the flux of the permanent magnets $\Phi_{\mathrm{PM}}(x_{\mathrm{rel}})$, which depends on the translator position and the flux damping induced by the load currents of the coil $\Phi_{\mathrm{c,damp}}$. When considering eddy currents in the translator and stator steel, the damping influence on the coil flux due to the eddy currents can be described by $\Phi_{\mathrm{E,damp}}$. The sum of the flux through the coil is given by:

$$\Phi_{\mathrm{coil}} = \Phi_{\mathrm{PM}} + \Phi_{\mathrm{c,damp}} + \Phi_{\mathrm{E,damp}} \tag{51}$$

The flux component $\Phi_{\mathrm{c,damp}}$ describes the flux induced by the coil current I_{coil} running through the coil inductance L_{coil}:

$$\Phi_{\mathrm{c,damp}} = I_{\mathrm{coil}} \cdot L_{\mathrm{coil}}. \tag{52}$$

For a detailed description of the eddy currents, a consideration of the field quantities like with the FEM model would be necessary. In the reduced order model derived here, only the influence of the eddy currents on the magnetic flux of the coils is taken into account. This property is described by $\Phi_{\mathrm{E,damp}}$ and can be considered as an equivalent coil, that shares the flux path with the actual generator coil. The equivalent eddy current

I_E arises from

$$I_\mathrm{E} = -\frac{\delta \Phi_\mathrm{E}}{\delta t} \cdot \frac{1}{R_\mathrm{steel}} \tag{53}$$

where Φ_E describes the flux component responsible for the equivalent current induced into the steel and R_steel describes the steel resistance. Applying eq. (52) to the equivalent inductance L_steel gives:

$$\Phi_\mathrm{E,damp} = -\frac{\delta \Phi_\mathrm{E}}{\delta t} \cdot \frac{L_\mathrm{steel}}{R_\mathrm{steel}} \tag{54}$$

If now the dependence of the fluxes on the translator position is considered, it can be assumed that the eddy current depends on the translator speed, since eq. (54) allows:

$$\Phi_\mathrm{E,damp}(x_\mathrm{rel}, t) = \frac{\delta x_\mathrm{rel}}{\delta t} \cdot \left(-\frac{\delta \Phi_\mathrm{E}(x_\mathrm{rel})}{\delta x} \right) \cdot \frac{L_\mathrm{steel}(x_\mathrm{rel})}{R_\mathrm{steel}}. \tag{55}$$

With

$$v_\mathrm{rel}(t) = \frac{\delta x_\mathrm{rel}}{\delta t} \tag{56}$$

$$\Phi'_\mathrm{E,damp}(x_\mathrm{rel}) = -\frac{\delta \Phi_\mathrm{E}(x_\mathrm{rel})}{\delta x_\mathrm{rel}} \cdot \frac{L_\mathrm{steel}(x_\mathrm{rel})}{R_\mathrm{steel}} \tag{57}$$

$\Phi_\mathrm{E,damp}(x_\mathrm{rel}, t)$ can be described by applying eqs. (56) and (57) to eq. (55):

$$\Phi_\mathrm{E,damp}(x_\mathrm{rel}, t) = v_\mathrm{rel}(t) \cdot \Phi'_\mathrm{E,damp}(x_\mathrm{rel}). \tag{58}$$

The damping of the magnetic flux through the coil, due to the eddy currents in the steel can therefore be described by the translator velocity and a position-dependent parameter $\Phi'_\mathrm{E,damp}(x_\mathrm{rel})$.
By applying eqs. (52) and (58) to eq. (51), a differential algebraic equation (DAE) can be derived:

$$\begin{aligned}
V_\mathrm{coil}(x_\mathrm{rel}, t) &= -N_\mathrm{coil} \frac{\delta \Phi_\mathrm{coil}(x_\mathrm{rel}, t)}{\delta t} \\
I_\mathrm{coil}(x_\mathrm{rel}, t) &= \frac{V_\mathrm{coil}(x_\mathrm{rel}, t)}{Z_\mathrm{load}(t)} \\
v_\mathrm{rel}(t) &= \frac{\delta x_\mathrm{rel}}{\delta t} \\
\Phi_\mathrm{coil}(x_\mathrm{rel}, t) &= \Phi_\mathrm{PM}(x_\mathrm{rel}) + I_\mathrm{coil}(x_\mathrm{rel}, t) \cdot L_\mathrm{coil}(x_\mathrm{rel}) + v_\mathrm{rel}(t) \cdot \Phi'_\mathrm{E,damp}(x_\mathrm{rel})
\end{aligned} \tag{59}$$

where N_coil stands for the number of coil turns, I_coil for the coil current and V_coil for the coil voltage. The variables V_coil and I_coil describe the interface to the electrical

domain, which allows to connect a load described by Z_{load}. To solve the DAE with respect to the state variables, the generator dependent parameters of N_{coil}, Φ_{PM} , L_{coil} and $\Phi'_{\text{E,damp}}$ need to be derived from the FEM model for a set of discrete points along the the translator position x_{rel} as described in the following paragraphs.

Determination of Coil Parameter Until now, only a single coil was considered. In order to describe a generator with several coils with the same model description, eq. (59) needs to be interpreted as vector equation, where $\vec{\Phi}_{\text{coil}}$, $\vec{V}_{\text{coil}}$ and $\vec{I}_{\text{coil}}$ represent vectors for the state variables of each coil and $\vec{L}_{\text{coil}}$ is the coil coupling inductance matrix. The inductance matrix consists of the coil inductance values $L_{i,j}$:

$$\vec{L}_{\text{coil}} = \begin{pmatrix} L_{1,1} & L_{1,2} & \dots & L_{1,n_{\text{s}}} \\ L_{2,1} & L_{2,2} & \dots & L_{2,n_{\text{s}}} \\ \vdots & \vdots & \ddots & \vdots \\ L_{n_{\text{s}},1} & L_{n_{\text{s}},2} & \dots & L_{n_{\text{s}},n_{\text{s}}} \end{pmatrix} \tag{60}$$

where all $L_{i=j}$ describe the coil inductance of coil i and all $L_{i\neq j}$ values describe the mutual inductance between coil i and coil j for a number of n_{s} coils.

To derive all generator parameters the FEM model is solved with a static solver configuration for the set of discrete translator positions $x_{\text{rel}} = [0 \dots \tau_{\text{p}}]$. For each position and each coil, the static magnetic flux through the coil i by the permanent magnets $\Phi_{\text{PM},i}$ is determined. To derive the coil inductance values, a constant current I_0 is applied to each coil separately and the corresponding magnetic flux $\Phi_{\text{coil},i,j}$ is derived, where the index i indicates the considered coil and j describes the coil excited with the current I_0. By subtracting the static flux $\Phi_{\text{PM},i}$ and dividing through the applied current, the inductance values can be calculated according to eqs. (51) and (52), since $\Phi_{\text{E,damp}} = 0$ in the static simulation:

$$\begin{aligned} \Phi_{\text{c,damp},i,j} &= \Phi_{\text{coil},i,j} - \Phi_{\text{PM},i} \\ L_{i,j} &= \frac{\Phi_{\text{c,damp},i,j}}{I_0} \end{aligned} \tag{61}$$

Consideration of the Eddy Effect To take into account the influence of the eddy currents on the magnetic flux of the coils, the values for the damping parameter $\Phi'_{\text{E,damp}}$ need to be determined from the FEM simulation. For that a transient simulation is conducted for a generator in open circuit configuration with constant translator speed of $v_0 = 0.5\,\frac{\text{m}}{\text{s}}$. The magnetic flux through each coil $\Phi_{\text{coil},i}$ is determined at the discrete translator positions $x_{\text{rel}} = [0 \dots \tau_{\text{p}}]$ and the static flux values $\Phi_{\text{PM},i}$ are subtracted.

According to eqs. (51) and (58) and since $\Phi_{\mathrm{c,damp}} = 0$ in open circuit configuration, the influence of the eddy currents on coil i is given by:

$$\begin{aligned} \Phi_{\mathrm{E,damp},i} &= \Phi_{\mathrm{coil},i} - \Phi_{\mathrm{PM},i} \\ \Phi'_{\mathrm{E,damp},i} &= \frac{\Phi_{\mathrm{E,damp},i}}{v_0} \end{aligned} \tag{62}$$

Electromagnetic Force Calculation The total forces of the generator $F_{\mathrm{d,el}}$ are the sum of the cogging forces, due to the longitudinal effect of the translator in the stators magnetic field F_{cog}, the damping due to the coil inductance F_{coil}, the damping due to the eddy current F_{eddy}:

$$F_{\mathrm{d,el}} = F_{\mathrm{cog}} + F_{\mathrm{coil}} + F_{\mathrm{E}} \tag{63}$$

The cogging forces are derived from the same static FEM simulation results, used to derive the static magnetic flux Φ_{PM}, for each discrete translator position $x_{\mathrm{rel}} = [0 \ \ldots \ \tau_{\mathrm{p}}]$. According to the conservation of energy approach, the forces due to the coil induction can be calculated from the induced electric power P_{coil} and the translator velocity v_{rel}:

$$P_{\mathrm{coil}} = \sum_{i=1}^{n_{\mathrm{s}}} V_{\mathrm{coil},i} \cdot I_{\mathrm{coil},i} \tag{64}$$

$$F_{\mathrm{coil}} = \frac{P_{\mathrm{coil}}}{v_{\mathrm{rel}}} \tag{65}$$

The force calculation due to the eddy currents, considers the equivalent coil from eq. (53), which allows to derive the induced power by the eddy currents with:

$$P_{\mathrm{E}} = \left(\delta \frac{\Phi_{\mathrm{E}}}{\delta t}\right)^2 \frac{1}{R_{\mathrm{steel}}} \tag{66}$$

$$F_{\mathrm{E}} = \frac{P_{\mathrm{E}}}{v_{\mathrm{rel}}} \tag{67}$$

Substituting $\frac{\delta}{\delta t}$ with $v_{\mathrm{rel}} \frac{\delta}{\delta x}$ in eqs. (66) and (67) allows derive a position dependent force parameter F'_{E} similar to the procedure from eq. (57):

$$\begin{aligned} F_{\mathrm{E}} &= {v_{\mathrm{rel}}}^2 \cdot \left(\delta \frac{\Phi_{\mathrm{E}}}{\delta x}\right)^2 \frac{1}{R_{\mathrm{steel}}} \frac{1}{v_{\mathrm{rel}}} \\ \Rightarrow F_{\mathrm{E}} &= v_{\mathrm{rel}} \cdot F'_{\mathrm{E}} \end{aligned} \tag{68}$$

The same FEM simulation used to calculate $\Phi'_{\mathrm{E,damp}}$ is now used to calculate F'_{E} from the derived values of F_{E} at the simulated velocity of $v_0 = 0.5\,\frac{\mathrm{m}}{\mathrm{s}}$:

$$F'_{\mathrm{E}} = \frac{F_{\mathrm{E}}}{v_0} \tag{69}$$

$$\tag{70}$$

Occurring friction forces from the bearing of the translator, can be considered in mechanical damping force $F_{\mathrm{d,mech}}$ from eq. (44).

6.5.4 Analytic Design Principles for FSPMLM

To adapt the FSPMLM geometry for a minimalistic, low-power harvesting approach, it is important to find ways to reduce cogging forces while increasing power output. This is achieved by deriving analytic design rules to optimize several geometric and electrical design parameters. This section considers the influences of various parameters on a physical level and derives design principles to reduce the number of free optimization parameters. Special focus is given to the relationship between the stator slot and translator pole arrangement.
So far, most WEC-applications that implemented FSPMLMs considered much larger systems with thrust forces in the range of several kilonewtons [239]. For the miniaturized system considered here, the working principle must be adapted while reducing the cogging forces and keeping sufficient EMF at low translator speeds.
One important step in the miniaturization is to increase the pole count of the translator (cf. figure 80) [244]. Compared to the regular pole count (cf. [240, 241, 245]) shown in

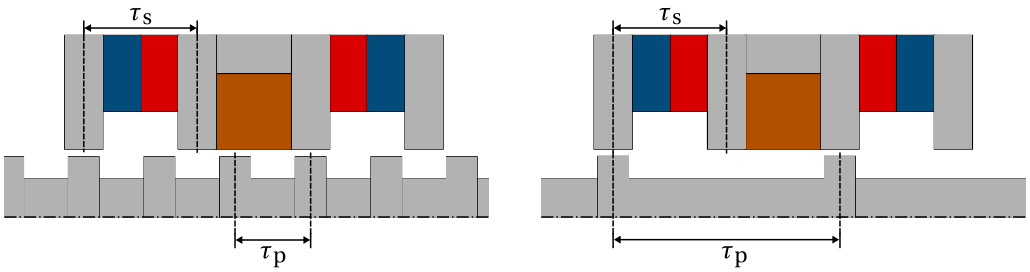

Figure 80: *FSPMLM with increased pole count (left) and regular pole count (right), with labels for the translator pole pitch τ_{p} and stator slot pitch τ_{s}.*

figure 77, the additional poles can reduce cogging forces, while increasing the switching frequency (cf. figure 81). The relationship between stator slot pitch and translator pole

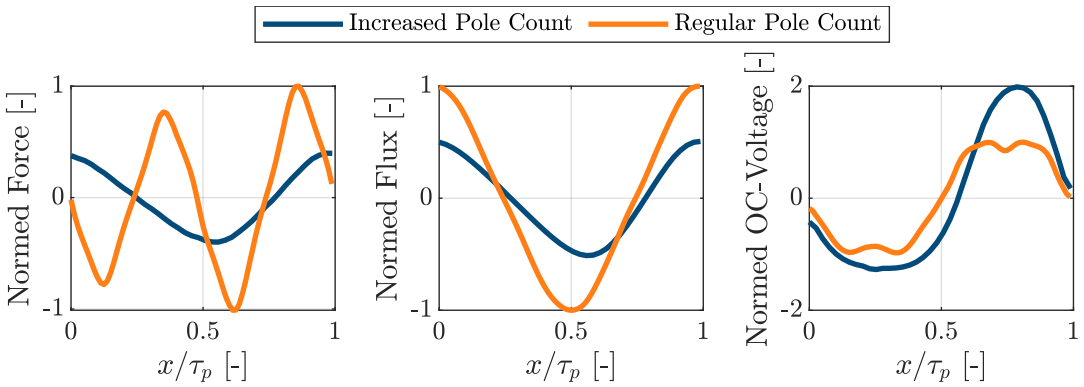

Figure 81: *FEM simulation results, comparing an increased to a regular translator pole count. All values are normalized to the maximum amplitude of the regular pole count results. The x-axis shows the translator position x_{rel} relative to the pole pitch τ_{p}.*

pitch for both cases can be described by [244]:

$$\text{Regular Pole Count:} \qquad 2 \cdot \tau_{\mathrm{s}} = \tau_{\mathrm{p}} \tag{71}$$

$$\text{Increased Pole Count:} \qquad 2 \cdot \tau_{\mathrm{s}} = 3 \cdot \tau_{\mathrm{p}} \tag{72}$$

An FEM simulation of a single stator segment is used to compare the influence of the pole count, for slow-moving translators at 0.1 $\frac{\mathrm{m}}{\mathrm{s}}$. Suitable parameters for the geometry were selected, the results are normalized to the maximum amplitude of the generator with regular pole count and the x-axis shows the translator position relative to the pole pitch τ_p (cf. figure 81). The generator with increased pole count shows resulting cogging forces and magnetic flux values lower to those of the generator with regular pole count, due to the increasing stray fluxes. However, the smaller pole pitch τ_{p} leads to a higher switching frequency, which increases the open circuit voltage and therefore allows a higher power output. Due to the benefits of the faster flux switching frequency, an increased pole count can be seen in several existing smaller implementations [238, 242]. A regular pole count is beneficial for larger applications with high thrust forces and speeds such as piston engines. [244, 245]
To increase the generators power output, multiple stator segments are aligned in series, as shown in figure 82. A regular translator pole pitch, as derived in eq. (72), leads to synchronous cogging of all stator segments, and therefore, the cogging forces accumulate unfavorably. By the introduction of a pole shift value δ_{p}, the cogging force can be distributed over the translator motion. The ratio of stator slot pitch and translator pole pitch from eq. (72) is changed to [244]:

$$\begin{aligned} 2 \cdot \tau_{\mathrm{s}} &= (3 + \delta_{\mathrm{p}}) \cdot \tau_{\mathrm{p}} \\ \Rightarrow \tau_{\mathrm{p}} &= \tau_{\mathrm{s}} \frac{2}{3 + \delta_{\mathrm{p}}} \end{aligned} \tag{73}$$

To achieve an even distribution, the shift factor δ_p must be related to the number of coils and stator segments n_s:

$$\delta_p = \pm \frac{n_{c,pair}}{n_s} \quad \forall\ n_{c,pair} \in \mathbb{N} \mid \left(n_{c,pair} < n_s,\ n_s \text{ is multiple of } n_{c,pair} \right) \tag{74}$$

where $n_{c,pair}$ stands for the number of synchronized coil pairs. For a sequential cogging of all n_s coils, $n_{c,pair}$ is equal to 1. With $n_{c,pair} = 2$, the stator is divided into two parts that have synchronous cogging. The number of coil pairs $n_{c,pair}$ must be an integer divisor of the number of coils n_s. Considering a four coil setup ($n_s = 4$), four different pole pitch values, lead to a uniform cogging distribution: $\delta_p = \pm 1/4$ and $\delta_p = \pm 1/2$. Figure 82 exemplary shows the pole pitch values of $\delta_p = 0$, $\delta_p = +1/2$ and $\delta_p = -1/4$. Using the FEM model, the resulting open circuit voltage and cogging force values can be

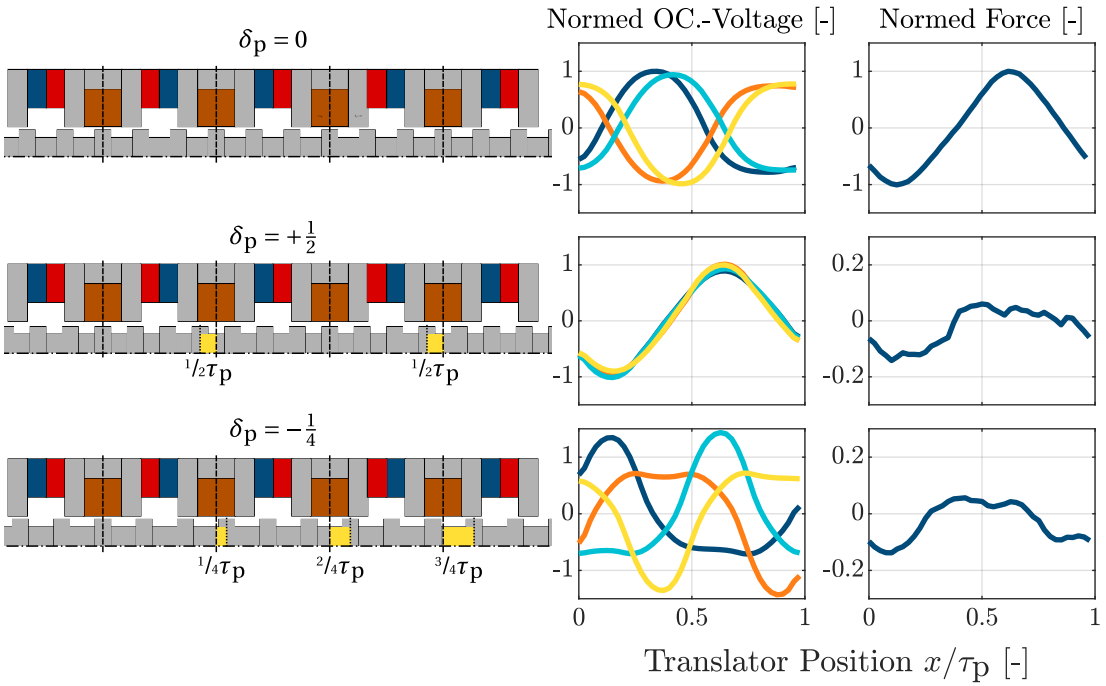

Figure 82: *Visualization of different pole shift δ_p values, the influence on the translator pitch (left) and the corresponding FEM simulation results for open circuit voltage and cogging force normalized to the values of $\delta_p = 0$ over the relative translator position (right).*

compared. The pole pitch of $\delta_p = +1/2$ leads to synchronized induction of the coil pairs (1,3) and (2,4), which show in-phase open circuit voltage values due to the opposing magnets (cf. figure 82). The pole pitch $\delta_p = -1/4$, evenly distributes the induction into the coils and leads to sequential cogging with a phase shift of 90°. The introduced pole shift results into significantly lower cogging forces compared to a slot pole ratio as of eq. (72).

6.5.5 Design Principle Validation

In this section, the analytically derived design rules from section 6.5.4 and the reduced order model description from section 6.5.3 are beeing validated based on FEM and prototype implementation results. At first, the parameterized FEM simulation is used to examine the previously derived optimal values for the stator and translator pole ratio (cf. eq. (74)). Figure 83 shows the FEM simulation results for the influence of the pol-shift value δ_p for a generator with constant electric load. Shown is the ratio of mean electric power $\overline{P}_\mathrm{el}$ to the average cogging force $\overline{F}_\mathrm{cog}$ and to the maximum amplitude of the cogging force $\widehat{F}_\mathrm{cog}$ normalized to the maximum value of the dataset. It can be

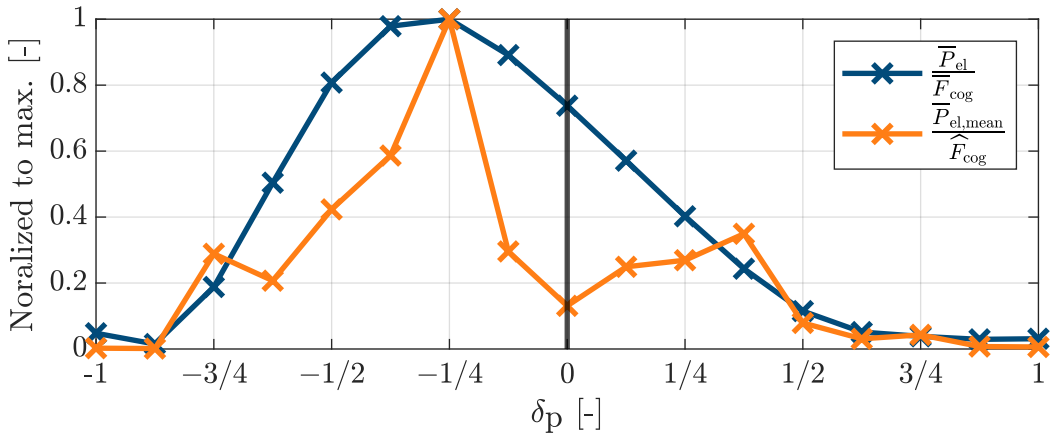

Figure 83: *FSPMLM pole shift FEM validation*

seen, that the derived values of $\delta_\mathrm{p} = \pm 1/4$ and $= \pm 1/2$ indeed show an improved ratio of power output to cogging force compared to a translator without pole shift $\delta_\mathrm{p} = 0$. A negative pole shift, that results in a larger pole pitch, shows generally better results for the here selected generator dimensions. This is probably due to unfavorable increasing stray fluxes for a translator with small pole pitch values. For $\delta_\mathrm{p} = +1/2$, the pole pitch seems to become so small that the even distribution of the cogging forces no longer has any advantage. The best results in the FEM simulation can be achieved with a pole pitch of $\delta_\mathrm{p} = -1/4$, which is why this value is used for the following dimensioning.
To further validate the derived design rules and models, a first prototype with three different translator designs (cf. tables 22 to 24) is implemented (cf. figure 84) and tested at constant velocity. A coil with 3000 windings and 0.1 mm wire diameter was used and connected to a matched load resistance so that $R_\mathrm{coil} = R_\mathrm{load} = 450\,\Omega$. Each translator was moved with a target speed of $0.1\,\frac{\mathrm{m}}{\mathrm{s}}$ and the actual velocity, voltage, and force were measured. Figure 86 compares the measurement and simulation results, whereas the FEM simulation takes into account the actual measured velocity of the translator motion. The measured voltage and power output agree very well with the simulation results with regard to phase and amplitude. The force measurements, on

r_T	W_S	W_T	H_{air}	τ_s
5 mm	2 mm	2 mm	0.5 mm	7 mm

Table 23: *Common dimensions of the generator prototype implementations.*

	$T_{+1/2}$	$T_{+1/4}$	$T_{-1/4}$
δ_p	+1/2	+1/4	−1/4
τ_p	4.0 mm	4.3 mm	5.1 mm
H_T	1.5 mm	2.0 mm	1.25 mm

Table 24: *Parameter differences between the tranlsator prototype implementations $T_{+1/2}$, $T_{+1/4}$ and $T_{-1/4}$.*

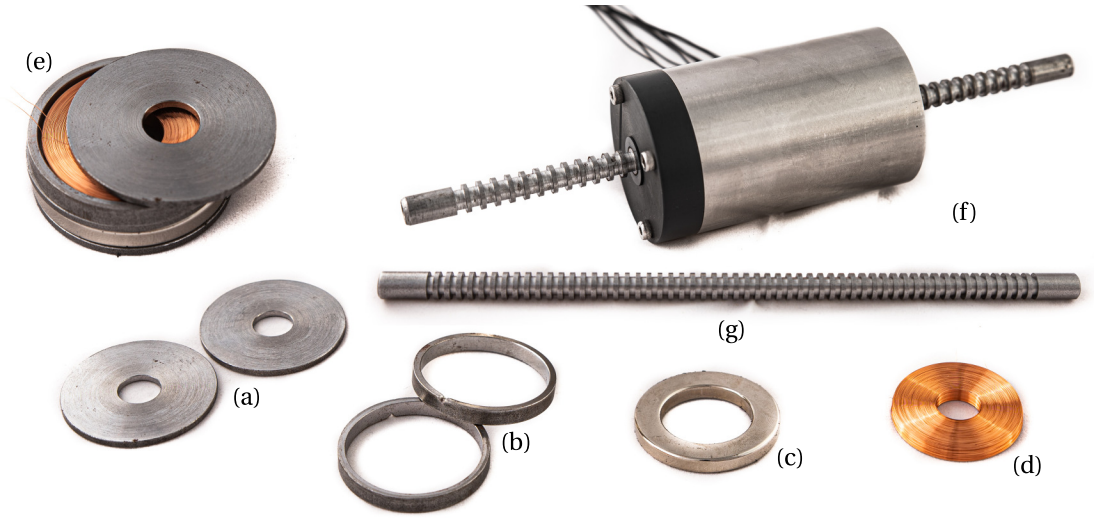

Figure 84: *a: Discs representing the stator tooth; b: Rings representing the coil spacer; c: Neodymium magnet; d: Coil; e: Assembled Stator segment; f: Assembled Generator Prototype; g: Translator implementation.*

the other hand, show a significant deviation. Further investigations confirmed, that the increased force resulted from high friction forces due to the selected plain bearings. With the given manufacturing tolerances, a slight radial offset exists between the stator and translator axis (cf. figure 85). This leads to increased longitudinal forces (F_{mag} in figure 85) in the radial direction of the offset, which in combination with the high friction coefficient of the plain bearings results in increased axial forces. To address this, an improved bearing concept for the translator is required, derived in section 6.10.1.

As already confirmed by the FEM analysis, also with the measurement results (cf. figure 86), the best performance was observed for a pole shift of $\delta_p = -1/4$, corresponding to $\delta_p = -1/n_s$. This configuration has a comparable large pole pitch τ_p and therefore

larger air gaps between the translator poles, reducing the radial forces due to the magnets. For a miniaturized FSPMLM it seems to be advantageous not to use too narrow translator configurations to minimize unwanted lateral forces.

The initial prototype of the generator validates the proposed design concept. A comparison between the simulation and experimental results indicates that the design rules derived are accurate and can be applied in subsequent parametric designs to determine the remaining generator parameters.

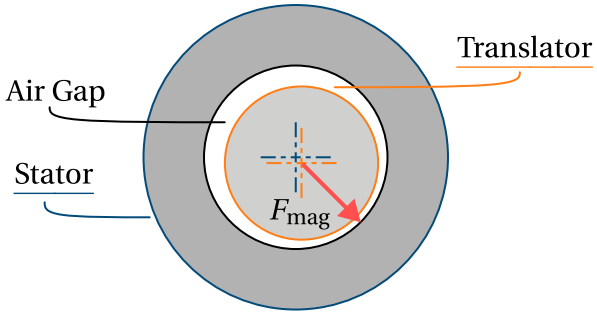

Figure 85: *Illustration of the radial misalignment between the translator and stator, causing an increase in bearing forces.*

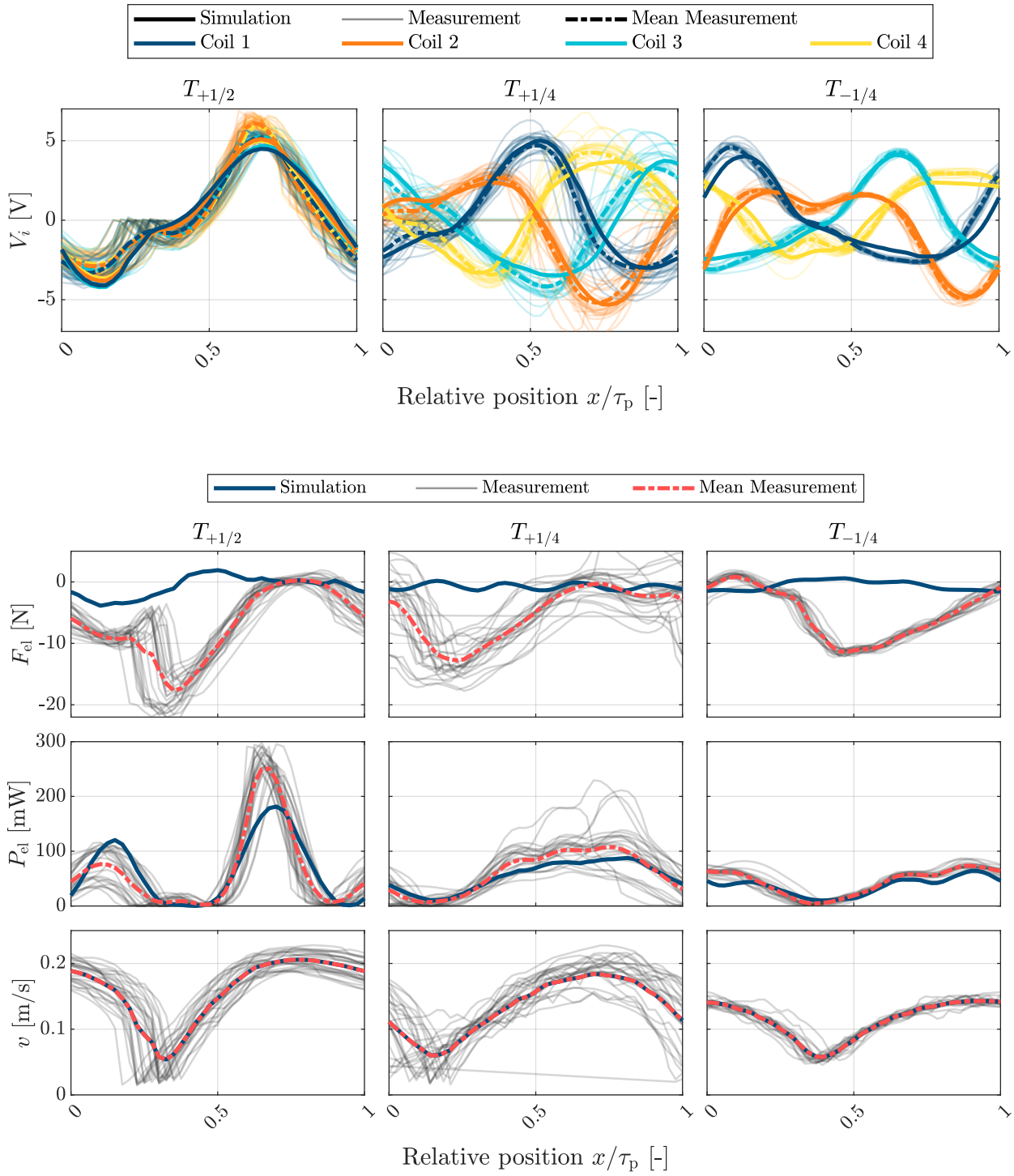

Figure 86: *Comparison of measurement and simulation data for one generator period's movement with three different translator dimensions. The voltage output of a single coil V_i, total electrical power over time P_{el}, mean power $\overline{P}_{el}$, cogging force F_{el}, and translator velocity v are shown as curves. [224]*

6.6 Rectification and Charging: Methods for Low-Power Harvesting Electronics

The energy harvested by the generator shall be used to recharge the drifter's energy storage. As the generator's coils produce an AC voltage, a rectification and charging circuit must be designed. The typically low voltage and power gains of energy harvesting systems, present challenges in designing an effective conditioning circuit. In this section, a charging circuit concept is developed for the previously presented WEC, which will serve as a circuit model to match the coil characteristics to the load conditions. To identify a suitable solution for the case at hand, the sub-functions of the circuit are initially identified, and solution concepts for sub-components are presented using a morphological box. As there are various implementation options available, selecting the right solution is essential.
The circuit to be designed needs to convert the irregular AC-voltage output of the coils to a regulated charging voltage for storage. A breakdown of the circuit's functions is shown in figure 87. The voltage of each coil needs to be rectified, and the sum of all

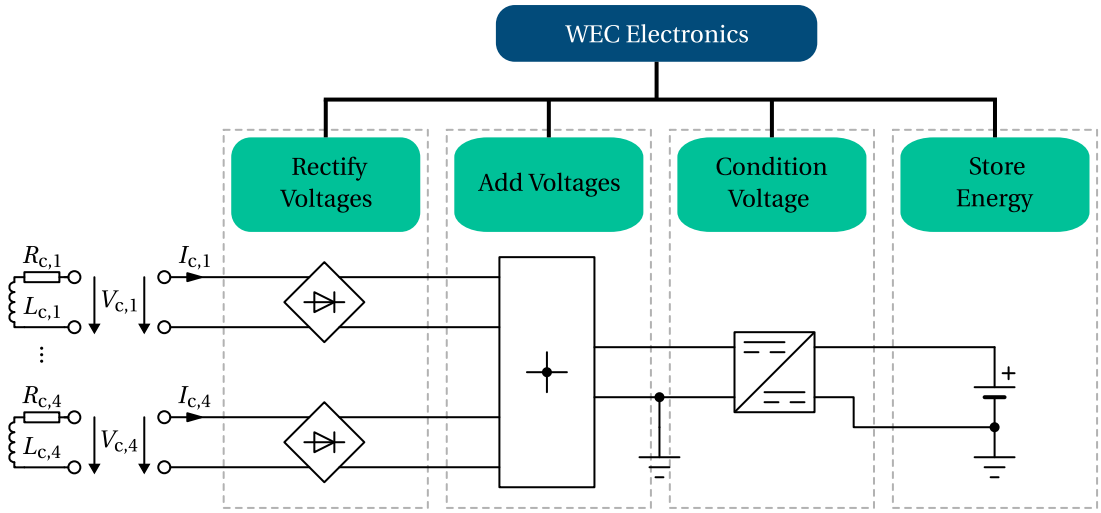

Figure 87: *Functional tree of the electronic charging circuit with a conceptual representation of the circuit components.*

rectified voltages needs to be built. The total rectified output voltage then needs to be conditioned for energy storage. For each coil, the load of the circuit is given by:

$$Z_{\text{load},i} = \frac{V_{c,i}}{I_{c,i}} \tag{75}$$

The maximum power output is achieved when the load impedance is matched to the coil impedance. The coil impedance is determined by the coil parameter, selected in section 6.9. The following design of the circuit considers different solutions for each

function, with the overall goal to maximize the power output of the system. All solution concepts are summarized in the morphological box in table 26

6.6.1 Voltage Rectification Approaches

The conventional approach for rectifying AC voltages is to form a bridge rectifier with diodes. It is common to connect a capacitor in series in order to smooth out the strongly fluctuating voltage [246]. Diode rectifiers have the disadvantage of high power loss and low efficiency due to the high forward voltage, especially for low-voltage applications.
An alternative implementation of a bridge rectifier circuit is to use MOSFETS. MOSFET rectifiers have the advantage that their voltage drop is significantly lower than that of diodes. However, this requires a sufficient gate voltage V_{GS}. Characteristic for MOSFET rectifiers is a hard voltage threshold shutting down the current flow. The losses are mainly caused by the on-resistance $R_{DS,on}$. MOSFETS are available with lower resistance than that of diodes, resulting in a significantly lower voltage drop.
In addition to the presented passive variants of rectification, active rectifier approaches also exist. In active rectification, the most efficient operation possible is to be achieved by controlled switching of MOSFETs [247]. However, the control requires a processing unit with knowledge of the current system state to be able to predict the switching.

6.6.2 Summation of Rectifier-Stages

Different methods can be used to connect the rectifier outputs (cf. table 26). The most conventional method is to connect all rectifiers in parallel. As a result, the current of all outputs is added and the voltage at all outputs is equal. Alternatively, the outputs can be connected in series. The addition of all voltages leads to a larger output voltage with a lower current compared to the parallel connection. The disadvantage of this circuit is that the total current must flow through all rectifiers connected in series. The current component of the first coil thus also flows through the diodes of the following rectifiers, so that the total power dissipation increases.
For systems with in-phase induction, there is a further possibility to connect the coils in pairs before the rectifier. For the derived generator concept, two coil pairs have synchronous curves, so a series connection of the two coils might be possible. Thereby, the number of diodes required and thus the power dissipation is significantly reduced.

6.6.3 Voltage-Level Conditioning Methods

The output of all rectifiers is an unregulated voltage that requires further conditioning to enable charging of the energy storage. The electric load for the coils is mainly determined by this conditioning circuit since the current drawn from the coils depends on it. A straightforward solution to convert the rectifier's output voltage to a regulated charging voltage is to facilitate a voltage regulator or switching converter IC. One problem, however, is that the output voltage can only be kept constant if the input voltage is sufficient, and the dead times at the input thus also have a direct effect on the charging behavior. The output of the conversion thus consists of irregular pulses, leading to an inefficient charging procedure. One possibility to counteract this is to implement a buffer that initially stores the output of the rectifier. By means of a logic circuit, the converter can then be operated from the buffer once a threshold value has been reached. By selecting the size of the buffer, the duty cycle of the converter is predetermined and a regulated charge cycle can be achieved.
Alternatively, existing IC solutions can be used. With a growing interest in energy harvesting systems, there is a number of integrated circuits available (cf. table 25), specifically suited for energy harvesting applications. Energy harvesting ICs are typically

	Device	$V_{\text{in,min}}$ [V]	$V_{\text{in,max}}$ [V]	I_{max} [mA]
e-Peas	*AEM30940* [248]	0.38	5	110
TI	*BQ25570* [249]	0.6	5.1 5	285
TI	*BQ25173* [250]	3	18	800
AD	*LTC3105* [251]	0.25	5	400
AD	*LTC4425* [252]	2.7	5.5	2000
AD	*ADP5092* [253]	0.38	3.3	300

Table 25: *List of energy harvesting ICs with the representation of the input ranges and the maximum output current; Analog Devices (AD); Texas Instruments (TI).*

based on boost chargers, offering a low startup voltage by additionally implemented charge pumps. In addition to voltage conversion, the circuits are designed to regulate the charging current of e.g. Li-Ion batteries. The devices may offer additional functions such as power monitors and battery state indicators. To optimize the power output of the system, many of the presented ICs offer maximum power point tracking (MPPT). The goal of MPPT is to adjust the input impedance of the IC to set the operating point. For this purpose, the open circuit voltage of the source is measured at regular intervals and the operating point for the next section is determined. Unfortunately, these MPPT systems are designed primarily for the operation of photovoltaic and therefore consider time intervals of several seconds for the adjustment of the load impedance. However, such a high time span is unfavorable for fast varying energy harvesting systems such as

the here considered WEC. If, for example, the open circuit measurement takes place just when the WEC is not moving, a very inefficient operating point is set for the next seconds.
Carandell et al. [254] have developed a novel approach that utilizes the fractional open circuit voltage method for wave energy harvesting in electromagnetic generators. The proposed method involves increasing the sampling time of the MPPT system, which is achieved by using an external circuit to boost the sampling frequency of the energy-harvesting IC, namely the *ADP5092* from Analog Devices. They implemented a sampling frequency of 30 Hz and achieved a 25% increase in power output compared to the unit using a lower sampling rate.

6.6.4 Energy Storage Considerations

Multiple rechargeable systems can be considered for energy storage, however, this study prioritizes energy harvesting, hence storage is not extensively considered. Only Li-ion batteries and supercapacitors are presented as options.
Operating Li-ion batteries is a straightforward approach as there are many ICs designed to use this type of battery. Very high storage capacities can be achieved and the costs are reasonable for the storage capacity. The biggest disadvantage is the degradation over time and the use of rare-earth, toxic, and hazardous materials. Super-capacitors can be considered as an alternative to reduce the number of toxins. Despite having a lower energy density than batteries, super-capacitors have a higher charging cycle life and can be manufactured without rare earth materials.
Li-Ion batteries typically operate at 3.7 V and require a charging voltage of around 4.2 V. To enable safe operation and charging, the charging voltage and current should maintain a controlled level. Super-capacitors can be selected for different voltage ranges and allow therefore also operation at Li-ion battery levels.

6.6.5 Evaluation and Selection of a Rectification and Charging Method

All solution concepts are summarized in the morphological box in table 26.
For the selection of the approach used here, first, the voltage conditioning circuit is considered, since it has a strong influence on the remaining selection. In addition to the voltage conditioning, the solution should also provide means for the input impedance matching to reach higher output power. The issue with energy harvesting ICs available in the market is that they have insufficiently low sampling rates for their MPPT function. The fractional open-circuit method proposed by Carandell et al. [254] with a higher sampling rate is a possible implementation but comes with higher circuit complexity.

Parameter	Configurations		
	Diode	**Passive MOSFET**	**Active Rectification**
Rectification	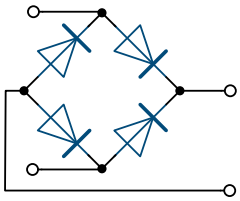	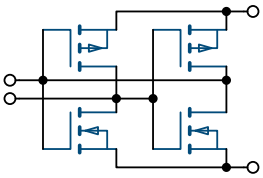	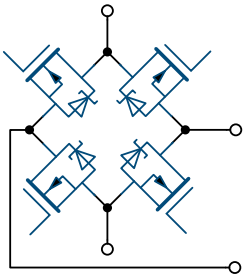
	Pairwise	**Series**	**Parallel**
Voltage Addition	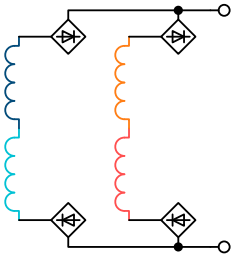	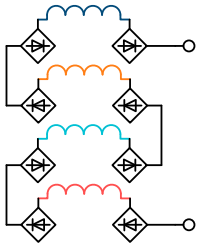	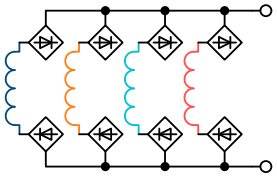
	DC/DC Converter	**Energy Harvesting IC**	**Fractional Open-Circuit Voltage**
Conditioning	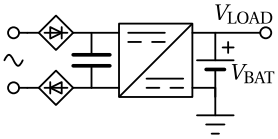	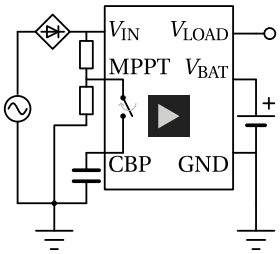	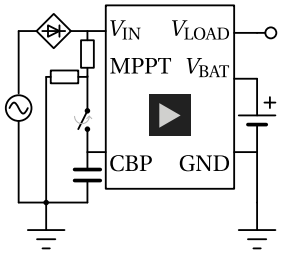
	Li-Ion Battery	**Super-Capacitor**	
Storage		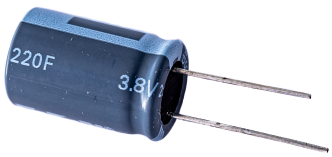	

Table 26: *Morphological box showing different solution concepts for the identified circuit functions (cf. figure 87).*

Therefore, the DC/DC converter circuit with a large capacitor for intermediate storage is chosen.
For rectification of the coil voltage, active and passive methods can be considered. Since an active rectification would require a more complex implementation and control algorithm, a passive approach is selected. Furthermore, active rectification prevents the harvester from self-starting. As soon as there is not enough power to operate the active rectification, the energy harvesting system cannot recover itself. For the passive MOSFET circuit, an additional diode would be required to prevent reverse flow from the buffer capacitor, reducing the efficiency gain of the MOSFET rectifier. Therefore a traditional diode bridge rectifier is selected to implement the rectification.
To keep the loss through the diode rectifier low, low forward voltage Schottky diodes are selected and the voltage operating range is chosen to minimize the forward voltage component. The pairwise connection is not suitable if the induction is not exactly synchronous. As experiments with the implemented generator have shown, the slightly different induction of the pairs connected in series leads to high peak currents and voltages, resulting in inefficient rectification. The rectifier is therefore used in the usual parallel connection. A Li-ion battery is initially used as the storage device in order to achieve the largest possible storage capacity.

6.6.6 Generator Electronics Design and Implementation

The charging circuit is implemented as follows: The voltage of all four coils is first rectified and stored temporarily in a large capacitor. This rectified DC voltage is then conditioned by a DC/DC converter to allow for controlled charging of the batteries. To enhance the charging current and maintain the DC/DC converter within its operating limits, a Schmitt trigger is utilized, switching the converter's input voltage through hysteresis control (cf. figure 88). By setting the resistor values $R_{\text{sch},1}$ to $R_{\text{sch},3}$ of the in-

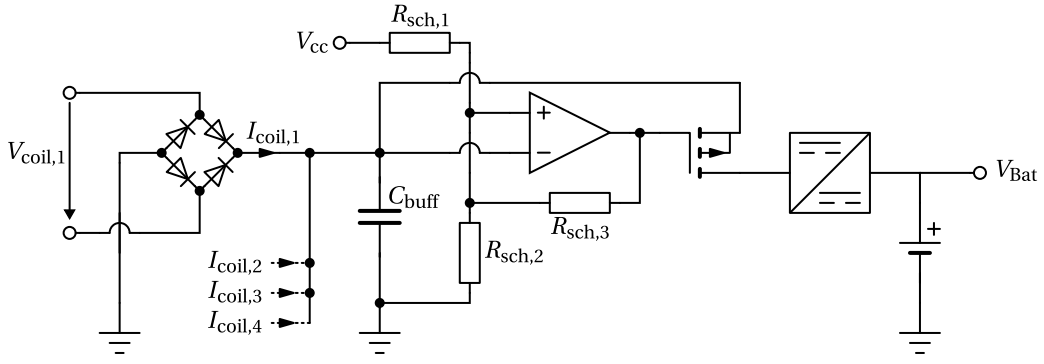

Figure 88: *Selected circuit design concept with rectification and charging components based on a Schmitt trigger.*

verted Schmitt trigger circuit, the voltage range of the capacitor C_{buff} is defined between $V_{\text{buff,high}}$ and $V_{\text{buff,low}}$.The capacitor voltage determines the electric load behavior for the generator and is therefore selected together with the coil parameters in section section 6.10.3. Depending on the selected voltage level, the DC/DC converter can either be a step-up or step-down converter to convert to the battery voltage V_{Bat}. The minimum input voltage for the DC/DC converter should not be less than 1.5 V, as this is a typical lower level for low-cost voltage converters. This requires the coils to reach voltages of at least $1.5\,\text{V} + V_{\text{rect}}$ whereas V_{rect} stands for the forward voltage of the rectification circuit. To address the higher forward voltage V_{rect} of the passive diode bridge, Shottky-Diodes with lower forward voltage are used.
The circuit is implemented on a single PCB as depicted in figure 89. The complete schematics of the electronics are presented in appendix A.5. Along with the charging circuit, additional provisions for voltage and current measurement are included to simplify power monitoring in subsequent generator testings. The circuit is tested in conjunction with the optimized generator testing described in section 6.10.

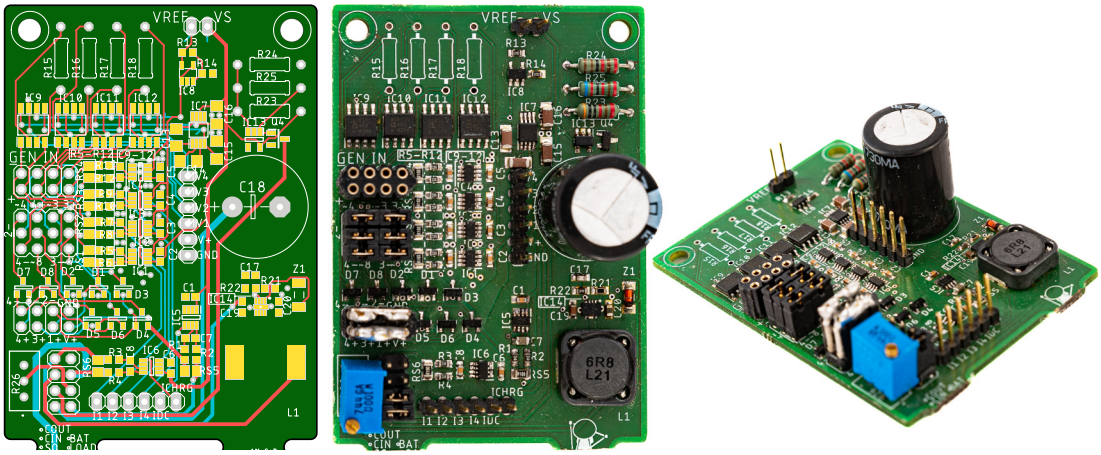

(a) (b) (c)

Figure 89: *PCB implementation of the rectification and charging circuit. a: Layout; b&c: Photo of implementation. See appendix A.5 for complete implementation schematics.*

6.7 Generator Geometry: Electromagnetic Optimization

For the given generator concept, geometry optimization must be performed to increase the overall performance. In the following, the optimization parameters are first derived and the objectives and approach are explained. The optimization uses parametric FEM simulation to find a generator configuration that provides high power output with low cogging forces.

6.7.1 Identification of Geometric Optimization Parameters

In section 6.5.2, the dimensions of the generator and the geometric parameters were introduced. Taking into account the selected magnet size from table 22, the derived translator pole shift from section 6.5 and the air gap size given by the implementation concept of section 6.10.1, all fixed geometric parameters are stated in table 27. Due

Description	Parameter	Value
Width of coil and magnet	W_{CM}	5 mm
Inner radius magnet	$r_{\mathrm{M,i}}$	12.5 mm
Outer radius magnet	$r_{\mathrm{M,o}}$	20 mm
Outer radius stator	$r_{\mathrm{S,o}}$	20 mm
Height of air gap	H_{air}	1 mm
Translator pole shift	δ_{p}	$-\frac{1}{4}$
Number of coils	n_{s}	4

Table 27: *Geometric parameters with constant values during the optimization*

to the given construction and the established design rules (cf. section 6.5.4), some parameters are directly dependent on each other. The stator slot pitch τ_{s} is determined by the magnet width W_{CM} and the stator tooth width W_{S}:

$$\tau_{\mathrm{s}} = W_{\mathrm{CM}} + W_{\mathrm{S}} \tag{76}$$

The inner radius of the stator $r_{\mathrm{S,i}}$ depends on the translator radius r_{T} and the air gap H_{air}:

$$r_{\mathrm{S,i}} = r_{\mathrm{T}} + H_{\mathrm{air}}. \tag{77}$$

Since the magnetic flux from the permanent magnets is introduced through the stator teeth into the translator poles, the ratio $\beta_{\mathrm{t,s}}$ of the stator tooth width W_{S} to the translator pole width W_{T} is an important design factor. Instead of changing the parameter

W_T directly, the width of the stator teeth W_S and the pole ratio $\beta_{t,s}$ are tuned in the optimization, determining the pole width W_T:

$$\begin{aligned} \beta_{t,s} &= \frac{W_T}{W_S} \\ \Rightarrow W_T &= \beta_{t,s} \cdot W_S \end{aligned} \tag{78}$$

It has to be ensured, that the pole width W_T cannot be larger than the translator pitch τ_p. All given analytic relationships between the geometric parameters are summarized in table 28. Due to this extensive predetermination, only four geometric parameters

Description	Relationship
Stator slot pitch	$\tau_s = W_S + W_{CM}$
Translator pole pitch	$\tau_p = \frac{2}{3+\delta_p} \cdot \tau_s$
Translator pole width	$W_T = \beta_{t,s} \cdot W_S$
Inner radius stator	$r_{S,i} = r_T + H_{air}$

Table 28: *Geometric dimensions which can be derived by analytic relationships from other parameters.*

remain for the optimization of the generator (cf. table 29). This is the width of the stator

Description	Parameter	Unit
Translator radius	r_T	[mm]
Stator tooth width	W_S	[mm]
Pole overlap	$\beta_{t,s}$	[−]
Height tanslator pole	H_T	[mm]

Table 29: *Geometric parameter which are tuned for the optimization*

tooth W_S, the radius of the translator r_T, as well as the parameters for determining the translator pole dimensions $\beta_{t,s}$ and H_T.
As the number of windings on the coil significantly affects the power output and efficiency of the generator, the coil parameter is chosen in section 6.10.3 after optimizing the generator geometry to match the coil parameters to the wave excitation and load conditions. However, it should be noted that the translator radius r_T has an impact on the amount of coil space available. A small translator radius leads to saturation in the translator which lowers the power output, a larger translator radius reduces the available coil space which also negatively affects the power output. A normalised coil-independent power potential is derived to allow a comparison of geometries with different coil spaces. The winding number of the coil N_{coil} is derived from the cross-sectional area of the coil space A_{coil} and the wire diameter d_{coil}. Accordingly, when the

wire diameters are equal, the number of windings is proportional to the coil space, while the resistance varies with the length of the wire, derived from the mean radius $r_{\text{coil,mean}}$ of the winding surface:

$$N_{\text{coil}} \sim A_{\text{coil}} \tag{79}$$

$$R_{\text{coil}} \sim A_{\text{coil}} \cdot r_{\text{coil,mean}} \tag{80}$$

Considering eq. (79) and the induced voltage V_{coil} into the coil by $-N_{\text{coil}} \frac{\delta \Phi}{\delta t}$, allows to derive a relationship to the output power:

$$V_{\text{coil}} \sim -A_{\text{coil}} \frac{\delta \Phi}{\delta t}$$

$$P_{\text{coil}} = \frac{V_{\text{coil}}^2}{R_{\text{coil}}}$$

$$\Rightarrow P_{\text{coil}} \sim \frac{A_{\text{coil}}}{r_{\text{coil,mean}}} \left(\frac{\delta \Phi}{\delta t} \right)^2 \tag{81}$$

$$\Psi = \frac{A_{\text{coil}}}{r_{\text{coil,mean}}} \left(\frac{\delta \Phi}{\delta t} \right)^2 \tag{82}$$

The coil independent power potential Ψ, allows to evaluate the available coil winding space and the magnetic flux potential at the same time. Since the absolute value of this potential does not permit any physical interpretation, it is only used for comparisons, normalized to the maximum value of the comparison Ψ_{N}.

6.7.2 Evaluation of Geometric Optimization Results

The optimization of the generator geometry is performed in two steps. At first, a large parametric simulation using the introduced FEM model is conducted. Subsequently, the results of the FEM simulation are compared and five best performing geometries are selected in order to consider those within the overall system. For this purpose, a reduced order model is derived based on the FEM models of the selected geometries to enable a coupled simulation using the mechanical model of the WEC. The simulation of the coupled system is conducted for irregular wave excitation, to allow the selection of the generator with the best overall performance.

Parametric Simulation Results In the FEM model for the parametric simulation, the translator is moved with a constant speed of 0.3 $\frac{\text{m}}{\text{s}}$ over the distance of one pole pitch τ_{p}. The velocity of 0.3 $\frac{\text{m}}{\text{s}}$ is the same velocity value used as a target value for the mechanical optimization in section 6.8 and therefore provides an operating point suitable for a

first performance comparison. The coils are simulated in an open circuit configuration, resulting in the induction forces being 0. For each of the four given optimization variables (cf. table 29), a parameter range is defined (cf. table 30), based experience values and possible manufacturing accuracy. In the parametric simulation, all combinations of

r_T	W_S	$\beta_{t,s}$	H_T
[5.5 : 0.5 : 8.5] mm	[2.5 : 0.5 : 4.5] mm	[0.7 : 0.05 : 1]	[1 : 0.25 : 2.5] mm

Table 30: *Geometric optimization parameter range using the notation* [*Start* : *Resolution* : *Stop*].

the given parameter range are simulated. Given the stated resolution of each range, the solution space is defined by $7 \times 7 \times 7 \times 5 = 1715$ different geometry simulations. For the evaluation of the resulting data set, the three values of $\overline{\Psi}_N$, $\overline{F}_{cog}$ and $\widehat{F}_{cog}$ are compared. For a single geometry, $\overline{\Psi}$ describes the coil independent power potential, averaged over the movement of one pole pitch. $\overline{\Psi}_N$ is the same value, normalized to the maximum value of $\overline{\Psi}$ in the whole data set. The force value $\overline{F}_{cog}$ describes the average cogging force over the movement of one pole pitch and $\widehat{F}_{cog}$ stands for the peak cogging force value of a single geometry. Figure 90 compares the results of all geometries within the geometric simulation, over the respective translator radius r_T. The average value for

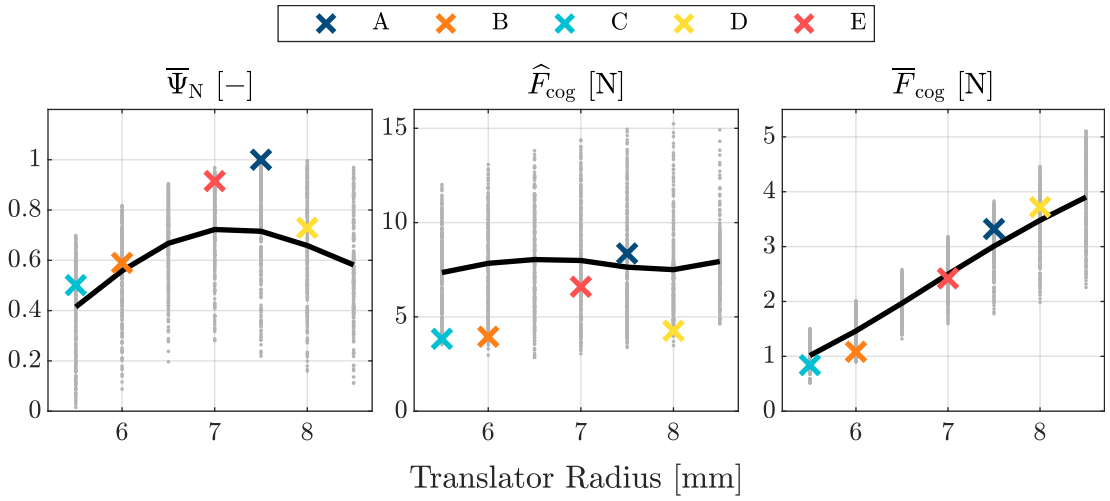

Figure 90: *Results of the parametric FEM simulation showing the average of the normalized coil independent power potential* Ψ *and the average and maximum cogging force values.*

each translator radius is shown by a black line. The geometry with the highest value for the coil independent power potential Ψ_N in this data set, is marked by A. Since this geometry also shows high values for the average and maximum cogging force, it is possible that this larger damping leads to a lower power output for the overall WEC system, compared to using a geometry with lower damping forces. Therefore a total of five geometries is selected to be later simulated in irregular waves using the reduced

order model. Four other geometries also consider the generators forces, by deriving an efficiency equivalent value. Since the mechanical power is the product of velocity and force, and since all results were simulated for the same translator speed, an efficiency equivalent value can be derived from $\frac{\overline{\Psi}_\mathrm{N}}{\overline{F}_\mathrm{cog}}$. Geometry *B* considers the influence of the average force $\overline{F}_\mathrm{cog}$ as well as the maximum force value $\widehat{F}_\mathrm{cog}$, by selecting the geometry with the maximum value for $\frac{\overline{\Psi}_\mathrm{N}}{\widehat{F}_\mathrm{cog}+\overline{F}_\mathrm{cog}}$. Similar to *B*, geometries *C* and *D* are derived from exclusively, either the average or the maximum force by selecting the maximum value of $\frac{\overline{\Psi}_\mathrm{N}}{\overline{F}_\mathrm{cog}}$ for *C* and $\frac{\overline{\Psi}_\mathrm{N}}{\widehat{F}_\mathrm{cog}}$ for *D*. During the search for geometry *E*, it was attempted to locate a geometry that had a high power output, similar to geometry *A*, while also examining the force values. For that, only geometries with force values which are lower than the average force value of all geometries with the same translator radius were considered. From this subgroup, only geometries with a normalized power potential greater than 0.9 were considered and the maximum of $\frac{\overline{\Psi}_\mathrm{N}}{\widehat{F}_\mathrm{cog}+\overline{F}_\mathrm{cog}}$ was selected for *E*.

	r_T	W_S	$\beta_\mathrm{t,s}$	H_T	max of:
A	7.5 mm	3.5 mm	0.85	2 mm	$\overline{\Psi}_\mathrm{N}$
B	6 mm	2.5 mm	0.7	2.25 mm	$\frac{\overline{\Psi}_\mathrm{N}}{\widehat{F}_\mathrm{cog}+\overline{F}_\mathrm{cog}}$
C	5.5 mm	2.5 mm	0.7	2 mm	$\frac{\overline{\Psi}_\mathrm{N}}{\overline{F}_\mathrm{cog}}$
D	8 mm	3.5 mm	0.85	1.5 mm	$\frac{\overline{\Psi}_\mathrm{N}}{\widehat{F}_\mathrm{cog}}$
E	7 mm	3 mm	0.8	2 mm	$\frac{\overline{\Psi}_\mathrm{N}}{\widehat{F}_\mathrm{cog}+\overline{F}_\mathrm{cog}}$ while $\widehat{F}_\mathrm{cog} < \mathrm{mean}\left(\widehat{F}_\mathrm{cog}\right)$ and $\overline{F}_\mathrm{cog} < \mathrm{mean}\left(\overline{F}_\mathrm{cog}\right)$ and $\overline{\Psi}_\mathrm{N} > 0.9$

Table 31: *Dimensions and relating maximum value criteria for optimized generator geometries A to E.*

Selection of Optimized Generator Geometry For the selected generator geometries, a reduced order model (cf. section 6.5.3) is derived to simulate the power output of the overall system in irregular waves. For that, a coupled simulation model is derived that combines the generator behavior with the motion dynamics of eq. (43). The total damping forces of the dynamic system from eq. (44) use the generator forces of the reduced order model, as well as the mechanical damping parameter summarized in

table 21. At the same time, the generator model uses the translator position and velocity of the motion dynamics. The differential equations of the generator and the WEC dynamics can be transferred into a single DAE, allowing to solve the coupled model in one step. The coupled simulation uses the WEC parameters of the prototype from the experiments (cf. table 20). A series of coupled simulations are conducted for a set of different sea states. Each sea state is described by a Pierson-Moscowitz spectrum with a significant wave height of $H_s = 2\,\text{m}$ and a peak frequency ω_P between 0.1 and 2 $\frac{\text{rad}}{\text{s}}$. For all geometries a wire diameter of $d_{coil} = 0.1\,\text{mm}$ is selected and the maximum possible winding number for the respective coil space is calculated. The coils are simulated in short circuit configuration to consider maximum possible currents and therefore, the maximum possible induction forces. Figure 91 shows the power output results for the selected generator geometries. It can be seen, that geometry *A* has the highest overall

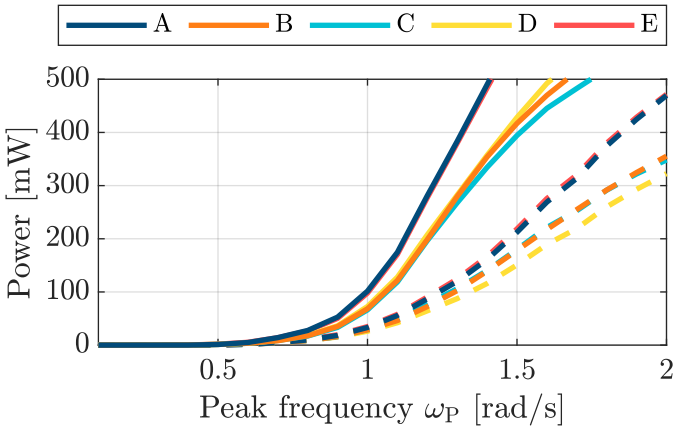

Figure 91: *Power output of the selected generator geometries from the parametric simulation for a series of simulations in random waves. The dashed line shows results with additional damping added. X-axis shows the peak frequency of the Pierson-Moscowitz spectrum with a significant wave height of* $H_s = 2\,\text{m}$.

power output, despite its higher cogging forces. Only geometry *E* can produce similar results but is not able to outperform *A*. Therefore, another set of simulations is conducted, increasing the damping of the WEC artificially, to take into account systems with higher friction values or degraded bearings. The applied friction is linear proportional to the translator radius and has a value of 75 $\frac{\text{Ns}}{\text{m}}$ for a translator with $r_T = 7.5\,\text{mm}$. Even with an added damping force of that large magnitude, the difference between the power output of geometries *A* and *E* is insignificantly small (cf. dashed line in figure 91). Therefore, the generator with geometry *A* is selected for the use in the WEC.

6.8 Mechanical Dynamics Optimization: The Coupled WEC System

With the generator geometry determined and the resulting forces established, the mechanical system can be optimized to maximize power output. To remain independent of the generator winding parameters, the optimization goal for the coupled system is to achieve the highest possible average speed, since generator power is proportional to the speed.
The system parameters stated in table 20 need to be optimized so that the response amplitude of the relative velocity between the buoy and the plate is increased. Since the orbital velocity of the water particles decreases with the water depth (cf. figure 67), larger values of ℓ_0 will lead to larger relative velocities between float and plate, as long as the orbital velocity at ℓ_0 is not 0. Therefore, the maximum possible value is selected which is defined by the requirements to be $\ell_0 = 0.5\,\mathrm{m}$. Furthermore, the parameters of the plate thickness H_p and connection rod radius r_c have only little influence on the dynamics. To reduce the number of optimization parameters, r_c is set to 0.01 m and H_p is set to 0.005 m. The remaining parameters are the radii r_b and r_p, the masses m_b and m_p as well as the spring stiffness K_s. These are determined using a Monte-Carlo simulation according to the procedure described in [224].
Optimization was performed for random seas with a Pierson-Moskowitz spectrum, considering peak frequencies $[\omega_\mathrm{min},\omega_\mathrm{max}] = [0.8, 1.2]\ \frac{\mathrm{rad}}{\mathrm{s}}$ and fixed significant wave height of either $H_\mathrm{s} = 2\,\mathrm{m}$ or $H_\mathrm{s} = 3\,\mathrm{m}$. All selected parameters are optimized to increase the relative velocities higher than $0.3\,\frac{\mathrm{m}}{\mathrm{s}}$. The system parameters to be optimized are restricted by a maximum value, stated in table 32, which ensures that the optimized system still meets the requirement of a compact drifter.

R_b & R_p	m_b & m_p	K_s
$< 0.3\,\mathrm{m}$	$< 5\,\mathrm{kg}$	$< 300\,\frac{\mathrm{N}}{\mathrm{m}}$

Table 32: *Maximum restrictions for system parameter*

The optimization problem is simulated for irregular seas (cf. appendix A.4.1) with $n_\mathrm{comp} = 100$ harmonic components and a simulation time of $t_\mathrm{end} = 40\,000\,\mathrm{s}$, using the interior-point method[255]. As a result, two different optimized system parameter sets were derived, as stated in table 33. To visualize the geometric changes, figure 92 compares the optimized geometries to the WEC of the experimental setup, considering their position in still water. Figure 93 shows the corresponding normalized histograms for $\omega_\mathrm{P} \in [0.1 \ldots 2]\ \frac{\mathrm{rad}}{\mathrm{s}}$ and $H_\mathrm{s} = 2\,\mathrm{m}$ to compare their response amplitude. With the optimized parameters, simulated relative velocities for given peak frequencies show a more broad distribution than those obtained with the initial experimental WEC setup.

System	r_b	r_p	r_c	m_b	m_p	H_p	ℓ	K_s
Opt. 1	0.10 m	0.25 m	0.01 m	0.93 kg	2.07 kg	5 cm	0.5 m	132.50 $\frac{N}{m}$
Opt. 2	0.09 m	0.29 m	0.01 m	4.99 kg	4.80 kg	5 cm	0.5 m	127.80 $\frac{N}{m}$

Table 33: *Dimensions of the optimized mechanical systems 1 and 2.*

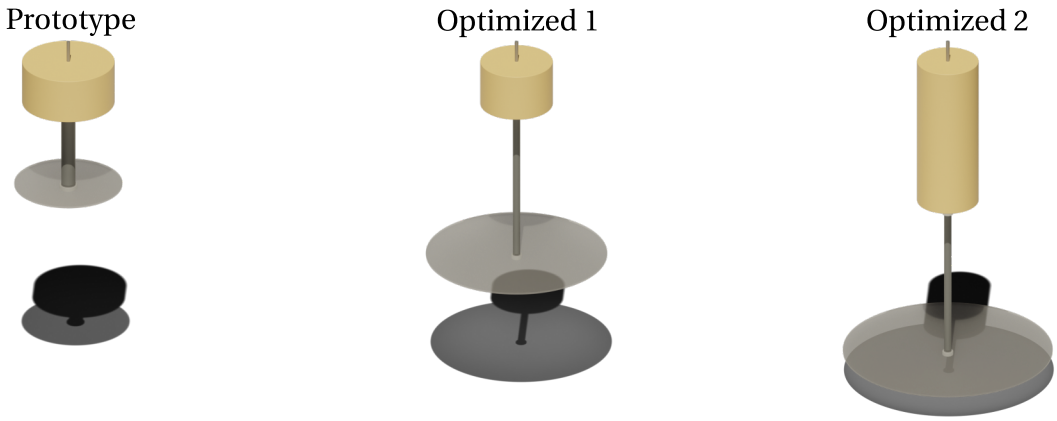

Figure 92: *Comparison of the dimensions of the WEC between the first prototype and the optimized parameters 1 and 2.*

Furthermore, the optimized parameters result in higher relative velocities at frequencies below 1.5 $\frac{rad}{s}$. Therefore, far more energy can be harvested by the systems 1 and 2, with the optimized parameters. The system of WEC 2 is a much heavier system with a total weight of nearly 10 kg and therefore exceeds the requirements for a lightweight and compact system. WEC 2 is only mentioned here to show that higher performance can be achieved with larger masses. The significantly lighter system WEC 1 can achieve similar performance to 2, while having similar geometric dimensions to those of the experimental prototype. In the optimization, there is a clear trend to choose the mass of the plate higher than that of the float, which can be explained by the higher inertia of the plate, resulting in larger relative velocities. A WEC designed for a drifter should utilize a large reactive plate and a high mass in the drogue, similar to the optimized system 1. The float should be buoyant and low in mass in order to move dynamically on the waves. Depending on the sea state, the spring stiffness has to be adapted. The system can be optimized further if the restrictions, due to the requirement of a compact drifter are omitted.

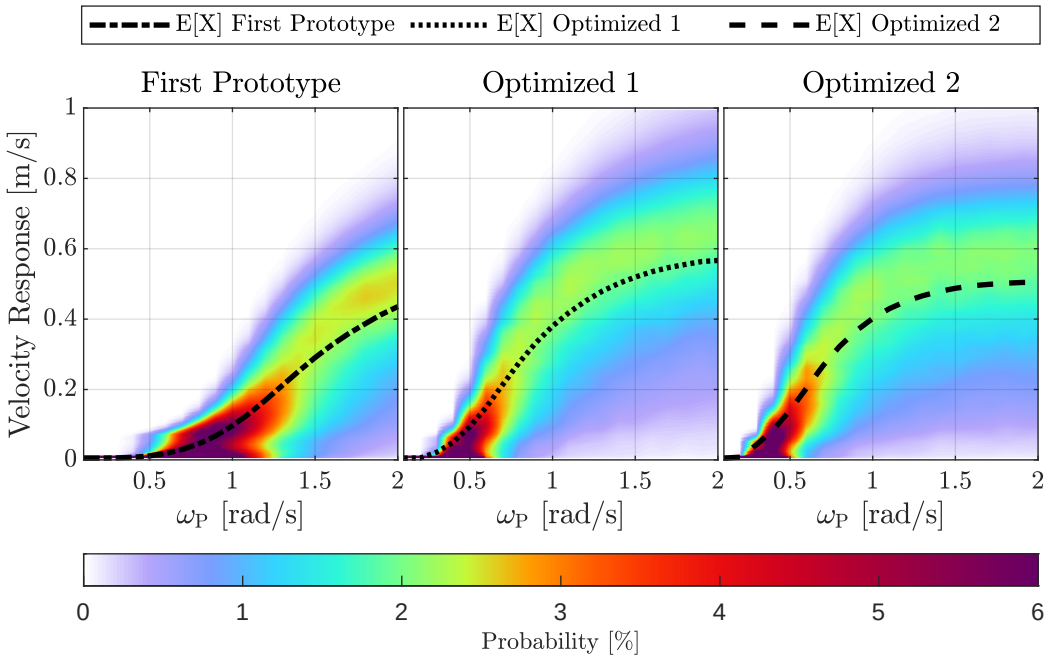

Figure 93: *Simulation results comparing the system response of the prototype WEC to the optimized systems* 1 *and* 2 *showing the normalized histograms for the probability of relative velocities in different sea states, using Pierson-Moscowitz peak Frequencies* $\omega_P \in [0.1 \ldots 2]\ \frac{\text{rad}}{\text{s}}$ *with a significant wave height of* $H_s = 2\,\text{m}$. *The dashed lines indicate the expected value* $\mathbb{E}[X]$ *of the velocity for each peak frequency.*

6.9 Electric Power Output Optimization Through Load Matching

With the model established, it's necessary to determine the parameters that describe the electrical load behavior of the rectification and charging circuit. To maximize the power output of the system, the coil parameters of the generator need to be matched to the circuit's load, described by Z_{load}:

$$Z_{\text{load}} = \frac{V_{\text{buff}} + V_{\text{rect}}}{I_{\text{coil},i}} \tag{83}$$

where $V_{\text{buff}} + V_{\text{rect}}$ stands for the buffer capacitor voltage and the forward voltage for rectification (cf. figure 88) and $I_{\text{coil},i}$ describes the current of a coil. The voltage of the coil strongly depends on the number of coil turns, which can be derived from the available coil space and the wire diameter. In the following, the two parameters of the wire diameter d_{coil} and the capacitor voltage V_{buff} need to be selected. Three different voltage levels of V_{buff} = [2,4,6]V volts and winding diameters between 0.05 and 0.2 mm are considered. The results of the power output are compared in figure 94. The overall

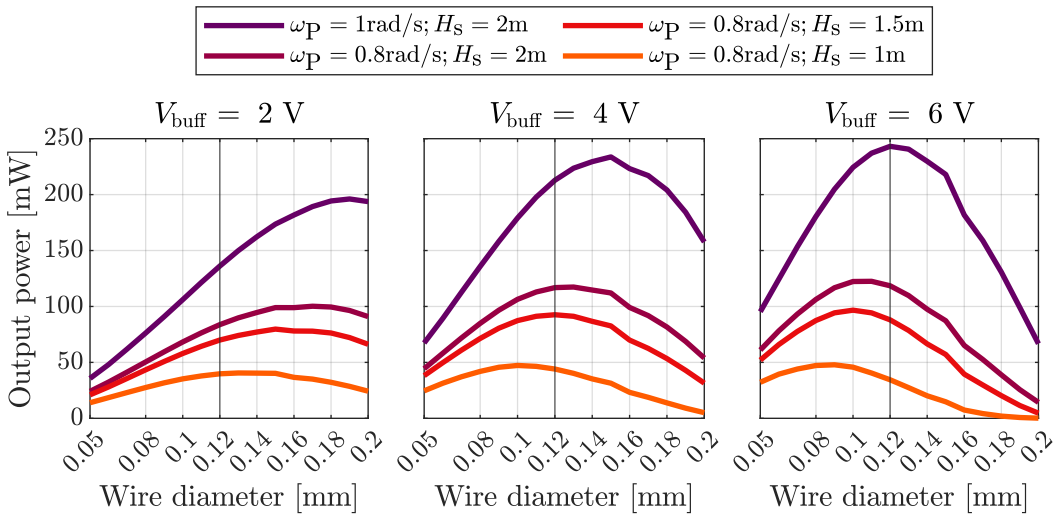

Figure 94: *Influence of capacitor voltage V_{buff} and wire diameter d_{coil} on the power output of the generator in irregular waves at different sea states. The selected diameter of* 0.12 mm *is highlighted in all plots.*

goal of the WEC is to cover the power demand of the electronics, which can be around 50 mW according to the requirement specification. This power should not only be served in good wave conditions, but also in sea spectra with lower power densities. Therefore, a series of simulations of the entire system with the excitation of irregular waves is carried out for each combination of voltage and wire diameter. Four different

sea states are simulated. Besides the defined operation spectrum with $\omega_P = 1\,\frac{\text{rad}}{\text{s}}$ and $H_s = 2\,\text{m}$, three lower power density spectra with with $\omega_P = 0.8\,\frac{\text{rad}}{\text{s}}$ and $H_s = [1,1.5,2]\text{m}$ are compared.
It can be seen, that with higher capacitor voltage values, the wire diameter should be selected lower, to allow more coil windings and therefore increase the induction voltage. The maximum power output is generated with a voltage level of 6 V and 0.12 mm winding diameter in the operation spectrum. For the spectrum with the lowest power density, a wire diameter of 0.1 mm at 4 V would be preferable. The 6 V and 4 V voltage level show significantly higher output power, compared to the 2 V level, while the largest power output is produced at 6 V and 0.12 mm in the operation spectrum. Since the overall difference between 4 and 6 V is marginal, the voltage closest to the battery voltage V_{Bat} is selected. By that, the power losses in the DC/DC converter can be minimized. Considering a 3.7 V Li-Ion battery, therefore suggest a capacitor voltage of 4 V. Since the power output with the higher power density spectra is way above the required 50 mW power output, the winding diameter is selected to increase the efficiency in sea states with lower energy potential. Here, 0.12 mm seems to bring a good trade-off, that brings high efficiencies for all sea states and is therefore selected for the coil winding diameter. With the given generator space, this leads to a winding number of 1800 turns. The calculated coil parameter are summarized in table 34.

d_{coil}	N_{coil}	R_{coil}
0.12 mm	1800	228 Ω

Table 34: *Derived coil parameters for the selected coil geometry.*

6.10 Optimized WEC System: Implementation and Verification

To validate the derived models and analyze the actual performance of the optimized generator, a prototype is implemented and tested. However, the first generator prototype presented in section 6.5.5 exhibited a significant increase in forces due to an axial mismatch of the translator and stator combined with poor translator bearings. Therefore, an improved concept is proposed, followed by the implementation and test on a test bench. The aim is to validate the simulation models and estimate the power output of the generator implementation.

6.10.1 Improved Mechanical Implementation and Bearing Concept

The main challenge of the generator implementation is the bearing of the translator due to the increased transverse force on the translator caused by radial reluctance forces. These forces are transformed into axial forces through the bearing. The initially used sleeve bearing had a high coefficient of friction, resulting in significantly larger axial forces compared to the simulated cogging forces (cf. section 6.5.5). To overcome this issue, a housing design and bearing concept is developed that still allows easy manufacturing and assembly.
The construction of the stator is relatively simple and consists of the arrangement of discs and magnets. The coils are fitted inside steel sleeves. All stator parts are assembled in the housing, consisting of a tube with two lids carrying the bearing. Linear ball bearings are used to reduce the coefficient of friction to lower the axial forces on the translator (cf. figure 95).

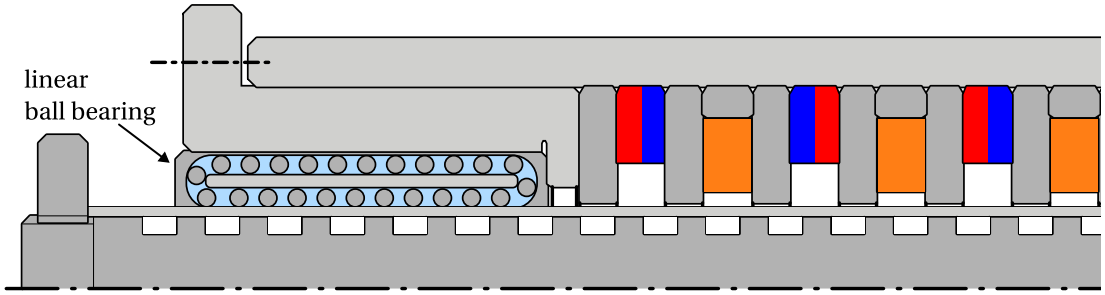

Figure 95: *Sketch of the implementation concept of the FSPMLM generator based on a linear bearing and a steel tube. See appendix A.5 for a technical drawing.*

To allow the bearings to roll smoothly on the translator, a continuous surface must be provided. This can be achieved by using a thin-walled continuous stainless-steel tube.

The translator is fitted inside the tube, and the bearings can roll on a smooth surface to reduce friction. Inside the tube sits the translator with its poles. While the use of the steel tube increases the air gap of the generator by the wall thickness of 0.5 mm, it also allows for a strong reduction of the forces due to the good bearing. This increase in the air gap does reduce the power output of the generator, but it is a necessary trade-off to achieve the benefits of the improved bearing design.
The technical drawing in appendix A.5 provides an overview of the generator's dimensions and mechanical implementation.

6.10.2 Model Validation and System Power Output Verification

The improved generator is implemented and tested on a testbench (cf. figure 96). The circuit outlined in section 6.6 is used for rectification and measurement of the coil voltages and currents. The translator is driven by a LinMot linear motor in the

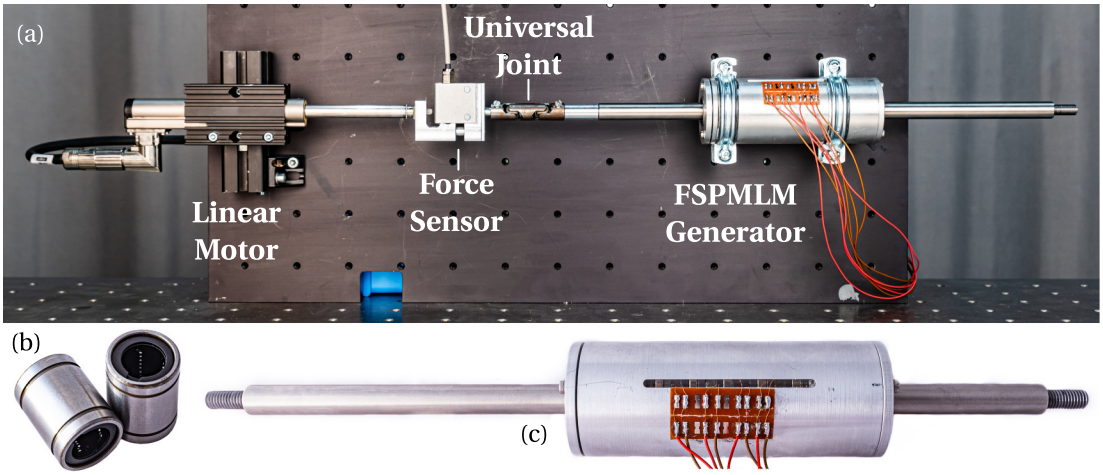

Figure 96: *a: Testbench implementation with the FSPMLM generator, force sensor and linear motor; b: Linear bearing implemented in the generator; c: Implemented FSPMLM generator.*

fixed stator and cogging forces are measured with a Burster 8512 [256] force sensor. The voltages and currents of the coils are monitored with the developed generator electronics.
In the first experiments, the behavior of the implemented generator is compared with the generator model to validate the system description. For this purpose, an open-circuit and a short-circuit measurement is carried out at a constant speed of 0.2 $\frac{\mathrm{m}}{\mathrm{s}}$. Figure 97 shows the comparison of the measurement results with the simulation data. The short circuit is implemented on the DC side of the rectifier and the coil current is measured. Both the short-circuit current and the open-circuit voltage are about 10% smaller compared to the simulated values but otherwise, show high agreement. The

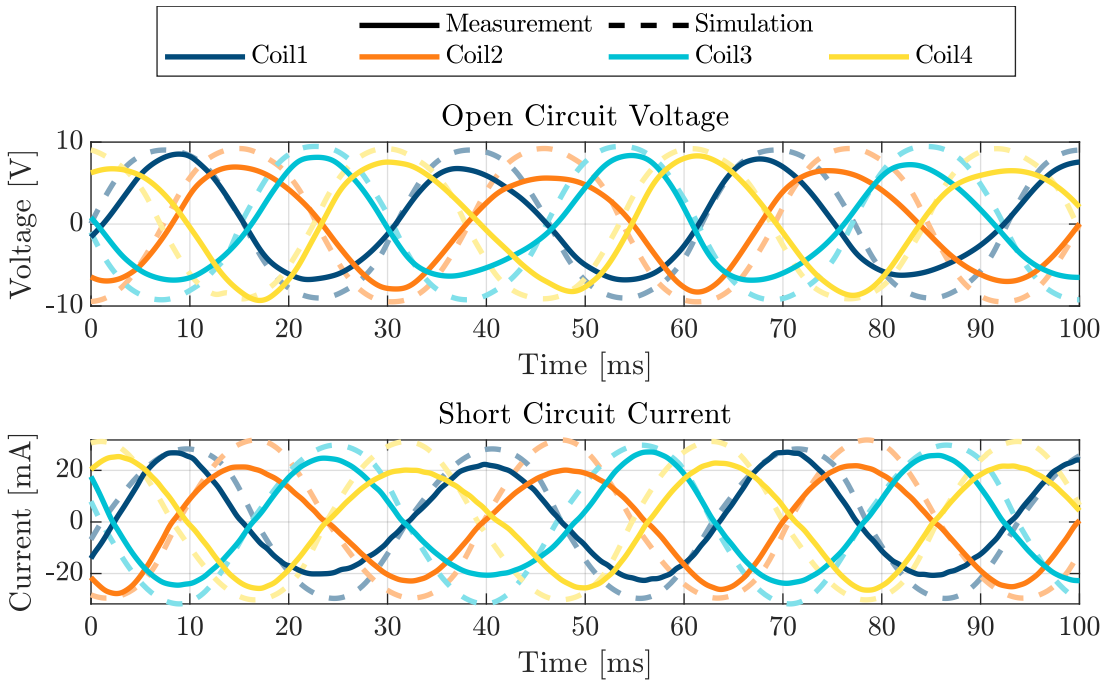

Figure 97: *Assessment of simulation and measurement results for short-circuit current and open-circuit voltage at a constant translator speed of* $0.2\,\frac{\mathrm{m}}{\mathrm{s}}$.

similarity of the deviation shows that the model description is valid, only the induction in the coils is smaller than in the model. This can be explained by a lower magnetic flux, resulting from e.g. weaker magnets than simulated or larger leakage fluxes due to the increased air gap.
In order to compare the cogging forces, the forces of the open circuit measurement are compared with the simulation (cf. figure 98). Here it is clear that the oscillation of the forces of the implemented generator is not as strong as simulated, but the upper force amplitude shows a good agreement with the measurement result. The lower oscillation can be explained by the fact that inertia and friction are not considered in the model. Compared to the first implemented prototype from section 6.5.5, the reduction of the frictional forces due to the linear bearings used (cf. figure 96b) becomes evident. The improved bearing thus also enables validation of the force modeling, which always showed strong deviations in the previous experiments (cf. figure 86). During the course of the experiments, rapid degradation of the bearings was noticed, causing an increase in the linear forces. This was caused by the linear ball bearings indenting the thin steel tube between the poles of the translator. To prevent similar occurrences in future designs, it is recommended to fill the air gaps between the translator poles with a material of equal hardness as steel, to prevent indentation.

In order to evaluate the overall performance of the generator in combination with the rectification and charging circuit, the voltage of the capacitor C_{buff} (cf. figure 88) is

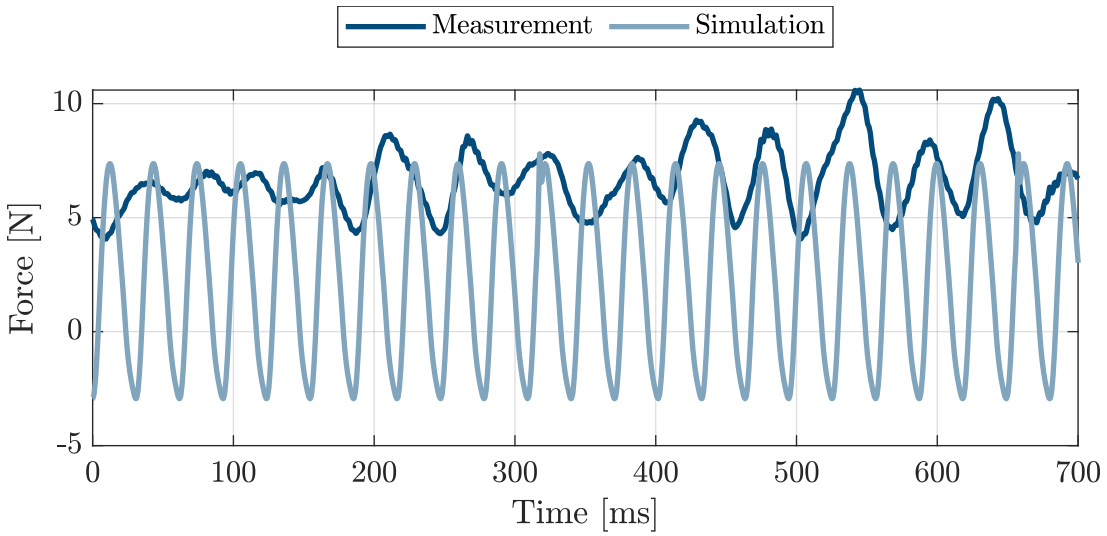

Figure 98: *Comparison of measured and simulated cogging forces at a translator speed of* $0.2\,\frac{\mathrm{m}}{\mathrm{s}}$ *without electrical load.*

measured in addition to the coil voltage and the coil current. Figure 99 shows the measurement data of an experiment in which the translator is continuously moved back and forth at a constant speed of $0.2\,\frac{\mathrm{m}}{\mathrm{s}}$. In addition to the coil voltage and the coil current, the voltage of the capacitor (V_{buff}) is also measured. The voltage in the capacitor increases until it reaches the hysteresis limit of approx. 4 V, causing the Schmitt trigger to switch (cf. A in figure 99). The capacitor then discharges to the lower hysteresis limit of approx. 3 V (cf. B in figure 99). The discharge of the capacitor was realized here by a short circuit at the input of the DC/DC converter since a minor design error in the supply of the DC/DC converter prevented its use. However, this does not affect the validation of the functionality of the rectifier and charging circuit, since the electric load for the coils is defined through the voltage level at the capacitor C_{buff}.
The comparison of the harvested DC power from the measurement with the average power at $0.2\,\frac{\mathrm{m}}{\mathrm{s}}$ from the simulation reveals that the actual generator has a slightly lower output compared to the ideal model (cf. C in figure 99). This can be attributed to the already mentioned reduced induction and additional non-idealities such as leakage currents and line resistances. Despite this, the generator still performs well as it closely follows the ideal simulation model and results in improved power output. The reduced air gap and the use of linear bearings result in reduced cogging forces. Compared to the previous prototype, the current implementation shows a noticeable improvement in both power output and reduced cogging forces, confirming the effectiveness of the optimization process.

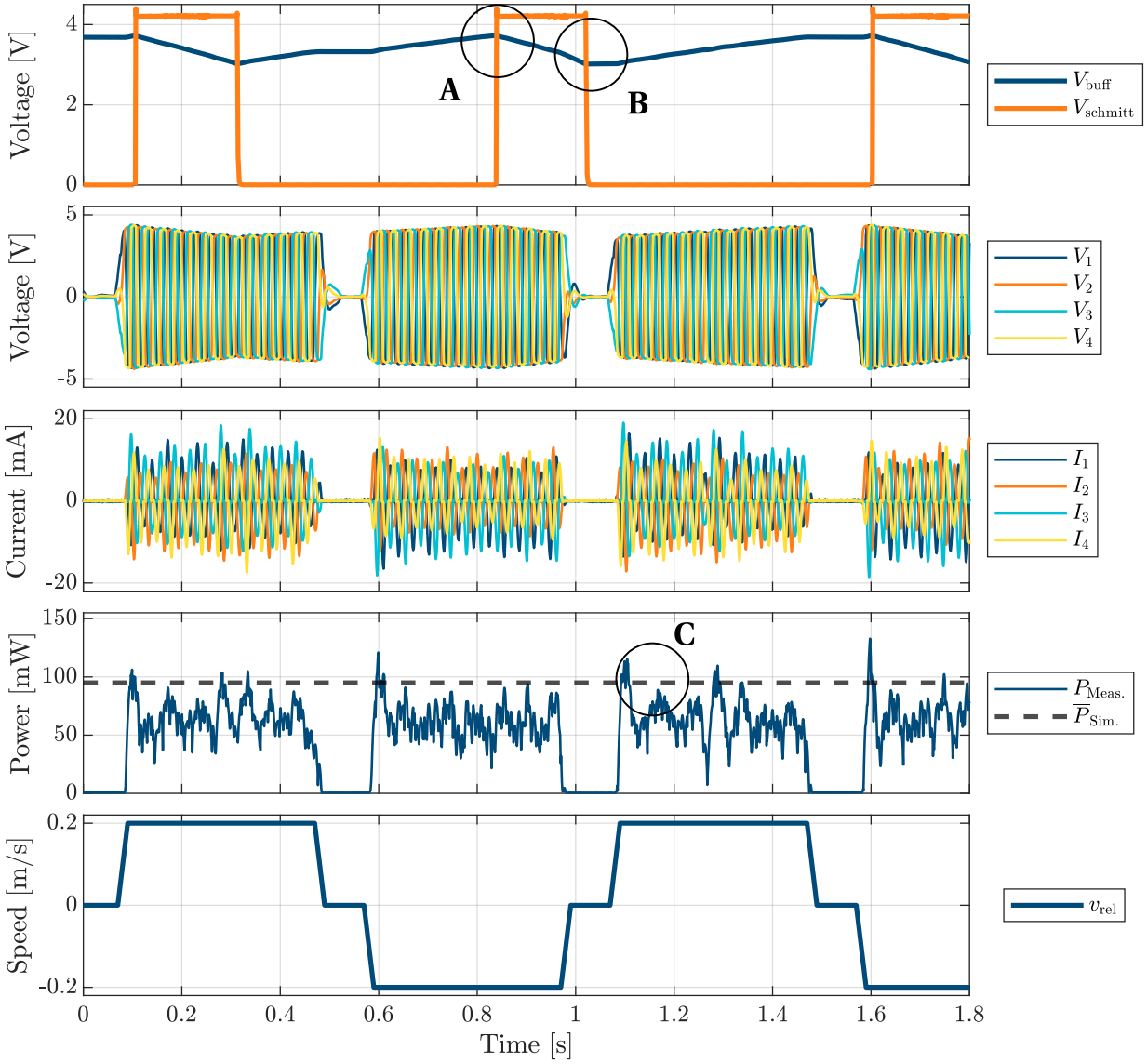

Figure 99: *Experimental results of translator's back-and-forth movement (top to bottom): Buffer capacitor voltage and Schmitt trigger output voltage; Coil voltages; Coil currents; Realized DC power compared to simulated average power at* $0.2\,\frac{\text{m}}{\text{s}}$*; Translator speed in the experiment.*

6.10.3 Estimating Wave Energy Harvesting Power Yield in Realistic Sea Conditions

A simulation of the coupled model (cf. 6.3.2) was carried out to evaluate the performance of the overall system in irregular sea states. Validation through testing would require a waterproof mechanical implementation in a drifter, which was beyond the scope of this work. The focus of this study was on electromagnetic design and optimization, and therefore, full integration into a drifter was not considered.
The selected generator geometry A from section 6.5 is simulated for the geometry of the experimental prototype and the optimized mechanical system 1 from section 6.8. Figure 100 shows the average power output of both systems in random waves with different peak frequencies ω_P at a significant wave height of $H_\mathrm{s} = 2\,\mathrm{m}$. It can be seen that

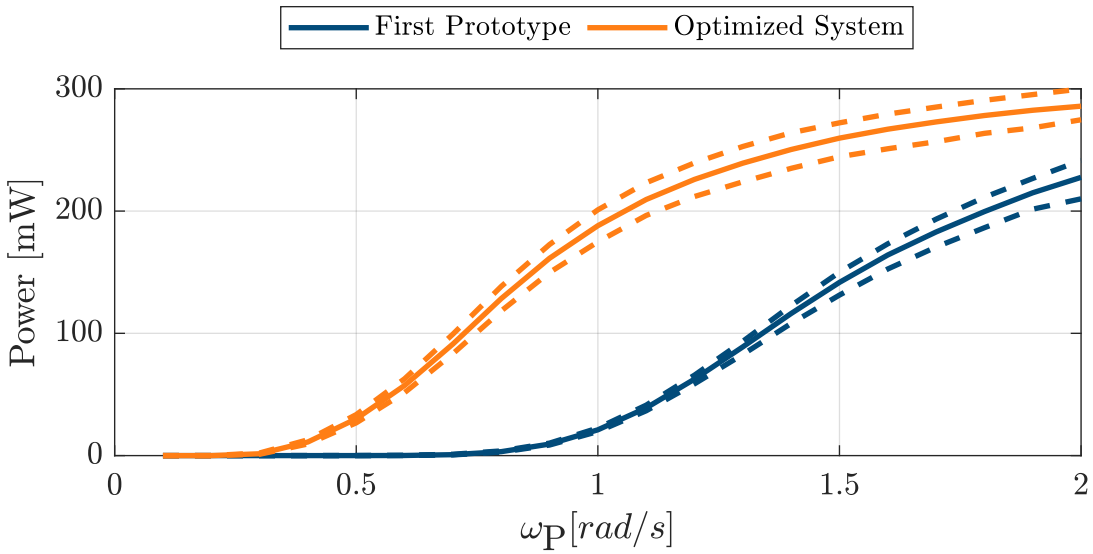

Figure 100: *Average power output of the optimized system compared to the first prototype implementation simulated in irregular sea states with peak frequencies between* $\omega_\mathrm{P} = [0.2 \ldots 2]\frac{\mathrm{rad}}{\mathrm{s}}$ *at* $H_\mathrm{s} = 2\,\mathrm{m}$.

the optimized system leads to increased power output, already at low peak frequencies. For the operation spectra at $\omega_\mathrm{P} = 1\frac{\mathrm{rad}}{\mathrm{s}}$, the selected WEC achieves an average power output of almost 200 mW compared to below 50 mW with the prototype system of the first experiments. The required power output of 50 mW can be achieved with the designed WEC in sea states with $H_\mathrm{s} = 2\,\mathrm{m}$ at peak frequencies of above $0.5\,\frac{\mathrm{m}}{\mathrm{s}}$.

6.11 Evaluation of Energy Harvesting Results

This chapter outlines a methodological approach for designing a wave energy harvesting system suitable for a self-sufficient ocean surface monitoring platform. The design approach considers the requirements of low wave excitation frequencies and a compact drifter with a short drogue for coastal applications while maintaining its outer appearance. To achieve this, a thorough review of wave energy harvesting methods was conducted, resulting in a WEC concept based on a self-reacting point absorber (SRPA) that utilizes a flux switching permanent magnet linear machine (FSPMLM) for power takeoff.

To optimize the overall power output of the system, a model-based design approach was employed, which considered the interdependencies of the mechanical, electromagnetic, and electric components. By optimizing the generator's electromagnetic properties, cogging forces were significantly reduced to below 10 N, thus minimizing the damping effect on the mechanical dynamics of the wave energy converter. To further enhance performance, a multi-domain optimization of the entire system was carried out.

The development effort has led to the creation of a highly promising wave energy harvesting prototype that is estimated to produce a power output of approximately 200 mW under realistic sea conditions in the North Sea. This power output is deemed sufficient for powering the monitoring system outlined in Section section 4, making it an ideal solution for long-term drifter deployments.

More work is needed to enhance the mechanical functionality of the wave energy harvesting method. Specifically, testing the overall system will require a waterproof housing that seamlessly integrates with a drifter. Additionally, exploring alternative manufacturing methods for the translator could improve the bearing concept. Eliminating the stainless-steel tube from the translator concept would also decrease the air gap and boost the generator's power output.

The wave energy harvesting system proposed, presents a valuable solution for meeting the energy needs of future drifters with advanced instrumentation. With ongoing research, the performance of the system can be further enhanced, increasing its potential for widespread deployment in sea surface monitoring applications.

7 Summary and Outlook

7.1 Summary

This thesis aims at enhancing the availability and accessibility of in-situ sea surface monitoring by facilitating a systematic design approach. By evaluating both, the potentials and limitations of current ocean drifter systems, it became apparent that available systems lack the flexibility needed to meet the requirements of a broad range of applications. To improve the monitoring capabilities for marine science, a low-cost and adaptable in-situ measurement platform is essential in order to enable high spatial resolution measurements of the sea surface and to allow customizable monitoring tasks. A system with customizable sensor integration and measurement settings as well as a self-sufficient power supply to handle long-term deployments is needed.

To address these issues, a system design for a multi-sensor platform with special consideration for data acquisition, energy supply, and data processing was proposed. The system-level design identified three main components with significant development prospects: a flexible measurement module, an embedded CT-sensor for salinity measurement, and a wave energy harvester for a sustainable power supply.

For the measurement module, the key characteristics of a flexible and user-friendly system architecture that allows for the customized implementation of sensors were investigated. It became evident that modular system architecture is essential to create a user-friendly and adaptable monitoring system. The module provides a hardware and software architecture enabling the flexibility necessary for various monitoring tasks. The system's central main board implements all essential tasks such as data processing, scheduling, and storage. In addition, the main board integrates the hardware required for most applications, such as GPS position, acceleration, and PHT sensor (pressure, humidity, and temperature), and controls the execution of the measurement cycles. The software structure is kept simple and implements a fault-tolerant design to ensure a reliable monitoring system. The main board is extendable with sensor and communication boards, allowing for an easy configuration of the measurement setup, the

required sensors, and the choice between different transmission methods. The proposed architecture was tested by deployment on an ocean drifter, effectively validating its performance. The resulting monitoring system shows promise for improving the accessibility and availability of in-situ ocean surface monitoring.

The second main component is an embedded CT-sensor intended for long-term, near-surface ocean monitoring to reduce monitoring costs and enable large-scale deployments. After a systematic analysis considering the physical fundamentals and environmental influences on conductivity and temperature measurement, design principles allowing to balance measurement uncertainty against cost were established. A sensor concept consisting of a transformer-type inductive conductivity sensor and a temperature measurement circuit based on a dual-slope analog-to-digital converter was proposed. A systematic analysis of the parameter influences, contributed to a deeper understanding of the sensor's functionality, allowing to focus the design on critical factors. A sensor prototype tested shows a promising accuracy (50 $\frac{\mathrm{mS}}{\mathrm{m}}$) with low systematic errors. The temperature sensor circuit delivers stable readings with high precision (up to 5 mK) but a systematic error in the sensor characteristic was identified. Overall, the CT-sensor exhibits promising results, indicating that the set requirements can be achieved with the proposed hardware revision. The sensor's low component costs demonstrate its potential to become a valuable tool for high-resolution sea surface monitoring applications. The fully self-contained CT-sensor allows compact integration into small monitoring instruments such as ocean drifters and shows great potential for improving the balance between accuracy and cost for sea surface salinity monitoring.

The increased demand for energy due to the rising instrumentation of monitoring platforms is addressed by the third component of the system design. To sustain long-term deployments regardless of location and season, a wave energy harvesting system for shallow water drifters was proposed. The WEC is based on a self-reacting point absorber (SRPA) and a flux switching permanent magnet linear machine (FSPMLM) for power take-off. The system was designed using a multi-domain development approach and a model-based design method, which effectively addressed the interdependencies in the development process. Simulation and optimization of the WEC showed an estimated average power output of 200 mW, which offers a new source of energy, particularly for shallow water drifters. Deep-water drifters with longer drogues are expected to produce a larger power output. The compact design of the system allows for integration into the drifter without altering its outer appearance, unlike other wave energy harvesting concepts. Further improvements proposed include creating a waterproof housing and exploring alternative manufacturing methods for the translator to enhance power output. The methodological approach used in the development of this wave energy harvesting system offers a promising solution for designing self-sufficient monitoring platforms, particularly for shallow water drifters, and has the potential to yield significant amounts of energy for long-term deployments.

7.2 Conclusion

The overall system design successfully identified areas for enhancement in ocean drifters and addressed crucial research questions through the development of three innovative components by utilizing a systematic design approach. This approach allowed efforts to be focused on areas that require modification, resulting in a more effective system design. The results of this work demonstrate the critical role of modular hardware and software architecture in the development of flexible and user-friendly monitoring systems. The findings emphasize a modular architecture to be a crucial characteristic that enables effective system functionality and flexibility. As such, it represents an indispensable tool that can significantly improve ocean surface observation.

The design principles established for the embedded low-cost CT-sensor demonstrate how to balance accuracy and affordability to improve the spatial resolution of sea surface monitoring. The results show that a model-based design approach is an effective tool for parameterizing the primary sensor, allowing measurement uncertainty to be optimized while focusing on critical design parameters. The findings highlight the importance of a component-level simulation model to account for the influences of the sensor's primary electronics. Moreover, it is crucial to continuously validate sensor prototypes through experiments in order to refine and enhance the system's functionality. This can be achieved by running multiple V-cycle loops.
The results indicate that employing a systematic approach to system design through model-based development can successfully manage interdependencies in the development process, as exemplified by the wave energy converter. Emphasizing individual subsystem optimization during early development, followed by integrated system optimization in later stages, was identified as a highly effective strategy. For coupled model optimization with large parameter spaces, it is critical to perform a physical analysis of the sub-components to derive basic model constraints to reduce the parameter space. Here, before optimizing the coupled system, optimizing the linear generator at the electromagnetic field level to increase power and reduce cogging forces was a critical step. Overall, the proposed optimization approach provides a reliable and efficient method for developing and optimizing wave energy converters and obtaining initial estimates for system prototypes.

In conclusion, this thesis has successfully addressed critical research questions through the proposal of innovative components and a methodical approach to system design. The findings of this work have the potential to significantly advance the innovation of sea surface monitoring, particularly in the areas of sensors and energy harvesting. All components contribute to the systematic design of an *Autonomous Multi Sensor Drifter*, the resulting and continuing project for ocean surface monitoring at the Institute for Mechatronics in Mechanics (iMEK) of the Hamburg University of Technology (TUHH).

7.3 Outlook

The Autonomous Multi Sensor Drifter project at the iMEK will build upon the work of this thesis. To identify any architectural drawbacks and unlock further development potential, it is necessary to carry out in-field tests with larger deployment numbers. Adopting an agile software development approach with continuous integration would be beneficial in this regard, as it would enable the system to be developed with a focus on continuous improvement, and the ability to test changes as frequently and early as possible.

The project should continue to build on model-based development approaches as they have proven useful in designing the CT-sensor and optimizing the wave energy harvesting system. While the early phases of development initially required the optimization of individual subcomponents, it would be feasible to adapt the coupled model to simplify the optimization of the overall system for future stages. This would facilitate adjustments in case of changing requirements or geometric adaptations during the design process. To achieve this, a Design of Experiments (DoE) method could be used, which allows the mapping of the entire optimization parameter space by selective sampling of experimental or simulation results. This enables the creation of mathematical regression models (metamodels) to consider the entire parameter space through a minimal number of simulations.

To simplify the coupling of subcomponents and to seamlessly integrate additional components, the utilization of the Functional Mockup Interface (FMI) can replace the current differential equation-based model description. This approach would enable the adoption of a common standard for physical model interaction, expanding the capabilities of the system model.

With regard to the technical advancement of the monitoring module, the implementation of two-way satellite communication is crucial to enable the reconfiguration of measurement cycles during deployment. Integration of additional communication boards, including the swarm satellite module, a GSM module, and a Lora module, should be pursued. The size of the PCB could be reduced to allow easier integration into smaller systems. A size reduction by half can be achieved if the PCB is assembled two-sided and a 4-layer layout is used.
In future software releases, a real-time operating system (RTOS) can be implemented between the middleware and the application layer to improve state machine scheduling and enable non-blocking and multi-threading capabilities. Incorporating an RTOS into the software framework would provide improved performance and reliability, as well as the ability to handle multiple tasks simultaneously.
To further improve the reliability and robustness of the monitoring system, it is important to consider fault tolerance and error-handling techniques. One way to achieve this

is to implement cyclic redundancy checks (CRC) or checksum mechanisms to verify the integrity of the transmitted data. In addition to these techniques, other error-handling mechanisms such as retry mechanisms can be considered to improve the overall robustness of the system. These techniques can help ensuring correct data transmission, processing, and storage even in the presence of errors or failures.

Improving the functionality and accuracy of the embedded CT-sensor requires several enhancements, which can be achieved by repeating the development V-cycle and validating additional sensor prototypes. A prototype with exchangeable secondary and primary electronics can facilitate swift modification of the design setup.
To improve the hardware of the conductivity sensor, it is crucial to implement the proposed revision in 5.3.6 and conduct further testing to determine measurement uncertainty and long-term stability. Determining the temperature sensor characteristic can also enhance accuracy.
To make the sensor functional, it is necessary to design calibration procedures for reliable and consistent measurements. Additionally, the software implementation for combined salinity measurement must be further developed to provide a communication interface and control logic that enables direct integration of the sensor into the measurement module.

The next step for the development of the wave energy harvesting system is the mechanical integration into a drifter. The testing of the waterproof sealing concept is required. One option for a waterproof integration is to fully enclose the translator with bellows, the drawback being high space consumption and complex construction. Another option is to use hydraulic seals, here the drawback would be increased frictional damping. Additionally, the stator electronics can be waterproofed by casting it to prevent permanent damage from water penetration. To further improve the power output of the generator, the translator manufacturing process could be redesigned to reduce the magnetic resistance attributed to the stainless-steel tube. This can be achieved by filling the space between the translator poles with a non-ferromagnetic material or by manufacturing the translator from several stacked disks of non-magnetic brass and steel.

Furthermore, a test on the system level is necessary by implementing a drifter, that utilizes the energy harvesting system and collects the data from the embedded CT-sensor by the measurement module.

A Appendix

A.1 Sensors and Measurements: Definition of Measurement Uncertainty

Measurement uncertainty is an important factor in the evaluation of sensor technologies, as it describes the reliability and accuracy of the measurements obtained. Considering the different definitions of measurement uncertainty in the literature and the different interpretations of the defining terms, this section aims to provide a clear definition of measurement uncertainty for the purposes of this thesis.

Measurement uncertainty refers to the range of values within which the true value of a measurement is believed to lie. Various factors must be considered when determining measurement uncertainty, including accuracy, precision and resolution.

Accuracy Accuracy is defined as the degree to which a measurement agrees with the true value of the quantity measured. In other words, accuracy is a measure of how close the measured value is to the true value. A measurement can be considered accurate if it is free from systematic errors such as instrument malfunctions or incorrect calibrations. For an ideal linear sensor characteristic, for example, the linearity error defines the accuracy of the sensor.

Precision Precision is defined as the extent to which repeated measurements of the same quantity give the same results. Precision is a measure of the reproducibility of measurements affected by random errors such as variations in temperature or power supply. Random noise errors affect almost every component of the sensor and contribute to lower measurement precision. A value for the precision of a set of measured values of the same quantity can be calculated by the standard deviation of the set.

Resolution In the scope of this work, the term resolution refers to the technical resolution of the measurement reading. The resolution describes the smallest change in the quantity being measured that can be distinguished. Here, the resolution is mainly influenced by the digital resolution such as the bit-resolution of the ADC or the size of the data type.

A.2 Practical Salinity Scale

The Practical Salinity Scale of 1978 (PSS-78) is the internationally recognized standard for measuring the salinity of seawater, and is used to convert conductivity data into salinity data. This scale has been adopted by oceanographic organizations worldwide and is widely considered to be the most accurate method for measuring seawater salinity. The PSS-78 is based on the conductivity ratio K_{15} and derives the salinity S by [21]:

$$S = a_0 + a_1 K_{15}^{\frac{1}{2}} + a_2 K_{15} + a_3 K_{15}^{\frac{3}{2}} + a_4 K_{15}^{2} + a_5 K_{15}^{\frac{5}{2}} \tag{84}$$

with K_{15} being the ratio to the conductivity value of seawater at 35 PSU and 15 °C, at atmospheric pressure.

$$\sigma(35\,\mathrm{PSU}, 15\,°\mathrm{C}, 0) = 4.2914\,\frac{\mathrm{S}}{\mathrm{m}} \tag{85}$$

$$K_{15} = \frac{\sigma(S, 15\,°\mathrm{C}, 0)}{\sigma(35\,\mathrm{PSU}, 15\,°\mathrm{C}, 0)}. \tag{86}$$

The coefficients of a_i are listed in table 35:

i	a_i	b_i	c_i	d_i	e_i
0	0.0080	0.0005	6.766097×10^{-1}		
1	−0.1692	−0.0056	2.00564×10^{-2}	3.426×10^{-2}	2.070×10^{-5}
2	25.3851	−0.0066	1.104259×10^{-4}	4.464×10^{-4}	-6.370×10^{-10}
3	14.0941	−0.0375	-6.9698×10^{-7}	4.215×10^{-1}	3.989×10^{-15}
4	−7.0261	0.0636	1.0031×10^{-9}	-3.107×10^{-3}	
5	2.7081	−0.0144			

Table 35: *Coefficients of the PSS-78.*

To calculate the conductivity ratio from in-situ conductivity measurements, the ratio R is derived from three factors:

$$R = \underbrace{\frac{\sigma(S,T,p)}{\sigma(S,T,0)}}_{R_\mathrm{p}} \underbrace{\frac{\sigma(S,T,0)}{\sigma(35\,\mathrm{PSU},T,0)}}_{R_\mathrm{T}} \underbrace{\frac{\sigma(35,T,0)}{\sigma(35\,\mathrm{PSU},15\,°\mathrm{C}}}_{r_\mathrm{T}} \tag{87}$$

whereas the temperature-dependent coefficient of standard seawater r_T is derived from

$$r_T = c_0 + c_1 T + c_2 T^2 + c_3 T^3 + c_4 T^4 \tag{88}$$

and the pressure coefficient R_p is derived from

$$R_P = 1 + \frac{p\left(e_1 + e_2 p + e_3 p^2\right)}{1 + d_1 T + d_2 T^2 + \left(d_3 + d_4 T\right) R}. \tag{89}$$

The temperature coefficient R_T can be derived from arranging eq. (87) to:

$$R_T = \frac{R}{R_p r_T} \tag{90}$$

Considering eqs. (84) to (86), this allows the calculation of the salinity S_T at temperature T according to:

$$S_T = a_0 + a_1 R_T^{1/2} + a_2 R_T + a_3 R_T^{3/2} + a_4 R_T^2 + a_5 R_T^{5/2} + \Delta S \text{ , where} \tag{91}$$

$$\Delta S = \frac{T - 15\,°\text{C}}{1 + 0.0162 \cdot \left(T - 15\,°\text{C}\right)} \left(b_0 + b_1 R_T^{1/2} + b_2 R_T + b_3 R_T^{3/2} + b_4 R_T^2 + b_5 R_T^{5/2}\right) \tag{92}$$

with the valid range of −2 °C to 35 °C and 0.2 PSU to 42 PSU. [21]
The conductivity to salinity characteristic for different temperatures at constant atmospheric pressure is visualized in figure 101.

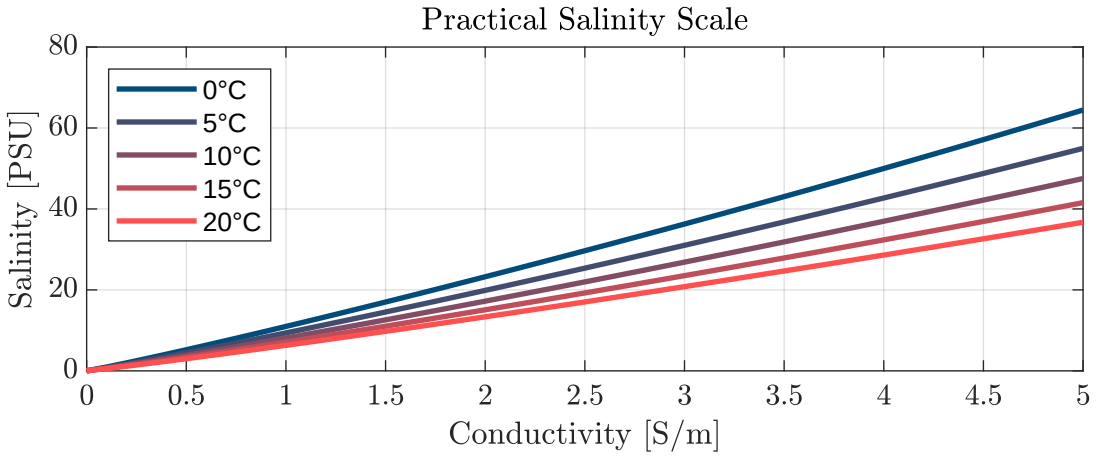

Figure 101: *Salinity over conducitivity for different temperatures at constant atmospheric pressure according to PSS-78.*

A.3 Communication Protocoll Definitions

The following tables define the status and error codes of the generic protocol presented in section 4.4.

Hex	Request Command	Hex	Response Command
0x00	reserved	0x14	reserved
0x01	REQUEST_GET_NUMBER_SENSORS	0x15	RESPONSE_GET_NUMBER_SENSORS
0x02	REQUEST_RESET	0x16	RESPONSE_RESET
0x03	REQUEST_BE_READY_TO_MEASURE	0x17	RESPONSE_BE_READY_TO_MEASURE
0x04	REQUEST_ACTIVATE_SENSOR	0x18	RESPONSE_ACTIVATE_SENSOR
0x05	REQUEST_GET_SENSOR_MAX_MEASURE_TIME	0x19	RESPONSE_GET_SENSOR_MAX_MEASURE_TIME
0x06	REQUEST_TRIGGER_SENSOR	0x1A	RESPONSE_TRIGGER_SENSOR
0x07	REQUEST_IS_SENSOR_MEASUREMENT_READY	0x1B	RESPONSE_IS_SENSOR_MEASUREMENT_READY
0x08	REQUEST_RETRIEVE_SENSOR_MEASUREMENT	0x1C	RESPONSE_RETRIEVE_SENSOR_MEASUREMENT
0x09	REQUEST_GET_STATE	0x1D	RESPONSE_GET_STATE

Table 36: *Translation of the request and response commands in the presentation layer.*

Hex	Return Code
0x00	MSG_RET_OK
0x01	MSG_RET_ERR
0x02	MSG_RET_SENSOR_NOT_AVAILABLE
0x03	MSG_RET_NO_MEASUREMENT_AVAILABLE
0x04	MSG_RET_SENSOR_BUSY_ONGOING_MEASUREMENT
0x05	MSG_RET_INVALID_PACKET
0x06	MSG_RET_FUNC_NOT_SUPPORTED

Table 37: *Translation of the return error codes in the presentation layer.*

A.4 Wave Properties

A.4.1 Sea States and Wave Spectra

In this work, the behavior of the WEC in water waves is simulated by considering two types of wave excitation: harmonic and random waves. Harmonics (a.k.a. regular) waves are periodic and have a constant frequency and wavelength. Random (a.k.a irregular) waves are non-repeating and have a diverse range of frequencies and wavelengths. The latter is often observed in the ocean and can be described using a statistical sea

spectrum. A sea spectrum represents the distribution of wave energy as a function of frequency or wave period. It provides an understanding of the sea state in terms of its frequency distribution.

To simulate a realistic sea surface, a superposition of many harmonic waves is used. Waves with frequencies ω, corresponding wave numbers $k_e(\omega)$, and amplitudes A are superposed for this, with the amplitudes obtained from the corresponding one-sided spectral density $S(\omega)$ [257, 258]. The Pierson-Moskowitz spectrum for deep water and the Joint North Sea Wave Project (JONSWAP) spectrum for shallow water waves are the most common sea spectral densities $S(\omega)$. The irregular long-crested sea surface can be determined for a given sea spectrum $S(\omega)$ by [224]:

$$Z(x,t) = \sum_{n=1}^{n_{\text{comp}}} \cos\big(\omega_n t - k_e(\omega_n)x + \varepsilon(\omega_n)\big)\sqrt{2S(\omega_n)\Delta\omega_n}, \tag{93}$$

where the spectrum is discretized into n_{comp} parts with respective widths $\Delta\omega_n$ and frequencies $\omega_n \in [\omega_{\min},\omega_{\max}]$ that do not have to be equidistant. Furthermore, $\varepsilon(\omega_n)$ is a phase shift that is distributed at random in the interval $[0,2\pi]$. The results for the Pierson-Moskowitz spectrum will be used in this work, which can be described by the peak frequency ω_P and the significant wave height H_s. If not explicitly stated, the peak frequency $\omega_P = 1\,\frac{\text{rad}}{\text{s}}$ and significant wave height $H_s = 2\,\text{m}$ are used in all subsequent calculations (cf. figure 102).

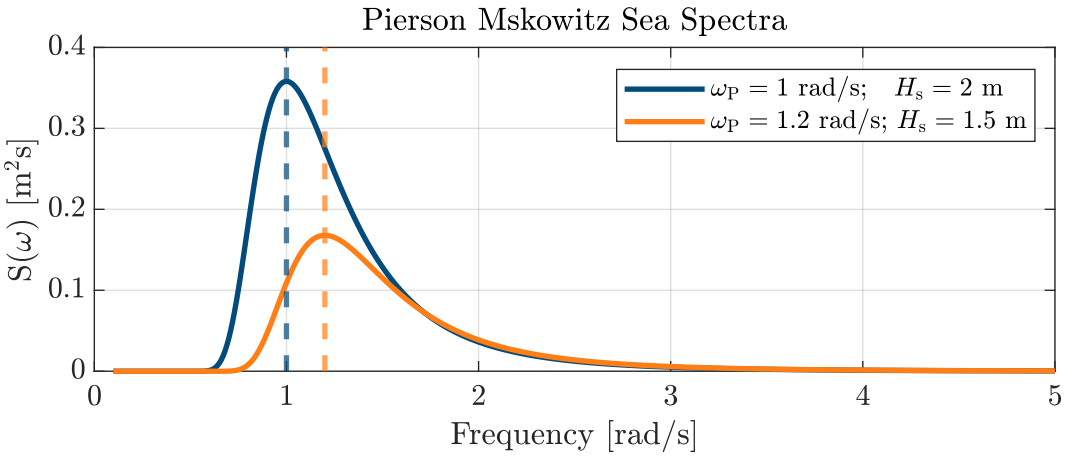

Figure 102: *Wave spectral density of two Pierson Moscowitz sea spectra with different peak frequencies (ω_P) and significant wave heights (H_s).*

A.4.2 Hydrodynamic Force and Pressure

The hydrodynamic force F_{h} can be derived from the integral of the acting hydrodynamic pressure p_{h} over the respective wetted surface A_w by

$$F_{\mathrm{h},w} = \iint_{A_w} p_{\mathrm{h}}(x,y,z,t)\, n_3 \mathrm{d}A \tag{94}$$

where n_3 describes the vertical normal vector pointing out of the fluid. The exact derivation of the hydrodynamic pressure p_{h} for harmonic and irregular waves is based on the potential flow theory and the results of Olaya et al. [223] and is described in detail in [224].

A.4.3 Wave Flume Parameter

For the experiments conducted in this thesis, the wave flume at the Institute of Mechanics and Ocean Engineering at the Hamburg University of Technology was utilized. The wave flume generates both harmonic and random waves through the back-and-forth motion of the wave flap. Detailed information about the maximum angles and other parameters of the wave flume can be found in Table 38.

Length	Width	Depth	Maximum wave height	Maximum wave frequency
12 m	1.50 m	1.50 m	0.6 m	2 Hz

Table 38: *Parameter values of the used wave flume.*

A.5 Circuits and Schematics

The following circuit drawings and schematics are attached:

- **AMuSeD_Main_V3:**
  Schematic of the main board PCB described in section 4.3
- **WEC_Measurement_PCB:**
  Schematic of the charging and rectification circuit described in section 6.6
- **Linear Generator Assembly Drawing:**
  Drawing of the FSPMLM Generator Assembly, designed in section 6

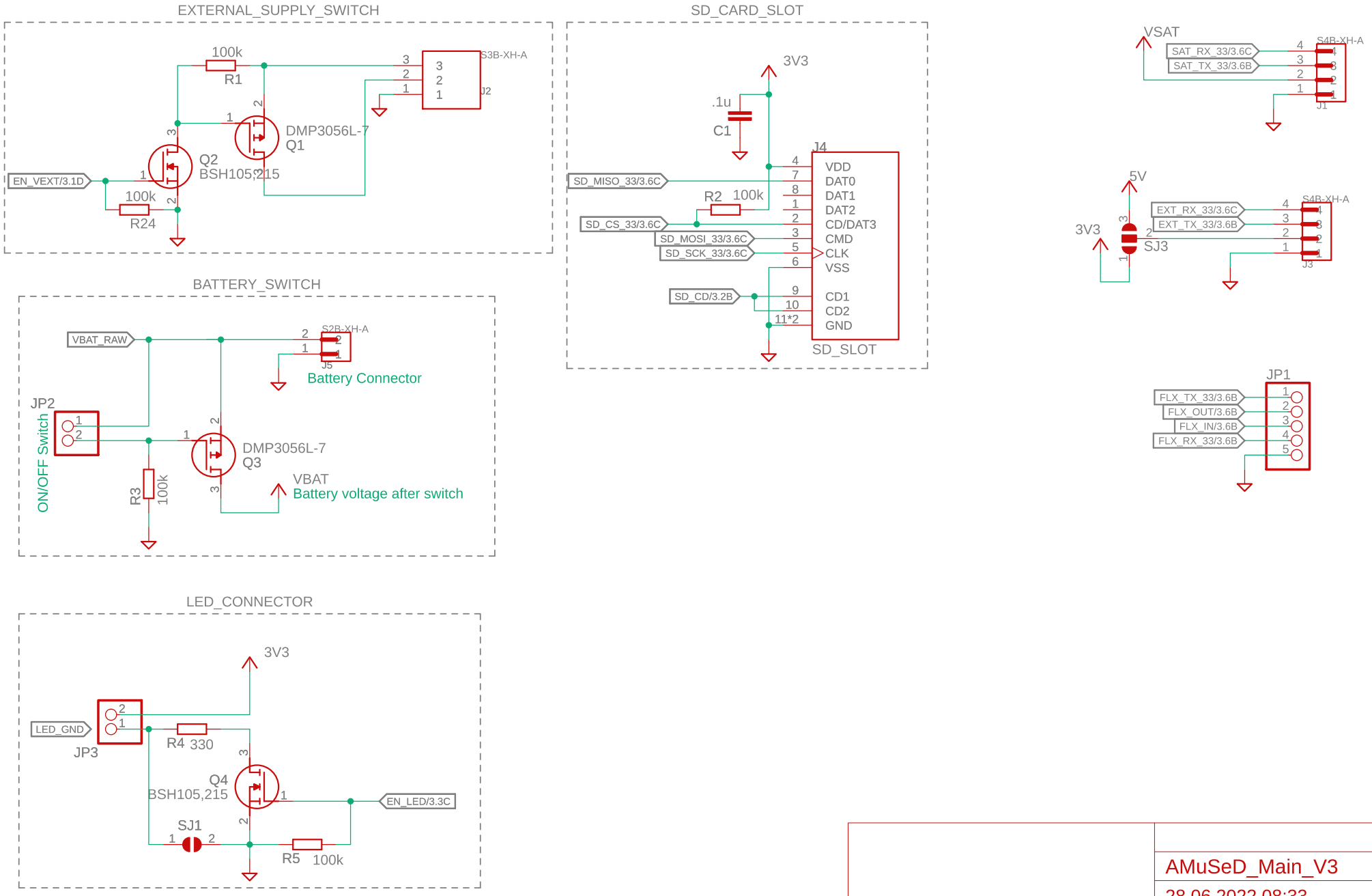

AMuSeD_Main_V3	
28.06.2022 08:33	
Sheet: 1/4	

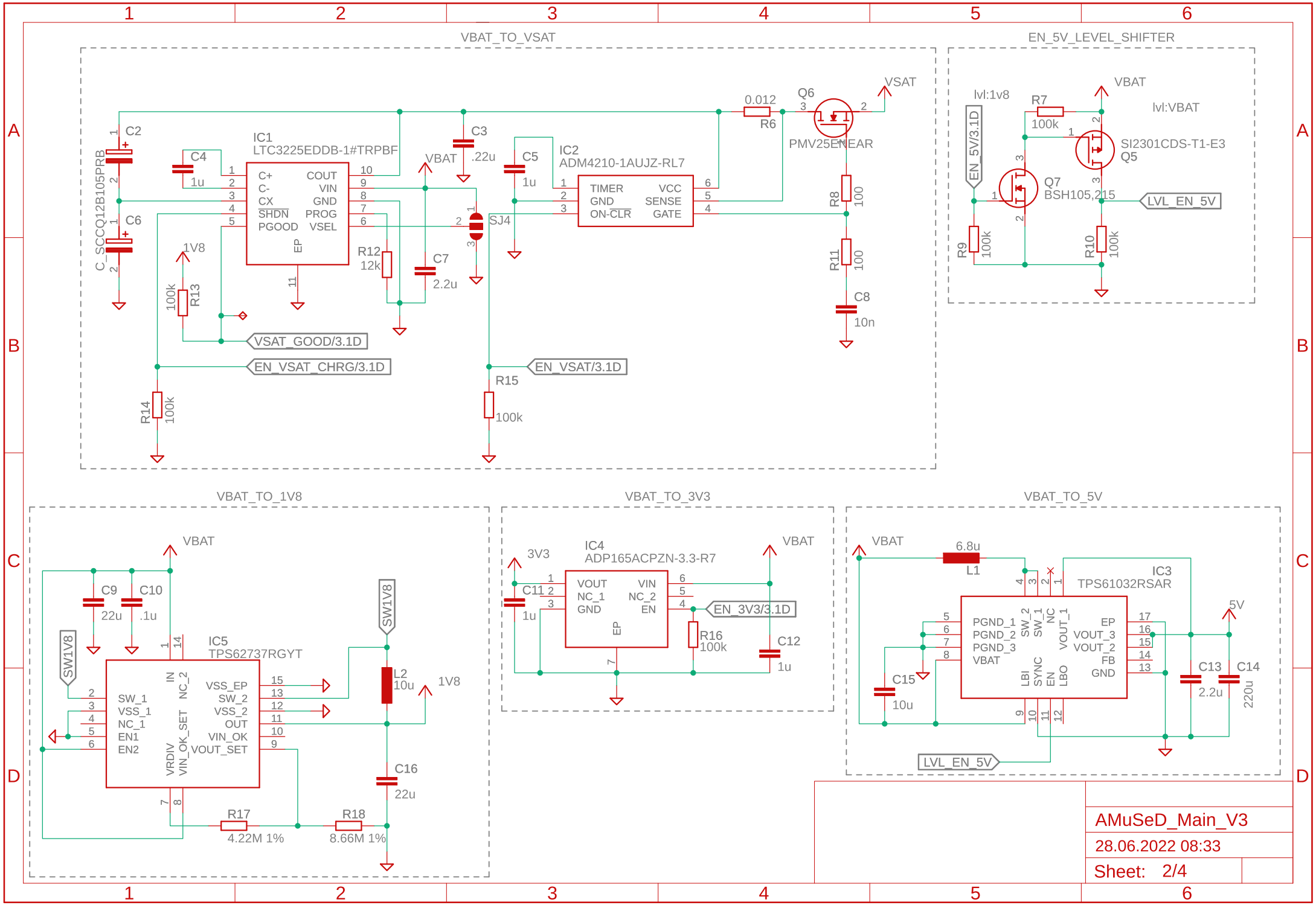
VBAT_TO_VSAT
EN_5V_LEVEL_SHIFTER
VBAT_TO_1V8
VBAT_TO_3V3
VBAT_TO_5V
IC1
LTC3225EDDB-1#TRPBF
IC2
ADM4210-1AUJZ-RL7
IC3
TPS61032RSAR
IC4
ADP165ACPZN-3.3-R7
IC5
TPS62737RGYT
C_SCCQ12B105PRB
PMV25ENEAR
SI2301CDS-T1-E3
Q5
Q7
BSH105,215
SJ4
VSAT
VBAT
3V3
1V8
5V
SW1V8
VSAT_GOOD/3.1D
EN_VSAT_CHRG/3.1D
EN_VSAT/3.1D
EN_3V3/3.1D
LVL_EN_5V
lvl:1v8
lvl:VBAT
EN_5V/3.1D
R4 4.22M 1%
R18 8.66M 1%
AMuSeD_Main_V3
28.06.2022 08:33
Sheet: 2/4

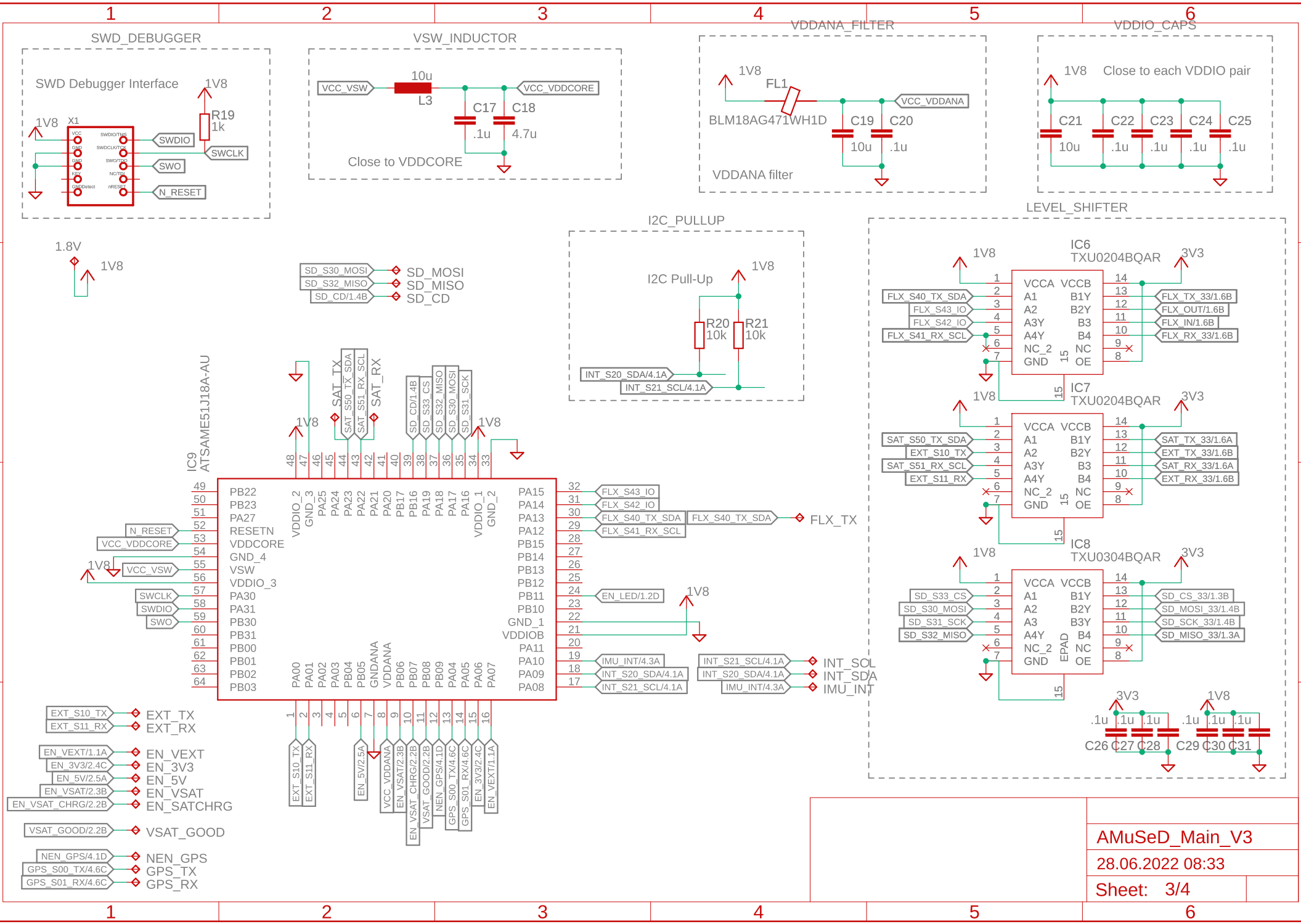
SWD_DEBUGGER
SWD Debugger Interface
1V8
X1
R19
1k
SWDIO
SWCLK
SWO
N_RESET
VSW_INDUCTOR
VCC_VSW
10u
L3
VCC_VDDCORE
C17
C18
.1u
4.7u
Close to VDDCORE
VDDANA_FILTER
FL1
BLM18AG471WH1D
VCC_VDDANA
C19
C20
10u
.1u
VDDANA filter
VDDIO_CAPS
Close to each VDDIO pair
C21
C22
C23
C24
C25
10u
.1u
1.8V
SD_S30_MOSI
SD_S32_MISO
SD_CD/1.4B
SD_MOSI
SD_MISO
SD_CD
I2C_PULLUP
I2C Pull-Up
R20
10k
R21
10k
INT_S20_SDA/4.1A
INT_S21_SCL/4.1A
LEVEL_SHIFTER
IC6
TXU0204BQAR
3V3
FLX_S40_TX_SDA
FLX_S43_IO
FLX_S42_IO
FLX_S41_RX_SCL
FLX_TX_33/1.6B
FLX_OUT/1.6B
FLX_IN/1.6B
FLX_RX_33/1.6B
IC7
TXU0204BQAR
SAT_S50_TX_SDA
EXT_S10_TX
SAT_S51_RX_SCL
EXT_S11_RX
SAT_TX_33/1.6A
EXT_TX_33/1.6B
SAT_RX_33/1.6A
EXT_RX_33/1.6B
IC8
TXU0304BQAR
SD_S33_CS
SD_S30_MOSI
SD_S31_SCK
SD_S32_MISO
SD_CS_33/1.3B
SD_MOSI_33/1.4B
SD_SCK_33/1.4B
SD_MISO_33/1.3A
C26
C27
C28
C29
C30
C31
IC9
ATSAME51J18A-AU
SAT_TX
SAT_RX
SD_S33_CS
SD_S32_MISO
SD_S30_MOSI
SD_S31_SCK
PB22
PB23
PA27
RESETN
VDDCORE
GND_4
VSW
VDDIO_3
PA30
PA31
PB30
PB31
PB00
PB01
PB02
PB03
PA15
PA14
PA13
PA12
PB15
PB14
PB13
PB12
PB11
PB10
GND_1
VDDIOB
PA11
PA10
PA09
PA08
FLX_TX
EN_LED/1.2D
IMU_INT/4.3A
INT_SCL
INT_SDA
IMU_INT
EXT_TX
EXT_RX
EN_VEXT
EN_3V3
EN_5V
EN_VSAT
EN_SATCHRG
VSAT_GOOD
NEN_GPS
GPS_TX
GPS_RX
AMuSeD_Main_V3
28.06.2022 08:33
Sheet: 3/4

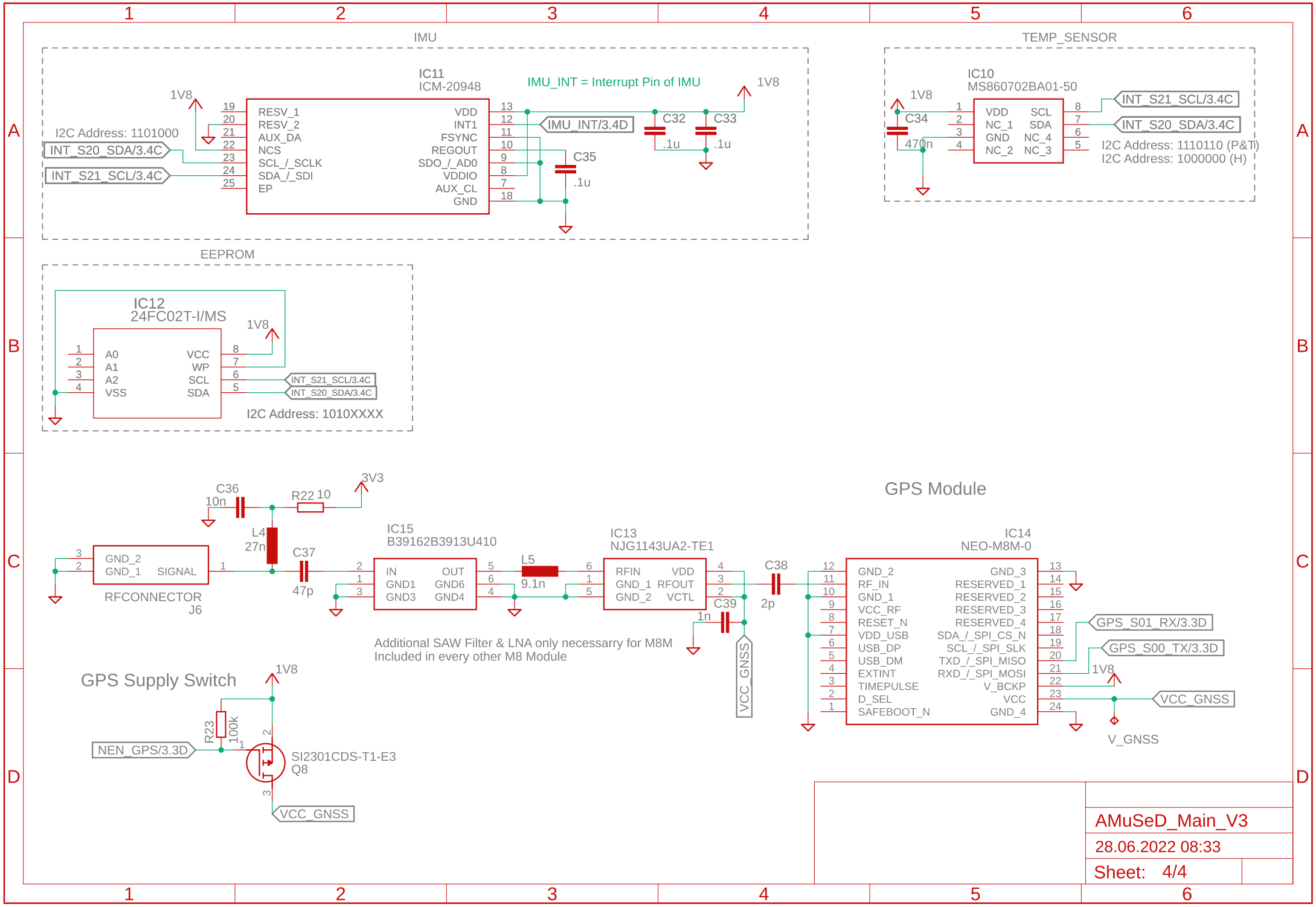
IMU
IC11
ICM-20948
IMU_INT = Interrupt Pin of IMU
1V8
I2C Address: 1101000
INT_S20_SDA/3.4C
INT_S21_SCL/3.4C
RESV_1
RESV_2
AUX_DA
NCS
SCL_/_SCLK
SDA_/_SDI
EP
VDD
INT1
FSYNC
REGOUT
SDO_/_AD0
VDDIO
AUX_CL
GND
IMU_INT/3.4D
C32
.1u
C33
.1u
C35
.1u
TEMP_SENSOR
IC10
MS860702BA01-50
C34
470n
VDD
NC_1
GND
NC_2
SCL
SDA
NC_4
NC_3
I2C Address: 1110110 (P&T)
I2C Address: 1000000 (H)
EEPROM
IC12
24FC02T-I/MS
A0
A1
A2
VSS
VCC
WP
SCL
SDA
I2C Address: 1010XXXX
C36
10n
R22 10
3V3
L4
27n
C37
47p
RFCONNECTOR
J6
GND_2
GND_1
SIGNAL
IC15
B39162B3913U410
IN
GND1
GND3
OUT
GND6
GND4
L5
9.1n
IC13
NJG1143UA2-TE1
RFIN
GND_1
GND_2
VDD
RFOUT
VCTL
C38
2p
C39
1n
VCC_GNSS
Additional SAW Filter & LNA only necessarry for M8M
Included in every other M8 Module
GPS Module
IC14
NEO-M8M-0
GND_2
RF_IN
GND_1
VCC_RF
RESET_N
VDD_USB
USB_DP
USB_DM
EXTINT
TIMEPULSE
D_SEL
SAFEBOOT_N
GND_3
RESERVED_1
RESERVED_2
RESERVED_3
RESERVED_4
SDA_/_SPI_CS_N
SCL_/_SPI_SLK
TXD_/_SPI_MISO
RXD_/_SPI_MOSI
V_BCKP
VCC
GND_4
GPS_S01_RX/3.3D
GPS_S00_TX/3.3D
1V8
VCC_GNSS
V_GNSS
GPS Supply Switch
1V8
R23
100k
NEN_GPS/3.3D
SI2301CDS-T1-E3
Q8
VCC_GNSS
AMuSeD_Main_V3
28.06.2022 08:33
Sheet: 4/4

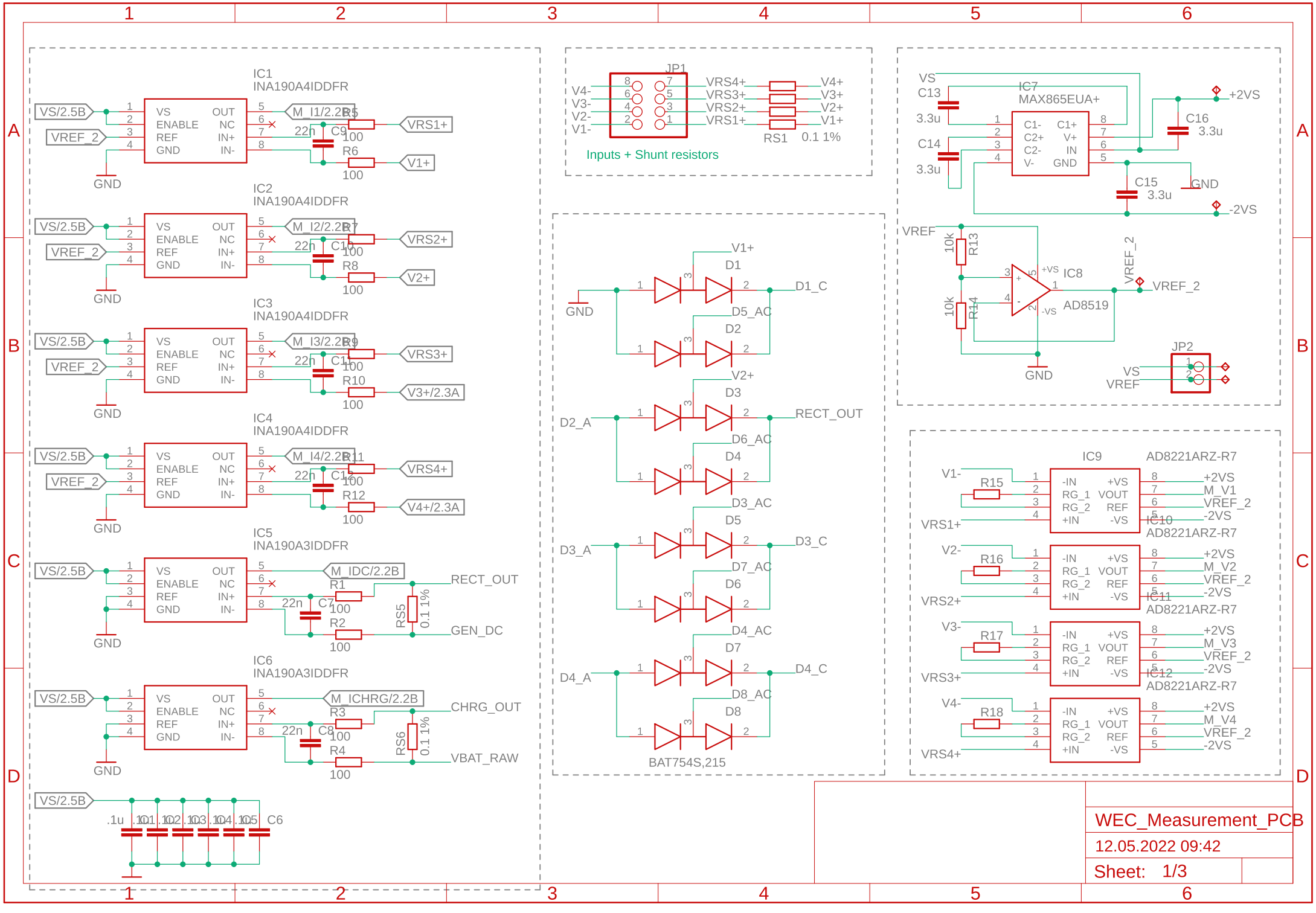
IC1
INA190A4IDDFR
IC2
INA190A4IDDFR
IC3
INA190A4IDDFR
IC4
INA190A4IDDFR
IC5
INA190A3IDDFR
IC6
INA190A3IDDFR
VS/2.5B
VREF_2
GND
VS
ENABLE
REF
GND
OUT
NC
IN+
IN-
M_I1/2.2B
M_I2/2.2B
M_I3/2.2B
M_I4/2.2B
M_IDC/2.2B
M_ICHRG/2.2B
22n
100
VRS1+
VRS2+
VRS3+
VRS4+
V1+
V2+
V3+/2.3A
V4+/2.3A
RECT_OUT
GEN_DC
CHRG_OUT
VBAT_RAW
RS5
RS6
0.1 1%
.1u
C6
JP1
V4-
V3-
V2-
V1-
VRS4+
VRS3+
VRS2+
VRS1+
RS1
0.1 1%
Inputs + Shunt resistors
D1
D2
D3
D4
D5
D6
D7
D8
D1_C
D2_A
D3_A
D4_A
D5_AC
D6_AC
D7_AC
D8_AC
BAT754S,215
IC7
MAX865EUA+
C1-
C2+
C2-
V-
C1+
V+
IN
3.3u
C13
C14
C15
C16
+2VS
-2VS
IC8
AD8519
VREF
10k
R13
R14
VREF_2
JP2
IC9
IC10
IC11
IC12
AD8221ARZ-R7
-IN
RG_1
RG_2
+IN
+VS
VOUT
REF
-VS
R15
R16
R17
R18
M_V1
M_V2
M_V3
M_V4
WEC_Measurement_PCB
12.05.2022 09:42
Sheet: 1/3

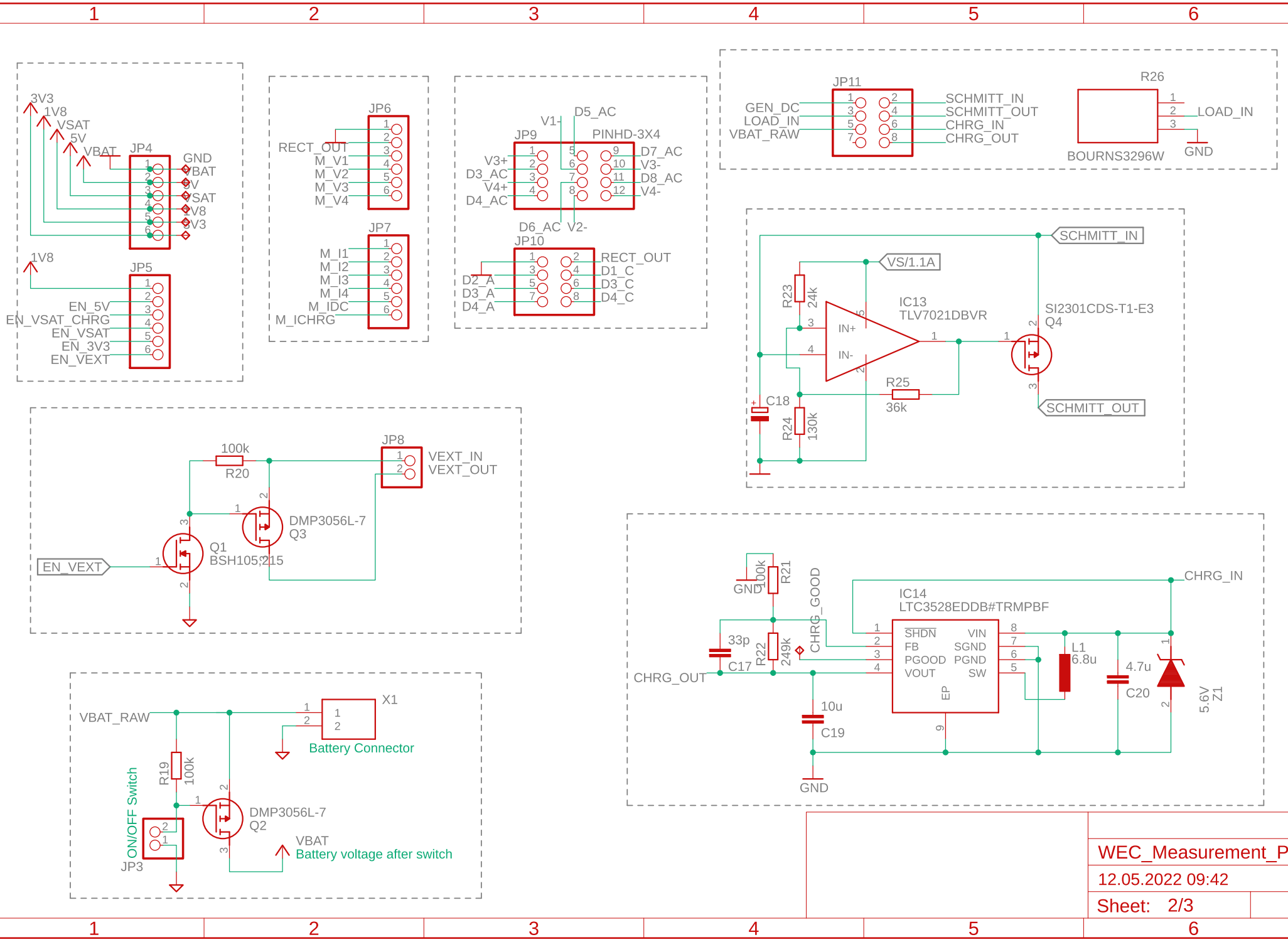
3V3
1V8
VSAT
5V
VBAT
JP4
GND
VBAT
5V
VSAT
1V8
3V3
1V8
JP5
EN_5V
EN_VSAT_CHRG
EN_VSAT
EN_3V3
EN_VEXT
JP6
RECT_OUT
M_V1
M_V2
M_V3
M_V4
JP7
M_I1
M_I2
M_I3
M_I4
M_IDC
M_ICHRG
V1-
D5_AC
JP9
PINHD-3X4
V3+
D3_AC
V4+
D4_AC
D7_AC
V3-
D8_AC
V4-
D6_AC
V2-
JP10
RECT_OUT
D2_A
D3_A
D4_A
D1_C
D3_C
D4_C
JP11
GEN_DC
LOAD_IN
VBAT_RAW
SCHMITT_IN
SCHMITT_OUT
CHRG_IN
CHRG_OUT
R26
LOAD_IN
BOURNS3296W
GND
SCHMITT_IN
VS/1.1A
R23
24k
IC13
TLV7021DBVR
IN+
IN-
SI2301CDS-T1-E3
Q4
R25
36k
C18
R24
130k
SCHMITT_OUT
100k
R20
JP8
VEXT_IN
VEXT_OUT
DMP3056L-7
Q3
Q1
BSH105,215
EN_VEXT
GND
100k
R21
CHRG_GOOD
IC14
LTC3528EDDB#TRMPBF
CHRG_IN
33p
C17
R22
249k
CHRG_OUT
SHDN
FB
PGOOD
VOUT
VIN
SGND
PGND
SW
EP
L1
6.8u
4.7u
C20
5.6V
Z1
10u
C19
GND
VBAT_RAW
X1
Battery Connector
R19
100k
ON/OFF Switch
JP3
DMP3056L-7
Q2
VBAT
Battery voltage after switch
WEC_Measurement_PCB
12.05.2022 09:42
Sheet: 2/3

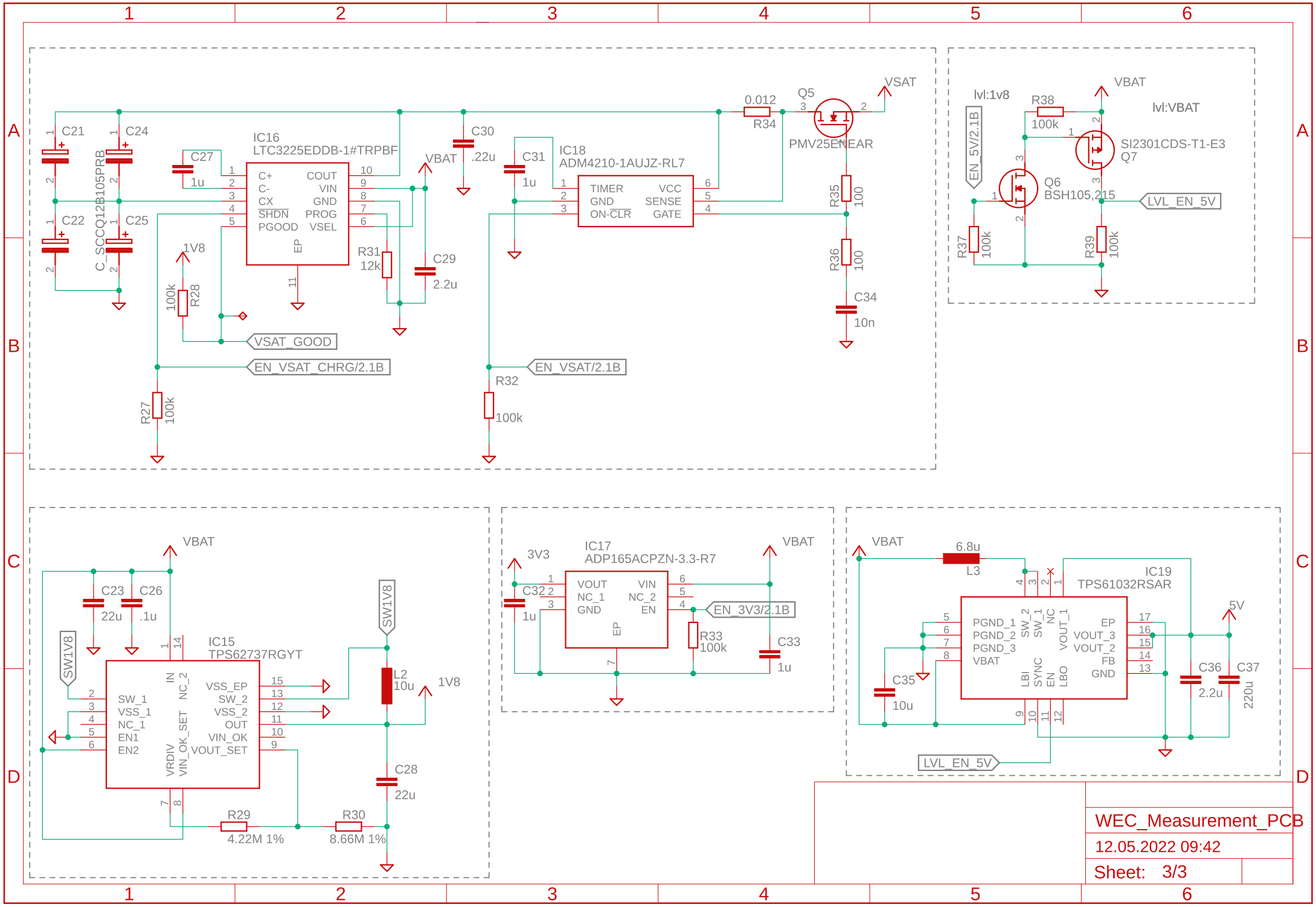

WEC_Measurement_PCB	
12.05.2022 09:42	
Sheet: 3/3	

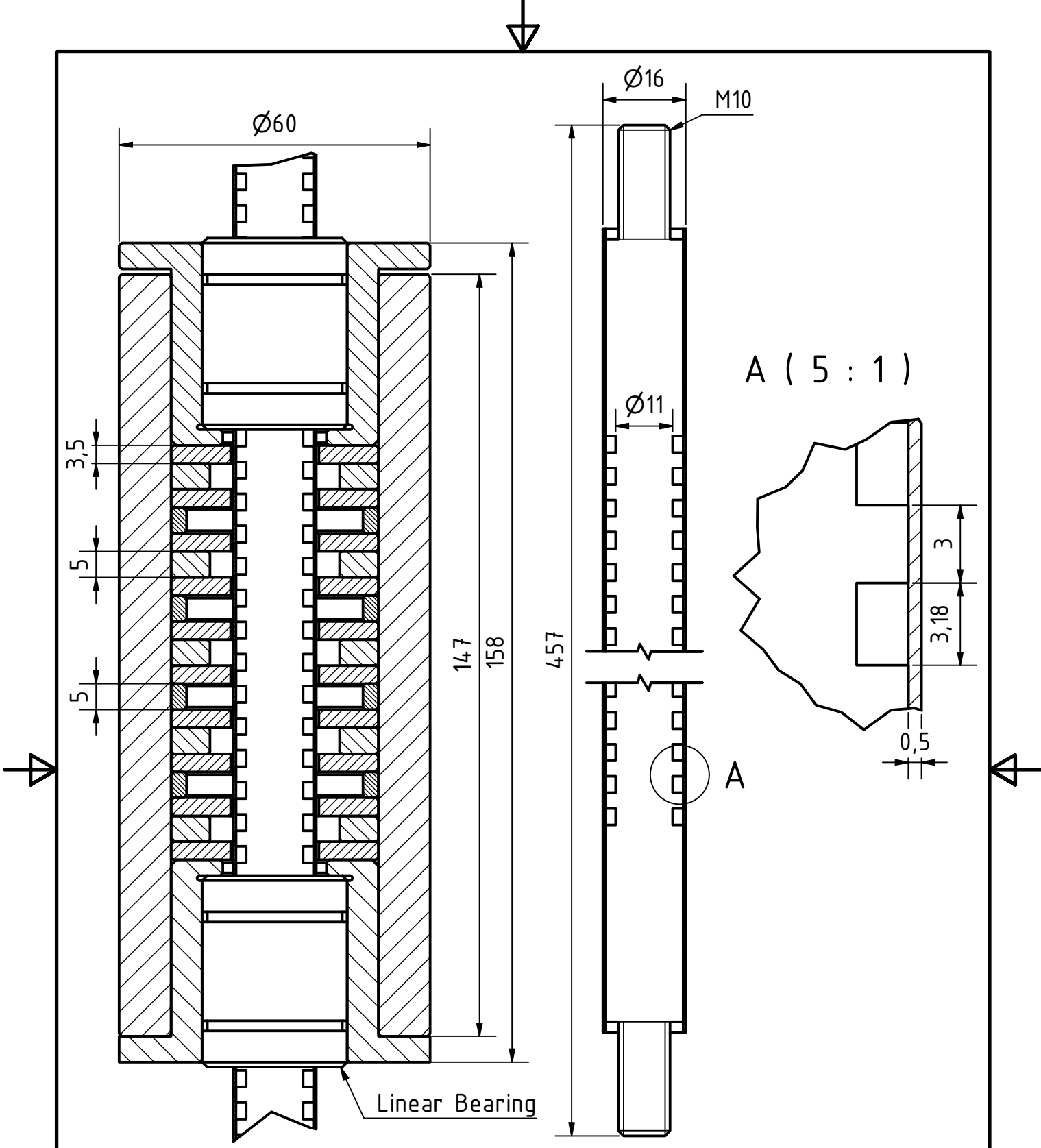

Hamburg University of Technology		FSPMLM Generator Linear Generator Assembly Drawing		
Author Julius Harms	Date 14.02.2023	Part Number.: Linear_Generator_V03 Drawing Number.: Linear_Generator_V03_Assembly		Rev: Rev: AA
	Date	Document-Type Assembly	Scale 1 : 1	Sheet 1/1

References

[1] UNFCCC. “The Paris Agreement - Publication”. In: *Paris Climate Change Conference - November 2015*. 2018 (cit. on p. 1).

[2] Daniel R. Tarry et al. “Drifter Observations Reveal Intense Vertical Velocity in a Surface Ocean Front”. In: *Geophysical Research Letters* 49.18 (2022-09). ISSN: 0094-8276. DOI: 10.1029/2022GL098969 (cit. on pp. 1, 5).

[3] Eric A. D’Asaro et al. “Advances in Observing and Understanding Small-Scale Open Ocean Circulation During the Gulf of Mexico Research Initiative Era”. In: *Frontiers in Marine Science* 7.May (2020-05), pp. 1–23. ISSN: 2296-7745. DOI: 10.3389/fmars.2020.00349 (cit. on pp. 1, 18).

[4] James C. McWilliams. “Oceanic Frontogenesis”. In: *Annual Review of Marine Science* 13.1 (2021-01), pp. 227–253. ISSN: 1941-1405. DOI: 10.1146/annurev-marine-032320-120725 (cit. on pp. 1, 5).

[5] Jens Meyerjürgens et al. “A state-of-the-art compact surface drifter reveals pathways of floating marine litter in the German Bight”. In: *Frontiers in Marine Science* 6.FEB (2019), p. 58. ISSN: 22967745. DOI: 10.3389/FMARS.2019.00058/BIBTEX (cit. on pp. 1, 18–21, 34, 58).

[6] Guillaume Novelli et al. “A Biodegradable Surface Drifter for Ocean Sampling on a Massive Scale”. In: *Journal of Atmospheric and Oceanic Technology* 34.11 (2017-11), pp. 2509–2532. ISSN: 0739-0572. DOI: 10.1175/JTECH-D-17-0055.1 (cit. on pp. 1, 19, 20, 34).

[7] Jack Butler and Camille M.L.S. Pagniello. “Emerging, Low-Cost Ocean Observing Technologies to Democratize Access to the Ocean”. In: *Oceanography* 34.4 (2021-12), pp. 94–95. ISSN: 10428275. DOI: 10.5670/OCEANOG.2021.SUPPLEMENT.02-35 (cit. on pp. 1, 4, 35).

[8] B. T. Glazer et al. “Low-cost embedded systems for democratizing ocean sensor technology in the coastal zone”. In: *AGUFM* 2017 (2017), H41J–1585 (cit. on pp. 1, 4, 35).

[9] Jens Meyerjürgens, Jens-Martin Herold, and Thomas Badewien. *SAIMIDRIS: Sailing Intelligent Micro Drifter Swarms | Universität Oldenburg | ICBM - Institut für Chemie und Biologie des Meeres*. URL: https://uol.de/icbm/msys/aktuelle-projekte/saimidris (visited on 2022-12-20) (cit. on pp. 2, 21).

[10] Hannah Ritchie, Max Roser, and Pablo Rosado. "CO2 and Greenhouse Gas Emissions". In: *Our World in Data* (2020) (cit. on p. 3).

[11] Bradley J. Cardinale et al. "Biodiversity loss and its impact on humanity". In: *Nature* 486.7401 (2012-06), pp. 59–67. ISSN: 0028-0836. DOI: 10.1038/nature11148 (cit. on p. 3).

[12] *Essential Climate Variables | World Meteorological Organization*. 2022. URL: https://public.wmo.int/en/programmes/global-climate-observing-system/essential-climate-variables (visited on 2022-11-19) (cit. on p. 4).

[13] Marco Giorgetta, Peter Korn, and Christian Reick. *ICON-ESM – MPI-M´s next-generation Earth system model | Max Planck Institute for Meteorology*. 2017. URL: https://mpimet.mpg.de/en/communication/focus-on/icon-earth-system-model (visited on 2023-02-17) (cit. on p. 4).

[14] Marcel Ricker et al. "Lagrangian Methods for Visualizing and Assessing Frontal Dynamics of Floating Marine Litter with a Focus on Tidal Basins". In: 2021. DOI: 10.1007/698_2021_812 (cit. on pp. 4, 5).

[15] Guillaume Novelli, Cédric M. Guigand, and Tamay M. Özgökmen. "Technological Advances in Drifters for Oil Transport Studies". In: *Marine Technology Society Journal* 52.6 (2018) (cit. on p. 4).

[16] Riccardo Gerin et al. "On the design of a sustainable ocean drifter for developing countries". In: *EAI Endorsed Transactions on Internet of Things* (2018-01). DOI: 10.4108/EAI.11-9-2018.155483 (cit. on pp. 4, 35, 37).

[17] Alistair Adcroft, Stephen Griffies, and Robert Hallberg. *Ocean Mesoscale Eddies – Geophysical Fluid Dynamics Laboratory | Princeton University Forrestal Campus*. URL: https://www.gfdl.noaa.gov/ocean-mesoscale-eddies/ (visited on 2022-11-18) (cit. on pp. 5, 6).

[18] James C. McWilliams. "Submesoscale currents in the ocean". In: *Proceedings of the Royal Society A: Mathematical, Physical and Engineering Sciences* 472.2189 (2016-05), p. 20160117. ISSN: 1364-5021. DOI: 10.1098/rspa.2016.0117 (cit. on p. 5).

[19] Jens Meyerjürgens et al. "Relative Dispersion of Surface Drifters in the North Sea: The Effect of Tides on Mesoscale Diffusivity". In: *Journal of Geophysical Research: Oceans* 125.8 (2020). ISSN: 21699291. DOI: 10.1029/2019JC015925 (cit. on p. 5).

[20] Jacqueline Boutin, Nicolas Reul, Rafael Catany, et al. "Overview of the CCI+ SSS project." In: *Geophysical Research Abstracts*. Vol. 21. 2019 (cit. on p. 5).

[21] Edward Lyn Lewis. “The Practical Salinity Scale 1978 and Its Antecedents”. In: *IEEE Journal of Oceanic Engineering* 5.1 (1980), pp. 3–8. ISSN: 15581691. DOI: 10.1109/JOE.1980.1145448 (cit. on pp. 6, 172, 173).

[22] Robert H. Tyler et al. “Electrical conductivity of the global ocean 1. Geomagnetism”. In: *Earth, Planets and Space* 69.1 (2017-12), pp. 1–10. ISSN: 18805981. DOI: 10.1186/S40623-017-0739-7/FIGURES/5 (cit. on p. 6).

[23] Tim P. Boyer et al. *World Ocean Atlas 2018 | NOAA National Centers for Environmental Information. Dataset.* 2018. URL: https://www.ncei.noaa.gov/archive/accession/NCEI-WOA18 (visited on 2022-11-18) (cit. on p. 6).

[24] Senliang Bao et al. “Comparison of Satellite-Derived Sea Surface Salinity Products from SMOS, Aquarius, and SMAP”. In: *Journal of Geophysical Research: Oceans* 124.3 (2019-03), pp. 1932–1944. ISSN: 2169-9291. DOI: 10.1029/2019JC014937 (cit. on p. 6).

[25] Wurl Oliver. *NorthSat-X: The North Sea from space: Using explainable artificial intelligence to improve satellite observations of climate change | University Oldenburg*. 2022. URL: https://uol.de/icbm/northsat-x (visited on 2022-11-14) (cit. on pp. 6, 16).

[26] Hiroshi Uchida et al. “Deep Ocean Temperature Measurement with an Uncertainty of 0.7 mK”. In: *Journal of Atmospheric and Oceanic Technology* 32.11 (2015-11), pp. 2199–2210. ISSN: 0739-0572. DOI: 10.1175/JTECH-D-15-0013.1 (cit. on pp. 6, 8).

[27] Joint Panel on Oceanographic Tables and Standards. *Processing of oceanographic station data*. Paris, France: United Nations Educational Scientific and Cultural, 1991-12. ISBN: 978-92-3-102756-7 (cit. on p. 7).

[28] *Sea-Bird Scientific*. 2022. URL: https://www.seabird.com/ (visited on 2023-02-24) (cit. on p. 8).

[29] Heinz Schelwat. *Sea & Sun Technology GmbH*. 2022. URL: https://www.sea-sun-tech.com/ (visited on 2023-02-24) (cit. on pp. 8, 12).

[30] Intergovernmental Oceanographic Commission and Commission of the European Communities. *Manual of quality control procedures for validation of oceanographic data*. Tech. rep. UNESCO, 1993 (cit. on pp. 8, 11, 12, 14).

[31] Sea-Bird Electronics. *Conductivity sensors for moored and autonomous operation*. 2003. URL: https://www.seabird.com/technical-papers/conductivity-sensors-for-moored-and-autonomous-operation (visited on 2023-02-24) (cit. on p. 9).

[32] Robert Lee and Walt Kester. “Fully Automatic Self-Calibrated Conductivity Measurement System”. In: *Analog Dialogue* 50 (2016) (cit. on p. 9).

[33] *Aqua TROLL 100 Data Logger | In-Situ Inc.* 2022. URL: https://in-situ.com/en/aqua-troll-100-data-logger (visited on 2023-02-05) (cit. on p. 9).

[34] A. Pederson. “A small "In situ" conductivity instrument”. In: *Ocean 73 - IEEE International Conference on Engineering in the Ocean Environment*. IEEE, 1973, pp. 68–75. DOI: 10.1109/OCEANS.1973.1161255 (cit. on pp. 9, 13).

[35] Matthew Jonathan Relis. “An electrodeless method for measuring the low-frequency conductivity of electrolytes”. PhD thesis. Massachusetts Institute of Technology, 1947 (cit. on p. 10).

[36] Matthew J Relis. “Method and apparatus for measuring the conductivity of an electrolyte”. US2542057A. 1948 (cit. on p. 10).

[37] Gerald Lee Esterson. *The induction conductivity indicator: a new method for conductivity measurement at sea*. Baltimore, Md, 1956 (cit. on p. 10).

[38] Gerald Lee Esterson. “Method and apparatus for measuring the conductivity of an electrolyte”. US3054946A. 1959 (cit. on p. 10).

[39] Hans Hinkelmann. “Gerät zur Schnellregistrierung in der Ozeanographie”. In: *Z. Agnew. Phys. IX* 10 (1957), pp. 505–513 (cit. on p. 10).

[40] Hans Hinkelmann. “Probe for the electrodeless measurement of the electrical conductivity of liquids”. DE1028679B. 1957 (cit. on p. 10).

[41] Hans Hinkelmann. “Ein Verfahren zur elektrodenlosen Messung der elektrischen Leitfähigkeit von Elektrolyten”. In: *Z. Agnew. Phys. IX* 11 (1958), pp. 500–503 (cit. on p. 10).

[42] Klaus Striggow and Reinhard Dankert. “The Exact Theory of Inductive Conductivity Sensors for Oceanographic Application”. In: *IEEE Journal of Oceanic Engineering* 10.2 (1985), pp. 175–179. ISSN: 15581691. DOI: 10.1109/JOE.1985.1145085 (cit. on pp. 10, 77, 78).

[43] Uldis Cirulis. “Conductivity sensor”. US3603873A. 1970 (cit. on p. 10).

[44] Francis T. Ogawa. “Remote conductivity sensor having transformer coupling in fluid flow path”. US4740755A. 1986 (cit. on p. 10).

[45] Hideki Wakamatsu. “Electromagnetic inductive probe”. US5793214A. 1997 (cit. on p. 10).

[46] Behzad Rezvani. “Toroid conductivity sensor”. US6414493B1. 2001 (cit. on p. 10).

[47] Andreas Eberheim et al. “Inductive conductivity measurement cell”. US8558557B2. 2008 (cit. on p. 10).

[48] Andreas Eberheim et al. “Inductive conductivity-measuring cell and method for operating such”. US8441267B2. 2009 (cit. on p. 10).

[49] Andreas Eberheim et al. “Conductivity sensor with switching between transmitting and receiving coil”. US8581575B2. 2010 (cit. on p. 10).

[50] Song Kang Hui et al. “A new design of inductive conductivity sensor for measuring electrolyte concentration in industrial field”. In: *Sensors and Actuators, A: Physical* 301 (2020-01). ISSN: 09244247. DOI: 10.1016/j.sna.2019.111761 (cit. on pp. 10, 78, 81, 82, 105).

[51] Mark Halverson, Eric Siegel, and Greg Johnson. “Inductive-conductivity cell”. In: *Sea Technology* 61.2 (2020), pp. 24–27 (cit. on pp. 10, 11, 24).

[52] Torsten Pechstein. “Inductive conductivity sensor and method for its production”. US9528955B2. 2012 (cit. on p. 10).

[53] A.J. Fougere. “New non-external field inductive conductivity sensor (NXIC) for long term deployments in biologically active regions”. In: (2002), pp. 623–630. DOI: 10.1109/oceans.2000.881324 (cit. on p. 10).

[54] Marco Völker, Andreas Eberheim, and Torsten Pechstein. “Inductive conductivity sensor”. US7965167B2. 2008 (cit. on p. 11).

[55] Marco Völker and Olaf Dössel. *Induktive Leitfähigkeitssensorik in der Industrieellen Anwendung | Karlsruher Institut für Technologie*. 2012. URL: www.ibt.kit.edu/1210.php (visited on 2022-11-16) (cit. on p. 11).

[56] I. Shkvorets and F. Johnson. “Advantages in performance of the RBR conductivity channel with Delrin™/ceramic inductive cell”. In: *MTS/IEEE Seattle, OCEANS 2010* (2010). DOI: 10.1109/OCEANS.2010.5664276 (cit. on p. 11).

[57] Nikolay Nezlin et al. “Assessment of long-term stability of inductive conductivity sensors at Argo floats”. In: *EGU General Assembly*. 2020 (cit. on p. 11).

[58] *Conductivity Temperature Sensor*. SBE 4. Datasheet (accessed 2023-02-17). Sea Bird Scientific. 2022-09. URL: https://www.seabird.com/sbe-4-conductivity-sensor/product-downloads?id=60762467707 (cit. on pp. 11–13).

[59] *Conductivity Sensor*. SST 7-pole-cell. Datasheet (accessed 2023-02-17). Sea & Sun Technology. 2015-09. URL: https://www.sea-sun-tech.com/wp-content/uploads/2015/09/01_Conductivity-1.pdf (cit. on pp. 11, 13).

[60] *Conductivity Sensor*. 3919B. Datasheet D344 (accessed 2023-02-17). Aanderaa. 2012-11. URL: https://www.aanderaa.com/media/pdfs/Conductivity-Sensor-3919.pdf (cit. on p. 12).

[61] *Small CTD*. RBRbrevio^3. Datasheet Rev. D (accessed 2023-02-17). RBR Ltd. 2021-06. URL: https://rbr-global.com/products/standard-loggers/rbrbrevio/ (cit. on pp. 12, 13).

[62] *Digital conductivity sensor Indumax*. CLS50D. Datasheet (accessed 2023-02-17). Endress+Hauser. 2022-01 (cit. on pp. 12, 74).

[63] *Operators Manual*. Aqua TROLL 100/200. Datasheet 0061342 (accessed 2023-02-17). In-Situ Inc. 2022-12. URL: https://in-situ.com/en/pub/media/support/documents/0061342.pdf (cit. on pp. 12, 58).

[64] *Environmental Monitoring of Conductivity + Temperature*. OCEAN CT. Datasheet (accessed 2023-02-17). D-2 Incorporated. 0018-02. URL: https://www.d-2.com/wp-content/uploads/2021/08/315-001R1.pdf (cit. on p. 12).

[65] G. Kirchhoff et al. "Development of a Low-Cost Inductive Conductivity Sensor". In: *AGUFM* 2019 (2019), OS21B–1745 (cit. on p. 12).

[66] Thanh Tung Pham et al. "A salinity sensor system for estuary studies". In: *OCEANS 2008* (2008). DOI: 10.1109/OCEANS.2008.5151868 (cit. on p. 12).

[67] Lorena Parra et al. "Low-cost Conductivity Sensor Based on Two Coils". In: 2013.November (2013), pp. 139–144 (cit. on p. 12).

[68] R. T. Wood et al. "A salinity sensor for long-term data collection in estuary studies". In: *MTS/IEEE Seattle, OCEANS 2010* (2010), pp. 1–6. DOI: 10.1109/OCEANS.2010.5664602 (cit. on p. 12).

[69] Guigen Liu et al. "A miniature fiber-optic sensor for high-resolution and high-speed temperature sensing in ocean environment". In: *SPIE Defense + Security* 9459 (2015-05), pp. 80–85. ISSN: 1996756X. DOI: 10.1117/12.2180168 (cit. on p. 13).

[70] Weilin Hou, Guigen Liu, and Ming Han. "A novel, high-resolution, high-speed fiber-optic temperature sensor for oceanographic applications". In: *2015 IEEE/OES 11th Current, Waves and Turbulence Measurement, CWTM 2015* (2015-04). DOI: 10.1109/CWTM.2015.7098149 (cit. on p. 13).

[71] A M Pederson. "An accurate low cost temperature sensor". In: *Trans. Marine Temperature Measurement Symp.* 1969, pp. 135–153 (cit. on p. 13).

[72] *OEM Temperature Sensor*. Datasheet R010Y (accessed 2023-02-17). Soundnine Inc. URL: https://www.soundnine.com/wp-content/uploads/Manuals/R010Y-OEM-Temp-Sensor-232.pdf (cit. on p. 14).

[73] *SMALL REALTIME SENSORS*. RBRcoda^3 T. Datasheet Rev. J (accessed 2023-02-17). RBR Ltd. 2022-09. URL: https://rbr-global.com/products/sensors/rbrcoda-t/ (cit. on p. 14).

[74] *Temperature sensor*. SST PT100. Datasheet (accessed 2023-02-17). Sea & Sun Technology. 2018-10. URL: https://www.sea-sun-tech.com/wp-content/uploads/2018/10/02_Temperatursensor.pdf (cit. on p. 14).

[75] *PREMIUM CTD TEMPERATURE SENSOR*. SBE 3plus. Datasheet DS53 (accessed 2023-02-17). Sea Bird Scientific. 2022-09. URL: https://www.seabird.com/sbe-3f-3plus-3s-oceanographic-temperature-sensor/product-downloads?id=60762467708 (cit. on p. 14).

[76] Mingwei Lin and Canjun Yang. "Ocean Observation Technologies: A Review". In: *Chinese Journal of Mechanical Engineering (English Edition)* 33.1 (2020-12), pp. 1–18. ISSN: 21928258. DOI: 10.1186/S10033-020-00449-Z/FIGURES/10 (cit. on pp. 15, 16).

[77] Tim Moltmann et al. "A Global Ocean Observing System (GOOS), delivered through enhanced collaboration across regions, communities, and new technologies". In: *Frontiers in Marine Science* 6.JUN (2019-06), p. 291. ISSN: 22967745. DOI: 10.3389/FMARS.2019.00291/BIBTEX (cit. on p. 15).

[78] *European Ocean Observing System*. URL: https://www.eoos-ocean.eu/ (visited on 2022-12-19) (cit. on p. 15).

[79] Daniel Roper et al. "Autosub Long Range 6000: A Multiple-Month Endurance AUV for Deep-Ocean Monitoring and Survey". In: *IEEE Journal of Oceanic Engineering* 46.4 (2021-10), pp. 1179–1191. ISSN: 15581691. DOI: 10.1109/JOE.2021.3058416 (cit. on p. 15).

[80] Stephen C. Riser et al. "Fifteen years of ocean observations with the global Argo array". In: *Nature Climate Change 2016 6:2* 6.2 (2016-01), pp. 145–153. ISSN: 1758-6798. DOI: 10.1038/nclimate2872 (cit. on p. 15).

[81] *Argos: Implementation status*. URL: https://argo.ucsd.edu/about/status/ (visited on 2022-12-19) (cit. on p. 16).

[82] Douglas C. Webb, Paul J. Simonetti, and Clayton P. Jones. "SLOCUM: An underwater glider propelled by environmental energy". In: *IEEE Journal of Oceanic Engineering* 26.4 (2001-10), pp. 447–452. ISSN: 03649059. DOI: 10.1109/48.972077 (cit. on pp. 16, 17).

[83] Charles C. Eriksen et al. "Seaglider: A long-range autonomous underwater vehicle for oceanographic research". In: *IEEE Journal of Oceanic Engineering* 26.4 (2001-10), pp. 424–436. ISSN: 03649059. DOI: 10.1109/48.972073 (cit. on p. 16).

[84] Wilhelm Petersen. "FerryBox systems: State-of-the-art in Europe and future development". In: *Journal of Marine Systems* 140.PA (2014-12), pp. 4–12. ISSN: 0924-7963. DOI: 10.1016/J.JMARSYS.2014.07.003 (cit. on p. 16).

[85] R. Venkatesan et al. "Two decades of operating the Indian moored buoy network: significance and impact". In: *https://doi.org/10.1080/1755876X.2016.1182792* 9.1 (2016), pp. 45–54. ISSN: 17558778. DOI: 10.1080/1755876X.2016.1182792 (cit. on p. 17).

[86] Paul Mahacek, Christopher A. Kitts, and Ignacio Mas. “Dynamic guarding of marine assets through cluster control of automated surface vessel fleets”. In: *IEEE/ASME Transactions on Mechatronics* 17.1 (2012-02), pp. 65–75. ISSN: 10834435. DOI: 10.1109/TMECH.2011.2174376 (cit. on p. 17).

[87] Seok In Sohn et al. “Design of a Fuel-Cell-Powered Catamaran-Type Unmanned Surface Vehicle”. In: *IEEE Journal of Oceanic Engineering* 40.2 (2015-04), pp. 388–396. ISSN: 03649059. DOI: 10.1109/JOE.2014.2315889 (cit. on p. 17).

[88] Yingjie Deng et al. “Parallel guidance and event-triggered robust fuzzy control for path following of autonomous wing-sailed catamaran”. In: *Ocean Engineering* 190 (2019-10), p. 106442. ISSN: 0029-8018. DOI: 10.1016/J.OCEANENG.2019.106442 (cit. on p. 17).

[89] *Message in a bottle | Federal Maritime and Hydrographic Agency*. URL: https://www.bsh.de/EN/The_BSH/Maritime_library/Message_in_a_bottle/message_in_a_bottle_node.html (visited on 2023-02-19) (cit. on p. 18).

[90] Rick Lumpkin, Tamay Özgökmen, and Luca Centurioni. “Advances in the Application of Surface Drifters”. In: *Annual Review of Marine Science* 9.1 (2017-01), pp. 59–81. DOI: 10.1146/ANNUREV-MARINE-010816-060641 (cit. on pp. 18, 21).

[91] Eric A. D’Asaro et al. “Correction for D’Asaro et al., Ocean convergence and the dispersion of flotsam”. In: *Proceedings of the National Academy of Sciences* 115.11 (2018-03). ISSN: 0027-8424. DOI: 10.1073/pnas.1802701115 (cit. on p. 18).

[92] Marcel Ricker et al. “Lagrangian Methods for Visualizing and Assessing Frontal Dynamics of Floating Marine Litter with a Focus on Tidal Basins”. In: *The Handbook of Environmental Chemistry*. Berlin, Heidelberg: Springer Berlin Heidelberg, 2021, pp. 1–36. DOI: 10.1007/698_2021_812 (cit. on p. 18).

[93] Pierre Marie Poulain, Luca Centurioni, and Tamay Özgökmen. “Comparing the Currents Measured by CARTHE, CODE and SVP Drifters as a Function of Wind and Wave Conditions in the Southwestern Mediterranean Sea”. In: *Sensors 2022, Vol. 22, Page 353* 22.1 (2022-01), p. 353. ISSN: 1424-8220. DOI: 10.3390/S22010353 (cit. on pp. 18, 23).

[94] Rick Lumpkin and Mayra Pazos. “Measuring surface currents with Surface Velocity Program drifters: the instrument, its data, and some recent results”. In: *Lagrangian Analysis and Prediction of Coastal and Ocean Dynamics* (2009-12), pp. 39–67. DOI: 10.1017/cbo9780511535901.003 (cit. on pp. 18, 109).

[95] Luca Centurioni et al. “A Global Ocean Observing System for Measuring Sea Level Atmospheric Pressure: Effects and Impacts on Numerical Weather Prediction”. In: *Bulletin of the American Meteorological Society* 98.2 (2017-02), pp. 231–238. ISSN: 0003-0007. DOI: 10.1175/BAMS-D-15-00080.1 (cit. on p. 18).

[96] *SURFACE VELOCITY PROGRAM (SVP) DRIFTER | Lagrangian Drifter Laboratory Scripps Institution of Oceanography*. 2023. URL: https://gdp.ucsd.edu/ldl/svp/ (visited on 2023-01-13) (cit. on pp. 19, 20, 34).

[97] *iSVP | MetOcean Telematics*. URL: https://metocean.com/products/isvp/ (visited on 2023-02-18) (cit. on p. 19).

[98] *Spotter Buoy by Sofar Ocean | Sofar Ocean*. 2022. URL: https://www.sofarocean.com/products/spotter (visited on 2022-10-27) (cit. on pp. 19, 20, 22).

[99] *GPS Drifting Buoys | Pacific Gyre, Inc*. 2023. URL: https://www.pacificgyre.com/ (visited on 2023-02-17) (cit. on pp. 19, 20).

[100] Russ E. Davis. "Drifter observations of coastal surface currents during CODE: The method and descriptive view". In: *Journal of Geophysical Research: Oceans* 90.C3 (1985-05), pp. 4741–4755. ISSN: 2156-2202. DOI: 10.1029/JC090IC03P04741 (cit. on p. 19).

[101] R. C. Beardsley and S. J. Lentz. "The Coastal Ocean Dynamics Experiment collection: An introduction". In: *Journal of Geophysical Research: Oceans* 92.C2 (1987-02), pp. 1455–1463. ISSN: 2156-2202. DOI: 10.1029/JC092IC02P01455 (cit. on p. 19).

[102] J CARTER OHLMANN. "Drifter Observations of Small-Scale Flows in the Philippine Archipelago". In: *Oceanography* 24.1 (2011), pp. 122–129. ISSN: 10428275, 2377617X (cit. on p. 20).

[103] *Sofar Spotter Technical Specifications*. 2021. URL: https://assets.website-files.com/6195779003438046f0c9adde/62d75d65671fc65363e28e7f_Spotter-3pager.pdf (visited on 2022-10-27) (cit. on pp. 20, 22).

[104] Zunibal. *Boyas marinas de pesca inteligentes*. 2021. URL: https://zunibal.com/ (visited on 2023-02-17) (cit. on p. 20).

[105] *Voyager Buoy – SLMB | Fastwave*. URL: https://voyagerbuoy.com/ (visited on 2023-02-17) (cit. on p. 20).

[106] *Track, Monitor, and Explore Without Limits. | MetOcean Telematics*. 2022. URL: https://metocean.com/ (visited on 2023-02-17) (cit. on p. 20).

[107] *QinetiQ Security & Defence Contractors | QinetiQ*. 2022. URL: https://www.qinetiq.com/ (visited on 2023-02-17) (cit. on p. 20).

[108] Lisa Emery et al. "Autonomous river drifting buoys applications and improvements". In: *OCEANS'11 - MTS/IEEE Kona, Program Book* (2011). DOI: 10.23919/OCEANS.2011.6107066 (cit. on p. 20).

[109] *MELOA Project*. 2023. URL: https://www.ec-meloa.eu/ (visited on 2023-02-17) (cit. on p. 20).

[110] *Institute for Chemistry and Biology of the Marine Environment | University of Oldenburg*. 2022-12. URL: https://uol.de/en/icbm (visited on 2023-02-17) (cit. on p. 20).

[111] Matias Carandell Widmer. "Contributions to the design of energy harvesting systems for autonomous sensors in low power marine applications". PhD thesis. 2022 (cit. on p. 20).

[112] E. V. Stanev et al. "Extreme westward surface drift in the North Sea: Public reports of stranded drifters and Lagrangian tracking". In: *Continental Shelf Research* 177 (2019-04), pp. 24–32. ISSN: 0278-4343. DOI: 10.1016/J.CSR.2019.03.003 (cit. on p. 21).

[113] Rogério Chumbinho et al. "The WAVY Drifters and Their Role in Ocean Observation". In: *9th EuroGOOS International conference*. Shom, Ifremer, and EuroGOOS AISBL, 2021, pp. 458–466 (cit. on pp. 21, 108).

[114] *Price List SVP Drifter | Pacific Gyre Inc*. 2022. URL: https://www.pacificgyre.com/pricelists/Content/prices/SVP_PriceList.htm (visited on 2022-09-30) (cit. on pp. 21, 34).

[115] Roger Hine et al. "The wave glider: A wave-powered autonomous marine vehicle". In: *MTS/IEEE Biloxi - Marine Technology for Our Future: Global and Local Challenges, OCEANS 2009* (2009). DOI: 10.23919/OCEANS.2009.5422129 (cit. on p. 22).

[116] Isabel A. Houghton et al. "Operational Assimilation of Spectral Wave Data From the Sofar Spotter Network". In: *Geophysical Research Letters* 49.15 (2022-08), e2022GL098973. ISSN: 1944-8007. DOI: 10.1029/2022GL098973 (cit. on p. 22).

[117] NASA Langley Atmospheric Science Data Center DAAC. *CERES Energy Balanced and Filled (EBAF) TOA and Surface Monthly means data in netCDF Edition 4.1*. 2022. DOI: 10.5067/Terra-Aqua/CERES/EBAF_L3B.004.1 (cit. on p. 22).

[118] NASA Langley Atmospheric Science Data Center DAAC. *CERES-MODIS and hourly geostationary cloud properties stratified by ISCCP cloud types for day and night*. 2022. DOI: 10.5067/Terra+Aqua/CERES/CldTypHist_L3.004 (cit. on p. 22).

[119] Clinton D. Haldeman et al. "Implementation of energy harvesting system for powering thermal gliders for long duration ocean research". In: *OCEANS 2015 - MTS/IEEE Washington* (2016-02). DOI: 10.23919/OCEANS.2015.7404559 (cit. on p. 22).

[120] Nurkhaizan Zulkepli et al. "Review of Thermoelectric Generators at Low Operating Temperatures: Working Principles and Materials". In: *Micromachines 2021, Vol. 12, Page 734* 12.7 (2021-06), p. 734. ISSN: 2072-666X. DOI: 10.3390/MI12070734 (cit. on p. 22).

[121] Pierre Marie Poulain et al. “Wind Effects on Drogued and Undrogued Drifters in the Eastern Mediterranean”. In: *Journal of Atmospheric and Oceanic Technology* 26.6 (2009-06), pp. 1144–1156. ISSN: 0739-0572. DOI: 10.1175/2008JTECHO618.1 (cit. on p. 23).

[122] Yu Cao, Nicholas Townsend, and Mingyi Tan. “Hybrid renewable energy system for ocean going platforms”. In: *OCEANS 2017 - Aberdeen* 2017-Octob (2017-10), pp. 1–7. DOI: 10.1109/OCEANSE.2017.8084799 (cit. on p. 23).

[123] Kester Gunn and Clym Stock-Williams. “Quantifying the global wave power resource”. In: *Renewable Energy* 44 (2012-08), pp. 296–304. ISSN: 0960-1481. DOI: 10.1016/J.RENENE.2012.01.101 (cit. on p. 23).

[124] A. Lopes Ribeiro et al. “Inductive conductivity cell for water salinity monitoring”. In: *18th IMEKO World Congress 2006: Metrology for a Sustainable Development* 2 (2006), pp. 1647–1650 (cit. on p. 24).

[125] *SPOT TRACE® SATELLITE TRACKING DEVICE | SPOT LLC*. 2023. URL: https://www.findmespot.com/products-services/spot-trace (visited on 2023-01-13) (cit. on p. 34).

[126] *SparkFun Artemis Global Tracker | SparkFun Electronics*. 2023. URL: https://www.sparkfun.com/products/18712 (visited on 2023-01-13) (cit. on p. 34).

[127] *Arribada Horizon ARTIC R2 Developer’s Kit | Arribada Initiative C.I.C.* 2023. URL: https://arribada.org/product/arribada-horizon-artic-r2-developers-kit/ (visited on 2023-01-13) (cit. on pp. 34, 35).

[128] Jean Rabault et al. “OpenMetBuoy-v2021: An Easy-to-Build, Affordable, Customizable, Open-Source Instrument for Oceanographic Measurements of Drift and Waves in Sea Ice and the Open Ocean”. In: *Geosciences 2022, Vol. 12, Page 110* 12.3 (2022-02), p. 110. ISSN: 2076-3263. DOI: 10.3390/GEOSCIENCES12030110. arXiv: 2201.08384 (cit. on pp. 35, 44, 45).

[129] N. G. Wright and H. K. Chan. “Low-cost Internet of Things ocean observation”. In: *OCEANS 2016 MTS/IEEE Monterey, OCE 2016* (2016-11). DOI: 10.1109/OCEANS.2016.7761137 (cit. on p. 35).

[130] Emily M Duncan et al. “Message in a bottle: Open source technology to track the movement of plastic pollution”. In: *PLOS ONE* 15.12 (2020), pp. 1–19. DOI: 10.1371/journal.pone.0242459 (cit. on p. 35).

[131] Globalstar. *Next Generation Connectivity From Both Space And Terrestrial Networks*. 2023. URL: https://www.globalstar.com/en-us/ (visited on 2023-01-13) (cit. on p. 36).

[132] *Improving ocean information and forecasting | ARGOS (CLS)*. 2023. URL: https://www.argos-system.org/applications-argos/oceanography/ (visited on 2023-01-13) (cit. on p. 36).

[133] *Oceanic Research | Iridium Communications Inc.* 2023. URL: https://www.iridium.com/markets/oceanic/ (visited on 2023-01-13) (cit. on p. 36).

[134] *GLOBAL AFFORDABLE CONNECTIVITY | SWARM.* 2023. URL: https://swarm.space/ (visited on 2023-01-13) (cit. on p. 36).

[135] Kineis. *Kineis IoT everywhere.* 2023. URL: https://www.kineis.com/en/ (visited on 2023-01-13) (cit. on p. 36).

[136] *WORLD'S MOST ADVANCED BROADBAND SATELLITE INTERNET | Starlink.* 2023. URL: https://www.starlink.com/technology (visited on 2023-01-13) (cit. on p. 36).

[137] *SAM D Family of Microcontrollers | Microchip Technology Inc.* 2023. URL: https://www.microchip.com/en-us/products/microcontrollers-and-microprocessors/32-bit-mcus/sam-32-bit-mcus/sam-d (visited on 2023-01-14) (cit. on p. 42).

[138] *SAM D5x/E5x Family Data Sheet.* ATSAME51J18A. Datasheet Rev. J (accessed 2023-02-18). Microchip Technology Inc. 2022. URL: https://www.microchip.com/en-us/product/ATSAME51J18A (cit. on pp. 42, 43).

[139] *SAM E Family of Microcontrollers | Microchip Technology Inc.* 2023. URL: https://www.microchip.com/en-us/products/microcontrollers-and-microprocessors/32-bit-mcus/sam-32-bit-mcus/sam-e (visited on 2023-01-14) (cit. on p. 43).

[140] *4-Bit Fixed Direction Voltage-Level Translator with Schmitt-Trigger Inputs.* TXU0204. Datasheet Rev. A (accessed 2023-02-18). Texas Instruments Inc. 2021-09. URL: https://www.ti.com/product/TXU0204/part-details/TXU0204BQAR (cit. on p. 43).

[141] *TPS6273x Programmable Output Voltage Ultra-Low Power Buck Converter.* TPS62737RGYT. Datasheet Rev. C (accessed 2023-02-18). Texas Instruments Inc. 2014-12. URL: https://www.ti.com/product/TPS62736 (cit. on pp. 43, 44).

[142] Bang S Lee. "Understanding the Terms and Definitions of LDO Voltage Regulators". In: *Texas Instruments Application Report* (1999) (cit. on p. 43).

[143] *Very Low Quiescent Current, 150 mA, LDO Regulator.* ADP165. Datasheet Rev. A (accessed 2023-02-19). Analog Devices Inc. 2014-11. URL: https://www.analog.com/adp165 (cit. on pp. 43, 44).

[144] *TPS6103x 96% Efficient Synchronous Boost Converter With 4A Switch.* TPS61032. Datasheet Rev. G (accessed 2023-02-18). Texas Instruments Inc. 2015-03. URL: https://www.ti.com/product/TPS61032 (cit. on pp. 43, 44).

[145] *Iridium 9603 SBD Transceiver Developer's Guide.* Tech. rep. Iridium Communications Inc., 2014 (cit. on pp. 43, 58).

[146] *150mA Supercapacitor Charger*. LTC3225. Datasheet Rev. B (accessed 2023-02-18). Analog Devices Inc. 2010-06. URL: https://www.analog.com/ltc3225 (cit. on pp. 43, 44).

[147] *Hot Swap Controller in 6-Lead TSOT Package*. ADM4210. Datasheet Rev. A (accessed 2023-02-19). Analog Devices Inc. 2013-11. URL: https://www.analog.com/adm4210 (cit. on p. 44).

[148] *ERINOME-II USER MANUAL*. ERINOME-II. Datasheet Rev. 002.000 (accessed 2023-02-18). Würth Elektronik eiSos GmbH & Co. KG. 2021-08. URL: https://www.we-online.com/de/components/products/ERINOME-II (cit. on p. 44).

[149] *Concurrent GNSS modules*. NEO-M8. Datasheet Rev. 12 (accessed 2023-02-18). U-Blox. 2022-12. URL: https://www.u-blox.com/en/product/neo-m8-series (cit. on p. 44).

[150] *iNEMO inertial module with embedded Machine Learning Core*. ISM330DHCX. Datasheet Rev. 7 (accessed 2023-02-18). STMicroelectronics. 2020-11. URL: https://www.st.com/en/mems-and-sensors/ism330dhcx (cit. on p. 45).

[151] *Digital output magnetic sensor*. LIS3MDL. Datasheet Rev. 6 (accessed 2023-02-18). STMicroelectronics. 2017-05. URL: https://www.st.com/en/mems-and-sensors/lis3mdl (cit. on p. 45).

[152] *iNEMO 6DoF inertial measurement unit (IMU)*. LSM6DSM. Datasheet Rev. 7 (accessed 2023-02-19). STMicroelectronics. 2017-09. URL: https://www.st.com/en/mems-and-sensors/lsm6dsm (cit. on p. 45).

[153] *World's Lowest-Power 9Axis MEMS MotionTracking Device*. ICM-20948. Datasheet Rev. 1.5 (accessed 2023-02-18). InvenSense TDK. 2021-09. URL: https://invensense.tdk.com/products/motion-tracking/9-axis/icm-20948/ (cit. on p. 45).

[154] *PHT Combination Sensor*. MS8607-02BA01. Datasheet (accessed 2023-02-18). TE Connectivity. 2017-06. URL: https://www.te.com/deu-de/product-CAT-BLPS0018.html (cit. on pp. 45, 46).

[155] *2Kb I2C compatible 2-wire Serial EEPROM*. 24FC02. Datasheet Rev. N (accessed 2023-02-18). Microchip Technology Inc. 2021-08. URL: https://www.microchip.com/en-us/product/24FC02 (cit. on p. 46).

[156] Hussien Saleh. "Software Implementation Of Energy-Efficient Self-Sufficient Modular Multi-Sensor Platform For Autonomous Ocean Drifter". Master Thesis. Hamburg University of Technology, 2022 (cit. on pp. 47, 54).

[157] Nrusingh Prasad Dash et al. "Event driven programming for embedded systems-a finite state machine based approach". In: *The Sixth International Conference on Systems*. 2011, pp. 23–28 (cit. on p. 50).

[158] *Information processing systems - Open Systems Interconnection - Basic Reference Model - Part 4: Management framework*. Standard. Geneva, CH: International Organization for Standardization, 1989-11 (cit. on p. 53).

[159] ChaN. *FatFs - Generic FAT Filesystem Module*. 2022. URL: http://elm-chan.org/fsw/ff/00index_e.html (visited on 2023-01-16) (cit. on p. 56).

[160] Juan Carlos Reyes Andrade. "Hardware Upgrade and Firmware Development of a Prototype for the Long and Short Range Communication of a Multi-Sensor-Plattform". Master Thesis. Hamburg University of Technology, 2022 (cit. on p. 56).

[161] Tahir Hasan. "Development and implementation of an interaction concept for the user-friendly operation of a modular environmental monitoring platform". Project Work. Hamburg University of Technology, 2022 (cit. on p. 56).

[162] *OCEAN CT Environmental Monitoring of Conductivity + Temperature | D-2 Incorporated*. 2020-02. URL: https://www.d-2.com/wp-content/uploads/2021/08/315-001R1.pdf (visited on 2022-12-03) (cit. on p. 64).

[163] *Conductivity Sensor Aanderaa Data Instruments | Xylem Inc*. 2021. URL: https://www.aanderaa.com/conductivity-sensor (visited on 2023-02-02) (cit. on p. 64).

[164] Yu Qian et al. "Review of salinity measurement technology based on optical fiber sensor". In: *Sensors and Actuators B: Chemical* 260 (2018-05), pp. 86–105. ISSN: 0925-4005. DOI: 10.1016/J.SNB.2017.12.077 (cit. on p. 69).

[165] Jose Rafael Guzman-Sepulveda et al. "Fiber optic sensor for high-sensitivity salinity measurement". In: *IEEE Photonics Technology Letters* 25.23 (2013), pp. 2323–2326. ISSN: 10411135. DOI: 10.1109/LPT.2013.2286132 (cit. on p. 69).

[166] Nicholas Kantack et al. "Robust Ocean Salinity Sensing". In: *Oceans Conference Record (IEEE)* 2021-Septe (2021). ISSN: 01977385. DOI: 10.23919/OCEANS44145.2021.9705686 (cit. on p. 69).

[167] Abu Bakar Md Ismail and Katsunori Shida. "Non-contact multi-sensing technique for the precise measurement of concentration of electrolytic solution". In: *Sensors and Actuators, A: Physical* 69.2 (1998-08), pp. 152–155. ISSN: 09244247. DOI: 10.1016/S0924-4247(98)00069-7 (cit. on p. 69).

[168] Lorena Parra et al. "Water Conductivity Measurements based on Electromagnetic fields". In: *Proceedings of the First International Conference on Computational Science and Engineering (CSE'13)* (2013), pp. 107–112 (cit. on p. 69).

[169] Abu Bakar Md. Ismail and Katsunori Shida. "New Contactless Inductive Sensor for the Measurement of Concentration of an Electrolytic Solution". In: *Japanese Journal of Applied Physics* 36.Part 1, No. 10 (1997-10), pp. 6558–6561. ISSN: 0021-4922. DOI: 10.1143/JJAP.36.6558 (cit. on p. 69).

[170] Makoto Sonehara, Nguyen Van Toai, and Toshiro Sato. “Fundamental Study of Non-Contact Water Salinity Sensor by Using Electromagnetic Means for Seawater Desalination Plants”. In: *IEEE Transactions on Magnetics* 52.7 (2016), pp. 1–4. ISSN: 00189464. DOI: 10.1109/TMAG.2016.2537921 (cit. on p. 69).

[171] Weichen Li, Yuying Chiang, and Chingfu Tsou. “A novel method for inspecting raw milk quality by using dual-coil inductance”. In: *Proceedings of the IEEE International Conference on Micro Electro Mechanical Systems (MEMS)*. Vol. 2016-Febru. Institute of Electrical and Electronics Engineers Inc., 2016-02, pp. 282–285. ISBN: 9781509019731. DOI: 10.1109/MEMSYS.2016.7421615 (cit. on pp. 69, 76).

[172] Xing Ding et al. “An inductive salt solution concentration sensor using a planar coil based on a PQCR-L circuit”. In: *Sensors and Actuators, A: Physical* 263 (2017-08), pp. 246–251. ISSN: 09244247. DOI: 10.1016/j.sna.2017.05.043 (cit. on pp. 69, 71, 76).

[173] Siansyun Liao et al. “A study of the effect of different coplanar dual-coil geometries on the performance of mutual inductance”. In: *Sensors and Actuators, A: Physical* 269 (2018-01), pp. 99–110. ISSN: 09244247. DOI: 10.1016/j.sna.2017.07.022 (cit. on pp. 69, 76).

[174] David R Lide. *CRC handbook of chemistry and physics*. Vol. 85. CRC press, 2004 (cit. on p. 71).

[175] Julius Harms and Thorsten A Kern. “Design and Potential Analysis of an Eddy Current Sensor for Inductive Conductivity Measurement in Fluids”. In: *Engineering Proceedings* 6.1 (2021-05), p. 54. ISSN: 2673-4591. DOI: 10.3390/I3S2021DRESDEN-10160 (cit. on p. 73).

[176] Yiğithan Kandur, Julius Harms, and Thorsten A. Kern. “Uncertainty Analysis for Low-Cost Transformer-Type Inductive Conductivity Sensors”. In: *Engineering Proceedings 2021,* 6 (2021-05), p. 52. ISSN: 2673-4591. DOI: 10.3390/I3S2021DRESDEN-10145 (cit. on pp. 80, 82).

[177] Finn Jannek Klar, Julius Harms, and Thorsten A. Kern. “On the Design of Low-Cost Inductive Conductivity Sensors for Salinity Measurement in Oceangoing IoT Applications”. In: *ITG-Fb. 303: Sensoren und Messsysteme*. 2022, pp. 390–394. ISBN: 978-3-8007-5835-7 (cit. on pp. 80, 82).

[178] *Product catalog: Ferrite materials | TDK Electronics AG*. 2023. URL: https://www.tdk-electronics.tdk.com/en/529404/products/product-catalog/ferrites-and-accessories/ferrite-materials (visited on 2023-01-31) (cit. on p. 81).

[179] Finn Jannek Klar. “Development and implementation of a manufacturing concept for a low-cost inductive conductivity sensor for maritime applications”. masterThesis. Technische Universität Hamburg, 2021. DOI: 10.15480/882.4123 (cit. on pp. 81, 84–86, 88, 95).

[180] *80 MHz Low-Power SC70 Op Amp*. MIC920. Datasheet Rev. A (accessed 2023-02-18). Microchip Technology Inc. 2019-10. URL: https://www.microchip.com/en-us/product/MIC920 (cit. on pp. 87, 91, 94).

[181] *Single 60MHz, 20V/µs Low Power, Rail-to-Rail Input and Output Precision Op Amps*. LT6220. Datasheet Rev. C (accessed 2023-02-18). Analog Devices Inc. 2015-05. URL: https://www.analog.com/lt6220.html (cit. on p. 94).

[182] *Hot Swap Controller in 6-Lead TSOT Package*. LTC6268. Datasheet Rev. 0 (accessed 2023-02-19). Analog Devices Inc. 2014-09. URL: https://www.analog.com/ltc6268 (cit. on p. 94).

[183] *Precision CMOS, Single-Supply, Rail-to-Rail, Input/Output Wideband Operational Amplifiers*. AD8602. Datasheet Rev. I (accessed 2023-02-18). Analog Devices Inc. 2020-10. URL: https://www.analog.com/ad8602 (cit. on p. 94).

[184] J. P. Bentley. "Temperature sensor characteristics and measurement system design". In: *Journal of Physics E: Scientific Instruments* 17.6 (1984-06), p. 430. ISSN: 0022-3735. DOI: 10.1088/0022-3735/17/6/002 (cit. on pp. 96, 97).

[185] M. A. Hopcroft et al. "Using the temperature dependence of resonator quality factor as a thermometer". In: *Applied Physics Letters* 91.1 (2007-07), p. 013505. ISSN: 0003-6951. DOI: 10.1063/1.2753758 (cit. on p. 96).

[186] K.A.A. Makinwa. *Smart Temperature Sensor Survey*. 2022. URL: http://ei.ewi.tudelft.nl/docs/TSensor_survey.xls (visited on 2022-02-18) (cit. on p. 96).

[187] K. A.A. Makinwa. "Smart temperature sensors in standard CMOS". In: *Procedia Engineering* 5 (2010-01), pp. 930–939. ISSN: 1877-7058. DOI: 10.1016/J.PROENG.2010.09.262 (cit. on p. 96).

[188] *IEC 60751:2008 Industrial platinium resistance thermometer and platinum temperature sensors*. Standard. Geneva, CH: International Electrotechnical Commission, 2008 (cit. on p. 97).

[189] Franz E. Wudy et al. "Fast micro-kelvin resolution thermometer based on NTC thermistors". In: *Journal of Chemical and Engineering Data* 56.12 (2011-12), pp. 4823–4828. ISSN: 00219568. DOI: 10.1021/je200780h (cit. on pp. 97–99).

[190] Jiahao Li et al. "Investigation of Calibration Equations for Ntc Thermistors Utilized in the Deep-Ocean Temperature Range". In: *SSRN Electronic Journal* (2022). ISSN: 1556-5068. DOI: 10.2139/SSRN.4241492 (cit. on pp. 97, 98).

[191] J V Pearce et al. "Guide to the Realization of the ITS-90 Metal Fixed Points for Contact Thermometry". In: *Guide to the Realization of the ITS-90*. International Committee for Weights and Measures, 2021 (cit. on p. 97).

[192] Hugh Preston-Thomas et al. "The International Temperature Scale of 1990(ITS-90)". In: *metrologia* 27.1 (1990), pp. 3–10 (cit. on p. 97).

[193] John S. Steinhart and Stanley R. Hart. “Calibration curves for thermistors”. In: *Deep Sea Research and Oceanographic Abstracts* 15.4 (1968-08), pp. 497–503. ISSN: 0011-7471. DOI: 10.1016/0011-7471(68)90057-0 (cit. on p. 97).

[194] Harold J Hoge. “Useful procedure in least squares, and tests of some equations for thermistors”. In: *Review of scientific instruments* 59.6 (1988), pp. 975–979 (cit. on p. 97).

[195] Jae Pil Chung and Se Woon Oh. “A residual compensation method for the calibration equation of negative temperature coefficient thermistors”. In: *Thermochimica Acta* 616 (2015-09), pp. 27–32. ISSN: 0040-6031. DOI: 10.1016/J.TCA.2015.07.015 (cit. on pp. 97, 103).

[196] Guang Liu et al. “Evaluation of different calibration equations for NTC thermistor applied to high-precision temperature measurement”. In: *Measurement* 120 (2018-05), pp. 21–27. ISSN: 0263-2241. DOI: 10.1016/J.MEASUREMENT.2018.02.007 (cit. on pp. 97, 103).

[197] *PS Baureihe - Austauschbare Standard-Präzisionsthermistoren | Littelfuse, Inc.* 2022. URL: https://www.littelfuse.de/products/temperature-sensors/leaded-thermistors/interchangeable-thermistors/standard-precision-ps (visited on 2023-02-03) (cit. on p. 97).

[198] P. H. Sydenham and G. C. Collins. “Thermistor controller with microkelvin stability (for strainmeter testbase temperature control)”. In: *Journal of Physics E: Scientific Instruments* 8.4 (1975-04), p. 311. ISSN: 0022-3735. DOI: 10.1088/0022-3735/8/4/022 (cit. on p. 98).

[199] Sining Pan and Kofi A. A. Makinwa. “Wien Bridge–Based Temperature Sensors”. In: *Resistor-based Temperature Sensors in CMOS Technology*. Springer, Cham, 2022, pp. 31–66. ISBN: 978-3-030-95284-6. DOI: 10.1007/978-3-030-95284-6_3 (cit. on pp. 98, 99).

[200] Mina Shahmohammadi, Kianoush Souri, and Kofi A.A. Makinwa. “A resistor-based temperature sensor for MEMS frequency references”. In: *2013 Proceedings of the ESSCIRC (ESSCIRC)*. IEEE, 2013-09, pp. 225–228. ISBN: 978-1-4799-0645-1. DOI: 10.1109/ESSCIRC.2013.6649113 (cit. on p. 98).

[201] Pyoungwon Park, David Ruffieux, and Kofi A.A. Makinwa. “A thermistor-based temperature sensor for a real-time clock with ±2ppm frequency stability”. In: *IEEE Journal of Solid-State Circuits* 50.7 (2015-07), pp. 1571–1580. ISSN: 00189200. DOI: 10.1109/JSSC.2015.2417806 (cit. on p. 99).

[202] Hans van Haren. “Philosophy and Application of High-Resolution Temperature Sensors for Stratified Waters”. In: *Sensors* 18.10 (2018-09), p. 3184. ISSN: 1424-8220. DOI: 10.3390/s18103184 (cit. on p. 99).

[203] Hans van Haren et al. “NIOZ3: Independent Temperature Sensors Sampling Yearlong Data at a Rate of 1 Hz”. In: *IEEE Journal of Oceanic Engineering* 34.3 (2009-07), pp. 315–322. ISSN: 0364-9059. DOI: 10.1109/JOE.2009.2021237 (cit. on p. 99).

[204] H. van Haren et al. “A Fast and Accurate Thermistor String 1”. In: *Journal of Atmospheric and Oceanic Technology* 18.2 (2001-02), pp. 256–265. ISSN: 0739-0572. DOI: 10.1175/1520-0426(2001)018<0256:AFAATS>2.0.CO;2 (cit. on p. 99).

[205] P. K. Madhavan Unni, M. K. Gunasekaran, and A. Kumar. “±30 μK temperature controller from 25 to 103 °C: Study and analysis”. In: *Review of Scientific Instruments* 74.1 (2003-01), pp. 231–242. ISSN: 0034-6748. DOI: 10.1063/1.1529299 (cit. on p. 99).

[206] Andrew J. Skinner and Martin F. Lambert. “Using smart sensor strings for continuous monitoring of temperature stratification in large water bodies”. In: *IEEE Sensors Journal* 6.6 (2006-12), pp. 1473–1481. ISSN: 1530437X. DOI: 10.1109/JSEN.2006.881373 (cit. on pp. 99, 100).

[207] Niklas Torz. “Fehleranalyse und Optimierung eines kostengünstigen und energieeffizienten Temperatursensors für die Ozeanographie”. Bachelor Thesis. Hamburg University of Technology, 2023 (cit. on pp. 100–102).

[208] Matias Carandell et al. “Design and testing of a kinetic energy harvester embedded into an oceanic drifter”. In: *IEEE Sensors Journal* 20.23 (2020-12), pp. 13930–13939. ISSN: 15581748. DOI: 10.1109/JSEN.2020.2976517 (cit. on pp. 107, 108).

[209] Aurélien Babarit. *Ocean Wave Energy Conversion: Resource, Technologies and Performance*. Elsevier Inc., 2017-11, pp. 1–262. ISBN: 9780081023907. DOI: 10.1016/C2016-0-01219-6 (cit. on p. 107).

[210] Ge Shi et al. “A piezoelectric vibration energy harvester for multi-directional and ultra-low frequency waves with magnetic coupling driven by rotating balls”. In: *Applied Energy* 310 (2022-03), p. 118511. ISSN: 0306-2619. DOI: 10.1016/J.APENERGY.2021.118511 (cit. on p. 107).

[211] C. Rodrigues et al. “Integrated study of triboelectric nanogenerator for ocean wave energy harvesting: Performance assessment in realistic sea conditions”. In: *Nano Energy* 84 (2021-06), p. 105890. ISSN: 2211-2855. DOI: 10.1016/J.NANOEN.2021.105890 (cit. on p. 108).

[212] Wenjun Ding et al. “Experimental investigation on an ocean kinetic energy harvester for underwater gliders”. In: *2015 IEEE Energy Conversion Congress and Exposition, ECCE 2015* (2015-10), pp. 1035–1038. DOI: 10.1109/ECCE.2015.7309802 (cit. on p. 108).

[213] Matias Carandell et al. “Electromagnetic rolling mass wave energy harvester for oceanic drifter applications”. In: *The European Physical Journal Special Topics 2022 231:8* 231.8 (2022-03), pp. 1475–1484. ISSN: 1951-6401. DOI: 10.1140/EPJS/S11734-022-00499-5 (cit. on p. 108).

[214] Yunfei Li et al. “Study of an electromagnetic ocean wave energy harvester driven by an efficient swing body toward the self-powered ocean buoy application”. In: *IEEE Access* 7 (2019), pp. 129758–129769. ISSN: 21693536. DOI: 10.1109/ACCESS.2019.2937587 (cit. on p. 108).

[215] Deanelle Symonds, Edward Davis, and R. Cengiz Ertekin. “Low-power autonomous wave energy capture device for remote sensing and communications applications”. In: *2010 IEEE Energy Conversion Congress and Exposition, ECCE 2010 - Proceedings* (2010), pp. 2392–2396. DOI: 10.1109/ECCE.2010.5617902 (cit. on p. 108).

[216] Guoheng Wu et al. “Experimental Analysis of a Novel Adaptively Counter-Rotating Wave Energy Converter for Powering Drifters”. In: *Journal of Marine Science and Engineering 2019, Vol. 7, Page 171* 7.6 (2019-06), p. 171. ISSN: 2077-1312. DOI: 10.3390/JMSE7060171 (cit. on pp. 108, 109).

[217] Hangil Joe et al. “Development of a flap-type mooring-less wave energy harvesting system for sensor buoy”. In: *Energy* 133 (2017-08), pp. 851–863. ISSN: 0360-5442. DOI: 10.1016/J.ENERGY.2017.05.143 (cit. on p. 108).

[218] Scott J. Beatty et al. “Experimental and numerical comparisons of self-reacting point absorber wave energy converters in regular waves”. In: *Ocean Engineering* 104 (2015-08), pp. 370–386. ISSN: 0029-8018. DOI: 10.1016/J.OCEANENG.2015.05.027 (cit. on pp. 109, 115).

[219] Changwei Liang and Lei Zuo. “On the dynamics and design of a two-body wave energy converter”. In: *Renewable Energy* 101 (2017-02), pp. 265–274. ISSN: 0960-1481. DOI: 10.1016/J.RENENE.2016.08.059 (cit. on pp. 109, 115).

[220] Eko Sasmito Hadi et al. “Experimental Studies of Interaction Forces Affect the Position of Vertical Plates on Oscillating Heave Plates with Cylindrical Bodies in Regular Waves”. In: *International Journal of Renewable Energy Development* 9.1 (2020-02), pp. 77–84. ISSN: 2252-4940. DOI: 10.14710/IJRED.9.1.77-84 (cit. on pp. 109, 115).

[221] Larry Berggren and Mickey Johansson. “Hydrodynamic coefficients of a wave energy device consisting of a buoy and a submerged plate”. In: *Applied Ocean Research* 14.1 (1992-01), pp. 51–58. ISSN: 0141-1187. DOI: 10.1016/0141-1187(92)90007-7 (cit. on p. 109).

[222] Håvard Eidsmoen. “Hydrodynamic parameters for a two-body axisymmetric system”. In: *Applied Ocean Research* 17.2 (1995-01), pp. 103–115. ISSN: 0141-1187. DOI: 10.1016/0141-1187(95)00003-J (cit. on p. 109).

[223] Sébastien Olaya, Jean Matthieu Bourgeot, and Mohamed El Hachemi Benbouzid. “Hydrodynamic Coefficient Computation for a Partially Submerged Wave Energy Converter”. In: *IEEE Journal of Oceanic Engineering* 40.3 (2015-07), pp. 522–535. ISSN: 03649059. DOI: 10.1109/JOE.2014.2344951 (cit. on pp. 109, 176).

[224] Julius Harms et al. “Design and optimization of a wave energy converter for drifting sensor platforms in realistic ocean waves”. In: *Applied Energy* 321.February (2022), p. 119303. ISSN: 03062619. DOI: 10.1016/j.apenergy.2022.119303 (cit. on pp. 118–120, 139, 153, 175, 176).

[225] Yi Du et al. “Comparison of linear primary permanent magnet vernier machine and linear vernier hybrid machine”. In: *IEEE Transactions on Magnetics* 50.11 (2014), pp. 10–13. ISSN: 00189464. DOI: 10.1109/TMAG.2014.2317805 (cit. on pp. 124, 125).

[226] Pooja Khatri and Xu Wang. “Comprehensive review of a linear electrical generator for ocean wave energy conversion”. In: *IET Renewable Power Generation* 14.6 (2020-04), pp. 949–958. ISSN: 1752-1424. DOI: 10.1049/IET-RPG.2019.0624 (cit. on pp. 124, 125).

[227] Juan Antonio García-Alzórriz et al. “A novel double-sided flat rectangular linear permanent magnets synchronous generator for sea wave energy application”. In: *ELECO 2011 - 7th International Conference on Electrical and Electronics Engineering* (2011), pp. 248–252 (cit. on p. 125).

[228] Jing Zhang et al. “Design and Experimental Analysis of AC Linear Generator with Halbach PM Arrays for Direct-Drive Wave Energy Conversion”. In: *IEEE Transactions on Applied Superconductivity* 24.3 (2014), pp. 14–17. ISSN: 10518223. DOI: 10.1109/TASC.2013.2292640 (cit. on p. 125).

[229] Jordi Garcia-Amoros, Pere Andrada, and Baldui Blanque. “Linear Switched Reluctance Motors”. In: *Modelling and Control of Switched Reluctance Machines* (2020-09). DOI: 10.5772/intechopen.89166 (cit. on p. 125).

[230] Jinhua Du et al. “Modeling of a linear switched reluctance machine and drive for wave energy conversion using matrix and tensor approach”. In: *IEEE Transactions on Magnetics* 46.6 (2010), pp. 1334–1337. ISSN: 00189464. DOI: 10.1109/TMAG.2010.2041041 (cit. on p. 125).

[231] S. E. Rauch and L. J. Johnson. “Design Principles of Flux-Switch Alternators”. In: *Transactions of the American Institute of Electrical Engineers. Part III: Power Apparatus and Systems* 74.3 (1955), pp. 1261–1268. DOI: 10.1109/AIEEPAS.1955.4499226 (cit. on p. 125).

[232] Emmanuel Hoang, Hamid Ben Ahmed, and Jean Lucidarme. “Switching flux permanent magnet polyphased synchronous machines”. In: *EPE 97* V1 (1997) (cit. on p. 125).

[233] J. T. Chen and Z. Q. Zhu. “Winding configurations and optimal stator and rotor pole combination of flux-switching PM brushless AC machines”. In: *IEEE Transactions on Energy Conversion* 25.2 (2010), pp. 293–302. ISSN: 08858969. DOI: 10.1109/TEC.2009.2032633 (cit. on p. 125).

[234] J. Wang et al. “A tubular flux-switching permanent magnet machine”. In: *Journal of Applied Physics* 103.7 (2008), pp. 103–106. ISSN: 00218979. DOI: 10.1063/1.2830541 (cit. on pp. 125, 126).

[235] D. Lo et al. “Computation of cogging force of a linear tubular flux switching permanent magnet machine using a hybrid analytical modeling”. In: *2018 IEEE International Magnetic Conference, INTERMAG 2018* 54.11 (2018). DOI: 10.1109/INTMAG.2018.8508771 (cit. on p. 125).

[236] Z. Q. Zhu et al. “Novel linear flux-switching permanent magnet machines”. In: *Proceedings of the 11th International Conference on Electrical Machines and Systems, ICEMS 2008* (2008), pp. 2948–2953 (cit. on p. 125).

[237] C. F. Wang et al. “A novel permanent magnet flux-switching linear motor”. In: *IET Conference Publications* 538 CP (2008), pp. 116–119. DOI: 10.1049/cp:20080494 (cit. on p. 125).

[238] Lei Huang et al. “A novel flux-switching permanent-magnet linear generator for wave energy extraction application”. In: *IEEE Transactions on Magnetics* 47.5 (2011-05), pp. 1034–1037. ISSN: 00189464. DOI: 10.1109/TMAG.2010.2093509 (cit. on pp. 125, 134).

[239] Jiabin Wang et al. “Design considerations for tubular flux-switching permanent magnet machines”. In: *IEEE Transactions on Magnetics* 44.11 PART 2 (2008), pp. 4026–4032. ISSN: 00189464. DOI: 10.1109/TMAG.2008.2002773 (cit. on pp. 125, 133).

[240] Wei Hua et al. “Analysis and optimization of back EMF waveform of a flux-switching permanent magnet motor”. In: *IEEE Transactions on Energy Conversion* 23.3 (2008), pp. 727–733. ISSN: 08858969. DOI: 10.1109/TEC.2008.918612 (cit. on pp. 125, 133).

[241] O. Farrok et al. “Design and Analysis of a Novel Lightweight Translator Permanent Magnet Linear Generator for Oceanic Wave Energy Conversion”. In: *IEEE Transactions on Magnetics* 53.11 (2017), pp. 10–13. ISSN: 00189464. DOI: 10.1109/TMAG.2017.2713770 (cit. on pp. 125, 133).

[242] Lei Huang et al. “Research on a tubular primary permanent-magnet linear generator for wave energy conversions”. In: *IEEE Transactions on Magnetics* 49.5 (2013), pp. 1917–1920. ISSN: 00189464. DOI: 10.1109/TMAG.2013.2239981 (cit. on pp. 126, 134).

[243] Peter Benner, Serkan Gugercin, and Karen Willcox. “A Survey of Projection-Based Model Reduction Methods for Parametric Dynamical Systems”. In: *SIAM Review* 57.4 (2015-01), pp. 483–531. ISSN: 0036-1445. DOI: 10.1137/130932715 (cit. on p. 128).

[244] Julius Harms and Thorsten A Kern. “Pole Pitch Optimization of a Flux Switching Permanent Magnet Linear Machine for Small Scale Wave Energy Harvesting”. In: *ACTUATOR 2022; International Conference and Exhibition on New Actuator Systems and Applications*. IEEE, 2022, pp. 228–231. ISBN: 978-3-8007-5894-4 (cit. on pp. 133, 134).

[245] Doudou Sarr Lo et al. “Cogging force reduction in linear tubular flux switching permanent-magnet machines”. In: *Open Physics* 16.1 (2018), pp. 243–248. ISSN: 23915471. DOI: 10.1515/phys-2018-0035 (cit. on pp. 133, 134).

[246] Mahesh Patil and Pankaj Rodey. “Uncontrolled rectifier”. In: *SpringerBriefs in Applied Sciences and Technology* 156 (2015), pp. 1–7. ISSN: 21915318. DOI: 10.1007/978-81-322-2328-3_1/TABLES/2 (cit. on p. 141).

[247] Christian Peters et al. “An ultra-low-voltage active rectifier for energy harvesting applications”. In: *ISCAS 2010 - 2010 IEEE International Symposium on Circuits and Systems: Nano-Bio Circuit Fabrics and Systems* (2010), pp. 889–892. DOI: 10.1109/ISCAS.2010.5537413 (cit. on p. 141).

[248] *RF Energy Harvesting*. AEM30940. Datasheet Rev. 1.4 (accessed 2023-02-21). e-peas semiconductors. URL: https://e-peas.com/product/aem30940/ (cit. on p. 142).

[249] *Ultra Low power Harvester power Management IC with boost charger*. BQ25570. Datasheet Rev. G (accessed 2023-02-21). Texas Instruments Inc. 2018-12. URL: https://www.ti.com/product/BQ25570 (cit. on p. 142).

[250] *800-mA linear charger for 1-cell to 4-cell supercapacitor*. BQ25173. Datasheet Rev. A (accessed 2023-02-21). Texas Instruments Inc. 2021-11. URL: https://www.ti.com/product/BQ25173 (cit. on p. 142).

[251] *400mA Step-Up DC/DC Converter with Maximum Power Point Control and 250mV Start-Up*. LTC3105. Datasheet Rev. B (accessed 2023-02-21). Analog Devices Inc. 2015-11. URL: https://www.analog.com/LTC3105 (cit. on p. 142).

[252] *Linear SuperCap Charger with Current-Limited Ideal Diode and V/I Monitor*. LTC4425. Datasheet Rev. A (accessed 2023-02-21). Analog Devices Inc. 2016-02. URL: https://www.analog.com/LTC4425 (cit. on p. 142).

[253] *Ultralow Power Energy Harvester PMU with MPPT and Charge Management*. ADP5092. Datasheet Rev. A (accessed 2023-02-21). Analog Devices Inc. 2017-05. URL: https://www.analog.com/ADP5092 (cit. on p. 142).

[254] Matias Carandell et al. "Effect of the Sampling Parameters in FOCV-MPPT Circuits for Fast-Varying EH Sources". In: *IEEE Transactions on Power Electronics* 38.2 (2023-02), pp. 2695–2708. ISSN: 0885-8993. DOI: 10.1109/TPEL.2022.3216109 (cit. on p. 143).

[255] Richard H. Byrd, Mary E. Hribar, and Jorge Nocedal. "An Interior Point Algorithm for Large-Scale Nonlinear Programming". In: *SIAM Journal on Optimization* 9.4 (1999-01), pp. 877–900. ISSN: 1052-6234. DOI: 10.1137/S1052623497325107 (cit. on p. 153).

[256] *S-Beam Tension and Compression Load Cell*. 8512. Datasheet Rev. 0 (accessed 2023-02-21). burster präzisionsmesstechnik gmbh & co kg. URL: https://www.burster.de/en/sensors/load-cells/bending-beam-load-cells/p/detail/8512 (cit. on p. 159).

[257] L Dostal and E Kreuzer. "Probabilistic approach to large amplitude ship rolling in random seas". In: *Proceedings of the Institution of Mechanical Engineers, Part C: Journal of Mechanical Engineering Science* 225.10 (2011-10), pp. 2464–2476. ISSN: 0954-4062. DOI: 10.1177/0954406211414523 (cit. on p. 175).

[258] L. Dostal, E. Kreuzer, and N. Sri Namachchivaya. "Non-standard stochastic averaging of large-amplitude ship rolling in random seas". In: *Proceedings of the Royal Society A: Mathematical, Physical and Engineering Sciences* 468.2148 (2012-12), pp. 4146–4173. ISSN: 1364-5021. DOI: 10.1098/rspa.2012.0258 (cit. on p. 175).